

**STUDIES IN MULTI-SCALE TURBULENT DYNAMICS OF THE
SOLAR WIND**

by
Rohit Chhiber

A dissertation submitted to the Faculty of the University of Delaware in partial fulfillment of the requirements for the degree of Doctor of Philosophy in Physics

Summer 2018

© 2018 Rohit Chhiber
All Rights Reserved

**STUDIES IN MULTI-SCALE TURBULENT DYNAMICS OF THE
SOLAR WIND**

by

Rohit Chhiber

Approved: _____
Edmund R. Nowak, Ph.D.
Chair of the Department of Physics and Astronomy

Approved: _____
George H. Watson, Ph.D.
Dean of the College of Arts and Sciences

Approved: _____
Ann L. Ardis, Ph.D.
Senior Vice Provost for Graduate and Professional Education

I certify that I have read this dissertation and that in my opinion it meets the academic and professional standard required by the University as a dissertation for the degree of Doctor of Philosophy.

Signed: _____

William H. Matthaeus, Ph.D.
Professor in charge of dissertation

I certify that I have read this dissertation and that in my opinion it meets the academic and professional standard required by the University as a dissertation for the degree of Doctor of Philosophy.

Signed: _____

Michael A. Shay, Ph.D.
Member of dissertation committee

I certify that I have read this dissertation and that in my opinion it meets the academic and professional standard required by the University as a dissertation for the degree of Doctor of Philosophy.

Signed: _____

Dermott Mullan, Ph.D.
Member of dissertation committee

I certify that I have read this dissertation and that in my opinion it meets the academic and professional standard required by the University as a dissertation for the degree of Doctor of Philosophy.

Signed: _____

I. Pablo Huq, Ph.D.
Member of dissertation committee

ACKNOWLEDGEMENTS

I would like to thank and acknowledge my thesis advisor, Bill Matthaeus, for being a mentor and a friend, and a constant source of inspiration and encouragement. Working with Bill over the last several years has been great fun, and has helped me grow both professionally and personally.

I am indebted to Arcadi Usmanov and Minping Wan for helping me get started with the simulations I have employed in my research. Arcadi introduced me to his global solar-wind code and provided several runs used in this dissertation. Minping provided valuable mentorship during the initial stages of my PhD career and introduced me to spectral MHD codes.

I began my study of turbulence and space physics alongside Tulasi Parashar, Jeffrey Tessein, and Prachanda Subedi, and I continue to cherish the camaraderie we have shared over the years. I would also like to acknowledge my other collaborators in research: Dave Ruffalo, Mel Goldstein, Craig DeForest, and Riddhi Bandyopadhyay. A special note of thanks to Alex Chasapis for initiating me into spacecraft-data analysis.

I have benefitted from discussions with several professors, colleagues, and visitors at the DPA, including Yan Yang, Colby Haggerty, Prayash Sharma, Debanjan Sengupta, Arakel Petrosyan, Francesco Pucci, Sean Oughton, Kittipat Malakit, Bennett Maruca, Ramiz Qudsi, and Mark Pultrone. Daniel DeMarco, Sansern Somboonsong, and Zelfhia Johnson were always responsive and helpful regarding computer-related issues. My dissertation committee members – Mike Shay, Dermott Mullan, and Pablo Huq – provided valuable feedback that has helped improve this thesis.

Finally, I would like to acknowledge my debt to the wonderful administrators and secretaries (especially Maura Perkins) who keep the administrative machinery

of the Department running smoothly, while cheerfully indulging the administrative absent-mindedness of us physicists.

TABLE OF CONTENTS

LIST OF TABLES	xi
LIST OF FIGURES	xii
ABSTRACT	xxiii
 Chapter	
1 INTRODUCTION	1
1.1 Background	1
1.1.1 The Discovery of the Solar Wind	1
1.1.2 Basic Properties of the Solar Wind	2
1.1.3 Heating and Acceleration of the Solar Wind	6
1.1.4 Turbulence in the Solar Wind	8
1.1.5 Modeling and Simulation of Turbulent Flows	13
1.1.6 Modeling and Simulation of Solar Wind Turbulence	19
1.1.7 Some Applications of Global Solar Wind Simulations with Turbulence Transport	22
1.2 Overview	25
2 MODELING THE SOLAR WIND	27
2.1 Parker's Hydrodynamic Model of the Solar Wind	27
2.2 The MHD Description of the Solar Wind	33
2.2.1 The Equations of MHD	33
2.2.2 Applicability of the MHD Description to the Solar Wind	36
2.2.3 Magnetohydrodynamic Waves	39
2.2.4 Elsässer Variable Representation of the MHD Equations	42
2.3 WKB Theory of Solar Wind Fluctuations	43

3	TURBULENCE	46
3.1	The Kolmogorov Theory	46
3.1.1	The Navier–Stokes Equation in Fourier Space	47
3.1.2	Spectral Transfer of Energy	49
3.1.3	The Kolmogorov Hypotheses	51
3.2	Closure Models for Turbulence	52
3.2.1	Eddy Viscosity Models	53
3.2.2	Turbulent Kinetic Energy and k - ϵ Models	54
3.2.3	Spectral Closure Models	57
3.3	MHD Turbulence in the Solar Wind	60
3.3.1	Cascades and Anisotropy in MHD Turbulence	60
3.3.2	Closure Models for MHD Turbulence	65
4	SOLAR WIND MODEL WITH TURBULENCE TRANSPORT AND HEATING	67
4.1	Two-fluid MHD Equations for the Solar Wind	67
4.2	Reynolds-averaged Mean-flow Equations	69
4.3	Modeling Collisional Energy Exchange and Electron Heat Flux	71
4.4	Turbulence Transport Equations	72
4.5	The Eddy Viscosity Approximation	77
4.6	Numerical Implementation and Initial/Boundary Conditions	79
4.7	Sample Solutions	82
5	COLLISIONAL AGE OF THE SOLAR WIND	88
5.1	Introduction	88
5.2	Background and Motivation	88
5.3	Three Formulations of Collisional Age	91
5.4	Simulation Results	94
5.5	Conclusions	100
5.A	Collisional Age vs Knudsen Number	102
5.B	Turbulence Age of the Solar Wind	102
6	COSMIC RAY DIFFUSION COEFFICIENTS THROUGHOUT	

THE INNER HELIOSPHERE	105
6.1 Introduction	105
6.2 Cosmic Ray Diffusion Tensor	109
6.2.1 Parallel Mean Free Path	111
6.2.2 Perpendicular Mean Free Path	112
6.3 Solar Wind Model	117
6.4 Simulation Results	119
6.4.1 Solar Wind Model Results	119
6.4.2 Radial Evolution of Mean Free Paths	121
6.4.3 Latitudinal Evolution of Mean Free Paths	127
6.4.4 Rigidity Dependence of Mean Free Paths	128
6.4.5 Meridional Plane Contours of Mean Free Paths	131
6.5 Conclusions and Discussion	133
6.A Turbulent Drag Coefficient	138
INTERLUDE I	140
7 WEAKENED MAGNETIZATION AND ONSET OF LARGE-SCALE TURBULENCE IN THE YOUNG SOLAR WIND — COMPARISONS OF REMOTE SENSING OBSERVATIONS WITH SIMULATION	141
7.1 Introduction	141
7.2 Background	141
7.3 Insights from <i>STEREO</i> Heliospheric Imaging	143
7.4 Solar Wind Model	145
7.5 Results	145
7.6 Discussion and Conclusions	151
7.A Range of Influence of Turbulence in Solar Wind Fluctuations: Estimating a Causality Threshold	154
7.A.1 Introduction	154
7.A.2 A Simple Estimate of the Causality Threshold	155
7.A.3 Numerical Estimates from Simulations and Observations	158
7.A.4 Discussion	161
8 CONTEXTUAL PREDICTIONS FOR PARKER SOLAR	

PROBE: CRITICAL SURFACES AND REGIONS	167
8.1 Introduction	167
8.2 Theoretical and Observational Background	169
8.3 Sampling of the Three-dimensional Heliosphere by Parker Solar Probe	171
8.4 Results	172
8.4.1 Surfaces: Meridional Plane Pictures	174
8.4.2 Remote Sensing Context	177
8.4.3 What <i>PSP</i> will see: Dipole-based Simulations	182
8.4.4 What <i>PSP</i> will see: Magnetogram-based simulations	187
8.5 Conclusions and Discussion	189
8.A Contextual Predictions for Parker Solar Probe: Turbulence and Taylor Hypothesis	192
8.A.1 Turbulence Properties along <i>PSP</i> trajectory	192
8.A.2 Validity of Taylor Hypothesis along <i>PSP</i> Trajectory	193
INTERLUDE II	201
9 MULTI-SPACECRAFT ANALYSES OF HIGHER-ORDER TURBULENCE STATISTICS IN THE EARTH'S MAGNETOSHEATH AND THE SOLAR WIND USING MAGNETOSPHERIC MULTISCALE OBSERVATIONS	202
9.1 Introduction	202
9.2 MMS Observations in the Solar Wind and the Magnetosheath	204
9.3 Diagnostics of Intermittent Turbulence	205
9.4 Computation of Magnetic Field Increments	211
9.5 Structure Functions and Spectra	212
9.6 Probability Density Functions	216
9.7 Scale-dependent Kurtosis	219
9.8 Conclusions and Discussion	221
10 CONCLUSIONS AND FUTURE WORK	225
BIBLIOGRAPHY	230
Appendix	
A PROPERTIES OF THE SOLAR WIND	260

B	ISOTROPIC TURBULENCE	262
B.1	Introduction	262
B.1.1	The Study of Homogeneous and Isotropic Turbulence	262
B.1.2	Mathematical Formulation of the Problem	263
B.2	Isotropic Turbulence in Real Space	263
B.2.1	Kinematics	263
B.2.1.1	Velocity Correlation Functions and Structure Functions	264
B.2.1.2	The Simplifications of Isotropy	267
B.2.2	Dynamics	269
B.3	Isotropic Turbulence in Spectral Space	271
B.3.1	The Transform of the Correlation Tensor and the Energy Spectrum	271
B.3.2	An Evolution Equation for $E(k)$	272
C	WKB ALFVÉN WAVE MODEL FOR THE SOLAR WIND	274
D	INVARIANCE OF AVERAGING METHODS FOR TURBULENCE SIMULATION	276
D.1	Implicit Averaging – Discretizing on a Numerical Grid	276
D.2	Reynolds Averaging (RA)	277
D.3	Filtering and LES	277
D.4	Generalized Central Moments and Averaging Invariance of the MHD Equations	278
E	PERMISSION LETTERS	282
E.1	Permission from Annual Reviews for Figure 1.6	282
E.2	Permission from Dr. Tulasi Parashar for Figure 2.2	283
E.3	Permission from the American Physical Society and Dr. William Matthaeus for Figure 3.1	284
E.4	Permission from Springer Nature for Figure 8.4	286
E.5	Permission from Dr. Prachanda Subedi for Figure B.1	287

LIST OF TABLES

4.1	Summary of constant model parameters	79
4.2	Boundary values used in the initial state for sample run	81
6.1	Parallel mfps in AU for 100 MeV protons at in the ecliptic region at 1 AU. B1, B2, and B3 are from Breech et al. [2008] ; P1 and P2 are from Pei et al. [2010] ; Cases 1 - 3 are our solutions for varying turbulence levels. Note that our calculation of λ_{\parallel} is independent of p .	127
9.1	Description of selected MMS data intervals and their average plasma properties. Here ‘MSH’ denotes magnetosheath and ‘SW’ denotes solar wind; The ‘Separation’ column indicates the mean separation between spacecraft; $ \langle \mathbf{B} \rangle $ is the absolute value of the mean magnetic field; $\delta B \equiv \sqrt{\langle \mathbf{B}(t) - \langle \mathbf{B} \rangle ^2 \rangle}$ is the rms magnetic fluctuation; $\langle n \rangle$ is the mean plasma density; d_i and d_e are the ion and electron inertial scales, respectively; β_p is the proton beta; V_A and V are the mean Alfvén speed and mean flow speed, respectively.	208
A.1	Properties of the interplanetary medium at 1 au in the ecliptic. . .	260
A.2	Characteristic lengths in the solar wind.	260
A.3	Characteristic times in the solar wind.	261
A.4	Characteristic speeds in the solar wind at 1 au.	261

LIST OF FIGURES

1.1	Meridional plane view showing the latitudinal distribution of solar wind speeds measured by <i>Ulysses</i> during its first polar orbit [McComas et al., 2000]. The background is a composite of three coronagraph images. <i>Image courtesy of NASA Marshall Space Flight Center.</i>	3
1.2	A sketch of the Archimedian spiral formed by the interplanetary magnetic field under the influence of the Sun’s rotation. <i>Image courtesy of NASA Goddard Space Flight Center.</i>	4
1.3	Artist’s concept of the heliosphere interacting with the interstellar medium. The hypothetical bow-shock/wave [e.g., Zank et al., 2013; Usmanov et al., 2016a] is depicted, along with the heliopause and the termination shock (see text). <i>Image courtesy of NASA.</i>	5
1.4	Formation of vortices in turbulent flow, seen in a study of falling water by Leonardo da Vinci, circa. 1508–9. <i>Image under public domain. Source: http://www.drawingsofleonardo.org/</i>	8
1.5	<i>Helios 2</i> observations of power density spectra of magnetic field fluctuations between 0.3 and 1 au. <i>Figure reproduced from Bruno and Carbone [2013] under the Creative Commons Attribution-Non-Commercial 3.0 Germany License.</i>	10
1.6	Schematic of turbulent cascade of energy. Recall that wavenumber is the inverse of spatial length, so the positive x -axis is in the direction of decreasing spatial scale. <i>Figure reproduced from Goldstein et al. [1995] with permission from Annual Reviews (see Appendix E).</i> . . .	10
2.1	The topology of solutions of Equation (2.5). Here $u_c \equiv a$, the isothermal sound speed.	30

2.2	Solutions of the isothermal Parker model of the solar wind (Equation 2.7). Heliocentric distance r is in m and the solar wind speed V_{sw} is in km s^{-1} . <i>Figure reproduced from Parashar [2011] with permission (see Appendix E).</i>	31
3.1	Comparison of hydrodynamics and MHD: (a) In hydrodynamics a mean or large-scale flow sweeps the small-scale eddies without affecting the energy transfer between length scales; (b) in MHD a mean or large-scale magnetic field \mathbf{B} sweeps oppositely propagating Alfvénic fluctuations \mathbf{z}_{\pm} , which affects the energy transfer, illustrated as distortions after the two types of fluctuation have passed through each other (see text). <i>Figure reproduced from Zhou et al. [2004] with permission from APS (see Appendix E).</i>	62
3.2	Visualization of fluctuations, energy spectra in the wavevector domain, and spatial correlation lengths ℓ , for 2D geometry (left) and slab geometry (right). Fluctuations with 2D geometry have wavevectors perpendicular to \mathbf{B}_0 and those with slab geometry have wavevectors aligned with \mathbf{B}_0 . <i>Figure reproduced from Narita [2018] under the Creative Commons Attribution 4.0 International License.</i>	64
4.1	Inner-region ($1 - 30 R_{\odot}$) results in the meridional plane at heliolongitude $\phi = 0.75^{\circ}$, from a simulation employing a solar dipole tilted by 10° relative to the solar rotation axis. The fields shown are: (a) radial velocity u_r , (b) proton density N_S , (c) magnetic field magnitude B , (d) turbulence energy density Z^2 , (e) cross helicity σ_c , (f) correlation scale of the fluctuations λ , (g) proton temperature T_S , (h) electron temperature T_E , and (i) meridional velocity u_{θ} [Usmanov et al., 2018].	83
4.2	Description follows from Figure 4.1, with a view of the outer region ($30 R_{\odot} - 5 \text{ au}$) [Usmanov et al., 2018].	84
4.3	Radial profiles along the pole for varying coronal base temperature T_0 . The fields shown are (a) radial velocity u_r , (b) proton temperature T_S , (c) electron temperature T_E , (d) turbulence energy density Z^2 , (e) correlation scale of the fluctuations λ , and (f) cross helicity σ_c [Usmanov et al., 2018].	85

4.4	Simulated profiles (red) for a source magnetic dipole on the Sun tilted by 10° (with respect to the solar rotation axis) versus <i>Ulysses</i> daily averages of plasma and magnetic field parameters measured during the first fast latitude transit of (Sep 13, 1994 to July 31, 1995). The parameters shown are: (a) the radial velocity u_r , (b) the number density of solar wind protons N_S and (c) their temperature T_S , (d) the radial B_r and (e) the azimuthal B_ϕ magnetic field, and (f) the electron temperature T_E . Two estimates of the proton temperature measured by <i>Ulysses</i> , “T-large” and “T-small”, are shown by solid and dotted lines, respectively [Usmanov et al., 2018].	86
5.1	Two-dimensional histograms of distributions of $T_{\perp p}/T_{\parallel p}$, T_α/T_p , and $\Delta V_{\alpha p}/C_A$ as functions of solar wind speed (left) and Coulomb number N_C (right). While nonthermal solar wind is generally associated with high speeds, these distributions suggest that the occurrence frequency is really determined by the Coulomb number N_C (equivalent to the local collisional age defined by Equation 5.6. <i>Figure reproduced from Kasper et al. [2017] under the Creative Commons Attribution 3.0 licence.</i>	90
5.2	Timescales as a function of radial distance, at 15° heliolatitude: collision timescale τ_c , expansion timescales τ_{exp1} and τ_{exp2} as defined in the text; nonlinear timescale τ_{NL}	96
5.3	Scatter of the timescales with varying heliolatitude; the solar equator is represented by black, with the color of the lines turning red towards the pole.	96
5.4	Comparison of A_c , A_{c1} , and A_{c2} at (top) 0° and (bottom) 55° heliolatitude. Dotted-dashed lines in green represent A_c , the numerically integrated age (Equation 5.5) for different initial positions. Solid black line is A_{c1} , the age computed using the point-wise formula Equation (5.6). Solid red line is A_{c2} , the analytical formula in Equation (5.9). The vertical dotted purple line is the approximate perihelion of <i>PSP</i> , $9 R_\odot$. The two vertical dashed blue lines mark the outer boundaries of the “inner region” and the “intermediate region” in the simulation (Appendix C).	98
5.5	Meridional planes from a 30° -tilted-dipole simulation showing the numerically integrated collisional age A_c with (a) $r_0 = 7 R_\odot$ and (b) $r_0 = 44 R_\odot$	100

5.B.1	Radial evolution of turbulence (black curves) and collisional (red curves) ages at 15° heliolatitude, computed from an untilted dipole simulation. The initial point of integration is taken at $45 R_\odot$; The dashed (dotted) curves represent solutions with turbulence levels doubled (halved) relative to a reference value (solid curve).	104
5.B.2	Meridional plane variation computed using the same parameters as in Figure 5.B.1.	104
6.1	Model results near the ecliptic plane, for a run with an untilted solar dipole, are compared with observational data from <i>Voyager 2</i> , <i>Helios</i> , and the NSSDC Omnitape. The Z^2 data are from Zank et al. [1996], and the λ data are from Smith et al. [2001]. The solid lines are from our simulations. The different symbols represent different methods of calculation. The dashed vertical lines represent the boundaries of the different simulation regions, with red marking the inner-intermediate region boundary at $20 R_\odot$, and blue marking the intermediate-outer region boundary at $45 R_\odot$, respectively. Note that the observations are for various times in the solar cycle, and are shown here for general context only.	121
6.2	Contour plots of the heliospheric magnetic field (B), the turbulence correlation scale (λ), and the turbulence energy (Z^2) in the meridional plane for an untilted solar dipole. The figures on the left cover $2 - 45 R_\odot$, and the ones on the right cover $0.21 - 3$ AU ($45 - 645 R_\odot$).	122
6.3	Radial dependence of the parallel (black), perpendicular (red), and radial (blue) mfps (a) near the ecliptic plane (7° heliolatitude) and (b) near the pole (86° heliolatitude). Also shown is $\lambda_\perp/\lambda_\parallel$ (green). The solid lines are for $p = -1$, the dotted lines for $p = 0$, the dashed lines for $p = 1$, and the dash-dotted lines for $p = 2$. Proton rigidity is 445 MV (100 MeV kinetic energy). Note that the curves for λ_\parallel and λ_{rr} coincide in (b).	123
6.4	Radial dependence of the parallel (black), perpendicular (red), and radial (blue) mfps near the ecliptic plane (7° heliolatitude), with a solar dipole having a 30° tilt. For our particular choice of azimuthal angle (26°), an HCS crossing occurs at 0.8 AU. Also shown is $\lambda_\perp/\lambda_\parallel$ (green). The solid lines are for $p = -1$, the dotted lines for $p = 0$, the dashed lines for $p = 1$, and the dash-dotted lines for $p = 2$. Proton rigidity is 445 MV (100 MeV kinetic energy).	125

6.5	Radial dependence of the parallel (black), perpendicular (red), and radial (blue) mfps (a) near the ecliptic plane (7° heliolatitude) and (b) in the polar region (86°), for varying turbulence amplitudes, with $p = 2$. The dashed and dotted lines represent simulations with the turbulence energy (Z^2) at the inner boundary of the outer region ($45 R_\odot$) doubled and halved, respectively, relative to a standard level. See text for more details. Note that the curves for λ_{\parallel} and λ_{rr} coincide in (b).	126
6.6	The top panel (a) shows the latitudinal dependence of parallel (solid lines) and perpendicular (dashed lines) mfps. The middle (b) and bottom (c) panels show the latitudinal variation of λ_{rr} and $\lambda_{\perp}/\lambda_{\parallel}$, respectively. All panels are for an untilted solar dipole and $p = 2$. Black, blue, green, and red lines represent radial distances of 0.02, 0.2, 1, and 3 AU (4, 45, 215, and $645 R_\odot$), respectively. Proton rigidity is 445 MV (100 MeV kinetic energy).	129
6.7	Rigidity dependence of λ_{\parallel} (solid line) and λ_{\perp} (dashed line), (a) near the ecliptic plane (7° heliolatitude), and (b) in the polar regions (86° heliolatitude), for an untilted solar dipole and $p = 2$. Black, blue, green, and red lines represent radial distances of 0.02, 0.2, 1, and 3 AU (4, 45, 215, and $645 R_\odot$), respectively.	130
6.8	Contour plots in the meridional plane of mfps, with a solar dipole that is untilted with respect to the solar rotation axis. The inner and intermediate regions ($2 - 45 R_\odot$) and the outer region ($0.21 - 3$ AU, or $45 - 645 R_\odot$) are shown separately. Proton rigidity is 445 MV (100 MeV kinetic energy) and $p = 2$	132
6.9	Contour plots of mfps in the meridional plane with azimuthal angle of 26° , with a solar dipole tilted 30° with respect to the solar rotation axis. The inner and intermediate regions ($2 - 45 R_\odot$) and the outer region ($0.21 - 3$ AU, or $45 - 645 R_\odot$) are shown separately. Proton rigidity is 445 MV (100 MeV kinetic energy) and $p = 2$	134
6.A.1	Turbulent drag coefficient computed from a simulation with a solar dipole that is untilted with respect to the solar rotation axis. The inner and intermediate regions ($2 - 45 R_\odot$) and the outer region ($0.21 - 3$ AU, or $45 - 645 R_\odot$) are shown separately.	139
7.1	Data from <i>Ulysses</i> ' fast latitude scan during 2007 – 2008 compared with Run II.	147

7.2	Left and center: Contours of proton density in a meridional plane from Run I (untilted dipole). Dotted black, solid white, and dashed green curves show sonic, Alfvén, and $\beta = 1$ surfaces. Right: Surfaces computed from the model superimposed on a processed <i>STEREO</i> image from Dec 16, 2008. <i>Helios</i> perihelion is shown as ‘ \oplus ’; first three perihelia of PSP are shown as ‘ \otimes ’.	148
7.3	Left and center: Contours of proton density in a meridional plane from Run II (Dec 2008 magnetogram). Right: Surfaces computed from the model superimposed on a processed <i>STEREO</i> image from Dec 16, 2008. Description of curves and symbols follows Figure 7.2.	148
7.4	Top: Structure functions of magnetic field from Run II at $20 - 60 R_{\odot}$. Black (red) solid (dashed) curve represents lag in the radial (polar) direction. Bottom: Ratio of polar structure function to radial structure function, computed at different heliocentric distances. A clear trend towards isotropization with increasing distance is evident.	150
7.A.1	(a) Diagram of homogeneous case. (b) Diagram of expanding case with constant radial speed U . The turbulent speeds associated with the points P and P’ are labeled v and v' , respectively. The expanding circles indicate the region of causal influence of turbulence.	156
7.A.2	Radial evolution of the turbulence region of influence L_T (solid black line) and the correlation scale λ (dotted blue line) computed from the simulation in the ecliptic plane. The dashed green line shows a least-squares fit to solar wind spacecraft data [Ruiz et al., 2014] that yields the power law $\lambda(r) = 0.89(r/1 \text{ AU})^{0.43} \times 10^6 \text{ km}$. The black diamonds represent L_T computed from spacecraft measurements. The tan-colored bar indicates the region where the flocculation is observed in <i>STEREO</i> images (Figure 7.2), and the approximate size of the flocculae (3 – 6 Gm). The radial locations of the innermost three perihelia of the <i>PSP</i> are shown as \oplus .	159
7.A.3	Meridional plane contours of the correlation scale λ , the turbulent ROI L_T , and their ratio λ/L_T .	160
7.A.4	Meridional plane contours of solar wind speed; circles represent an estimate of the expanding region of influence of turbulent fluctuations, starting from $20 R_{\odot}$ (above the Alfvén point). The red (blue) circles represent the ROI of a point at 60° (35°) heliolatitude.	162

7.A.5	Meridional plane contours of solar wind speed; circles represent an estimate of the expanding region of influence of turbulent fluctuations, starting from $20 R_{\odot}$ (above the Alfvén point). The red (blue) circles represent the ROI of a point at 60° (40°) heliolatitude.	162
7.A.6	Meridional plane contours of solar wind speed; circles represent an estimate of the expanding region of influence of turbulent fluctuations, starting from $20 R_{\odot}$ (above the Alfvén point). The red (blue) circles represent the ROI of a point at a low heliolatitude of 12° (-13°). The two points with an initial angular separation of 25° may influence each other via turbulence, in contrast to the high-latitude case in Figure 7.A.4.	163
7.A.7	Here we assume that the turbulent speed of propagation stays constant with heliocentric distance. At the Alfvén point, this speed is $\sim 100 \text{ km s}^{-1}$. The red and blue points lie at heliolatitudes of 60° and 30° , respectively.	163
7.A.8	Turbulence ROI from the simulation superposed on a <i>STEREO</i> image showing the development of flocculation.	164
8.1	<i>PSP</i> trajectory in HCI coordinates (see text for details). The origin is the Solar center of mass and the <i>XY</i> -plane is the Solar equatorial plane. The red curves show the trajectory in 3D space and the blue curves are its projections onto the <i>XY</i> , <i>XZ</i> , and <i>YZ</i> planes. The ‘*’ symbol and blue dot represent the positions of the Sun and Earth, respectively.	173
8.2	Meridional planes from untilted dipole Run I-A (top) and 30° tilted dipole Run I-D (bottom). The black curves show the sonic surface (solid line using c_s with just proton pressure and dashed line using c'_s which includes proton and electron pressures; see text), the white curve shows the Alfvén surface, and the green curves show the first unity β surface (solid line shows $\beta_p = 1$ and dashed line shows $\beta_{p+e} = 1$).	176
8.3	Green curves show the first unity beta surfaces (solid line for $\beta_p = 1$; dashed line for $\beta_{p+e} = 1$) computed from the model superimposed on <i>STEREO</i> image from DeForest et al. [2016]. White ‘+’ shows location of enhanced turbulence inferred by Lotova et al. [1985] (see Figure 8.6); <i>Helios</i> perihelion is shown as ‘ \oplus ’; the lowest three perihelia of the <i>PSP</i> are shown as ‘ \otimes ’.	178

8.4	<p>Transonic regions from Lotova et al. [1997], showing the transition from spherically symmetric but jagged morphology at solar maximum (1989), to oblateness at the poles during solar minimum (1994; see Figure A.1). <i>Figure reproduced from Lotova et al. [1997] with permission from Springer Nature (see Appendix E).</i></p>	180
8.5	<p>Sonic surfaces (solid line using c_s with just proton pressure and dashed line using c'_s which includes proton and electron pressures; see text) from Runs II-A and II-B, using solar maximum (July 1989) and solar minimum (July 1994) magnetograms, respectively. The transition from solar maximum to solar minimum is qualitatively consistent with the one seen in Figure 8.4.</p>	181
8.6	<p>Enhanced scintillation ($m\nu$) region from the observations of Lotova et al. [1985], seen as a bump at $\sim 20 - 30 R_\odot$ in the dashed red curve. The radial solar wind speed V_r (dotted blue curve) and the turbulence energy density (per unit mass) Z^2 (solid black curve) from Run I-A are also shown, along with shaded bands representing the locations of the Alfvén (pale blue band) and sonic (grey band) surfaces in the ecliptic region of the simulation. The final three perihelia of the <i>PSP</i> are represented as \oplus symbols.</p>	183
8.7	<p><i>PSP</i> crossings of the critical surfaces are illustrated by a sequence of meridional planes that contain the spacecraft trajectory. The 8th orbit is depicted in a 10° dipole simulation (Run I-C; see top panel of Figure 8.9), representing solar-minimum conditions. The sonic, Alfvén, and first (proton+electron) beta unity surfaces are depicted as solid pink, solid blue, and dashed green curves, which are superposed on contours of proton density. The <i>PSP</i> position is at the center of the yellow ‘+’ symbol. A video animation is available online.</p>	184
8.8	<p><i>PSP</i> surface crossings from simulations with 0° (top) and 5° (bottom) dipole tilt. In each plot, the top section shows the radial and latitudinal position of the <i>PSP</i> for each orbit, and the radial position of the critical surfaces, at the angular position of the <i>PSP</i>. The bottom section shows the time spent by the <i>PSP</i> under each surface, per orbit. The striped green, lavender, and narrow red bars represent the $\beta = 1$, Alfvén, and sonic surfaces, respectively.</p>	186
8.9	<p><i>PSP</i> surface crossings from simulations with a 10° (top) and a 30° (bottom) dipole tilt. The description of the elements of the figures follows Figure 8.8.</p>	188

8.10	<i>PSP</i> surface crossings for a July 1994 solar minimum magnetogram run (top) and a July 1989 solar max magnetogram run (bottom). The description of the elements of the figures follows Figure 8.8.	190
8.A.1	Top: Turbulence energy density Z^2 (units of $\text{km}^2 \text{s}^{-2}$) in a meridional plane in the region $1 - 30 R_{\odot}$, from an untilted dipole simulation. Bottom: Z^2 along <i>PSP</i> trajectory for selected orbits. Direction of arrows indicates inward/outward sections of orbits.	194
8.A.2	Top: Correlation scale of fluctuations (λ ; units of R_{\odot}) in a meridional plane in the region $1 - 30 R_{\odot}$, from an untilted dipole simulation. Bottom: λ along <i>PSP</i> trajectory for selected orbits. Direction of arrows indicates inward/outward sections of orbits.	195
8.A.3	Top: Normalized cross helicity σ_c in a meridional plane in the region $1 - 30 R_{\odot}$, from an untilted dipole simulation. Bottom: σ_c along <i>PSP</i> trajectory for selected orbits. Direction of arrows indicates inward/outward sections of orbits.	196
8.A.4	Relative strength of the two Elsässer modes along the <i>PSP</i> trajectory.	197
8.A.5	Top: The plotted ratios compare the transit speed of the solar wind plasma in the <i>PSP</i> frame $ \mathbf{U}_w - \mathbf{V}_{PSP} $ to the Alfvén speed V_A (solid blue curve) and the characteristic speed of turbulent distortion $\delta V = Z$ (dashed black curve). Directions of arrows indicate ingoing and outgoing parts of the <i>PSP</i> trajectory. Regions shaded green, orange, and red represent, respectively, high (ratio < 0.1), moderate ($0.10 < \text{ratio} < 0.33$), and low (ratio > 0.33) degrees of validity of the Taylor hypothesis. Bottom: Tests of “modified” Taylor hypotheses along the <i>PSP</i> trajectory (see text).	199
9.1	Artist’s impression of the Earth’s magnetosphere. <i>Image courtesy of NASA/Goddard/Aaron Kaase.</i>	203
9.2	Top: MMS orbit on 2016 January 24, when the spacecraft was in the magnetosheath. Bottom: MMS1 observations of the components of magnetic field strength.	206
9.3	Top: MMS orbit on 2017 November 24, when the spacecraft was in the solar wind. Bottom: MMS1 observations of the components of magnetic field strength.	207

9.4	MMS formation on 2016 January 24, when the spacecraft was in the magnetosheath. For our purposes, the configuration on 2017 November 24 was similar to the one shown here.	209
9.5	Second, fourth, and sixth-order structure functions of B_x (solid lines) in (top) magnetosheath and (bottom) solar wind. Structure functions of B_y and B_z are shown as dashed and dotted lines. Two-spacecraft structure functions of B_x are plotted using filled symbols that indicate different spacecraft pairings, labeled in the top right corner of each panel. Note that structure functions of order p have been normalized by the p^{th} power of the rms magnetic fluctuation, and the lag ℓ has been normalized to units of the ion inertial length d_i . The single-spacecraft structure functions have been computed using MMS1 measurements.	214
9.6	Equivalent spectra computed from the second-order structure function of the x -component of the magnetic field, in the magnetosheath (top) and the solar wind (bottom), shown as a function of equivalent wavenumber $k^* = 1/\lambda$, where λ is the lag. The single-spacecraft MMS1 result is shown as a solid black line, and multi-spacecraft values are plotted as filled symbols. The FFT spectrum of the x -component of \mathbf{B} is shown in a translucent purple shade. Dotted lines corresponding to spectral slopes of $-5/3$ and $-8/3$ are shown for reference, and the red vertical line marks the inertial length d_i . .	217
9.7	PDFs of the increment in the x -component of the magnetic field, in the magnetosheath (top) and the solar wind (bottom), using MMS1 measurements. The different lags used are listed in the top-right corner of the figures, in units of d_i ($= 38.54$ km in magnetosheath; 75.98 km in solar wind). The dashed green curve represents a Gaussian PDF, and the horizontal axes are normalized by the standard deviation of the increment $\sigma(\Delta B_x)$	218
9.8	PDFs of the increment in the x -component of the magnetic field, in the magnetosheath (top) and the solar wind (bottom), using MMS1 measurements (blue squares) and the lag between MMS1 and MMS2 (red line). The lag in the top panel corresponds to 13 km (or $\sim 0.35 d_i$), and that in the bottom panel to 16 km (or $\sim 0.21 d_i$). These lags are the average separations for the two spacecraft considered. The dashed green curve represents a Gaussian PDF, and the horizontal axes are normalized by the standard deviation of the increment $\sigma(\Delta B_x)$	220

9.9	Scale-dependent kurtosis as a function of lag, for increments of the three components of the magnetic field, in the magnetosheath (top) and the solar wind (bottom). Single-spacecraft results using MMS1 are shown as lines, and direct two-spacecraft measurements are plotted using filled symbols.	222
A.1	The solar sunspot cycle. More sunspots indicate higher solar activity. <i>Image courtesy of NASA Marshall Space Flight Center.</i>	261
B.1	Longitudinal (f) and transverse (g) correlation functions, shown as functions of varying lag r . $f(r)$ is believed to always be positive for incompressible flow ($\nabla \cdot \mathbf{u} = 0$), while $g(r)$ can be negative if $\nabla \times \mathbf{u} \neq 0$ and eddies span the lag r . <i>Figure reproduced from Subedi [2017] with permission (see Appendix E)</i>	266

ABSTRACT

The solar wind is the continuous outflow of plasma from the Sun, driven by the pressure difference between the hot corona and the interstellar medium. This complex, dynamically evolving flow permeates all of interplanetary space, and its behavior and properties have significant implications for near-Earth space weather, the health of space travelers, and the proper functioning of both terrestrial and space-faring electronic systems. As the only astrophysical plasma where direct spacecraft measurements are possible, the solar wind provides an archetype of a strongly turbulent magnetized system.

This dissertation examines several problems within the context of multi-scale turbulent dynamics of the solar wind, employing a “model heliosphere” produced by a well-tested global two-fluid magnetohydrodynamic (MHD) code. The three-dimensional simulations are based on a Reynolds-averaging approach, in which resolved large-scale flow is self-consistently coupled to smaller-scale fluctuations by means of a dynamical turbulence transport model. The focus is on the inner heliosphere (coronal surface to 3 astronomical units); effects of solar variability are incorporated through changing source magnetic dipole tilts and magnetogram-derived boundary data from different solar-activity epochs.

The simulations are used to study the collisional history of the solar wind; full integral calculations of the collisional age are compared with simpler one-point estimates commonly employed in observational work, the relationship between the collisional age and the Knudsen number is clarified, and the collisional age is contrasted with the turbulent age of the solar wind.

The diffusion tensor that describes scattering of energetic particles by magnetic fluctuations is evaluated throughout the inner-heliosphere, with the heliospheric current

sheet emerging as a region of strong diffusion perpendicular to the magnetic field. The rigidity-dependence of the parallel diffusion coefficient is shown to evolve with heliocentric distance.

Critical (sonic, Alfvénic, and plasma-beta unity) surfaces that mark the transition of the magnetically-structured corona into the predominantly hydrodynamic solar wind are localized. The flow in regions propinquitous to these surfaces is investigated, and simulation results are compared with a variety of remote sensing observations. The often-overlooked concept of a “range of influence” that limits the length scales at which fluctuations may interact in the expanding solar wind is discussed.

With the importance of the critical surfaces established, contextual predictions for the soon-to-be-launched *Parker Solar Probe* (*PSP*) mission are provided by combining the simulations with the spacecraft’s planned trajectory. *PSP* crossings of the critical surfaces are simulated, and the turbulence environment likely to be observed during early orbits is discussed.

In an ancillary observational study, comparative statistical analyses of multi-scale intermittent turbulence in the Earth’s magnetosheath and the solar wind are performed, employing high-resolution multi-spacecraft data provided by the Magnetospheric Multiscale mission. Strong signatures of intermittent turbulent structures at electron and ion scales in the magnetosheath are observed. These signatures appear to be absent at sub-ion scales in the solar wind, which does, nevertheless, exhibit intermittency in the inertial range. The findings also include different power-law spectral behavior in the two regions. Comparisons of a multi-spacecraft technique with single-spacecraft estimates permits a verification of the accuracy of the Taylor “frozen-in” hypothesis.

I saw that one enquiry only gave occasion to another, that book referred to book, that to search was not always to find, and to find was not always to be informed; and that thus to persue perfection, was, like the first inhabitants of Arcadia, to chace the sun, which, when they had reached the hill where he seemed to rest, was still beheld at the same distance from them.

— Samuel Johnson, A Dictionary of the English Language

Chapter 1

INTRODUCTION

The solar wind is the extension of the Sun's atmosphere into interplanetary space, driven by the pressure difference between the solar corona and the local interstellar medium. Since its theoretical prediction by Eugene Parker in the middle of the 20th Century and subsequent observational confirmation by near-Earth spacecraft, observational and interpretive studies have established the dynamic, complex, and multi-scale nature of the solar wind plasma. The present work examines several aspects of the dynamics of the solar wind, with a focus on the properties, the evolution, and the effects of the associated turbulent fluctuations. In this chapter we briefly introduce the physical systems and problems considered, and provide an overview of this thesis.

1.1 Background

In the following sections we briefly review some observational and theoretical perspectives on solar wind and turbulence studies, motivating the problems considered in this thesis in the process.

1.1.1 The Discovery of the Solar Wind

Astronomers in the not-too-distant past believed that the Sun was an ideal, placid sphere, devoid of activity. Gravity was thought to be the only agent connecting celestial objects in the Solar System. Galileo's discovery of sunspots in the 17th Century was an early indication of solar activity, but at the time these were thought to reflect the passage of inner planets across our view of the solar disk, rather than a physical process that was occurring in the Sun. William Herschel's 1804 study claiming that

prices of wheat were correlated with sunspots, controversial to this day, was a pioneering exploration of relations between solar variability and climate. The 11-year solar activity cycle was discovered in the middle of the 19th Century by Samuel Schwabe and Rudolf Wolf. In 1859, a British astronomer named Richard Carrington observed a giant solar flare [Carrington, 1859], which was followed by the most intense magnetic storm that had ever been recorded on Earth, leading to telegraph failures all over North Africa and Europe. All these observations, however, were thought to be coincidental, since a physical understanding of the underlying processes was lacking.

In 1943, analysis of coronal spectral lines led to a reliable estimate of the temperature of the solar corona at 1 – 2 million degrees. This posed the mystery, unresolved till today, of how the atmosphere of the Sun is heated to a degree that is orders of magnitude larger than the photospheric temperature of about 5000 K. Sydney Chapman’s model of a *static* solar atmosphere [Chapman and Zirin, 1957] found itself at loggerheads with Ludwig Biermann’s observations of a continuous supersonic gas flow from the Sun that deflected the tails of comets [Biermann, 1957]. Eugene Parker’s work [Parker, 1958, 1965b] on a dynamical solar wind, driven by the pressure gradient between the hot corona and the local interstellar medium, was met with initial skepticism [see, e.g., Obridko and Vaisberg, 2017]. However, since the triumphant observational confirmation of a supersonic solar wind [Gringauz et al., 1960; Bonetti et al., 1963; Snyder et al., 1963; Neugebauer and Snyder, 1966], Parker’s models have served as the foundation of our current physical understanding of this astrophysical system.

1.1.2 Basic Properties of the Solar Wind

The solar wind has its source in the Sun’s corona, which is the extremely hot ($\sim 10^6$ K) outer atmosphere of the star. The high temperature produces an ionized, but approximately neutral plasma, that is energetic enough to escape the gravitational pull of the Sun. Protons and electrons (resulting from ionization of hydrogen) are the primary constituents, with the bulk of the momentum carried by the former. Helium ions are also observed with an abundance of 4 – 5%, in addition to infrequently detected

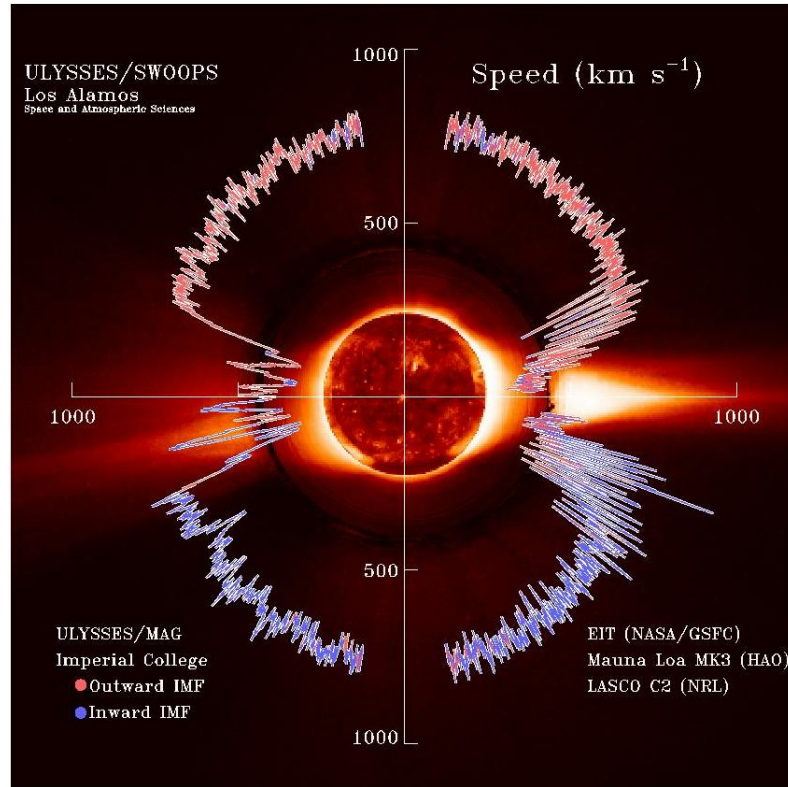


Figure 1.1: Meridional plane view showing the latitudinal distribution of solar wind speeds measured by *Ulysses* during its first polar orbit [McComas et al., 2000]. The background is a composite of three coronagraph images. *Image courtesy of NASA Marshall Space Flight Center.*

heavier elements, including O, Si, and Fe. The average density of the solar wind plasma is about 10 particles per cm^3 , which makes it weakly collisional. The flow is supersonic and directed radially outward for the most part, with a variable speed, although a distinction is possible between a $\sim 350 \text{ km s}^{-1}$ slow wind and a $\sim 750 \text{ km s}^{-1}$ fast wind. During periods of low solar activity (solar minimum; see Figure A.1), slow and fast winds usually emanate from low and high heliolatitudes, respectively [McComas et al., 2000]. Figure 1.1 shows the latitudinal distribution of solar wind speeds measured by the *Ulysses* spacecraft during solar minimum conditions. It is also apparent that the low-latitude slow wind tends to be denser than polar wind.

Apart from the density and the speed, the solar wind may also be characterized

SOLAR WIND

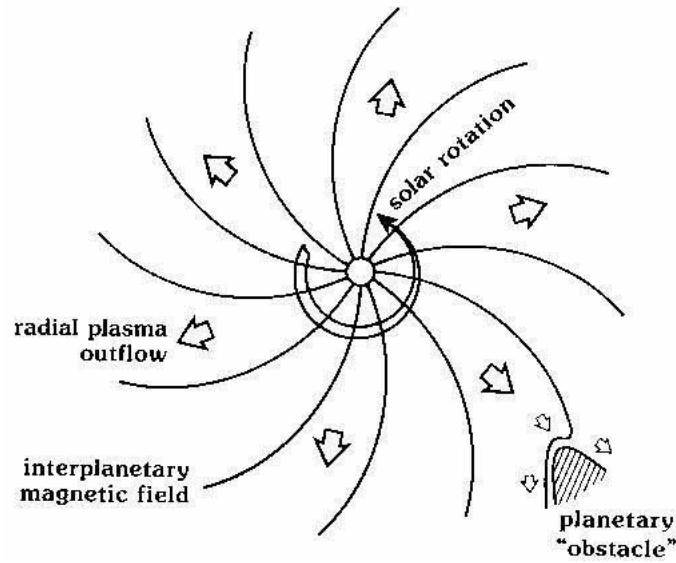


Figure 1.2: A sketch of the Archimedian spiral formed by the interplanetary magnetic field under the influence of the Sun’s rotation. *Image courtesy of [NASA Goddard Space Flight Center](#).*

by a magnetic field, of solar origin, that is induced by solar rotation to twist into a vast Archimedian spiral [e.g., [Hundhausen, 1972](#)], as shown in Figure 1.2. At the solar source, the magnetic field may be approximated as dipolar, with the dipole’s axis tilted by varying degrees to the solar rotation axis [e.g., [Owens and Forsyth, 2013](#)]. The strength of this interplanetary magnetic field (IMF) is $O(nT)$ at 1 au. Fast wind emanates from *coronal holes*, large regions on the solar surface with low density and temperature, and open magnetic field lines that stretch out into space. Slow wind emerges from the so-called “streamer belt” regions generally found at lower latitudes, characterized by closed loops of magnetic field lines.

The solar wind and the IMF extend throughout the solar system, thus establishing the *heliosphere*. This bubble-like region of space extends about 100 au from the Sun, and is maintained by the solar wind against the external pressure of the *interstellar medium* that permeates the Milky Way Galaxy [see e.g., [Zank, 1999](#)]. The

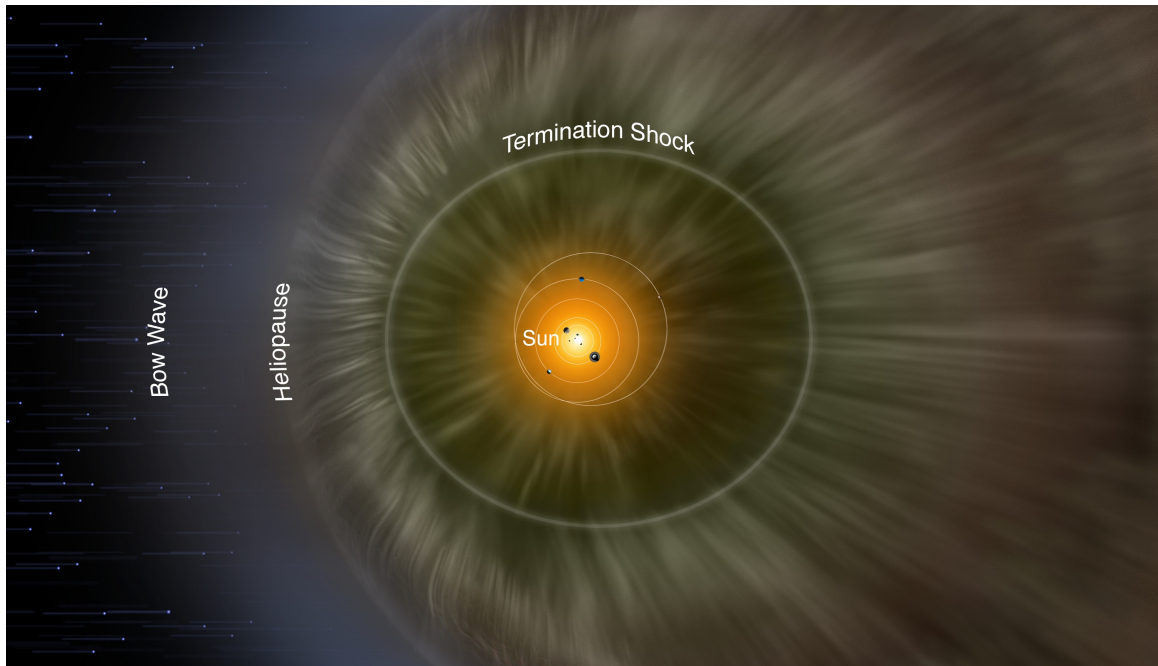


Figure 1.3: Artist’s concept of the heliosphere interacting with the interstellar medium. The hypothetical bow-shock/wave [e.g., [Zank et al., 2013](#); [Usmanov et al., 2016a](#)] is depicted, along with the heliopause and the termination shock (see text). *Image courtesy of NASA.*

flow of the wind slows abruptly at the *termination shock*, which the *Voyager* spacecraft crossed recently. The transitional zone between the termination shock and the outermost boundary of the heliosphere (the *heliopause*) is known as the *heliosheath*. It is believed that *Voyager 1* departed from the heliosphere in 2012, when it detected a sudden forty-fold decrease in plasma density. Figure 1.3 depicts an artist’s concept of the heliosphere interacting with the interstellar medium.

During the solar wind’s traversal of the heliosphere, it interacts with planetary magnetic fields (*magnetospheres*; see planetary “obstacle” in Figure 1.2) as well as their outer atmospheres. This has consequences for the Earth – our magnetosphere protects us from the high energy particles in the solar wind, but an unusually large ejection of plasma from the sun (a *solar storm*) may disrupt terrestrial electrical and communication systems. The hazards of solar energetic particles lead to *space weather*

constituting an ever-present concern for the health of astronauts [Parker, 2005] and the safety of electronic components in spacecraft [Tylka et al., 1997]. The same solar storms are also responsible for the well known *aurora borealis*, also known as the northern lights.

1.1.3 Heating and Acceleration of the Solar Wind

It has been known since the time of the earliest models of the solar wind [Parker, 1958] that the flow arises due to the pressure difference between the hot corona and the local interstellar medium. The details of the processes that heat the corona and accelerate the wind, however, are not completely understood, despite decades of research. An enduring puzzle is the question of how the 5000 K photosphere transitions into the million K corona. Researchers agree that the source of the energy lies in the convection zone below the sun’s surface, where hot plasma from the Sun’s interior swirls up to the surface on timescales of minutes to hours, and descends back after cooling. A number of physical mechanisms such as magnetohydrodynamic (MHD) waves, turbulence, and magnetic reconnection have been proposed to explain the transfer of energy from the solar surface to coronal heights of $10^4 - 10^5$ km [e.g., Cranmer and van Ballegoijen, 2005; Klimchuk, 2006; Zirker and Engvold, 2017].

Above coronal heights, this energy goes further towards the heating and acceleration of the solar wind [e.g., Hundhausen, 1972; Leer et al., 1982; Meyer-Vernet, 2007]. Parker [1965b] realized that while a purely thermally driven wind model¹ could easily produce the observed low to moderate wind speeds, the fast wind would require some source of energy addition above the coronal base. Further, the expansion of the solar wind is observed to be highly *nonadiabatic* in the sense that proton temperature drops much slower than what is expected for a freely expanding ideal gas. For spherically symmetric adiabatic expansion, one would expect the temperature $T(r)$ to vary with

¹ In a thermally driven, wind the thermal pressure gradient is the driving force and the solar gravitational field produces the retarding force.

density as $T \sim 1/r^{4/3}$.² However, *Voyager* observations out to 20 au [Richardson et al., 1995] indicate that $T \sim 1/\sqrt{r}$. Clearly, some process is adding internal energy to the wind over an extended distance.

Coleman [1968] originally suggested that a *turbulence cascade* readily provides a source for heating and accelerating the solar wind. The appeal of this scenario lies in the fact that the large scales of the flow carry substantial energy and can act as a reservoir of heat, provided some mechanism exists that facilitates the transfer of energy from the large scales to the smaller molecular scales, where it can dissipate in the form of heat.³ Such an efficient transfer of energy across a wide expanse of scales is a hallmark of turbulence [e.g., McComb, 1990], which can also play a role in enabling the enhanced spatial transport of mass, momentum, energy, and magnetic fields [e.g., Tennekes and Lumley, 1972; Brandenburg and Lazarian, 2013]. In the decades since Coleman’s pioneering work, countless studies have confirmed that turbulent fluctuations are ubiquitous in the interplanetary plasma, and that the turbulent cascade is active and influential in the dynamics of the solar wind, with an estimated internal energy addition rate of approximately $1000 \text{ J km}^{-1} \text{ s}^{-1}$ [Matthaeus and Velli, 2011, and references therein]. We briefly introduce turbulent flows in the next section, and extend the discussion to the context of the solar wind. A more detailed account is given in Chapters 2 and 3. Succinct reviews of solar wind turbulence may also be found in, e.g., Horbury et al. [2005] and Matthaeus and Velli [2011].

² For an ideal gas, $T \sim P/\rho$ (up to a constant factor), where P is the pressure and ρ is the mass density. We also have $P \sim \rho^\gamma$, where γ is the polytropic index, equal to $5/3$ for an adiabatic process. This yields $T \sim \rho^{2/3}$. Noting that conservation of mass in a spherically symmetric expansion implies $\rho \propto 1/r^2$, we arrive at $T \sim 1/r^{4/3}$.

³ The solar wind is known to be a weakly collisional medium, and the usual viscous dissipative processes that rely on collisions to produce heat are not very effective. The mechanisms that enable dissipation in the collisionless solar wind plasma are an active topic of current research [e.g., Schekochihin et al., 2009; Alexandrova et al., 2013; Servidio et al., 2015; Howes, 2017; Yang et al., 2017]. See also Pezzi [2017].



Figure 1.4: Formation of vortices in turbulent flow, seen in a study of falling water by Leonardo da Vinci, circa. 1508–9. *Image under public domain. Source: <http://www.drawingsofleonardo.org/>*

1.1.4 Turbulence in the Solar Wind

Turbulence may be defined as the “swirling motion of fluids that occurs irregularly in space and time” [Sreenivasan, 1999]. Some of the earliest observations of turbulent flow are found in Leonardo da Vinci’s sketches of flowing water (Figure 1.4), and while a serious scientific study has been pursued in the last century, a solution to the fundamental problem of a predictive theory of turbulence has remained elusive [Liepmann, 1979]. Nevertheless, the importance of turbulence is beyond dispute, and turbulent flows are abundant in nature and in industrial applications – hurricane boundaries, the dispersion of pollutants in the atmosphere, and galactic jets, to name a few. In fact, turbulence is considered to be the natural state of a flow, as opposed to *laminar* (smooth) flow, which is relatively rare.

Turbulence arises from the *nonlinear* interactions of random processes, and involves the simultaneous excitation and dynamical coupling of a wide range of length

scales. The notions of scaling and universality across scales have proven to be powerful tools in studying turbulence [e.g., Kolmogorov, 1941a; Yaghot and Orszag, 1986]. The size of turbulent fluctuations is large, and often comparable to that of the average “background” flow. As mentioned in the previous section, turbulence can enhance dissipative and transport processes. This enhancement is related to the turbulent *cascade*, which transfers energy from larger scales to smaller scales, where it can be dissipated. Importantly, turbulence is a feature of the *flow*, and not of the fluid.

The source of turbulence lies in *gradients*, which may be present in any physical field – velocity, density, pressure, and so on [Montgomery, 1989]. As an example, the shearing between two adjacent streams flowing with different velocities may trigger the Kelvin-Helmholtz instability [e.g., Choudhuri, 1998], which creates eddy-like vortices at the boundary between the streams. Such gradients are abundant in the solar wind – the interface between slow and fast wind streams provides sites where the Kelvin-Helmholtz instability could be triggered [Roberts et al., 1992], and the shocks associated with flares and corotating interaction regions⁴ are rife with discontinuities in pressure, magnetic fields, velocities, and densities [Hundhausen, 1972; Gosling and Pizzo, 1999].

With Coleman’s 1968 observations of powerlaw wavenumber spectra, the solar wind became the first astrophysical system for which direct measurements of turbulence became possible.⁵ The existence of a powerlaw spectrum is a strong signature of a cascading turbulence process, and several studies have reinforced the robustness of this result [e.g., Jokipii, 1973; Matthaeus and Goldstein, 1982; Tu and Marsch, 1995; Bruno and Carbone, 2013]. Figure 1.5 shows typical solar wind spectra, displaying the familiar $-5/3$ Kolmogorov slope.

⁴ Corotating interaction regions form when slow and fast streams mix radially due to solar rotation [e.g., Hundhausen, 1972].

⁵ Space Physics is a relatively young science that began with the dawn of the space age in the middle of the 20th Century. It is distinguished from the broader field of Astronomy by the availability of *in-situ* measurements, that is, spacecraft probes’ *direct* observations of the interplanetary medium, as opposed to the remote sensing observations of distant astronomical objects.

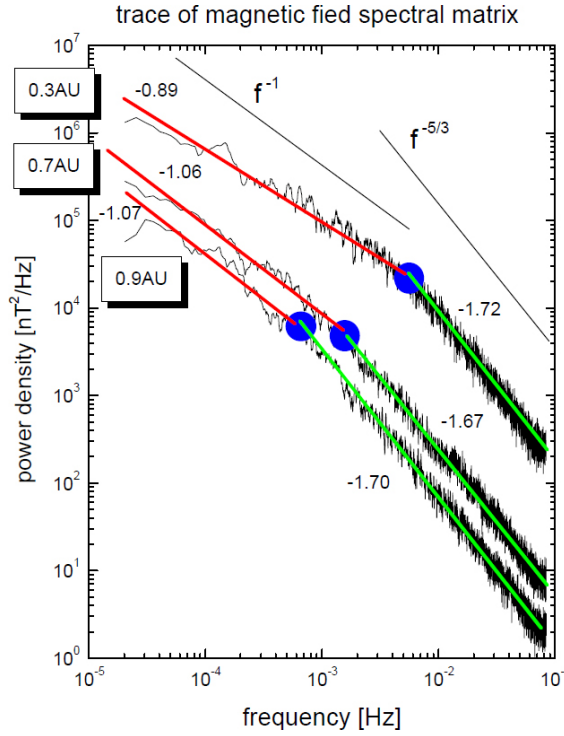


Figure 1.5: *Helios 2* observations of power density spectra of magnetic field fluctuations between 0.3 and 1 au. *Figure reproduced from Bruno and Carbone [2013] under the Creative Commons Attribution-Non-Commercial 3.0 Germany License.*

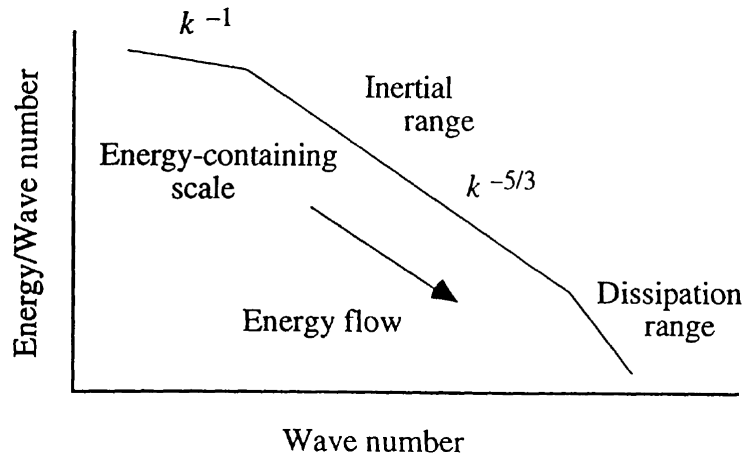


Figure 1.6: Schematic of turbulent cascade of energy. Recall that wavenumber is the inverse of spatial length, so the positive x -axis is in the direction of decreasing spatial scale. *Figure reproduced from Goldstein et al. [1995] with permission from Annual Reviews (see Appendix E).*

We can use Figure 1.5 to introduce the important concepts of the *energy-containing scales* and the *inertial range*. The energy-containing scale corresponds to the largest structures, or eddies, in the system, which supply energy to the intermediate range of scales known as the inertial range. The inertial range is thought to be self-similar, and amenable to analysis using theories that invoke statistical equilibrium [Kolmogorov, 1941a; Batchelor, 1953]. The transfer of energy from the energy-containing scale to the inertial range continues into the small, molecular scales of the dissipation range. This cascade of energy across scales is pictured as a schematic in Figure 1.6. The size of the largest eddies in the system corresponds to the “break point” frequency, or the “knee” that marks the boundary between the energy-containing scales and the inertial range. These spectral breaks are shown as blue circles in Figure 1.5. At the other end of the spectrum, there is a second knee that marks the onset of the dissipation range [Leamon et al., 1998], as shown in Figure 1.6.⁶

Another landmark study in solar wind turbulence was carried out by Belcher and Davis [1971], who demonstrated that the nature of the fluctuations was Alfvénic; that is, the magnetic and velocity fluctuations were correlated, as one expects for an Alfvén wave [e.g., Choudhuri, 1998]. A related phenomenon is the so-called “Alfvén effect”, or the equipartition of energy between velocity and magnetic fluctuations [Kraichnan, 1965a; Matthaeus and Goldstein, 1982], again as expected for linear Alfvén waves. The dichotomy between the wave-like Alfvénicity of solar wind fluctuations and the nonlinear couplings intrinsic to the turbulent cascade will be discussed further in Chapters 2 and 3. For now, we remark that the evolution of the spectral break towards low frequencies (i.e., larger scales) with increasing distance from the Sun, as seen in Figure 1.5, suggests that turbulence in the solar wind is actively evolving. Further evidence of this is provided by the observed systematic reduction of Alfvénicity with increasing radial distance [Bavassano et al., 1982b,a; Roberts et al., 1987b,a; Breech et al., 2005].

⁶ A *second* spectral knee in the dissipation range has also been detected in recent high resolution solar wind observations [Sahraoui et al., 2009]. The first and second dissipation range breakpoints correspond to characteristic proton and electron scales, respectively, and mark the spatial scales where proton and electron kinetic effects become relevant.

A fundamental difference between the nature of hydrodynamic turbulence and MHD turbulence is the *anisotropy* that arises due to the presence of a background magnetic field, which introduces a preferred spatial direction.⁷ It is well known that fluctuations in the solar wind tend to be perpendicular to the local magnetic field [Belcher and Davis, 1971]. This is known as amplitude (or variance) anisotropy. In addition, the fluctuations also exhibit *spectral* anisotropy – energy tends to lie in wavevectors that are perpendicular to the mean magnetic field. This may be understood from the known suppression of spectral transfer parallel to the mean magnetic field, which leads to a concentration of turbulent energy in the perpendicular direction [e.g., Shebalin et al., 1983; Oughton et al., 2015, ; see also Section 3.3.1].

An idealized model of anisotropic turbulence in the solar wind is the so-called two-component model, which consists of a minor species of “slab” fluctuations with power in wavevectors parallel to the magnetic field, and a majority “2D” component with power in perpendicular wavevectors [Matthaeus et al., 1990]. The slab component is related to wave-like Alfvénic fluctuations that propagate along the magnetic field, while the two dimensional fluctuations correspond to strong turbulence arising from nonlinear couplings. Bieber et al. [1996] presented strong evidence in support of this two-component model, and they concluded that about 20% of the power resided in slab fluctuations, while about 80% was in 2D. This result has significant implications for the propagation of energetic particles in the heliosphere and beyond. These particles are scattered by fluctuations in the magnetic field, but respond differently to slab and 2D fluctuations [e.g., Shalchi, 2009].

In the modern era of turbulence research, *intermittency* has been established as an essential feature of turbulent flow. Indeed, Kolmogorov himself revised his theory to account for departures from universality and Gaussianity in realistic flows [Kolmogorov, 1962]. Intermittency, the “burstiness” or “patchiness” of a signal, is associated with

⁷ A background mean velocity can be eliminated by means of a Galilean transformation, and statistical isotropy is therefore a convenient assumption in hydrodynamic homogeneous turbulence theory [Batchelor, 1953]. See Appendix B.

sharp gradients, inhomogeneities, and coherent structures, and is now a well-established property of solar wind turbulence [e.g., [Marsch and Tu, 1997](#); [Sorriso-Valvo et al., 1999](#); [Matthaeus et al., 2015](#)]. Small-scale intermittent structures, such as the current sheets that form naturally in plasma turbulence [e.g., [Dmitruk et al., 2004](#)], are thought to play a role in the heating and dissipation of the solar wind plasma [[Osman et al., 2012](#); [Wu et al., 2013](#)] and in the acceleration of energetic particles in the heliosphere [[Tessein et al., 2013](#)]. In one of the projects carried out for this thesis, we perform a study of intermittency in the solar wind and the Earth’s magnetosheath using high-resolution data from the Magnetospheric Multiscale mission [[Chhiber et al., 2018a](#)].

We end this section by emphasizing the relevance of solar wind turbulence to the broader field of astrophysics, and to turbulence in general. Turbulence is thought to play a role in several astrophysical systems and processes, ranging from stellar convection and accretion disks to galaxy clusters, and even in the generation of primordial fields in the early universe [e.g., [Brandenburg and Nordlund, 2011](#), and references therein]. However, as noted earlier, the solar wind is the only astrophysical plasma where direct measurements using spacecraft are possible. The knowledge gleaned from studying turbulence in the solar wind can contribute to our understanding of this phenomenon in other astrophysical systems. Furthermore, the solar wind is interesting from the perspective of someone trying to understand better the fundamental problem of turbulence, since it provides an archetype of a strongly turbulent magnetized system with characteristic length scales far larger than those of terrestrial turbulent systems. Indeed, the solar wind is sometimes referred to as the largest “turbulence laboratory” accessible to researchers, where theories of turbulence and the associated notions of universality and self-similarity across scales may be put to the test [e.g., [Bruno and Carbone, 2013](#)].

1.1.5 Modeling and Simulation of Turbulent Flows

In this section we introduce some fundamental issues that arise in modeling and numerical simulation of turbulent flow. We examine the general closure problem

of stochastic nonlinear equations, and introduce the different paradigms for numerical simulation, based on the number of degrees of freedom resolved. Any attempt to model turbulence in the solar wind must, of necessity, grapple with these general issues.

The governing equation of fluid flow⁸ is the Navier-Stokes equation. Despite having been written down in the 19th Century, our mathematical understanding of this equation remains minimal. Indeed, the Clay Mathematics Institute lists the Navier-Stokes equation as one of the problems whose solution would receive a US \$1 million [Millenium Prize](#). The solution of the “turbulence problem” is tied up with the difficulties in solving this equation. In particular, the very nonlinearity that produces turbulence also presents mathematical challenges that have thwarted attempts at a statistical solution.⁹

For an incompressible Newtonian fluid [e.g., [Batchelor, 2000](#)], the Navier-Stokes equation may be written as

$$\frac{\partial U_\alpha}{\partial t} + U_\beta \frac{\partial U_\alpha}{\partial x_\beta} = -\frac{1}{\rho} \frac{\partial P}{\partial x_\alpha} + \nu \nabla^2 U_\alpha, \quad (1.1)$$

where U is the fluid velocity, P is the fluid pressure, ρ is the fluid density, ν is the kinematic viscosity of the fluid, and the summation convention for repeated indices is employed. Equation (1.1) essentially expresses the conservation of momentum of the fluid (i.e., Newton’s second law of motion), with the left hand side expressing the derivative of the velocity along the fluid trajectory (the Lagrangian derivative), and the right hand side representing forces due to pressure gradients and internal friction. The equation may be derived in a macroscopic fashion from the methods of continuum

⁸ In a fluid description the details of the microscopic motion of the *discrete* constituent particles are *smoothed* (or “*averaged out*”), to arrive at a description of the medium in terms of a *continuum*. Conventionally, this continuum description is considered valid in the limit that the particle mean free paths are small compared to the macroscopic scales of the flow, which requires that the medium be collisional.

⁹ Turbulence is often considered to be a nondeterministic phenomenon described by random fields. Therefore a statistical approach is usually adopted. However, there is also a branch of turbulence research that is concerned with *deterministic* chaos [[Ruelle, 1990](#)]. This thesis stays within the statistical approach.

mechanics, or from kinetic theory by taking moments of the Boltzmann equation for the distribution function of a gas of discrete microscopic particles [e.g., [Choudhuri, 1998](#)].

The relative importance of nonlinear interactions and viscous damping may be measured by the ratio of the nonlinear and viscous terms in Equation (1.1). This dimensionless ratio, called the *Reynolds number*, may be expressed as

$$\text{Re} = \frac{UL}{\nu}, \quad (1.2)$$

where U and L are velocity and length scales characteristic of the flow, and ν is the kinematic viscosity of the fluid. When the nonlinear term is much stronger than viscous effects, Re is large and the flow becomes turbulent. In flows with boundaries this usually happens at Re greater than about 2000 [[Reynolds, 1883](#)].

We will now give a brief conceptual demonstration of the fundamental problem of statistical turbulence modeling. Rearranging Equation (1.1), we obtain

$$\left(\frac{\partial}{\partial t} - \nu \nabla^2 \right) U_\alpha = - \frac{\partial U_\alpha}{\partial x_\beta} U_\beta - \frac{1}{\rho} \frac{\partial P}{\partial x_\alpha}, \quad (1.3)$$

which can be written in the symbolic form:

$$L_0 U = L_1 U U + L_2 P, \quad (1.4)$$

where the tensor indices have been suppressed for simplicity, and L_0, L_1 , and L_2 represent the respective differential operators.

Next, to obtain a statistical equation for the mean velocity, we average each term of Equation (1.4) and get

$$L_0 \langle U \rangle = L_1 \langle U U \rangle + L_2 \langle P \rangle, \quad (1.5)$$

where $\langle \dots \rangle$ denotes an appropriate averaging operation. Note that for an incompressible fluid, the pressure P is related to U through the continuity equation [e.g., [Lesieur, 2012](#)]. This implies that a solution for the mean velocity $\langle U \rangle$ depends only on the second moment of the velocity $\langle UU \rangle$, ρ and ν being constant. We might try to find an equation for $\langle UU \rangle$ by multiplying each term of Equation (1.4) with U and then averaging:

$$L_0 \langle UU \rangle = L_1 \langle UUU \rangle + L_2 \langle UP \rangle, \quad (1.6)$$

which depends on the *third* moment. We can multiply Equation (1.4) in turn by UU , UUU , and so on, and then average, thus generating a hierarchy of moment equations

$$\begin{aligned} L_0 \langle UUU \rangle &= L_1 \langle UUUU \rangle + L_2 \langle UUP \rangle \\ L_0 \langle UUUU \rangle &= L_1 \langle UUUUU \rangle + L_2 \langle UUUP \rangle \\ &\vdots \end{aligned} \quad (1.7)$$

That is, taking this procedure to n steps, we will have an open set of n equations involving $n + 1$ moments. The problem of closing this hierarchy of moment equations is referred to as the “closure problem”, and is the underlying problem of turbulence modeling. We will encounter this problem at several points over the course of this thesis.

An important technique, widely used in turbulence modeling, is the *Reynolds decomposition* [[Reynolds, 1895](#)], in which the velocity field is split into a mean \bar{U}_α and a fluctuation u_α about the mean:

$$U_\alpha = \bar{U}_\alpha + u_\alpha, \quad (1.8)$$

where, by construction, the fluctuations have zero mean: $\langle u_\alpha \rangle = 0$. Decomposing the pressure in a similar fashion and substituting the decomposed fields into Equation

(1.1), we then average the resulting equation term by term to find

$$\frac{\partial \bar{U}_\alpha}{\partial t} + \bar{U}_\beta \frac{\partial \bar{U}_\alpha}{\partial x_\beta} + \frac{\partial}{\partial x_\beta} \langle u_\alpha u_\beta \rangle = -\frac{1}{\rho} \frac{\partial \bar{P}}{\partial x_\alpha} + \nu \nabla^2 \bar{U}_\alpha, \quad (1.9)$$

where we have used the property $\langle \bar{U} u \rangle = \bar{U} \langle u \rangle = 0$. Comparing this equation with Equation (1.1), one sees that the equation for the mean flow is identical to the Navier-Stokes equations written for the mean velocity and pressure, but with the additional term involving $\langle u_\alpha u_\beta \rangle$, representing another instance of the closure problem.

Equation (1.9) is called the Reynolds equation and $\langle u_\alpha u_\beta \rangle$ is the Reynolds stress. The Reynolds stress represents the influence of the turbulent fluctuations on the mean flow, and is a manifestation of the cross-scale couplings intrinsic to turbulence. An analogy may be drawn between the Reynolds stress and the viscous stresses due to random molecular interactions, with the implication that $\langle u_\alpha u_\beta \rangle$ may be modeled in terms of the mean rate of strain and an effective turbulent viscosity. We will discuss closure models for the Reynolds stress and its MHD analogs in later chapters. We will also discuss some subtleties related to the type of averaging operator used in the decomposition of mean and turbulent components of the flow.

We can already see how the Reynolds stress may be used to model enhanced transport and dissipation in the solar wind via turbulence. Note, however, that the Reynolds equation (1.9) still has a quadratic nonlinearity in the velocity¹⁰, and analytical solutions have proven to be notoriously difficult to find. Given this state of affairs, numerical computation has emerged as a powerful tool to study turbulent flows, especially with the advent of powerful computers in the last few decades. We now introduce the three standard approaches used in computer simulations of turbulence.

We begin by considering the numerical simulation of the *unaveraged* Navier-Stokes equation. After all, these equations carry the complete flow information, prior to a separation into mean and fluctuating components. Simulations of unaveraged

¹⁰ The pressure may be expressed in terms of the velocity for incompressible flow in the form of a solution to a Poisson equation, and this form is both non-local and nonlinear [see, e.g., [McComb, 1990](#)].

flow equations are called *direct numerical simulations* (DNS). In a DNS, all scales of the motion must be resolved for an accurate representation of cross-scale turbulent couplings. The range of scales that are active in a turbulent flow may be expressed in terms of the Reynolds number [e.g., [McComb, 1990](#)]:

$$\text{Re}^{3/4} \sim \frac{L}{\eta}, \quad (1.10)$$

where L is a characteristic scale of the largest eddies in the flow, and η is the dissipation scale (see discussion of [Figure 1.6](#)). The larger the separation of scales involved in the flow, the larger the Reynolds number. The range of scales and the Re that can be resolved in a simulation is limited, however, by computational expense. For the smallest scale in the flow to be resolved, the grid scale Δ must be *at most* η . As a measure of computational cost, the total number of floating point operations (FLOPS) required for a simulation may be estimated by the product of the number of modes (or degrees of freedom) and the number of time steps. This product is approximately $(L/\Delta)^4 \gtrsim (L/\eta)^4 \sim \text{Re}^3$ for a three dimensional simulation [[Pope, 2000](#)]. Astrophysical systems tend to have enormous Reynolds numbers due to the large length scales and low viscosities involved (see [Equation 1.2](#)). As an example, the solar convection zone has $\text{Re} \sim 10^{14}$ [[Canuto, 1994](#)]. A DNS of this system over one dynamical time scale would need roughly 10^{42} FLOPS, which would take longer than the current age of the Universe by the fastest computers of the day. Improvements in computational power in the near future are unlikely to alleviate these constraints. It is imperative, therefore, that we consider ways of reducing the number of degrees of freedom that need to be resolved in a simulation.

In several applications it is not absolutely necessary to resolve all the degrees of freedom in a simulation of high- Re turbulence. This is the philosophy underlying the *large eddy simulation* (LES) approach. An LES employs a filtering operation to retain only the large scales (the energy containing scales and the larger structures of the inertial range), with the cutoff scale specified by the grid scale Δ . The criterion

defining an LES is therefore

$$L \gg \Delta \gg \eta. \quad (1.11)$$

The interaction of the large and small scales is incorporated using a model, and the major challenge in this approach is the development of an appropriate model that reasonably accounts for “subgrid-scale” effects [e.g., [Lesieur and Metais, 1996](#)].

The Reynolds-averaging approach discussed earlier can be thought of as a limiting case that arises when the filter scale is comparable to the energy-containing scales, so that only the mean flow is resolved by the simulation, with all turbulent fluctuations treated as subgrid-scale [see [Germano, 1992](#)]. In [Appendix D](#) we will discuss further the relationship between the LES and the Reynolds-averaging approaches, specifically within the context of solar wind simulation.

1.1.6 Modeling and Simulation of Solar Wind Turbulence

All three numerical approaches – DNS, LES, and Reynolds-averaging – are relevant to solar wind studies. MHD¹¹ DNS has been used to study the details of several features of solar wind turbulence, including anisotropy [e.g., [Shebalin et al., 1983](#); [Oughton et al., 1994](#)], intermittency [e.g., [Wan et al., 2009, 2012a](#); [Zhdankin et al., 2012](#)], and particle energization [e.g., [Dmitruk et al., 2004](#)]. These simulations are very useful for gaining insight into the physical mechanisms and inertial range dynamics at play at the *local* level, but cannot resolve the large system-size scales of the solar wind. In fact, for three dimensional (3D) *global* simulation of the solar wind with realistic boundary conditions, even the LES approach is computationally very expensive. The largest scales in a global simulation of the solar wind are of the order of 1 au (= 1.5×10^8 km), while the correlation scale, or the size of the largest turbulent structures,

¹¹ Magnetohydrodynamics is the study of the properties of electrically conducting fluids. It combines the usual hydrodynamic equations that describe the flow of a fluid with Maxwell’s equations for electromagnetic fields [e.g., [Choudhuri, 1998](#)]. In a collisionless medium such as the solar wind, particle mean free paths are not small compared to the macroscopic length scales of the system, and the validity of the fluid (continuum) approximation may be questioned. We will describe the equations of MHD and discuss their validity in the context of the solar wind in [Chapter 2](#).

is about 10^6 km at 1 au [e.g., [Ruiz et al., 2014](#)]. Since an LES must resolve scales much smaller than the correlation scale (Equation 1.11), it would ideally require four decades of resolution in each dimension. Nevertheless, the LES approach (which is rather well-established in hydrodynamics, particularly in engineering applications) holds promise for astrophysical simulation, and will likely receive more attention with increases in computational power in the near future [[Miesch et al., 2015](#); [Schmidt, 2015](#)].

The Reynolds-averaging approach provides a paradigm for global solar wind simulation that is computationally affordable when the focus is on the large-scale mean flow. In Reynolds-averaged Navier-Stokes (RANS) simulations, the turbulent fluctuations are not explicitly resolved, and models (of varying sophistication) are employed to incorporate the influence of the turbulence on the mean flow. The models used range from simple representations of the turbulent stress in terms of the mean-flow gradients [e.g., [Pope, 2000](#)], to dynamical equations that describe statistical descriptors of the turbulence [[Yoshizawa et al., 2003](#)]. We will review some of the modeling techniques in later chapters, since the major part of this thesis is concerned with the use of MHD-RANS simulations to study various aspects of solar wind dynamics.

A detailed description of the solar wind model used here is given in Chapter 4. Briefly, the model is derived from the application of the Reynolds decomposition (Equation 1.8) to the *two-fluid* MHD equations in a frame corotating with the Sun. The set includes mass and momentum conservation equations for protons in the solar wind, the induction equation for the magnetic field, and two separate energy equations for protons and electrons. With the Reynolds decomposition, the velocity and magnetic fields are split into mean and fluctuating components; the mean component is associated with the large scales of motion, assumed to be deterministic, while the fluctuating component is assumed to be of arbitrary amplitude, random in nature, and residing at small scales.

Subtracting the mean-flow equations from the full MHD equations yields a set

of equations for the turbulent fluctuations. Using approximations and closures appropriate to the solar wind, these latter set of equations are developed into a dynamical model describing the transport of *three statistical descriptors of turbulence* – the *turbulence energy*, the *cross helicity* (the correlation of velocity and magnetic fluctuations), and the *correlation length* of the turbulence (the length scale associated with energy-containing fluctuations). The turbulence transport equations are coupled to the mean-flow equations, thus enabling a self-consistent modeling of cross-scale turbulent interactions. The large-scale flow is influenced by turbulent dissipation and transport, and the small-scale turbulence is constrained by the global geometry of the solar wind and driven by gradients in the large-scale fields.

We emphasize the above distinct feature of this model, in contrast to most other efforts that tend to focus on either the large scale flow or the smaller-scale fluctuations. When the focus is on bulk properties of the solar wind, turbulence is usually incorporated by parametric heat deposition [e.g., [Habbal et al., 1995](#); [McKenzie et al., 1995](#)], or WKB waves in a homogeneous background [e.g., [Jacques, 1978](#); [Usmanov et al., 2000](#)]. On the other hand, studies that focus on the transport of solar wind fluctuations generally prescribe constant background flow speeds and Parker-spiral-type magnetic fields [e.g., [Breech et al., 2008](#); [Verdini et al., 2010](#)], or neglect the influence of fluctuations on the background fields [e.g., [Shiota et al., 2017](#)].

The RANS-MHD model described above has been developed over the last decade and is well-tested, with several comparisons of numerical simulations and observations indicating good agreement [[Usmanov et al., 2011, 2012, 2014](#); [Airapetian and Usmanov, 2016](#); [Usmanov et al., 2016a,b, 2018](#)]. In recent years, the model has been used to study some “applied” problems [[Chhiber et al., 2016a, 2017a, 2018c,d,e,b](#)] which form a major part of this thesis, and we introduce these in the next section.

1.1.7 Some Applications of Global Solar Wind Simulations with Turbulence Transport

The numerical solution of the system of coupled nonlinear equations described above generates a model heliosphere, with 3D representations of both the large-scale solar wind and the statistical properties of turbulent fluctuations. Varying boundary conditions at the inner coronal surface can be used to simulate different epochs of solar activity, with periods of high (low) solar activity represented by large (small) tilts of the source magnetic dipole [Usmanov et al., 2012]. Boundary conditions derived from magnetograms corresponding to both solar minimum and solar maximum epochs can also be employed [Usmanov et al., 2014]. With these tools in hand, the simulations may be used to study several aspects of the global dynamics of the solar wind. We briefly introduce these topics here.

Collisional age of the solar wind: Although the solar wind plasma is frequently described as collisionless, it is better regarded as weakly collisional, since there is extensive observational evidence for the role played by collisions in regulating various kinetic processes [e.g., Marsch, 2006]. Recent observational surveys show that a simple local estimate of the *collisional age* – the number of binary Coulomb collisions experienced by a plasma parcel – provides a convincing organization of a number of nonequilibrium kinetic plasma features [Kasper et al., 2008; Maruca et al., 2013; Kasper et al., 2017]. Most studies employ *local* calculations of the collisional age at the point of spacecraft observations. The “age”, however, as a measure of the collisional *history* of a particle, must depend on the path of a plasma parcel in the expanding solar wind, and this necessitates an integral formulation. The age calculation is particularly sensitive to near-Sun regions, and those contributions may influence the accuracy of the local one-point estimate. This leads to another issue – where do we start counting collisions? And which starting point corresponds to the local estimate that refers only to observations at one point? We address these questions constructively in the present study by computing the cumulative collisional age starting from various points in the solar atmosphere. We also develop an analytical approximation and compare it with the

standard local estimate and the improved estimate [Chhiber et al., 2016a].

Cosmic ray diffusion tensor: Apart from the constituent particles of the solar wind, the heliosphere is also populated by the so-called *energetic particles*, which possess energies greater than typical “background” solar wind particles. These energetic particles may have their origin in different sources, such as solar flares and supernova remnants, but they are generally grouped under the umbrella term “cosmic rays” [Kunow et al., 1991].

Cosmic rays (CRs) are strongly guided and scattered by the solar wind and the turbulent fluctuations that transport with it [Parker, 1956, 1964; Jokipii, 1966], with resonant scattering of particles by fluctuations of size comparable to a particle’s gyroradius. The propagation of CRs is generally assumed to be diffusive, and a key ingredient in our understanding of the heliospheric modulation of energetic particles is their diffusion tensor [Parker, 1965a]. In turn, the specification of this tensor throughout the heliosphere requires not only a knowledge of the diffusion process, but also of the large-scale solar wind and the turbulence by which the particles are scattered.

We use the model heliospheres generated by our simulations to compute the distribution of the diffusion tensor throughout the inner heliosphere. We also develop a new model for the component of the tensor that describes diffusion perpendicular to the mean magnetic field [Chhiber et al., 2017a].

Critical surfaces in the solar wind: The transition of the solar corona into the solar wind is accomplished by several dynamical changes in the nature of the flow. The inner corona is magnetically structured, subsonic, and sub-Alfvénic (i.e., slower than the speed of an Alfvén wave), but as the solar plasma flows out from the corona into the young solar wind, it transforms into a supersonic and super-Alfvénic flow that is dominated by hydrodynamics. Recent work indicates that this transition may coincide with the onset of large-scale turbulence [DeForest et al., 2016; Chhiber et al., 2018c,b].

Useful markers that characterize this transition are the sonic critical surface (defined by the set of points where the wind turns supersonic), the Alfvén critical

surface (where the wind turns super-Alfvénic), and the first $\beta = 1$ surface (the plasma- β is the ratio of gas to magnetic pressure). We use our global solar wind model to localize the critical surfaces and to investigate the flow in propinquitous regions. The turbulence model coupled to the bulk flow equations enables an investigation of turbulence properties of the flow in the vicinity of critical regions. The simulation results are compared with a variety of remote sensing observations.

Range of influence of turbulence in solar wind fluctuations: We discuss the often overlooked concept of a “*range of influence*” of turbulence that limits the length scales at which solar wind fluctuations may interact. These length scales are limited by the expansion of the solar wind, since two plasma parcels may move away from each other before they can interact via turbulence. This has quantitative implications for interpretation of single spacecraft observations, for numerical simulations of the expanding solar wind, and for turbulence modeling in a Reynolds-averaging approach. We use the global simulations to estimate the distribution of this causality threshold throughout the inner heliosphere, and explore its relationship with the correlation scale of solar wind fluctuations [Chhiber et al., 2018b].

Contextual predictions for the Parker Solar Probe mission: We have deliberately focused on the inner heliosphere (below 5 au) in all the studies mentioned above. This is with a view toward the imminent launch of the Parker Solar Probe (*PSP*) mission [Fox et al., 2016], which will approach the Sun closer than any prior spacecraft (with a perihelion of about $9.8 R_{\odot}$), providing unprecedented high-resolution measurements of the solar corona and the young solar wind. The main objectives of the mission are discovery of the structure and dynamics of the coronal magnetic field and understanding the processes that heat and accelerate the wind and accelerate and transport energetic particles.

As the *PSP* makes its high resolution in-situ measurements, a knowledge of the large-scale environment within which these observations exist is of vital importance. We use our global simulations, along with a simulated *PSP* trajectory, to provide contextual predictions for the spacecraft in terms of the computed critical surfaces

[Chhiber et al., 2018d]. We also examine the turbulence environment the *PSP* is likely to find itself in, and discuss issues pertaining to the use of the Taylor frozen-in hypothesis¹² with the spacecraft’s in-situ observations [Chhiber et al., 2018e].

1.2 Overview

In this introductory chapter, we reviewed the basic properties of the solar wind and the heliosphere (summarized in tabular form in Appendix A), and motivated the need for a physical mechanism that provides extended heating and acceleration to the system. We argued that turbulence is a natural candidate for such a mechanism, and discussed the salient properties of turbulent fluctuations observed in the solar wind. A general overview of issues that arise in the modeling and numerical simulation of turbulent flows was given, with the discussion extended to the context of heliospheric turbulence. We introduced the RANS-MHD approach as a computationally viable solution to the challenging problem of modeling cross-scale turbulent couplings, and we briefly described the global solar wind simulation based on this approach that has been used in this work. The application of this simulation to several problems related to solar wind dynamics was discussed.

In the next two chapters, we continue a discussion of background topics on solar wind modeling and turbulence that were introduced in the preceding sections. Further background on the classic theory of homogeneous and isotropic hydrodynamic turbulence may be found in Appendix B. A detailed description of the global RANS-MHD solar wind model used in this study is presented in Chapter 4. Appendix D presents some preliminary work on the relationship between the Reynolds-averaging approach and large eddy simulations in the context of the solar wind. Making use of the solar wind model presented in Chapter 4, Chapters 5 – 8 explore the topics introduced

¹² In-situ spacecraft measurements provide researchers with a time series in the spacecraft frame. From these, the Taylor hypothesis [Taylor, 1938] permits one to infer knowledge regarding the *spatial* variation of turbulent flow, by assuming that the bulk flow sweeps turbulent structures past the spacecraft before they are appreciably distorted. That is, the mean solar wind speed must be much larger than the characteristic fluctuation speed. This condition is likely to be violated at *PSP* perihelia.

in the previous section (1.1.7), and form the bulk of the research conducted for this thesis. In Chapter 9, we switch to a somewhat more *local* perspective on heliospheric turbulence, and present an observational study of intermittent turbulence in the solar wind and in the Earth's magnetosheath, using the latest high-resolution data from the Magnetospheric Multiscale (MMS) mission. This chapter also includes some tests of the Taylor hypothesis, accomplished by a comparison of single-spacecraft time series with multi-spacecraft analyses. The final chapter summarizes this work and discusses possible future extensions.

Chapter 2

MODELING THE SOLAR WIND

In Chapter 1 we made some historical remarks on the discovery of the solar wind and discussed the basic properties of the system. Appendix A provides a summary, in tabular form, of the salient properties and characteristic scales of the interplanetary medium. We will continue the discussion here by reviewing Parker’s hydrodynamical model [Parker, 1958] and its prediction of a supersonic flow that expands radially outward from the Sun. We will then introduce the equations of magnetohydrodynamics (MHD), which enable self-consistent modeling of the interaction of the flow with the solar magnetic field and form the basis of most modern solar wind models. The MHD equations admit wave solutions, and we will briefly discuss these, and the related WKB model of solar wind acceleration and heating.

2.1 Parker’s Hydrodynamic Model of the Solar Wind

By 1950, observational evidence had made it clear that the solar corona had a characteristic temperature of about a million degrees K. It was known that hydrogen is ionized at these temperatures, which implied that the corona was primarily a proton-electron plasma, with the more mobile electrons responsible for the bulk of the thermal conductivity. At coronal temperatures, this thermal conductivity was expected to be extremely high: $\sim 10^9 \text{ ergs cm}^{-1} \text{ s}^{-1} \text{ deg}^{-1}$, which is twenty times that of copper at room temperature. Chapman and Zirin [1957] explored the implications of this high conductivity in a model of a *static* corona that extended into interplanetary space. Even though the predictions of this model for near-Earth densities appeared to match observations, its prediction of pressure at large distances from the Sun was too high

compared with the pressure in the interstellar medium, by several orders of magnitude [e.g., [Hundhausen, 1972](#)].

Motivated by Biermann’s [\[1957\]](#) observations of deflected comet tails, Parker [\[1958\]](#) attempted to resolve the discrepancy by considering the possibility of a steadily expanding corona. In the simplest spherically symmetric, and stationary case, the heliocentric position r is the only independent variable, and the equations that describe the system are the continuity equation expressing conservation of mass:

$$\frac{1}{r^2} \frac{d}{dr} (r^2 \rho U) = 0, \quad (2.1)$$

and the equation expressing conservation of momentum for a fluid:

$$\rho U \frac{dU}{dr} = -\frac{dP}{dr} - \rho \frac{GM_\odot}{r^2}, \quad (2.2)$$

where U is the radial speed of expansion, P is the pressure, G is the gravitational constant, and M_\odot is the solar mass. The solar wind is assumed to be an electrically neutral proton-electron gas, with the mass density determined by the much heavier protons: $\rho = nm_p$, where n is the proton number density and m_p is the proton mass. The equation of state is $P = nk(T_e + T_p)$, where k is the Boltzmann constant and T_e and T_p are the electron and proton temperatures, respectively.

In addition to the mass and momentum conservation equations, an equation of energy conservation may also be written [see, e.g., [Hundhausen, 1972](#)], which would include a term specifying any sources or sinks of energy. The solution of the system of these three nonlinear conservation equations is not a simple task; instead, here we make the simplifying assumption of an isothermal equation of state: $P = 2nkT$ where $T = \frac{1}{2}(T_e + T_p)$ is constant. This assumption effectively implies a solution of the energy equation with an unspecified source of heating that enforces the constant temperature.

The equations above may now be closed, with momentum conservation expressed as

$$nmU \frac{dU}{dr} = -2kT \frac{dn}{dr} - nm \frac{GM_{\odot}}{r^2}, \quad (2.3)$$

and the first integral of Equation (2.1):

$$4\pi nUr^2 = \text{constant}, \quad (2.4)$$

which expresses the constancy of proton flux passing through a spherical surface centered at the Sun. Eliminating n from (2.3) using (2.4), we get

$$\frac{1}{U} \frac{dU}{dr} = \left(\frac{2a^2}{r} - \frac{GM_{\odot}}{r^2} \right) / (U^2 - a^2), \quad (2.5)$$

where $a \equiv (2kT/m)^{-1/2}$ is the isothermal speed of sound.

Let us consider the range $r_0 \leq r < \infty$, where r_0 is the lower boundary of the isothermal region. This boundary would lie a little higher than the photospheric radius. The numerator of the right-hand side of (2.5) vanishes when

$$r = r_c \equiv GM_{\odot}/2a^2, \quad (2.6)$$

where r_c is the so-called “*critical radius*”. Such a distance exists in this isothermal wind if

$$GM_{\odot}/2a^2 > r_0, \quad \text{or} \quad T < GM_{\odot}m/4kr_0.$$

It can be seen from Equation (2.5) that the gradient of the velocity is zero at $r = r_c$, *unless* $U(r_c) = a$, in which case dU/dr has the same sign for all r ; in other words, U is either monotonically increasing or decreasing. Similarly, when $U = a$ we have $dU/dr = \pm\infty$, *unless* $r = r_c$. Therefore the only solution with a positive velocity gradient for all r must pass through the critical radius.

Figure 2.1 shows the topology of solutions of Equation (2.5). Since it is known that coronal velocities are small, the cases with a negative velocity gradient below r_c

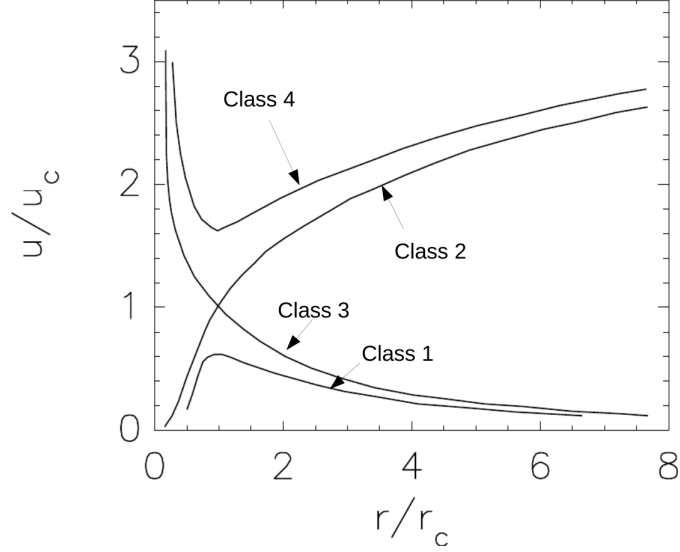


Figure 2.1: The topology of solutions of Equation (2.5). Here $u_c \equiv a$, the isothermal sound speed.

(Classes 3 and 4) may be ruled out. Class 1 stays subsonic, and it can be shown that at large r it results in pressures too high to match those found in the interstellar medium [e.g., [Hundhausen, 1972](#)]. The solution of physical interest is therefore Class 2, which is transonic, with a monotonically increasing velocity that becomes equal to the sound speed at the critical radius. This critical radius is also called the *sonic point*.

Equation (2.5) may be readily solved for the transonic case by first rewriting it as

$$\frac{1}{2} \frac{dU^2}{dr} - \frac{a^2}{2} \frac{dU^2}{dr} \frac{1}{U^2} = \frac{2a^2}{r} - \frac{GM_\odot}{r^2},$$

which is readily integrated to yield

$$\frac{U^2}{2} - a^2 \ln(U) = 2a^2 \ln(r) + \frac{GM_\odot}{r} + C, \quad (2.7)$$

where C is a constant of integration that can be determined by the condition $U(r_c) = a$. These solutions are shown for a range of coronal temperatures in Figure 2.2. The speeds were in general agreement with the values inferred by [Biermann \[1957\]](#).

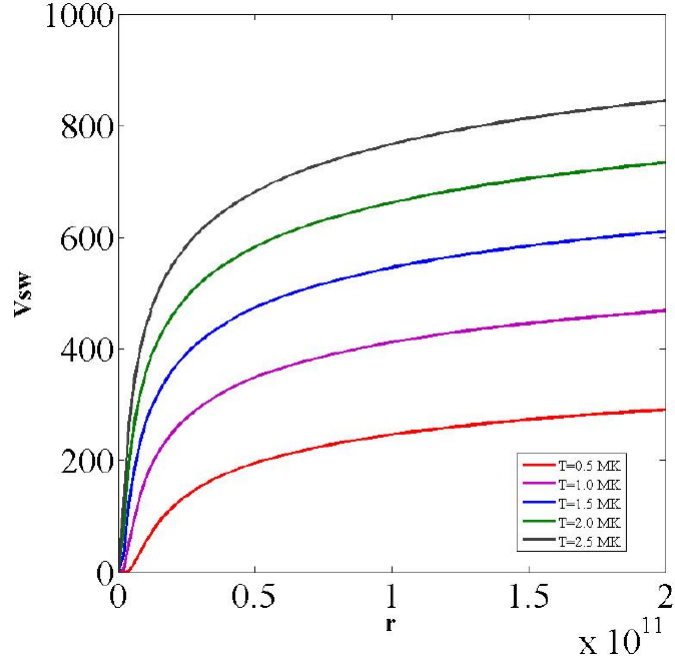


Figure 2.2: Solutions of the isothermal Parker model of the solar wind (Equation 2.7). Heliocentric distance r is in m and the solar wind speed V_{sw} is in km s^{-1} . Figure reproduced from Parashar [2011] with permission (see Appendix E).

Parker’s simple considerations demonstrated the existence of a unique supersonic solution to the equations of motion of an expanding isothermal corona; this solution was in agreement with values of the flow speed inferred by indirect measurements and could also be reconciled with the known properties of the interstellar medium. As stated in Chapter 1, the existence of the solar wind was confirmed soon after by direct in-situ spacecraft measurements [Gringauz et al., 1960; Bonetti et al., 1963; Snyder et al., 1963; Neugebauer and Snyder, 1966].

However, as was also discussed in Chapter 1, the solar wind exhibits variation and structure on a variety of different levels, such as variation with solar cycle, fast and slow wind streams, and turbulent fluctuations. These effects cannot be captured by the simple one-dimensional (1D) model discussed above, which is also unsatisfactory in its use of an unspecified heating source. Parker did examine the implications of

coronal outflow and solar rotation on the magnetic field of the Sun [Parker, 1958]. He reasoned that the high electrical conductivity of the coronal plasma allowed the use of the “frozen-in” approximation for magnetic field lines (i.e., the plasma diffuses very slowly in the direction perpendicular to the magnetic field, so the field lines are constrained to flow with the plasma [see, e.g., Choudhuri, 1998]), which leads to their being drawn out into an Archimedian spiral due to solar rotation (see Figure 1.2). For a spherically symmetric geometry, these considerations lead to the following expressions for the components of the magnetic field in heliocentric spherical polar coordinates (r, ϕ, θ) :

$$\left. \begin{aligned} B_r(r, \phi, \theta) &= B(r_0, \phi_0, \theta) \left(\frac{r_0}{r}\right)^2, \\ B_\phi(r, \phi, \theta) &= -B(r_0, \phi_0, \theta) \frac{\omega r_0}{U_{sw}} \frac{r_0}{r} \sin \theta, \\ B_\theta &= 0, \end{aligned} \right\} \quad (2.8)$$

where θ is the co-latitude measured from the solar rotation axis, ϕ is the azimuthal angle, ϕ_0 is an initial position at a reference distance r_0 , U_{sw} is a constant solar wind speed, and $\omega = 2.7 \times 10^{-6}$ radians sec^{-1} is the angular velocity of solar rotation.

The Parker spiral magnetic field is commonly used as an approximation for the large-scale interplanetary magnetic field (IMF) [Owens and Forsyth, 2013], but a more accurate and self-consistent description is provided by the three-dimensional (3D) equations of MHD, which couple Maxwell’s equations for electromagnetic fields with the equations for fluid flow. The use of MHD to describe the solar wind allows for the inclusion of effects due to magnetic forces, which were first examined by Weber and Davis [1967].¹ With the advent of powerful computers in recent decades, it has become possible to obtain numerical solutions for MHD-based solar wind models in more than one dimension. Some of the earliest efforts in this area include the works by Pneuman and Kopp [1971] and Pizzo [1978].

¹ Magnetic effects can also be significant at kinetic scales in the solar wind, as in the inhibition of thermal conduction across the magnetic field [e.g., Chapter III of Hundhausen, 1972] and the possibility of non-collisional energy exchange mechanisms acting via plasma waves and instabilities [e.g., Marsch, 2006].

2.2 The MHD Description of the Solar Wind

Cowling’s [1957] classic text gives a concise account of MHD, while a more modern and extended treatment may be found in Choudhuri [1998]. We introduce the equations of MHD and provide a brief overview of their linear solutions in this section. We also discuss the applicability of the MHD description to the weakly collisional solar wind plasma.

2.2.1 The Equations of MHD

The kinetic theory of plasmas is not yet fully developed, and the “microscopic” derivation of fluid equations, beginning with the equation for a particle distribution function, is not as straightforward as the corresponding derivation for a neutral gas [Chapman and Cowling, 1991]. One reason for this is the different nature of collisions in ionized and neutral gases; a collision between neutral particles is a sharp, well-defined event, but in a plasma, the constituent charged particles interact via long-range forces that produce small deflections in the trajectory of a particle, and these deflections add up over time. Collisions are neglected in the *Vlasov* description [Montgomery and Tidman, 1964], but a part of their effect is retained by the use of coarse-grained fields that arise from the collective “smoothed” interactions of particles.

The “macroscopic” derivation [e.g., Choudhuri, 1998] leads to equations representing conservation of mass and momentum:

$$\frac{\partial \rho}{\partial t} + \nabla \cdot (\rho \mathbf{v}) = 0, \quad (2.9)$$

$$\frac{\partial \mathbf{v}}{\partial t} + (\mathbf{v} \cdot \nabla) \mathbf{v} = \mathbf{F} - \frac{1}{\rho} \nabla p + \frac{1}{\rho c} \mathbf{j} \times \mathbf{B} + \nu \nabla^2 \mathbf{v}, \quad (2.10)$$

where ρ is the mass density of the fluid, \mathbf{v} is the fluid velocity, p is the fluid pressure, \mathbf{F} is an external body force, c is the speed of light in a vacuum, ν is the kinematic viscosity, \mathbf{j} is the electric current density, and \mathbf{B} is the magnetic field strength. These equations are applicable to low-frequency systems, where high-frequency processes that

could create charge separation are not relevant. The high conductivity of the system ensures that electric fields are eliminated at rapid timescales (see next paragraph).

Equations (2.9) and (2.10) are to be combined with Maxwell's equations for electromagnetic fields in a vacuum [e.g., [Jackson, 1975](#)]:

$$\nabla \cdot \mathbf{E} = 4\pi\rho_e, \quad (2.11)$$

$$\nabla \cdot \mathbf{B} = 0, \quad (2.12)$$

$$\nabla \times \mathbf{B} = \frac{4\pi}{c}\mathbf{j} + \frac{1}{c}\frac{\partial\mathbf{E}}{\partial t}, \quad (2.13)$$

$$\nabla \times \mathbf{E} = -\frac{1}{c}\frac{\partial\mathbf{B}}{\partial t}. \quad (2.14)$$

Here \mathbf{E} is the electric field strength and ρ_e is the electric charge density. In the case of highly conducting plasmas, the displacement current $c^{-1}\partial_t\mathbf{E}$ in Ampere's law (2.13) can be neglected, since electrons respond to changes in the electric field on timescales much shorter than the timescale associated with significant variation in the electric field. This means that the electric current term $4\pi\mathbf{j}/c$ is much larger than the displacement current term, and Equation (2.13) reduces to

$$\nabla \times \mathbf{B} = \frac{4\pi}{c}\mathbf{j}. \quad (2.15)$$

This lets us eliminate the current from the the momentum equation (2.10) to get

$$\frac{\partial\mathbf{v}}{\partial t} + (\mathbf{v} \cdot \nabla)\mathbf{v} = \mathbf{F} - \frac{1}{\rho}\nabla p + \frac{1}{4\pi\rho}(\nabla \times \mathbf{B}) \times \mathbf{B} + \nu\nabla^2\mathbf{v}. \quad (2.16)$$

Next, to obtain a dynamical equation for the magnetic field, we assume that Ohm's law holds in the form [[Choudhuri, 1998](#)]

$$\mathbf{j} = \sigma \left(\mathbf{E} + \frac{\mathbf{v}}{c} \times \mathbf{B} \right), \quad (2.17)$$

where σ is the electrical conductivity. Combining (2.15) and (2.17), we can express the

electric field in terms of the velocity and the magnetic field:

$$\mathbf{E} = \frac{c}{4\pi\sigma} \nabla \times \mathbf{B} - \frac{\mathbf{v}}{c} \times \mathbf{B}. \quad (2.18)$$

The above considerations demonstrate that the electric field is not an independent variable in the MHD description. Combining (2.18) and (2.14) yields the so-called *induction equation*:

$$\frac{\partial \mathbf{B}}{\partial t} = \nabla \times (\mathbf{v} \times \mathbf{B}) + \eta \nabla^2 \mathbf{B}, \quad (2.19)$$

where $\eta \equiv c^2/(4\pi\sigma)$ is the *magnetic diffusivity* or *resistivity*.

Equations (2.9), (2.16), and (2.19), along with the solenoidality condition (2.12) constitute the equations of single-fluid MHD. An energy evolution equation may also be included [e.g., Bittencourt, 2004], but we do not consider that here, noting that one way to close the system is with a polytropic equation of the form $p\rho^{-\gamma} = \text{constant}$. We rewrite (2.16) and (2.19) using standard vector identities, and collect the MHD equations in the form:

$$\frac{\partial \rho}{\partial t} + \nabla \cdot (\rho \mathbf{v}) = 0, \quad (2.20)$$

$$\left(\frac{\partial}{\partial t} + \mathbf{v} \cdot \nabla \right) \mathbf{v} = \mathbf{F} - \frac{1}{\rho} \nabla \left(p + \frac{B^2}{8\pi} \right) + \frac{(\mathbf{B} \cdot \nabla) \mathbf{B}}{4\pi\rho} + \nu \nabla^2 \mathbf{v}, \quad (2.21)$$

$$\left(\frac{\partial}{\partial t} + \mathbf{v} \cdot \nabla \right) \mathbf{B} = (\mathbf{B} \cdot \nabla) \mathbf{v} - \mathbf{B} \nabla \cdot \mathbf{v} + \eta \nabla^2 \mathbf{B}. \quad (2.22)$$

Equation (2.21) makes it clear that the magnetic field introduces a pressure $B^2/8\pi$. The other magnetic term $(\mathbf{B} \cdot \nabla) \mathbf{B}$ can be shown to produce a *tension* along magnetic field lines [e.g., Choudhuri, 1998]. In the absence of a magnetic field, (2.21) reduces to the Navier–Stokes equation (1.1) for a neutral fluid. Note that the above equations are valid for compressible flow; for incompressible flow, (2.20) reduces to a solenoidality constraint on the velocity: $\nabla \cdot \mathbf{v} = 0$.

We can define a *magnetic Reynolds number*, analogously to the fluid Reynolds

number from Section 1.1.5, as the dimensionless ratio of the two terms on the right-hand side of the induction equation (2.19):

$$\mathcal{R}_M = \frac{VB/L}{\eta B/L^2} = \frac{LV}{\eta}, \quad (2.23)$$

where V, B , and L are typical values of velocity, magnetic field strength, and length in the system. It is generally the case that $\mathcal{R}_M \ll 1$ in laboratory plasmas, while $\mathcal{R}_M \gg 1$ in astrophysical systems, due to the typically large length scales in the latter. This means that the first term on the r.h.s. of Equation (2.19) can be neglected in laboratory plasmas, leading to a diffusion equation for the magnetic field. On the other hand, in astrophysical plasmas the induction equation may be written as

$$\text{Astrophysics : } \quad \frac{\partial \mathbf{B}}{\partial t} \approx \nabla \times (\mathbf{v} \times \mathbf{B}), \quad (2.24)$$

where the ‘ \approx ’ sign becomes the ‘=’ sign in the *ideal MHD limit* of infinite conductivity (or zero resistivity). An important consequence of the ideal induction equation is *Alfvén’s theorem of flux-freezing*, which asserts that magnetic fields are frozen into the plasma and therefore move with the fluid [e.g., Choudhuri, 1998].

The MHD equations, together with appropriate boundary conditions, can in principle be solved to yield the spatial and temporal evolution of the physical fields. However, as in the case of the Navier–Stokes equation, the nonlinear nature of the equations has, so far, precluded their general analytical solution. Recent increases in computational power have enabled progress in numerical approaches, but the problem of inadequate resolution in simulations remains, as discussed in Section 1.1.5.

2.2.2 Applicability of the MHD Description to the Solar Wind

We now discuss some issues pertaining to the validity of the MHD description to the solar wind. Let us first consider the validity of the underlying *plasma approximation* [e.g., Choudhuri, 1998]. The coronal plasma is hot enough to ionize its primary chemical constituents (H & He), but the plasma approximation requires that the ionized gas be

charge-neutral over distances of physical interest, or quasi-neutral. For typical solar wind parameters (Appendix A) the *Debye length*, or the length beyond which a plasma can be considered charge-neutral, is $\lambda_D \sim 6$ m. A measure of the strength of collective behaviour in a plasma is given by the dimensionless *plasma parameter* $g = 1/(n\lambda_D^3)$, where n is the number density of ions. When g is small, the number of particles interacting collectively is large, but the *strength* of interactions is small, and the plasma can be described as a classical ideal gas. In the solar wind, $g \sim 10^{-10}$, so the plasma description is clearly on a very strong footing.

Moving on to the validity of the MHD description introduced in the previous section, two approximations need to be justified, namely the continuum hypothesis and the single-fluid approximation. In a neutral fluid, it is straightforward to test whether the continuum hypothesis is applicable to a system – if the characteristic system size is much larger than the mean free path (mfp) between collisions, then any volume of size larger than the mfp but smaller than the system size may be considered to be a fluid element, since discrete particle motions are restricted to be confined within the fluid element by collisions. As mentioned in the previous section, collisions in a plasma are not well-defined events due to the long range of inter-particle interactions, and consequently we do not have a good understanding of the scales at which the magnetofluid description breaks down.

Fortunately, some justification for the continuum approximation in a plasma may be found by appeal to a characteristic small length-scale introduced by the presence of a magnetic field – the particle’s *gyroradius*, which defines the cross-sectional area within which the particle revolves around a magnetic field. In the solar wind, the collision mfp is around 1 au, but the gyroradius is about 50 – 100 km near earth, and smaller close to the Sun. Since this latter scale is much smaller than the characteristic system size of the solar wind, the fluid approximation may have some validity, at least in directions perpendicular to the magnetic field. Further justification for the fluid approximation in plasmas may be found in the notion of “anomalous collisions” that result from plasma microinstabilities [Hasegawa and Sato, 1989].

In recent years, many studies have investigated the finer details of solar wind heating and dissipation within a kinetic description [e.g., [Schekochihin et al., 2009](#); [Servidio et al., 2015](#); [Howes, 2017](#); [Yang et al., 2017](#)]. Several notable properties of the solar wind plasma, such as proton temperature anisotropies and differential flow between protons and helium ions [e.g., [Marsch, 2006](#)], require kinetic descriptions. However, the large-scale features of solar wind turbulence are represented adequately in a fluid description [e.g., [Tu and Marsch, 1995](#); [Goldstein et al., 1995](#); [Bruno and Carbone, 2013](#); [Matthaeus et al., 2015](#); [Makwana et al., 2015](#); [Parashar et al., 2015](#)]. In particular, the MHD description is *indispensable* for *global* simulation of the solar wind, where the largest length scales in the system span *at least* a few solar radii ($1 R_{\odot} = 6.9 \times 10^5$ km). Kinetic effects come into play at the ion-inertial scale, which is roughly 90 km at 1 au [e.g., [Schekochihin et al., 2009](#)] and becomes smaller closer to the Sun. Current and foreseeable computational resources do not permit the resolution of this wide range of scales (see discussion around Equation 1.10).

We now remark on the validity of the single-fluid approximation in the solar wind. This description is usually considered applicable to high-density and low-temperature fluids, where collisions between different constituent species can establish an equilibrium state characterized by a single local velocity and temperature. However, the low density interplanetary plasma is *not* collisional, and electron and proton temperatures can be significantly different. In high speed streams, the proton temperature is observed to be about a factor of two larger than the electron temperature [[Cranmer et al., 2009](#); [Usmanov et al., 2014](#)], which is surprising when one considers the fact that the electrons are believed to be more thermally conductive.

The momentum of the solar wind is mostly carried by the much heavier ions, and therefore in the single-fluid description of solar wind flow, we can reasonably neglect the electron velocity. The more mobile electrons provide the high conductivity and enforce charge-neutrality. The neglect of the α -particle (helium ions) contribution to the momentum of the solar wind may not be entirely justified in all situations, however. Even though these heavy ions make up just 4% of the ion composition, their masses

can make up for their small number, especially in the fast wind where they can be faster than protons [e.g., [Marsch, 2006](#)].

We end this section by noting that even though the MHD equations (2.20) – (2.22) are valid for compressible flow, much of the theoretical work on transport of turbulent fluctuations in the solar wind makes the simplifying assumption of local (or small-scale) incompressibility [[Matthaeus and Goldstein, 1982](#); [Zhou and Matthaeus, 1990b](#); [Tu and Marsch, 1995](#); [Matthaeus et al., 1999c](#); [Breech et al., 2008](#); [Oughton et al., 2011](#); [Zank et al., 2012, 2017](#)]. There is substantial observational and numerical evidence indicating that in the presence of a magnetic field, turbulent dynamics are *nearly incompressible* in nature [[Shebalin et al., 1983](#); [Roberts et al., 1987b,a](#); [Matthaeus et al., 1990](#); [Oughton et al., 1994](#)]. The theory of nearly incompressible turbulence [[Klainerman and Majda, 1981, 1982](#); [Matthaeus and Brown, 1988](#); [Zank and Matthaeus, 1991, 1993](#)] provides a foundation for these observations. Further, observations of interplanetary turbulence indicate a dominance of incompressive Alfvén modes, while compressive magnetosonic modes are susceptible to damping (see Section 2.2.3, below).

The solar wind model we use in this work is a two-fluid model, in the sense that we include two separate equations for proton and electron temperatures, with the momentum of the wind assumed to be carried by protons. In addition, the model treats the large-scale flow as compressible, while the small-scale MHD fluctuations are assumed to be incompressible. Further details are presented in Chapter 4.

2.2.3 Magnetohydrodynamic Waves

Observations show that large-amplitude fluctuations are present in the interplanetary medium [[Belcher and Davis, 1971](#)]. The most commonly observed variations are considered to be hydromagnetic in nature, since they correspond to spatial scales larger than the proton gyroradius. We will briefly review the wave solutions of the MHD equations here. A kinetic theory of hydromagnetic waves in a collisionless plasma may be developed analogously to the fluid theory [[Barnes, 1979](#)].

We will restrict ourselves to the simplified case of a uniform, inviscid, perfectly conducting plasma, in the presence of a uniform magnetic field.² The linearization of the MHD equations following the usual perturbation analysis leads to small-amplitude plane wave solutions [e.g., [Bittencourt, 2004](#)]. Solutions of *finite* amplitude may be found in the special case where spatial variation occurs only in one direction (say, the z -axis), and all fields are functions of a single scalar characteristic function $\phi(z, t)$ [[Barnes and Hollweg, 1974](#)]. Here we will adopt this framework, which is of relevance to the solar wind. Three classes of solutions are obtained:

- (i) **Nonpropagating Structures:** The velocity $v_z = v_{z0}$ and the total pressure $p + B^2/8\pi$ (see Equation 2.21) are constants for these structures, which merely convect with the fluid and satisfy the equation $\phi_t + v_z\phi_z = 0$. These structures include the tangential pressure balance and the “entropy wave”. All varying quantities are functions only of $z - v_{z0}t$, implying stationarity in the rest frame of the plasma.
- (ii) **Transverse Alfvén Waves:** When $\phi_t + v_z\phi_z \neq 0$, we get propagating waves. The simple Alfvén wave is purely transverse and incompressive, with constant v_z, p, ρ , and \mathbf{B}_\perp (The ‘ \perp ’ subscript indicates the plane transverse to the z direction). The tension in the magnetic field lines provides the restoring force, and the speed of propagation along the z direction is the Alfvén speed $V_{Az} \equiv B_z/(4\pi\rho)^{1/2}$. We also have

$$\mathbf{v}_\perp = \mp V_{Az} \mathbf{B}_\perp / B_z + \text{const}, \quad (2.25)$$

implying that the plasma “tracks” the magnetic field, as expected from the frozen-in theorem. These waves satisfy the equations $\phi_t + (v_z \pm V_{Az})\phi_z = 0$, and propagate parallel or antiparallel to the mean magnetic field (which is directed along the z -axis here).

² The presence of additional effects like viscosity results in a damping of the waves [e.g., [Bittencourt, 2004](#), Chapter 15].

(iii) **Magnetoacoustic Waves:** The second type of propagating structure is a mix of magnetic and acoustic modes, with both pressure and magnetic variations acting as restoring forces. These longitudinal compressive waves satisfy the equations $\phi_t + (v_z \pm V_{f,s})\phi_z = 0$. Here V_f and V_s are the propagation speeds of the *fast* and *slow magnetosonic* modes, respectively, defined as

$$V_{f,s}^2 = \frac{1}{2} \left[V_A^2 + V_s^2 \pm \sqrt{(V_A^2 + V_s^2)^2 - 4V_s^2 V_A^2} \right], \quad (2.26)$$

where $V_s = \sqrt{\gamma p / \rho}$ is the sound speed, and $V_A^2 = B^2 / (4\pi\rho)$. In the fast mode, the pressure and magnetic restoring forces are roughly in phase, leading to propagation faster than the slow mode, in which the restoring forces are roughly out of phase. Both modes may steepen into shocks if the dissipation is sufficiently weak.

Within the context of the solar wind, early observations of wave-like fluctuations [Coleman, 1966, 1967] were followed by the landmark study by Belcher and Davis [1971], who used the correlation coefficient between the velocity and the magnetic field (see Equation 2.25) to test the preponderance of Alfvénic fluctuations. They concluded that Alfvén waves dominate the fluctuations in the wavelength range 10^3 to 5×10^6 km more than 50% of the time, and that these waves propagate outward from the Sun (in the plasma frame). The dominance of “pure” Alfvén waves was especially marked in fast wind streams. In contrast, magnetosonic modes are rarely observed.

These observations are generally consistent with theory [Barnes, 1979], which predicts that Alfvén modes are resistant to damping due to the various mechanisms that are active in a collisionless plasma (e.g., Landau damping). One would therefore expect to find pure Alfvén modes in regions that are less likely to be sites of large-scale turbulence, such as fast wind streams. Nevertheless, we would like to remind the reader of the several observations (Section 1.1.4) which suggest that strong nonlinear interactions also play a crucial role in the evolution of solar wind fluctuations.

2.2.4 Elsässer Variable Representation of the MHD Equations

The [Elsässer \[1950\]](#) variables allow for an alternative interpretation of the MHD equations in terms of “inward” and “outward” propagating fluctuations. These variables are defined as the sum and the difference of the velocity and magnetic fluctuations:

$$\mathbf{z}^{\pm} = \mathbf{v} \pm \mathbf{b}/\sqrt{4\pi\rho}, \quad (2.27)$$

where the magnetic fluctuation has been normalized to Alfvén speed units and the density is constant for the incompressible case. The relation to Alfvén mode propagation may be seen as follows. The direction of propagation of an Alfvén wave can be specified by the wavenumber $\mathbf{k} \sim -\mathbf{v} \times \mathbf{b}$; this reflects the fact that Alfvén waves have velocity and magnetic perturbations that are perpendicular to the each other and to the direction of propagation, which lies parallel or antiparallel to the mean magnetic field. If the solar magnetic field is directed outward (positive radial direction), then fluctuations satisfying $\mathbf{v} = -\mathbf{b}/\sqrt{4\pi\rho}$ (equivalent to $\mathbf{z}^+ = 0$) are purely outward propagating waves. Similarly, fluctuations with $\mathbf{v} = \mathbf{b}/\sqrt{4\pi\rho}$ (equivalent to $\mathbf{z}^- = 0$) would be purely inward propagating. Note that for an inward directed mean magnetic field \mathbf{z}^+ (\mathbf{z}^-) would represent outward (inward) propagating fluctuations.

We write the MHD equations in Elsässer form by adding and subtracting Equations (2.21) and (2.22), to find, for the incompressible case [e.g., [Biskamp, 2003](#); [Bruno and Carbone, 2013](#)],

$$\frac{\partial \mathbf{z}^{\pm}}{\partial t} + \mathbf{z}^{\mp} \cdot \nabla \mathbf{z}^{\pm} = -\nabla P_{\text{tot}} + \frac{1}{2}(\nu + \eta)\nabla^2 \mathbf{z}^{\pm} + \frac{1}{2}(\nu - \eta)\nabla^2 \mathbf{z}^{\mp}, \quad (2.28)$$

$$\nabla \cdot \mathbf{z}^{\pm} = 0, \quad (2.29)$$

where P_{tot} is the combined fluid and magnetic pressure. Equation (2.28) reveals that nonlinear couplings can occur only between fluctuations propagating in opposite directions, since the only nonlinear term is $\mathbf{z}^{\mp} \cdot \nabla \mathbf{z}^{\pm}$. Therefore, if one begins with a state in which either of \mathbf{z}^{\pm} is zero, then the nonlinear terms are zero, and we simply have

linear waves propagating along the mean magnetic field.

2.3 WKB Theory of Solar Wind Fluctuations

Observations of wave-like fluctuations in the solar wind with energy densities comparable to the unperturbed magnetic and thermal energy densities [Belcher and Davis, 1971] motivated the development of solar wind models that included momentum and energy transport by waves [Barnes, 1979, and references therein]. These early models were based on the WKB or eikonal approximation, which assumes that the waves propagate in a *weakly inhomogeneous* background fluid; i.e., variations in the background are small over times and distances that are comparable to the waves' periods and wavelengths. Further, it is assumed that the waves have small amplitudes, which leads to a linearized system with Alfvén modes as the leading-order solutions. The waves produce two effects on the background flow: heating due to dissipation of the wave energy into thermal energy, and the direct transfer of momentum and energy from wave stresses that perform work on the expanding solar wind [e.g., Jacques, 1977; Usmanov et al., 2000]. Heinemann and Olbert [1980] generalized the WKB model to include finite-wavelength (“non-WKB”) effects. WKB theory yields a simple equation for the evolution of the average amplitude of magnetic fluctuations, and its tractability is a major reason for the model’s enduring popularity [e.g., Cranmer et al., 2007].

Some predictions of WKB theory are in accord with observations. In particular, the radial evolution of magnetic fluctuation energy is observed to behave as r^{-3} [Belcher and Davis, 1971; Roberts et al., 1990], in striking agreement with the WKB prediction [Barnes, 1979; Zank et al., 1996]. WKB theory also predicts that only outward propagating modes can exist above the Alfvén critical radius³. This is reasonable if one assumes that the waves are generated close to the Sun, below the Alfvén radius. All inward propagating modes would then move toward the Sun, since their net motion (flow velocity + wave velocity) would be inward below the Alfvén point. In contrast,

³ At this point the solar wind speed becomes equal to the Alfvén speed.

outward Alfvénic modes generated close to the Sun would simply be advected into interplanetary space by the solar wind.

However, several observations point to deficiencies in the WKB model. The predicted equipartition of magnetic and kinetic energy fluctuations is not consistent with observations, which indicate a 2:1 excess of magnetic energy [Roberts et al., 1990; Zank et al., 1996]. Observations also indicate that interplanetary fluctuations become less Alfvénic with increasing heliocentric distance [Roberts et al., 1987b,a]. Further, WKB theory predicts that the minimum-variance direction (MVD) of the fluctuations should be radially aligned, while observations indicate that the MVD is aligned with the mean magnetic field [Klein et al., 1991]. Extensions of WKB theory to include finite-wavelength effects have not succeeded in pushing it towards better agreement with observations [Hollweg, 1990; Matthaeus et al., 1994b; Goldstein et al., 1995].

In response to the inadequacy of wave-based models of solar wind fluctuations, a variety of turbulence transport models have been developed in recent decades that attempt to capture the effects of nonlinear couplings in a more complete way [Tu, 1988; Marsch and Tu, 1989; Zhou and Matthaeus, 1990b,a; Matthaeus et al., 1994a; Zank et al., 1996; Matthaeus et al., 1999b; Breech et al., 2008; Verdini et al., 2010; Usmanov et al., 2011; Oughton et al., 2011; Zank et al., 2012, 2017]. These models are based on a scale-separation between the slowly varying large-scale flow and the rapidly varying plasma fluctuations, with the small scales assumed to be nearly incompressible [Zank and Matthaeus, 1993]. A set of equations for the fluctuating quantities are derived by subtracting ensemble-averaged equations from the equations for the complete fields. The turbulence equations may be solved self-consistently with the equations for the large-scale flow [e.g., Usmanov et al., 2014], or a constant mean velocity and a Parker-type magnetic field (Equation 2.8) may be employed [e.g., Adhikari et al., 2017].

The nonlinear terms arising in these turbulence transport equations require closure approximations (see Sections 1.1.5 and 3.2). Assuming that the scale-separation is valid, the small-scale turbulence can be treated locally using homogeneous turbulence theory. The assumption of small-scale incompressibility allows one to employ

Kolmogorov-style phenomenological approaches based on scale-similarity [[Zhou and Matthaeus, 1990a](#); [Hossain et al., 1995](#); [Verma, 2004](#)].

The preceding paragraphs serve to motivate the necessity of an improved understanding of turbulence and its modeling. We have made preliminary remarks on this theme in [Sections 1.1.5](#) and [1.1.6](#), and we continue the discussion in the next chapter, before presenting the solar wind model used in this work in [Chapter 4](#).

Chapter 3

TURBULENCE

In Chapter 1, we discussed the ubiquity of turbulence in the interplanetary medium, and the crucial role turbulent fluctuations are thought to play in heating and accelerating the solar wind plasma. We then introduced some fundamental issues that arise in the modeling and numerical simulation of turbulent flows. It is clear from the final section of the previous chapter that a complete model of the solar wind must include the effects of turbulence transport, and therefore needs to grapple with the problem of turbulence and its modeling.

In this chapter, we continue our discussion of the fundamental aspects of fluid turbulence, including the Kolmogorov cascade, spectral transfer of energy, and the statistical properties of turbulent fields. Standard approaches to overcoming the closure problem will be reviewed, and we will extend the discussion to magnetofluid turbulence in the solar wind.

3.1 The Kolmogorov Theory

Most approaches to turbulence modeling, even in the case of magnetofluids, are largely based on fundamental ideas that were developed in the context of incompressible neutral fluid hydrodynamics. Accordingly, we resume our discussion of turbulence by rewriting the Navier–Stokes equation (introduced in Section 1.1.5) for incompressible flow

$$\frac{\partial \mathbf{u}}{\partial t} + \mathbf{u} \cdot \nabla \mathbf{u} = -\frac{1}{\rho_0} \nabla P + \nu \nabla^2 \mathbf{u}, \quad (3.1)$$

where ρ_0 is a constant density, \mathbf{u} is the velocity of the turbulent flow, P is the fluid pressure, and ν is the kinematic viscosity. Note that the above equation is for the

turbulent part of the flow (see Equation 1.8); any mean flow can be eliminated by a Galilean transformation [Batchelor, 1953]. In order to better understand the nature of the nonlinear term, we will examine this equation in Fourier space. This will set the stage for a discussion of the Kolmogorov hypothesis of spectral transfer of energy across the inertial range.

3.1.1 The Navier–Stokes Equation in Fourier Space

We define the Fourier transform \hat{f} of a function f as

$$\hat{f}(\mathbf{k}, t) = \left(\frac{1}{2\pi}\right)^3 \int e^{-i\mathbf{k}\cdot\mathbf{x}} f(\mathbf{x}, t) d\mathbf{x}, \quad (3.2)$$

where \mathbf{k} is the wavevector and the integral is performed over the entire domain of \mathbf{x} . The inverse Fourier transform relation is

$$f(\mathbf{x}, t) = \int e^{i\mathbf{k}\cdot\mathbf{x}} \hat{f}(\mathbf{k}, t) d\mathbf{k}, \quad (3.3)$$

where the integral is performed over the entire domain of \mathbf{k} . Recall that the Fourier transform permits one to distinguish between the different scales present in a signal, with the wavenumber k corresponding to a spatial scale $\sim 1/k$ [see, e.g., Section 8.1.2 of Davidson, 2015].

By taking the derivative of the Equation (3.3) with respect to x_α , it can easily be seen that the Fourier transform of $\partial_{x_\alpha} f$ is $ik_\alpha \hat{f}$, and therefore $\nabla^2 f = -k^2 f$. The incompressibility condition $\nabla \cdot \mathbf{u} = 0$ then implies that

$$\mathbf{k} \cdot \hat{\mathbf{u}} = 0, \quad (3.4)$$

so that the velocity $\hat{\mathbf{u}}(\mathbf{k}, t)$ is in a plane perpendicular to \mathbf{k} .

To write the Navier–Stokes equation in Fourier space, we first note that the Fourier transforms of the first term on the LHS and the second term on the RHS become $\partial_t \hat{\mathbf{u}}$ and $\nu k^2 \hat{\mathbf{u}}$, respectively. Due to Equation (3.4) both these terms lie on the

plane perpendicular to \mathbf{k} , but the Fourier transform of the pressure gradient $i\hat{P}\mathbf{k}$ is parallel to \mathbf{k} . This implies that the Fourier transform of $\mathbf{u} \cdot \nabla \mathbf{u} + \nabla P/\rho_0$ must be the projection of the Fourier transform of $\mathbf{u} \cdot \nabla \mathbf{u}$ on the plane perpendicular to \mathbf{k} . Using the convolution theorem [e.g., Lesieur, 2012, Chapter 5], the Fourier transform (FT) of the α -component of the nonlinear term is

$$\text{FT} \left[u_\beta \frac{\partial u_\alpha}{\partial x_\beta} \right] = \text{FT} \left[\frac{(\partial u_\alpha u_\beta)}{\partial x_\beta} \right] = ik_\beta \int_{\mathbf{p}+\mathbf{q}=\mathbf{k}} \hat{u}_\alpha(\mathbf{p}, t) \hat{u}_\beta(\mathbf{q}, t) d\mathbf{p}, \quad (3.5)$$

where the summation convention is used and we have made use of the solenoidality of \mathbf{u} . The projection of this term on the plane perpendicular to \mathbf{k} can be expressed in terms of the operator

$$\mathcal{P}_{\alpha\beta}(\mathbf{k}) = \delta_{\alpha\beta} - \frac{k_\alpha k_\beta}{k^2}, \quad (3.6)$$

which acts on a vector \mathbf{A} such that $\mathcal{P}_{\alpha\beta}(\mathbf{k})A_\beta$ is the α -component of the projection of \mathbf{A} upon the plane perpendicular to \mathbf{k} [e.g., Lesieur, 2012, Chapter 5].

Putting all this together, we can finally write the Navier–Stokes equation in Fourier (or *spectral*) space:

$$\left(\frac{\partial}{\partial t} + \nu k^2 \right) \hat{u}_\alpha(\mathbf{k}, t) = -ik_\gamma \mathcal{P}_{\alpha\beta}(\mathbf{k}) \int_{\mathbf{p}+\mathbf{q}=\mathbf{k}} \hat{u}_\beta(\mathbf{p}, t) \hat{u}_\gamma(\mathbf{q}, t) d\mathbf{p}. \quad (3.7)$$

This equation describes the evolution of the \mathbf{k} Fourier component of the velocity field. The RHS of Equation (3.7) is the α -component of $\mathbf{u} \cdot \nabla \mathbf{u} + \nabla P/\rho_0$ in Fourier space. We see that the nonlinear term involves *triad* interactions between wave vectors such that $\mathbf{k} = \mathbf{p} + \mathbf{q}$, so these nonlinear interactions imply that velocity Fourier coefficients with wavenumbers \mathbf{p} and \mathbf{q} are coupled together to contribute to the Fourier coefficient with wavenumber \mathbf{k} . The nonlinear term then is the total contribution from all such interactions in wavenumber space. We interpret a wavenumber k with structures of size $2\pi/k$ (or simply $\sim 1/k$), so this discussion explicitly demonstrates the turbulent coupling of structures of different spatial scales; in principle, every Fourier mode of the velocity field is coupled to every other mode, which makes for a very difficult physical

problem. Before discussing the simplifying hypotheses that Kolmogorov made to tackle the issue, we briefly discuss the spectral transfer of energy in turbulence by examining the spectral equation for energy.

3.1.2 Spectral Transfer of Energy

An evolution equation for the ensemble-averaged turbulent energy – the *von Kármán–Howarth* equation [de Kármán and Howarth, 1938] – is derived in Appendix B. The spectral form of this equation is (see Section B.3.2)

$$\frac{\partial E(k, t)}{\partial t} = T(k, t) - 2\nu k^2 E(k, t), \quad (3.8)$$

where $E(k, t)$ is the *energy spectrum* that represents the distribution of energy in wavenumber space¹, and $T(k, t)$ is the nonlinear term that redistributes energy in wavenumber space. In terms of the energy cascade, the energy in the system at small k (large scales) is transferred by the nonlinear term $T(k, t)$ to large k (small scales), where it is dissipated by the viscous term.

It is instructive to consider the absence of nonlinearity, so that (3.8) has the solution

$$E(k, t) = E(k, t_0)e^{-2\nu k^2(t-t_0)}, \quad (3.9)$$

where t_0 is an arbitrary initial time. The energy in a mode k therefore decays at a rate $2\nu k^2$, independent of other modes. Clearly, the decay is faster for large k . This reflects the fact that since the viscosity is a small parameter, viscous effects are only important when the velocity gradients (captured mathematically by ∇^2 in Equation 3.1) are large. We can therefore expect the nonlinear term to transfer energy from small k (the large scales where energy is produced, e.g., at a shear boundary) to large values of k where dissipation will be concentrated.

¹ Note that $E(k)$ is an energy density in wavenumber space, with the average kinetic energy per unit mass given by $\langle \mathbf{u}^2 \rangle / 2 = \int_0^\infty E(k) dk$.

We now consider the range of wavenumbers involved in the cascade. The lowest wavenumber is associated with the largest eddies in the system, which are bounded by the system size (L , say), so that

$$k_L \sim 1/L. \quad (3.10)$$

The upper cut-off wavenumber is expected to be determined by the viscous dissipation, which involves two physical parameters – the viscosity ν and the energy *dissipation rate* ϵ [energy transfer per unit mass per unit time; see, e.g., [McComb, 1990](#)]. On dimensional grounds, the dissipation length scale is

$$l_d \sim \left(\frac{\nu^3}{\epsilon} \right)^{1/4}, \quad (3.11)$$

with the associated wavenumber given by

$$k_d \sim \left(\frac{\epsilon}{\nu^3} \right)^{1/4}. \quad (3.12)$$

Note that k_L is determined by the properties of the particular system under study, while the largest wavenumbers are determined by the general parameters ϵ and ν . In the limit of infinite Reynolds number (Equation 1.2) the ratio of k_d to k_L is infinitely large.

These dimensional estimates have empirical support; it has been known since the classic experiments of [Taylor \[1938\]](#) that the energy is determined by the lowest wavenumbers and the dissipation rate is determined by the largest wavenumbers, and the two ranges do not overlap even for modest Reynolds numbers. The inertial (non-linear) term provides the link between the energy-containing range and the dissipation range, and we can introduce the intermediate *inertial range* of wavenumbers k defined by $k_d \gg k \gg k_L$ (see Figure 1.6). The separation of the inertial range from the two extreme ends is of crucial importance to the study of turbulence, since it allows us to consider the nonlinear transfer of energy independently of the details of its input and dissipation. These ideas were first formalized by A. N. Kolmogorov [[1941a](#); [1941b](#)], and

we consider these next.

3.1.3 The Kolmogorov Hypotheses

Equation (3.7) tells us that, in principle, each Fourier mode is coupled to every other mode. A simplifying assumption would be to assume that distant wavevectors are only weakly coupled; that is, the nonlinear interactions are *local*. A physical justification may be offered by the observation that only eddies of comparable size produce a mutual distortion or shearing effect; if two eddies are greatly separated in size, then the larger eddy would simply convect the smaller one. This notion, together with the existence of an inertial range that is well-separated from the energy input and dissipation scales, leads us to consider the possibility of a *universal* form for the energy spectrum.

Kolmogorov’s hypotheses are essentially similarity principles for the energy spectrum. He postulated that energy input from the largest scales is cascaded to smaller and smaller wavenumbers at a *constant* rate ϵ . The inertial range eddies maintain this “equilibrium” by transferring energy at the same rate. For such eddies of size l and speed v , the dissipation rate must be expressible in terms of just these two properties, since they are independent of the system scale and the viscous ranges. We define a *nonlinear time* $\tau_{nl} = \lambda/v$, also called the *eddy turnover time*, which may be considered to be the approximate time it takes for an eddy to distort appreciably due to nonlinear interactions. Noting that the decay rate has dimensions of $[v^2/\tau_{nl}]$, we have, on dimensional grounds,²

$$\epsilon \sim \frac{v^3}{l}. \quad (3.13)$$

We can use this result to express the ratio of the system scale to the dissipation scale in terms of the Reynolds number. Noting that Equation (3.13) implies $\epsilon \sim V^3/L$,

² The earliest theoretical justification for Equation (3.13) was provided by [de Kármán and Howarth \[1938\]](#), and it is often referred to as the von Karman–Howarth decay law.

where V is a characteristic velocity associated with scale L , we combine Equation (1.2) with Equation (3.11) to find

$$\frac{L}{l_d} \sim \text{Re}^{3/4}. \quad (3.14)$$

The next postulate states that the energy spectrum $E(k)$ at a scale k in the inertial range is determined only by the dissipation rate and the wavenumber k . Noting that the spectrum has dimensions of v^2/k and using (3.13) to express the speed v in terms of ϵ , we get

$$E(k) = C\epsilon^{2/3}k^{-5/3}, \quad (3.15)$$

where we have used $k \sim 1/l$, and C is a constant. This dependence of the energy spectrum on the $-5/3^{\text{rd}}$ power of k is the famous Kolmogorov power-law.

The empirical verification of Equation (3.15) requires measurements over a large inertial range, for which the Reynolds number must be large (Equation 3.14). Although large Re are difficult to achieve in the laboratory, measurements of natural turbulence in a variety of physical systems have established the correctness of Kolmogorov’s ideas, and the dimensionless constant C has been found to have a universal value close to 1.5 [Monin and Yaglom, 1971].

Note that the arguments presented here are not restricted to the idealized situation of isotropic turbulence. Even in the presence of large-scale inhomogeneities, one can argue that the inertial range cascade occurs in a state of “local isotropy”, provided that the eddies concerned are smaller than the inhomogeneity scale. This amounts to the usual requirement that the Reynolds number be high. Indeed, as we will discuss in Section 3.3, even magnetized fluctuations, like those found in the the solar wind, often exhibit a $-5/3^{\text{rd}}$ power law.

3.2 Closure Models for Turbulence

The closure problem of turbulence was introduced in Section 1.1.5. This problem is a general feature of any stochastic nonlinear systems; any attempt at a statistical formulation of a nonlinear system will produce an open heirarchy of moment equations

(e.g. Equations 1.5 -1.7), with the $n+1^{\text{th}}$ moment appearing in the equation for the n^{th} moment. Another example is seen in Equation (3.8) for the evolution of the second-order velocity correlation $E(k, t)$ (see Appendix B), where the nonlinear term $T(k, t)$ contains the third-order correlation (Equation B.51). The challenge then is to express higher order moment(s) in terms of lower order moments, so that the hierarchy may be truncated at a finite order, thus closing the system of equations.

In the context of turbulence modeling, the closure problem often takes the form of the appearance of turbulent fluctuations in the mean-flow equations. An example is Equation (1.9), where the equation for the mean flow involves the Reynolds stress $\langle u_\alpha u_\beta \rangle$, which represents the influence of the fluctuations on the mean flow. Many closure models are based on analogies between the turbulent mixing of eddies and the random motion of molecules in a gas. This gives rise to the concept of an effective *turbulent viscosity*, which we introduce next.

3.2.1 Eddy Viscosity Models

The *turbulent eddy viscosity* is based on the idea that the collective interaction of eddies can be modeled analogously to the kinetic theory model for the viscosity in a dilute gas [e.g., Reif, 1965, Chapter 12]:

$$\text{mean viscous shear stress} = \rho\nu \frac{d\bar{U}_i}{dx_j}. \quad (3.16)$$

This suggests a simple closure model for the Reynolds stress in Equation (1.9):

$$\langle u_i u_j \rangle = -\nu_T \frac{d\bar{U}_i}{dx_j}, \quad (3.17)$$

where ν_T is the kinematic eddy viscosity. On dimensional grounds, we can write the general form

$$\nu_T = u^* \ell_m, \quad (3.18)$$

where u^* is a characteristic turbulent velocity scale and ℓ_m is a characteristic *mixing-length* over which eddies distort; the mixing-length plays a role analogous to the molecular mean free path.

The eddy viscosity is in general a position of time and position – an example is the Smagorinsky [1963] model which expresses ν_T in terms of the mean strain rate $\bar{S}_{ij} \equiv \frac{1}{2} \left(\frac{\partial \bar{U}_i}{\partial x_j} + \frac{\partial \bar{U}_j}{\partial x_i} \right)$:

$$\nu_T = \ell_m^2 (2\bar{S}_{ij}\bar{S}_{ij})^{1/2}. \quad (3.19)$$

The eddy viscosity approximation is not valid in all situations, but is generally reasonable in the case of simple shear flows [Pope, 2000, Chapter 10]. First introduced by Boussinesq [1877], it is still widely used in turbulence modeling. However, one drawback of the model is the presence of one or more free parameters, which must be adjusted empirically to specific flows.³ In addition, there may be circumstances (e.g., decaying grid turbulence) when the mean velocity gradients are zero (leading Equation 3.17 to predict that the Reynolds stress vanishes) but the turbulent velocity u^* does not actually vanish. This leads us to the more sophisticated turbulent kinetic energy models.

3.2.2 Turbulent Kinetic Energy and k - ϵ Models

In the so-called k - ϵ models, the mean-flow Reynolds equation (1.9) is solved simultaneously with one or more equations for turbulence quantities such as the energy and the mixing length. Here the eddy viscosity approximation takes the form

$$\langle u_i u_j \rangle = \frac{2}{3} k \delta_{ij} - \nu_T \left(\frac{d\bar{U}_i}{dx_j} + \frac{d\bar{U}_j}{dx_i} \right), \quad (3.20)$$

where δ_{ij} is the Kronecker delta and $k \equiv \langle u_i u_i \rangle / 2$ is the turbulent kinetic energy per unit mass (see also Appendix B). That is, k is the isotropic part of the Reynolds stress tensor, while the anisotropic deviatoric part [e.g., Pope, 2000] is modeled using the eddy

³ The dynamic eddy viscosity model of [Germano et al., 1991] has significantly reduced the arbitrariness of the constants.

viscosity approximation. A transport equation for k can be derived by first obtaining an equation for the turbulent velocity, through subtracting the Reynolds equation for the mean flow (1.9) from the full Navier–Stokes equation (1.1), multiplying it by the turbulent velocity, and then averaging. This procedure is demonstrated in Section B.2.2 of Appendix B.

The turbulent kinetic energy equation usually takes the form [e.g., [McComb, 1990](#); [Pope, 2000](#)]

$$\frac{\partial k}{\partial t} + \bar{U}_\beta \frac{\partial k}{\partial x_\beta} = -\nabla \cdot \mathbf{T} + \mathcal{P} - \epsilon. \quad (3.21)$$

Here \mathbf{T} is a “flux” term that is responsible for the diffusion of turbulent energy through space due to nonlinear and viscous actions; since it is written in the form of a divergence, it does not contribute to the global energy balance. \mathcal{P} is a “production” term that takes the form $-\langle u_i u_j \rangle \frac{\partial \bar{U}_i}{\partial x_j}$; it is generally positive and represents the flow of energy from the mean flow to the turbulence. The third term on the RHS is the irreversible viscous dissipation into heat. Equation (3.21) may be compared with Equation (3.8), which is derived in Appendix B for the isotropic case without a mean flow.

The energy flux \mathbf{T} involves triple moments of the turbulent velocity along with a viscous diffusion effect, and is normally modeled using a gradient-diffusion hypothesis that asserts a flux of k along the gradient of k :

$$\mathbf{T} = -\frac{\nu_\Gamma}{\sigma_k} \nabla k, \quad (3.22)$$

where σ_k is an empirical constant generally taken to be unity.

For high Reynolds number flows, the dissipation rate is modeled as (compare with Equation 3.13)

$$\epsilon = C_D \frac{k^{3/2}}{\ell_m}, \quad (3.23)$$

where C_D is a model constant. The model is closed by assuming an eddy viscosity of the form

$$\nu_\Gamma = ck^{1/2}\ell_m \quad (3.24)$$

where c is another constant. The mean flow Reynolds equation (1.9) is solved with the Reynolds stress provided by Equation (3.20), which requires solving Equation (3.21) together with the closures for \mathbf{T} , ϵ , and ν_T .

Energy-equation models have a modest advantage over the simpler models of the previous section, but the drawback of having to specify ℓ_m remains. The next level of sophistication is the introduction of a second turbulence transport equation from which the mixing-length may be calculated. Such models are called two-equation models, and the k - ϵ model is the most popular of the type.

The mixing-length can be eliminated between Equations (3.24) and (3.23) to yield $\nu_T = C_\mu k^2/\epsilon$, where C_μ is a new constant. An equation for ϵ is written analogously to Equation (3.21)

$$\frac{\partial \epsilon}{\partial t} + \bar{U}_\beta \frac{\partial \epsilon}{\partial x_\beta} = -C_\epsilon \nabla \cdot \mathbf{T}_\epsilon + C_{\epsilon 1} \mathcal{P}_\epsilon - C_{\epsilon 2} \frac{\epsilon^2}{k}, \quad (3.25)$$

where new model constants are introduced and the various terms on the right hand side are analogous to those in (3.21) [e.g., McComb, 1990; Pope, 2000].

The k - ϵ model is the simplest *complete* turbulence model, and it has the widest range of applicability. Its performance in complex flows can be inaccurate, however, and the model constants may require adjustment depending on the specific application. When the concept of the eddy viscosity breaks down, one has to resort to turbulence stress modeling, where the full equation for the Reynolds stress $\langle u_i u_j \rangle$ ⁴ is solved.

The transport model for solar wind fluctuations that we use in the present dissertation is similar in approach to the two-equation model discussed here. However, instead of equations for the turbulent kinetic energy and the mixing length, we solve three transport equations for the turbulence energy (magnetic + kinetic), the correlation scale (analogous to the mixing length), and the cross helicity (the correlation between the velocity and magnetic fluctuations). Some of the closures used are similar

⁴ Equation (B.32), for the case of no mean flow.

to those introduced in this section, and we will discuss the extensions of these closures to a magnetofluid in Section 3.3.

3.2.3 Spectral Closure Models

The models discussed in the previous section discussed semi-empirical closures in real space, which are favored in applications. Here we briefly review some statistical closures in spectral space, which tend to be associated with formal theoretical approaches to turbulence.

An example of a spectral eddy viscosity model is Heisenberg's [1948] theory, which begins with the equation for the energy spectrum (3.8). If we integrate this equation up to an arbitrary wavenumber k' , then the effect of the nonlinear term can be interpreted as a removal of energy from wavenumbers $k < k'$ due to a transfer to modes $k > k'$. This drain of energy due to turbulence may be modeled analogously to viscous dissipation, by using the hypothesis

$$\int_0^{k'} T(k, t) dk = -2\nu_T(k', t) \int_0^{k'} E(k, t) k^2 dk, \quad (3.26)$$

where ν_T is the kinematic spectral eddy viscosity, which represents the effects of an integral from k' to infinity. On dimensional grounds, the Heisenberg-type eddy viscosity is written

$$\nu_T(k', t) = A \int_{k'}^{\infty} j^{-3/2} [E(j, t)]^{1/2} dj, \quad (3.27)$$

so that the energy spectrum equation is

$$\int_0^{k'} \left\{ \frac{dE}{dt} \right\} dk = -2\{\nu + \nu_T(k', t)\} \int_0^{k'} E(k, t) k^2 dk. \quad (3.28)$$

In the stationary case, this model yields the Kolmogorov $-5/3$ power law in the inertial range [Batchelor, 1953].

Several more rigorous spectral closure theories are based on the *quasi-normal* (QN) *hypothesis*, which concerns itself with the detailed structure of the nonlinear

term $T(k, t)$ and the moment hierarchy that determines this quantity (in principle). As noted earlier, $T(k, t)$ involves third-order moments; the evolution equation for this quantity will involve the fourth-order moments of the turbulent velocity (see Equation 1.7). The basis of the QN hypothesis lies in terminating the hierarchy by expressing the fourth-order moment as a sum over products of second-order moments. This is done by assuming that all even-order moments are related the way they are for a normal distribution. One can then write symbolically [e.g., Davidson, 2015]

$$\langle uuuu \rangle = \langle uu \rangle \langle uu \rangle. \quad (3.29)$$

Note that this does not imply that the turbulent velocity distribution is normal, which would be a much stronger assumption, and would be inconsistent with the existence of the third-order moment (or *triple correlation*) that is responsible for nonlinear energy transfer.

The QN approximation yields an expression for the third-order moments $T(k, t)$, which can then be substituted in Equation (3.8) to arrive at a closed equation for the energy spectrum. The basic QN model, however, leads to negative values for the energy spectrum for certain wavenumbers, and also predicts an excessive growth rate for the triple correlations. In response to these defects, several refinements have been developed over the years. These include Orszag’s 1970 “eddy-damping” approximation which adds a damping term that represents the decorrelating influence of nonlinear distortions, and the “Markovian” approximation that asserts the constancy of the spectrum over a damping time. Together, these form the EDQNM (Eddy-damped quasi-normal Markovian) theory [e.g., Davidson, 2015, and references therein].

All the closure models discussed so far have been based on *one-point correlations* that have the form $\langle u_i(\mathbf{x}, t) u_j(\mathbf{x}, t) \rangle$; they measure the correlation of the turbulent velocity field at a single point in space and time. A fuller description of the structure of a turbulent flow requires closures for the *two-point correlation* $\langle u_i(\mathbf{x}, t) u_j(\mathbf{x}', t') \rangle$, where (\mathbf{x}, t) and (\mathbf{x}', t') are points separated (or lagged) in space and time (see also

Section B.2.1.1). The archetype of such a closure theory is Kraichnan’s [1959] Direct Interaction Approximation (DIA).

The DIA proceeds through a formal perturbation expansion in a parameter δ (eventually set equal to unity), in which the lowest-order velocity field has a Gaussian distribution and the quadratic nonlinearity in the spectral Navier–Stokes equation (3.7) is of order δ . The theory consists of two simultaneous equations; one for the two-time spectral correlation function $Q(k; t, t')$ and another for the propagator (Green’s function) $G(k; t, t')$, which is the response of the turbulent field to a perturbation.⁵ The perturbation expansion is truncated at the second-order terms which involve the interaction of the three wavenumbers (\mathbf{k} , \mathbf{p} , and \mathbf{q} in Equation 3.7) that characterize the nonlinearity of the Navier–Stokes equation. This is the “direct interaction”; the neglected higher-order terms involve interactions via intermediate wavenumbers [e.g., McComb, 1990, Chapter 6].

The DIA predicts an energy spectrum with a $-3/2$ powerlaw, in contrast to the Kolmogorov $-5/3$ law. It was realized that the discrepancy arose because the DIA included spurious low-wavenumber effects on the inertial range wavenumbers. Kraichnan [1965b] reworked the DIA in a Lagrangian framework,⁶ which yielded a spectrum in agreement with Kolmogorov theory.

We will not delve further into the details of the DIA, but we note here that an extension of the DIA to MHD will be employed as a closure in our solar wind turbulence transport model. Further remarks on this *two-scale direct interaction approximation* (TSDIA) will be made in the next Chapter.

⁵ The function of the propagator may be understood symbolically as $X(t) = G(t - t')X(t')$; G represents the “propagation” of a variable X from its initial state at time t' to a final state at t [McComb, 1990, Chapter 5].

⁶ We have so far relied on the Eulerian description of fluid motion, in which our primary dependent variable is the velocity field $\mathbf{u}(\mathbf{x}, t)$. This tells us the value of the fluid velocity at any point (\mathbf{x}, t) in space-time. In Lagrangian coordinates one follows the motion of a particular fluid particle, and the primary variable becomes the position of the particle relative to some origin. The velocity of the particle is then given by the time derivative of the position vector [e.g., McComb, 1990, Chapter 12].

3.3 MHD Turbulence in the Solar Wind

In the first two sections of this chapter we reviewed some fundamental topics relating to the turbulent energy cascade and turbulence modeling for hydrodynamics. These ideas serve as a foundation for theories of the turbulent cascade and closure in MHD. We briefly discuss these below.

We derived the equations of MHD in a heuristic fashion and discussed their applicability to the solar wind in Chapter 2, noting that there is some justification for using the incompressible limit. Even in the simplest case, assuming homogeneity, isotropy, and stationarity, MHD turbulence is more complex than hydrodynamic turbulence. There are two distinct fields to grapple with – the velocity and the magnetic field. The large scale magnetic field introduces a preferred direction, which leads to anisotropy in the fluctuations. In addition to the eddy turnover time from hydrodynamics, at least one new time-scale is introduced – the Alfvén time (the time taken by a fluctuation to traverse a given length at the Alfvén speed).

On the bright side, observations of MHD-scale fluctuations in the solar wind⁷ indicate a broad-band inertial range spanning at least a few decades. This implies that the energy-containing scales are well-separated from the dissipation range [Leamon et al., 1998], and we can expect the hypotheses of inertial range universality to carry over from the hydrodynamic case. The correlation scale (the size of the largest structures) of solar wind fluctuations is about 0.02 au ($\sim 10^6$ km) at Earth orbit, which is much smaller than the system size (1 au). The inertial range extends roughly three decades below the correlation scale, ending at the ion inertial scale (~ 100 km). Therefore one can also develop scale-separated turbulence transport models of the type discussed in Section 3.2.

3.3.1 Cascades and Anisotropy in MHD Turbulence

To understand the influence of the magnetic field on the turbulent cascade, we visualize fluctuations as counterpropagating Alfvén modes \mathbf{z}_{\pm} (see Section 2.2.4)

⁷ Several properties of solar wind turbulence were discussed in Section 1.1.4.

that travel along a large-scale magnetic field. In this simplified picture, hydrodynamic eddies (Figure 3.1(a)) are convected (or swept) by a large-scale flow without affecting the “internal” interactions between eddies of similar sizes, thus preserving the locality of the cascade in wavenumber space. However, in the MHD case (Figure 3.1(b)), the magnetic field sweeps eddies past each other at the Alfvén speed (Section 2.2.3), which is large for a strong mean magnetic field. The large Alfvén speed implies that the Alfvén time τ_A is much smaller than the eddy turnover time: $\tau_A \ll \tau_{nl}$. Eddies are thus swept past each other before they can interact nonlinearly to an appreciable extent, which results in an inhibition of spectral transfer.⁸

This phenomenology, independently developed by Iroshnikov [1964] and Kraichnan [1965a], results in an energy spectrum of the form $E(k) \sim k^{-3/2}$. We see that this spectrum is less steep than the Kolmogorov spectrum (3.15), which reflects the weaker spectral transfer in the MHD case.

The Iroshnikov–Kraichnan (IK) spectrum was a major advance, but it is now known that it neglects the inherent anisotropy of the system [e.g., Zhou et al., 2004; Oughton and Matthaeus, 2005]. There exist many fluctuations with $\mathbf{k} \perp \mathbf{B}_0$, for which $\tau_A(\mathbf{k}) \rightarrow \infty$, where \mathbf{B}_0 is the mean magnetic field; modes with $\mathbf{k} \cdot \mathbf{B}_0 = 0$ are called 2D modes, while those with $\mathbf{k} \cdot \mathbf{B}_0 \approx 0$ are called quasi-2D modes. The mean field then suppresses the cascade in the parallel direction, but the Alfvén time scale is not sufficiently small in the perpendicular direction compared to the nonlinear distortion time scale for Alfvén-wave sweeping effects to dominate nonlinear “straining”, and therefore the cascade proceeds relatively unimpeded in the \mathbf{k}_\perp -space. In the “critical balance” limit of Goldreich and Sridhar [1995], $\tau_{nl} \approx \tau_A$.

When the turbulence is sufficiently 2D, the dynamics are similar to those of purely 2D MHD turbulence, and become nearly independent of \mathbf{B}_0 . This scenario is consistent with numerical simulations [Shebalin et al., 1983; Oughton et al., 1994] and laboratory experiments [Robinson and Rusbridge, 1971] that indicate the development

⁸ Recall that only oppositely propagating Alfvén modes interact (Equation 2.28).

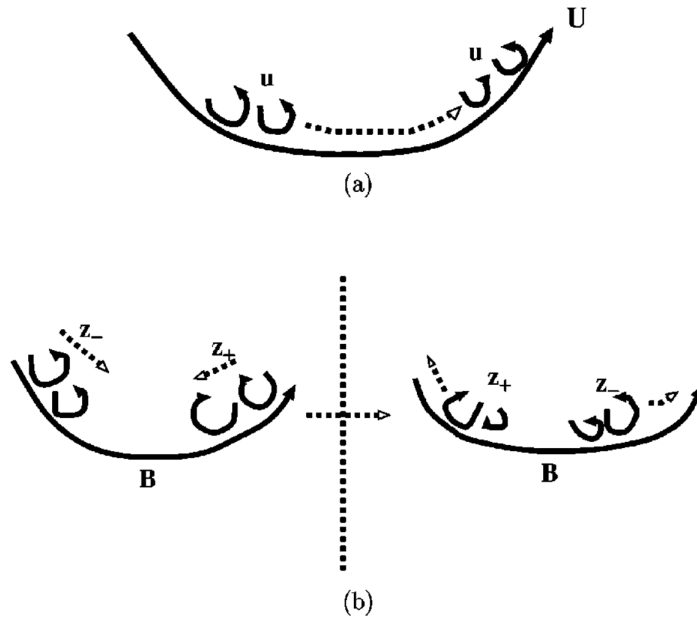


Figure 3.1: Comparison of hydrodynamics and MHD: (a) In hydrodynamics a mean or large-scale flow sweeps the small-scale eddies without affecting the energy transfer between length scales; (b) in MHD a mean or large-scale magnetic field \mathbf{B} sweeps oppositely propagating Alfvénic fluctuations \mathbf{z}_{\pm} , which affects the energy transfer, illustrated as distortions after the two types of fluctuation have passed through each other (see text). *Figure reproduced from Zhou et al. [2004] with permission from APS (see Appendix E).*

of a strong and persistent anisotropy in the presence of a mean field, with energy preferentially building up in wavemodes perpendicular to \mathbf{B}_0 . In this limit, the dynamics are “hydro-like”, and one expects a “strong-turbulence” $k^{-5/3}$ energy spectrum. Indeed, solar wind fluctuations exhibit spectral indices (Figure 1.5) that are close to the Kolmogorov value [e.g., Horbury et al., 2005]. Observations also indicate a *spectral anisotropy* where wavemodes perpendicular to the mean field carry 80% of the energy in the fluctuations [Matthaeus et al., 1990; Bieber et al., 1996; Horbury et al., 2005].

A popular model of anisotropic solar wind fluctuations is the so-called *two-component* model composed of “slab + 2D” fluctuations [Matthaeus et al., 1995]. For slab modes, $\mathbf{k} = k_{\parallel}\hat{\mathbf{B}}_0$, while 2D modes have $\mathbf{k} \cdot \mathbf{B}_0 = 0$. The slab component can be thought of as a superposition of propagating Alfvén waves, and the 2D component corresponds to strong turbulence. Both types of fluctuations generally have amplitudes confined within a plane transverse to \mathbf{B}_0 . In a coordinate system with \mathbf{B}_0 in the z -direction, the fluctuating magnetic field can be written as

$$\mathbf{b}(x, y, z) = \mathbf{b}_{2D}(x, y) + \mathbf{b}_{\text{slab}}(z), \quad (3.30)$$

so that the 2D fluctuations do not vary in the z -direction, while the slab fluctuations are constant within an x - y plane (see Figure 3.2). The modal energy spectrum⁹ for the “slab+2D” model is $E_{\text{mod}}(\mathbf{k}) = E_{\text{slab}}(k_{\parallel})\delta(k_x)\delta(k_y) + E_{2D}(k_x, k_y)\delta(k_z)$, where δ is the Dirac-delta function. As shown in Figure 3.2, the 2D spectrum is elongated along $k_{\perp} = (k_x^2 + k_y^2)^{1/2}$, since the cascade proceeds preferentially in the direction perpendicular to the mean field, resulting in spectral transfer to large k_{\perp} and a smaller perpendicular correlation length ℓ_{\perp} . This is reversed for the slab case.

In the context of the solar wind, the slab component may be identified with

⁹ The modal spectrum $E_{\text{mod}}(\mathbf{k})$ describes the distribution of energy in three-dimensional wavevector space, with the total energy given by $\int \int \int E_{\text{mod}}(\mathbf{k}) d^3\mathbf{k}$. The omnidirectional spectrum $E(k)$ is obtained by integrating the modal spectrum over the two angular coordinates of a spherical coordinate system in k -space: $E(k) = \int \int d\theta d\phi k^2 \sin \theta E(k, \theta, \phi)$, and is of particular importance in isotropic turbulence. An example of an omnidirectional spectrum is the Kolmogorov spectrum given by Equation (3.15).

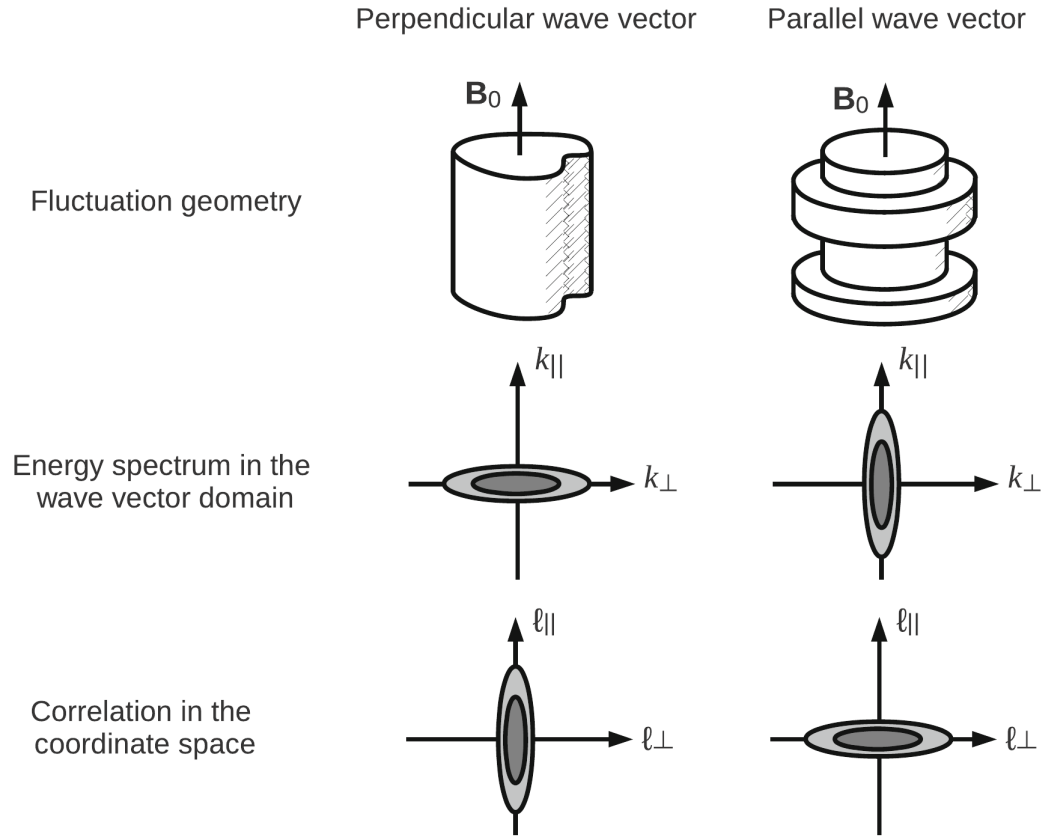


Figure 3.2: Visualization of fluctuations, energy spectra in the wavevector domain, and spatial correlation lengths ℓ , for 2D geometry (left) and slab geometry (right). Fluctuations with 2D geometry have wavevectors perpendicular to \mathbf{B}_0 and those with slab geometry have wavevectors aligned with \mathbf{B}_0 . *Figure reproduced from Narita [2018] under the Creative Commons Attribution 4.0 International License.*

Alfvén waves that are a remnant of photospheric dynamics, and the 2D component is introduced in the lower corona or arises dynamically.

The spectral anisotropy of solar wind fluctuations has important consequences for the scattering of energetic particles. In particular, “slab” models of interplanetary fluctuations [Jokipii, 1966] predict mean free paths that are too small when compared with observations [e.g., Fisk, 1979]. This discrepancy is resolved by the inclusion of 2D fluctuations [Bieber et al., 1996]. In Chapter 6 we will use the two-component model in combination with our global solar wind simulations to study the anisotropic diffusion of cosmic rays in the heliosphere.

3.3.2 Closure Models for MHD Turbulence

The Reynolds-averaging procedure (Section 1.1.5) can be applied to the MHD equations to arrive at a mean-field description [Krause and Raedler, 1980], but one again runs into the familiar closure problem. MHD extensions of some of the closure models reviewed in Section 3.2 can be found in, e.g., Yoshizawa et al. [2003] and Miesch et al. [2015].

Here we briefly discuss the MHD generalization of the von Karman–Howarth decay law (Equation 3.13), which is often used as a closure to model the nonlinear terms in the turbulent energy equation. We use the Reynolds decomposition of the Elsässer variables into a mean and fluctuating part and apply the usual Reynolds-averaging procedure to Equations (2.28). Assuming that the pressure fluctuations are negligible, we arrive at an equation for the fluctuating fields by subtracting the mean equations from the full equations [e.g., Zank, 2014, Chapter 6]¹⁰

$$\frac{\partial \mathbf{z}_{\pm}}{\partial t} = -\mathbf{z}_{\mp} \cdot \nabla \mathbf{z}_{\pm}, \quad (3.31)$$

where we have neglected the convection term. An equation for the average fluctuation

¹⁰ Note the change in notation compared to Equation (2.28).

energy density in \mathbf{z}_+ modes can be written as

$$\begin{aligned}\frac{\partial}{\partial t}\langle z_+^2 \rangle &= -2\langle \mathbf{z}_+ \cdot (\mathbf{z}_- \cdot \nabla \mathbf{z}_+) \rangle \\ &\sim -\langle z_+^2 \rangle \frac{\langle z_-^2 \rangle^{-1/2}}{\lambda_+},\end{aligned}\tag{3.32}$$

in analogy with the dimensional analysis leading to Equation (3.13). A similar equation can be written for $\langle z_-^2 \rangle$. The nonlinear term therefore couples the energy decay in \mathbf{z}_\pm modes to the energy in \mathbf{z}_\mp modes, via a characteristic length scale λ_\pm . In the simple case of $\mathbf{z}_+ = \mathbf{z}_-$, we have, for the turbulent energy dissipation rate

$$\frac{\partial Z^2}{\partial t} \sim -\frac{Z^3}{\lambda},\tag{3.33}$$

where $Z^2 = \langle z_\pm^2 \rangle$ is the average turbulent energy density. A similar closure will be used in our solar wind model, presented in the next Chapter.

Chapter 4

SOLAR WIND MODEL WITH TURBULENCE TRANSPORT AND HEATING

In this chapter we describe the solar wind model that has been used in several of the studies performed in this thesis. We use ideas from the preceding chapters to combine a model of the large-scale flow with a turbulence transport model. We will begin with two-fluid MHD equations for fully 3D compressible solar wind flow and use the Reynolds-averaging procedure to derive a set of equations for the mean flow. These are coupled to turbulence equations for the energy-containing fluctuations, and closures similar to those discussed in the previous chapter will be used to complete the set of equations. We will briefly discuss the numerical implementation of the model, and present some basic results.

These simulations have been developed over the last two decades [Usmanov, 1993; Usmanov et al., 2000; Usmanov and Goldstein, 2003; Usmanov et al., 2011, 2012, 2014], and we include several more recent improvements [Usmanov et al., 2018]. Antecedents of the turbulence transport model presented here may be found in Tu [1988], Marsch and Tu [1989], Zhou and Matthaeus [1990b], Zhou and Matthaeus [1990a], Matthaeus et al. [1994a], Zank et al. [1996], Matthaeus et al. [1999b], and Breech et al. [2008].

4.1 Two-fluid MHD Equations for the Solar Wind

We assume that the solar wind is a fully ionized plasma composed of electrons and protons. As discussed in Section 2.2.2, protons carry the bulk of the momentum of the flow, but the temperature of the electrons can be significantly different from that of protons due to the weak collisionality of the plasma [e.g., Marsch, 2006]. Accordingly,

we begin with two-fluid¹ ideal (inviscid) MHD equations (Section 2.2.1) – one equation for the solar wind momentum and two separate energy equations for protons and electrons. Together with the equation of continuity and the induction equation, we have, in the frame corotating with the Sun [Usmanov et al., 2011, 2014, 2018]:

$$\frac{\partial \tilde{\rho}}{\partial t} + \nabla \cdot (\tilde{\rho} \tilde{\mathbf{v}}) = 0, \quad (4.1)$$

$$\begin{aligned} \frac{\partial \tilde{\mathbf{v}}}{\partial t} + (\tilde{\mathbf{v}} \cdot \nabla) \tilde{\mathbf{v}} + \frac{1}{\tilde{\rho}} \nabla (\tilde{P}_S + \tilde{P}_E) - \frac{(\nabla \times \tilde{\mathbf{B}}) \times \tilde{\mathbf{B}}}{4\pi \tilde{\rho}} \\ + \frac{GM_\odot}{r^2} \hat{\mathbf{r}} + 2\boldsymbol{\Omega} \times \tilde{\mathbf{v}} + \boldsymbol{\Omega} \times (\boldsymbol{\Omega} \times \mathbf{r}) = 0, \end{aligned} \quad (4.2)$$

$$\frac{\partial \tilde{\mathbf{B}}}{\partial t} = \nabla \times (\tilde{\mathbf{v}} \times \tilde{\mathbf{B}}), \quad (4.3)$$

$$\frac{\partial \tilde{P}_S}{\partial t} + (\tilde{\mathbf{v}} \cdot \nabla) \tilde{P}_S + \gamma \tilde{P}_S \nabla \cdot \tilde{\mathbf{v}} = (\gamma - 1) \left(\frac{\tilde{P}_E - \tilde{P}_S}{\tau_{SE}} + f_p Q_T \right), \quad (4.4)$$

$$\begin{aligned} \frac{\partial \tilde{P}_E}{\partial t} + (\tilde{\mathbf{v}} \cdot \nabla) \tilde{P}_E + \gamma \tilde{P}_E \nabla \cdot \tilde{\mathbf{v}} = \\ (\gamma - 1) \left[\frac{\tilde{P}_S - \tilde{P}_E}{\tau_{SE}} - \nabla \cdot \mathbf{q}_E + (1 - f_p) Q_T \right], \end{aligned} \quad (4.5)$$

where the independent variables are the heliocentric position vector \mathbf{r} and the time t . The dependent variables are the velocity in the corotating frame $\tilde{\mathbf{v}}$, the magnetic field $\tilde{\mathbf{B}}$, the mass density $\tilde{\rho}$ and thermal pressure \tilde{P}_S of solar wind (thermal) protons, and the thermal pressure of electrons \tilde{P}_E . All pressures are assumed to be isotropic. Note that we neglect the electron mass m_e compared with the proton mass m_p , so the solar wind mass density is $\tilde{\rho} = m_p \tilde{N}_S$, where \tilde{N}_S is the proton number density

¹ It would perhaps be more appropriate to call the model a “two-temperature” model, but the term “two-fluid” has gained wide acceptance in the community following the pioneering work of [Sturrock and Hartle \[1966\]](#) and [Hartle and Sturrock \[1968\]](#).

(the requirement of charge neutrality requires that \tilde{N}_S be equal to the electron number density). The parameters appearing in the equations are the sidereal solar rotation rate Ω , the gravitational constant G , the adiabatic index γ ($= 5/3$, the adiabatic value), the solar mass M_\odot , and the fraction of turbulent energy absorbed by protons f_p [Breech et al., 2009; Matthaeus et al., 2016a]. Other terms, defined in the next section, are the proton-electron Coulomb collision time-scale τ_{SE} , the electron heat flux \mathbf{q}_E , and a source term Q_T of energy deposition/extraction due to turbulent dissipation, which is divided between protons and electrons.

Note that we have neglected the heat flux carried by protons, since the lighter and more mobile electrons dominate the bulk of the solar wind’s heat flux [Marsch, 2006]. We have also neglected the momentum of alpha particles, which can be as high as 20% of the solar wind’s momentum [e.g., Meyer-Vernet, 2007]. The model has the capability to include pickup proton effects that arise due to charge exchange with interstellar hydrogen, but we neglect these here, since our focus is on the inner heliosphere (inside 5 au), and pickup proton effects are relevant only in the outer heliosphere [e.g., Usmanov et al., 2014, and references therein].

4.2 Reynolds-averaged Mean-flow Equations

As discussed in Section 1.1.5, it is not computationally feasible to resolve all relevant scales of the system in a simulation, and so we follow the Reynolds-averaging approach to get a set of equations for the mean flow. All physical fields, e.g., $\tilde{\mathbf{a}}$, are separated into a mean and a fluctuating component

$$\tilde{\mathbf{a}} = \mathbf{a} + \mathbf{a}', \quad (4.6)$$

making use of an averaging operation: $\mathbf{a} = \langle \tilde{\mathbf{a}} \rangle$. This ensemble average is associated with the large scales of motion, assumed to be deterministic. The quantity \mathbf{a}' is a fluctuating component, here assumed to be of arbitrary amplitude, random in nature, and residing at small scales. By construction, $\langle \mathbf{a}' \rangle = 0$.

To derive the mean-flow equations, the decomposed fields are substituted into Equations (4.1) – (4.5). The fluctuating (small-scale) component is assumed to be incompressible (see Sections 2.2.2 and 3.3.1 for a discussion of applicability of this assumption to the solar wind), and we neglect density and pressure fluctuations. The ensemble averaging operator $\langle \dots \rangle$ is then applied to these equations, to get the *Reynolds-averaged MHD* (or MHD-RANS) equations:

$$\frac{\partial \rho}{\partial t} + \nabla \cdot (\rho \mathbf{v}) = 0, \quad (4.7)$$

$$\begin{aligned} \frac{\partial(\rho \mathbf{v})}{\partial t} + \nabla \cdot \left[\rho \mathbf{v} \mathbf{v} - \frac{1}{4\pi} \mathbf{B} \mathbf{B} + \left(P_S + P_E + \frac{\langle B'^2 \rangle}{8\pi} + \frac{B^2}{8\pi} \right) \mathbf{I} + \underline{\mathcal{R}} \right] \\ + \rho \left[\frac{GM_\odot}{r^2} \hat{\mathbf{r}} + 2\boldsymbol{\Omega} \times \mathbf{v} + \boldsymbol{\Omega} \times (\boldsymbol{\Omega} \times \mathbf{r}) \right] = 0, \end{aligned} \quad (4.8)$$

$$\frac{\partial \mathbf{B}}{\partial t} = \nabla \times (\mathbf{v} \times \mathbf{B} + \underline{\boldsymbol{\varepsilon}}_m \sqrt{4\pi\rho}), \quad (4.9)$$

$$\frac{\partial P_S}{\partial t} + (\mathbf{v} \cdot \nabla) P_S + \gamma P_S \nabla \cdot \mathbf{v} = (\gamma - 1) \left(\frac{P_E - P_S}{\tau_{SE}} + \underline{f_p Q_T} \right), \quad (4.10)$$

$$\begin{aligned} \frac{\partial P_E}{\partial t} + (\mathbf{v} \cdot \nabla) P_E + \gamma P_E \nabla \cdot \mathbf{v} = \\ (\gamma - 1) \left[\frac{P_S - P_E}{\tau_{SE}} - \nabla \cdot \mathbf{q}_E + \underline{(1 - f_p) Q_T} \right], \end{aligned} \quad (4.11)$$

where the momentum equation is now written in conservative form, the *MHD Reynolds stress tensor* is (compare with its hydrodynamic counterpart in Equation 1.9)

$$\mathcal{R} = \left\langle \rho \mathbf{v}' \mathbf{v}' - \frac{\mathbf{B}' \mathbf{B}'}{4\pi} \right\rangle, \quad (4.12)$$

and the *mean turbulent electric field* [Krause and Raedler, 1980] is

$$\boldsymbol{\varepsilon}_m = \frac{\langle \mathbf{v}' \times \mathbf{B}' \rangle}{4\pi\rho}. \quad (4.13)$$

The underbracketed terms in the Reynolds-averaged equations (4.7) – (4.11) represent the interaction of the turbulent fluctuations with the mean flow. Note that the turbulence terms are *averaged*, so they represent the *mean* effect of the fluctuations. We therefore require only a *statistical* description of the turbulence to model these terms, and a representation of the actual fluctuations is not required. Before we discuss the transport equations for the statistical descriptors of turbulence, we will describe the two other terms required to close the MHD-RANS system – the proton-electron Coulomb collision time scale τ_{SE} and the electron heat flux \mathbf{q}_E .

4.3 Modeling Collisional Energy Exchange and Electron Heat Flux

The collision terms in Equations (4.10) and (4.11) model the energy exchange between protons and electrons (note that any energy lost by electrons is gained by protons, and vice versa). The collisional time scale of Coulomb collisions between protons and electrons can be written as $\tau_{SE} = 1/\nu_E$, where ν_E is the electron-proton collision rate [Spitzer, 1965; Hartle and Sturrock, 1968] given by

$$\nu_E = \frac{8(2\pi m_e)^{1/2} e^4 N_E \ln \Lambda}{3m_p (k_B T_E)^{3/2}}, \quad (4.14)$$

and $\ln \Lambda$ is the Coulomb logarithm given by

$$\ln \Lambda = \ln \left[\frac{3(k_B T_E)^{3/2}}{2\pi^{1/2} e^3 N_E^{1/2}} \right]. \quad (4.15)$$

In Equations (4.14) and (4.15) $N_E(=N_S)$ is the electron number density, e is the elementary charge, and k_B is the Boltzmann constant.

Electrons carry the bulk of the heat flux in the solar wind due to their low mass, and provide additional heating [Feldman et al., 1975]. Below 5 – 10 R_\odot we approximate

electron heat flux by the classical collision dominated model of [Spitzer and Härm \[1953\]](#) [see also [Chhiber et al., 2016a](#)]: $\mathbf{q}_S = -\kappa \hat{\mathbf{B}}(\hat{\mathbf{B}} \cdot \nabla)T_E$, where T_E is the electron temperature, $\hat{\mathbf{B}}$ is a unit vector along the magnetic field, and $\kappa = 8.4 \times 10^{-7} T_E^{5/2}$ ergs $\text{cm}^{-1} \text{s}^{-1} \text{K}^{-7/2}$ [[Spitzer, 1965](#)]. Above $5 - 10 R_\odot$ we adopt Hollweg’s “collisionless” model: $\mathbf{q}_H = (3/2)\alpha_H P_E \mathbf{v}$ [[Hollweg, 1974, 1976](#)], where α_H is a factor of order unity. Hollweg’s “collisionless” approximation was later recovered by [Canullo et al. \[1996\]](#) from their solution of the Fokker-Planck equation in the limit $r \geq 6 R_\odot$ for suprathermal electrons originating near the coronal base. [Cranmer et al. \[2009\]](#) recently demonstrated that Hollweg’s formula with $\alpha_H = 1.05$ corresponds closely to *Helios* and *Ulysses* observations. Note that the velocity in the Hollweg approximation is the velocity in the rotating frame \mathbf{v} , since the electron heat flux is directed along the magnetic field, which lies parallel to \mathbf{v} in steady-state conditions [[Pizzo, 1982](#)].

Following [Chandran et al. \[2011\]](#), we interpolate between the collisional and collisionless regimes by defining

$$\mathbf{q}_E = \psi \mathbf{q}_H + (1 - \psi) \mathbf{q}_S, \quad (4.16)$$

where

$$\psi = \frac{(r/r_H)^2}{1 + (r/r_H)^2} \quad (4.17)$$

and r_H is a free parameter of order $5 R_\odot$.

4.4 Turbulence Transport Equations

To close the system of equations (4.7) – (4.11) we must specify forms for the three turbulence quantities Q_T , \mathcal{R} , and ϵ_m . In addition to closing the mean-flow system, we would also like to have a model for the transport of solar wind fluctuations. We begin by subtracting the mean momentum equation (4.8) from the full momentum equation

(4.2) to obtain

$$\begin{aligned} \frac{\partial \mathbf{v}'}{\partial t} = & -(\mathbf{v} \cdot \nabla) \mathbf{v}' - (\mathbf{v}' \cdot \nabla) \mathbf{v} - (\mathbf{v}' \cdot \nabla) \mathbf{v}' + (\mathbf{V}_A \cdot \nabla) \mathbf{b}' - \mathbf{b}' (\nabla \cdot \mathbf{V}_A) + (\mathbf{b}' \cdot \nabla) \mathbf{V}_A \\ & - \mathbf{V}_A (\nabla \cdot \mathbf{b}') + (\mathbf{b}' \cdot \nabla) \mathbf{b}' - \mathbf{b}' (\nabla \cdot \mathbf{b}') + \frac{1}{\rho} \nabla \cdot \mathcal{R} - 2\boldsymbol{\Omega} \times \mathbf{v}', \end{aligned} \quad (4.18)$$

where we have introduced the mean Alfvén velocity $\mathbf{V}_A = \mathbf{B}(4\pi\rho)^{-1/2}$, and $\mathbf{b}' = \mathbf{B}'(4\pi\rho)^{-1/2}$ is the magnetic fluctuation normalized to Alfvén speed units. Subtracting Equation (4.9) from Equation (4.3), we obtain

$$\begin{aligned} \frac{\partial \mathbf{b}'}{\partial t} = & (\mathbf{b}' \cdot \nabla) \mathbf{v} + (\mathbf{V}_A \cdot \nabla) \mathbf{v}' - (\mathbf{v} \cdot \nabla) \mathbf{b}' - (\mathbf{v}' \cdot \nabla) \mathbf{V}_A - \frac{\mathbf{b}'}{2} \nabla \cdot \mathbf{v} - \frac{\mathbf{V}_A}{2} \nabla \cdot \mathbf{v}' \\ & + (\mathbf{b}' \cdot \nabla) \mathbf{v}' - (\mathbf{v}' \cdot \nabla) \mathbf{b}' - \frac{\mathbf{b}'}{2} \nabla \cdot \mathbf{v}' - \frac{\nabla \times (\rho^{1/2} \boldsymbol{\varepsilon}_m)}{\rho^{1/2}}. \end{aligned} \quad (4.19)$$

Equations (4.18) and (4.19) describe the evolution of the velocity and magnetic fluctuations \mathbf{v}' and \mathbf{b}' , respectively. In a simulation that resolves the mean flow, we cannot achieve sufficient resolution to simultaneously resolve the fluctuation scales (see Section 1.1.6), and we would therefore like to examine the average evolution of the fluctuations. We begin by deriving an equation for the statistical quantity $Z^2 = \langle v'^2 + b'^2 \rangle$, which is twice the turbulence energy per unit mass. Multiplying Equation (4.18) by \mathbf{v}' and Equation (4.19) by \mathbf{b}' , adding the resulting equations, and applying the Reynolds averaging operator,² we obtain the following equation for Z^2 :

$$\begin{aligned} \frac{\partial Z^2}{\partial t} + (\mathbf{v} \cdot \nabla) Z^2 + \frac{Z^2(1 - \sigma_D)}{2} \nabla \cdot \mathbf{u} + \frac{2}{\rho} \mathcal{R} : \nabla \mathbf{u} + 2\boldsymbol{\varepsilon}_m \cdot (\nabla \times \mathbf{V}_A) \\ - (\mathbf{V}_A \cdot \nabla)(Z^2 \sigma_c) + Z^2 \sigma_c (\nabla \cdot \mathbf{V}_A) = NL_1, \end{aligned} \quad (4.20)$$

where $\mathbf{u} = \mathbf{v} + \boldsymbol{\Omega} \times \mathbf{r}$ is the velocity in the inertial frame, $\sigma_c = 2\langle \mathbf{v}' \cdot \mathbf{b}' \rangle Z^{-2}$ is the *normalized cross helicity* and $\sigma_D = \langle v'^2 - b'^2 \rangle / Z^2$ is the *normalized energy difference* between velocity and magnetic fluctuations. In deriving (4.20) we have assumed small-scale incompressibility ($\nabla \cdot \mathbf{v}' = 0$), and the velocity and magnetic fluctuations are

² This procedure is illustrated for the hydrodynamic case in Section B.2.2.

taken to be transverse to the mean magnetic field (see Section 3.3.1), so that $\mathbf{v}' \cdot \mathbf{V}_A = \mathbf{b}' \cdot \mathbf{V}_A = 0$. The fourth term on the LHS of (4.20) is the double inner product of the Reynolds stress tensor and the velocity gradient tensor, and NL_1 consolidates the local nonlinear terms [see Breech et al., 2008] that involve the primitive (not statistical) turbulence variables \mathbf{v}' and \mathbf{b}' . Both \mathcal{R} and NL_1 require closure approximations, while σ_D is treated as a constant parameter³ equal to $-1/3$, justified by observations [Matthaeus and Goldstein, 1982; Roberts et al., 1987b; Milano et al., 2004; Perri and Balogh, 2010].

Note that we can relate Z^2 to the “inward” and “outward” Elsässer modes (see Section 2.2.4) by recalling the definitions

$$\mathbf{z}_\pm = \mathbf{v}' \pm \mathbf{b}', \quad (4.21)$$

so that

$$Z^2 = \langle |\mathbf{v}'|^2 + |\mathbf{b}'|^2 \rangle = \frac{\langle |\mathbf{z}_+|^2 + |\mathbf{z}_-|^2 \rangle}{2} = \frac{Z_+^2 + Z_-^2}{2}, \quad (4.22)$$

where we have defined $Z_\pm^2 = \langle |\mathbf{z}_\pm|^2 \rangle$ as the average energy density in the two Elsässer modes.

The next statistical descriptor of turbulence we are interested in is the normalized cross helicity:

$$\sigma_c \equiv \frac{2\langle \mathbf{v}' \cdot \mathbf{b}' \rangle}{Z^2} = \frac{Z_+^2 - Z_-^2}{Z_+^2 + Z_-^2}. \quad (4.23)$$

The cross helicity measures the correlation of velocity and magnetic fluctuations (or the Alfvénicity; see Section 2.2.3). From Equation (4.23) it can be seen that σ_c is also a measure of the energy difference between inward and outward modes. We can easily derive the identity

$$Z_\pm^2 = (1 \pm \sigma_c)Z^2. \quad (4.24)$$

Zero cross helicity indicates that both inward and outward modes are present in equal

³ [cf. Zank et al., 2017; Adhikari et al., 2017].

measure, while a cross helicity of $\sim \pm 1$ suggests a dominance of one type of mode. Nonlinear effects (such as shear driving) are associated with a reduction in the cross helicity, as is observed in the solar wind [Roberts et al., 1987b,a; Matthaeus et al., 2004; Breech et al., 2005].

To obtain an equation for σ_c we multiply Equation (4.18) by \mathbf{b}' and Equation (4.19) by \mathbf{v}' , add the resulting equations, and apply the Reynolds-averaging operator to get

$$\begin{aligned} \frac{\partial(Z^2\sigma_c)}{\partial t} + (\mathbf{v} \cdot \nabla)(Z^2\sigma_c) - (\mathbf{V}_A \cdot \nabla)Z^2 + \frac{Z^2\sigma_c}{2}\nabla \cdot \mathbf{u} + \frac{2}{\rho}\mathcal{R} : \nabla\mathbf{V}_A \\ + 2\boldsymbol{\varepsilon}_m \cdot (\nabla \times \mathbf{u}) + (1 - \sigma_D)Z^2\nabla \cdot \mathbf{V}_A = NL_2, \end{aligned} \quad (4.25)$$

where NL_2 once again consolidates the local nonlinear terms.

To model the nonlinear terms in Equations (4.20) and (4.25), we use the modified von Kármán-Howarth phenomenology discussed in Section 3.3.2, according to which we have

$$\frac{d}{dt}Z_{\pm}^2 = -\frac{\alpha}{\lambda}Z_{\pm}^2Z_{\mp}, \quad (4.26)$$

where we do not distinguish between the similarity length scales associated with the two Elsässer modes and assume one correlation scale λ [cf. Zank et al., 2017]; α is a Kármán–Taylor constant [see Matthaeus et al., 1996; Breech et al., 2008]. On using Equation (4.24), this gives us

$$\frac{d}{dt}Z^2 = -\alpha f^+(\sigma_c)\frac{Z^3}{\lambda}, \quad (4.27)$$

where $f^+(\sigma_c)$ is a function of cross helicity defined as [Matthaeus et al., 2004]

$$f^{\pm}(\sigma_c) = \frac{(1 - \sigma_c^2)^{1/2}}{2} [(1 + \sigma_c)^{1/2} \pm (1 - \sigma_c)^{1/2}]. \quad (4.28)$$

Accordingly, we approximate $NL_1 = -\alpha f^+(\sigma_c)Z^3/\lambda$ and $NL_2 = -\alpha f^-(\sigma_c)Z^3/\lambda$ [Matthaeus et al., 2004; Breech et al., 2008; Usmanov et al., 2014].

These closures involve the correlation scale (λ) of the fluctuations, which naturally becomes our third statistical descriptor of turbulence. This is defined as an integral of the two-point spatial correlation of the fluctuations, with the integral performed over the separation (or lag) between the two points, ranging from zero to infinite lag (see Equation B.14). On dimensional grounds, the von Kármán–Taylor model for the evolution of λ can be written

$$\frac{d\lambda}{dt} = \beta \frac{\lambda}{\tau_{nl}} = \beta Z, \quad (4.29)$$

where β is another Kármán–Taylor constant [see Matthaeus et al., 1996; Breech et al., 2008] and $\tau_{nl} = \lambda/Z$ is the eddy-turnover time. The nonzero cross helicity generalization of this model is [Matthaeus et al., 2004; Breech et al., 2008; Usmanov et al., 2014]

$$\frac{\partial \lambda}{\partial t} + (\mathbf{v} \cdot \nabla) \lambda = \beta f^+(\sigma_c) Z, \quad (4.30)$$

With the closures for the nonlinear terms substituted into Equations (4.20) and (4.25), we get

$$\begin{aligned} \frac{\partial Z^2}{\partial t} + (\mathbf{v} \cdot \nabla) Z^2 + \frac{Z^2(1 - \sigma_D)}{2} \nabla \cdot \mathbf{u} + \frac{2}{\rho} \mathcal{R} : \nabla \mathbf{u} + 2\boldsymbol{\varepsilon}_m \cdot (\nabla \times \mathbf{V}_A) \\ - (\mathbf{V}_A \cdot \nabla)(Z^2 \sigma_c) + Z^2 \sigma_c (\nabla \cdot \mathbf{V}_A) = -\alpha f^+(\sigma_c) Z^3 / \lambda, \end{aligned} \quad (4.31)$$

and

$$\begin{aligned} \frac{\partial(Z^2 \sigma_c)}{\partial t} + (\mathbf{v} \cdot \nabla)(Z^2 \sigma_c) - (\mathbf{V}_A \cdot \nabla) Z^2 + \frac{Z^2 \sigma_c}{2} \nabla \cdot \mathbf{u} + \frac{2}{\rho} \mathcal{R} : \nabla \mathbf{V}_A \\ + 2\boldsymbol{\varepsilon}_m \cdot (\nabla \times \mathbf{u}) + (1 - \sigma_D) Z^2 \nabla \cdot \mathbf{V}_A = -\alpha f^-(\sigma_c) Z^3 / \lambda. \end{aligned} \quad (4.32)$$

Equations (4.30) – (4.32) are the transport equations for the three statistical descriptors of turbulence λ , Z^2 , and σ_c . They are coupled to the mean-field equations through the terms involving Q_T , \mathcal{R} , and $\boldsymbol{\varepsilon}_m$. The following key assumptions were made

in deriving the turbulence transport equations: local incompressibility, definite turbulence symmetry, constant normalized energy difference σ_D , and a single correlation length λ [cf. Zank et al., 2017]. Notably, we set the polytropic index to the adiabatic value $\gamma = 5/3$, so that solar wind heating emerges from the turbulent cascade and the divergence of electron heat flux, without additional *ad hoc* sources. We also note that Usmanov et al. [2014] made the additional assumption $\mathbf{V}_A \ll \mathbf{u}$, which is valid beyond ~ 0.3 au. Our generalization of the turbulence transport equations to flow speeds comparable to the Alfvén speed makes them well suited for application to the solar corona [Usmanov et al., 2018]. We require further closures for the Reynolds stress \mathcal{R} and the mean turbulent electric field $\boldsymbol{\varepsilon}$, along with specification of the Kármán–Taylor constants α and β as well as the constant turbulent energy difference σ_D .

Before discussing the models for \mathcal{R} and $\boldsymbol{\varepsilon}$, we note that the RHS of Equation (4.31) is the loss rate of turbulence energy due to conversion into thermal energy of protons and electrons. The source/sink term in the mean energy equations (4.10) and (4.11) consequently takes the form

$$Q_T = \frac{\alpha f^+(\sigma_c) \rho Z^3}{2\lambda}. \quad (4.33)$$

We also note that the mean turbulent magnetic field pressure in the RHS of Equation (4.8) can be expressed in terms of known turbulence variables in the form $\langle B'^2 \rangle / (8\pi) = (1 - \sigma_D) \rho Z^2 / 4$.

4.5 The Eddy Viscosity Approximation

We reviewed the eddy viscosity approximation for the Reynolds stress in Section 3.2, in the context of hydrodynamics. This model has served as the inspiration for several sophisticated closure models for MHD [e.g., Yoshizawa et al., 2003]; the basic underlying idea is the expression of the turbulent stress in terms of gradients of the mean velocity and magnetic fields and an eddy (turbulent) viscosity. Here we use a two-scale extension of the direct interaction approximation – the *TSDIA* [Yoshizawa

et al., 2003] – to model \mathcal{R} and $\boldsymbol{\varepsilon}$.

As discussed in Section 3.2.3, the DIA is a perturbation expansion theory for isotropic, homogeneous, strong turbulence in fluids. The two-scale extension introduces effects of inhomogeneity due to a mean magnetic field, rotation etc., by way of introducing slowly and rapidly varying variables. The effect of the slow (inhomogeneous) variables on the faster (homogeneous and isotropic) fluctuations is incorporated through perturbations on the latter. Inhomogeneities therefore appear as higher-order effects in the perturbation theory.

The interested reader can find a concise review of the TSDIA in Appendix A of Yokoi [2013]. Here we simply state the relevant results for \mathcal{R} and $\boldsymbol{\varepsilon}$ used in our model. For the MHD Reynolds stress we have [Yokoi et al., 2008]

$$\frac{1}{\rho}\mathcal{R} = \frac{2}{3}K_R\mathbf{I} - \nu_K\mathcal{S} + \nu_M\mathcal{M}, \quad (4.34)$$

where ν_K and ν_M are (kinematic) eddy viscosity coefficients, $K_R = \sigma_D Z^2/2$, and \mathcal{S} and \mathcal{M} are the strain rates of the mean inertial-frame velocity \mathbf{u} and the mean Alfvén velocity, respectively. \mathcal{S} and \mathcal{M} are deviatoric symmetric tensors given by

$$\mathcal{S} = \nabla\mathbf{u} + \nabla\mathbf{u}^T - \frac{2}{3}(\nabla\cdot\mathbf{u})\mathbf{I}, \quad \mathcal{M} = \nabla\mathbf{V}_A + \nabla\mathbf{V}_A^T - \frac{2}{3}(\nabla\cdot\mathbf{V}_A)\mathbf{I}, \quad (4.35)$$

where \mathbf{I} is the unit matrix and the superscript T denotes a matrix transpose operation. The diagonal components of the Reynolds stress tensor (4.34) are normal stresses and the off-diagonal components are shear stresses.

The turbulent electric field is given by [Yokoi et al., 2008]

$$\boldsymbol{\varepsilon}_m = \bar{\alpha}\mathbf{B} - \bar{\beta}\nabla\times\mathbf{V}_A + \bar{\gamma}\nabla\times\mathbf{v}, \quad (4.36)$$

with $\nu_K = (7/5)\bar{\beta}$ and $\nu_M = (7/5)\bar{\gamma}$. The eddy viscosity coefficients can be approximated as [see Usmanov et al., 2014] $\nu_K \approx 0.27Z\lambda$ and $\nu_M \approx 0.22\sigma_c Z\lambda$. Note that a higher-order frame rotation related term has been neglected in Equation (4.34)[see

Table 4.1: Summary of constant model parameters

Symbol	Description	Value
σ_D	normalized energy difference (residual energy)	$-1/3$
γ	adiabatic index	$5/3$
α_H	constant in Hollweg’s collisionless heat flux	1.05
α, β	Kármán–Taylor constants	2, 0.128
f_p	fraction of turbulent heating for protons	0.6
r_H	collisional/collisionless electron heat flux transition region	$5 R_\odot$

Yokoi, 2013], while frame rotation has been taken into account in Equation (4.36), which contains the mean *vorticity* in the rotating frame ($\nabla \times \mathbf{v}$). We neglect the $\bar{\alpha}$ term⁴ in Equation (4.36) since Marsch and Tu [1992] did not find a linear correlation between $\boldsymbol{\varepsilon}$ and \mathbf{B} in *Helios* observations.

4.6 Numerical Implementation and Initial/Boundary Conditions

With the closure approximations discussed above, the governing system of equations of our solar wind model are the mean-flow equations (4.7) – (4.11), which are coupled to the turbulence transport equations (4.30) – (4.32). The constant parameters used in the model are listed in Table 4.1. The model equations are concurrently solved numerically in the spherical shell between the base of the solar corona (just above the “transition region” that marks the transition of the chromosphere into the corona [e.g., Cranmer et al., 2007]) and the outer boundary of 3 or 5 au.

The computational region is divided into two sub-regions. The inner (coronal) subregion extends from the coronal base at $1 R_\odot$ to $30 R_\odot$; the outer (solar wind) region extends from $30 R_\odot$ to a maximum heliocentric distance of 5 au. It is computationally advantageous to maintain a division into subregions because the time step is restricted

⁴ This term is responsible for the α -effect, or the turbulent (dynamo-like) generation of large-scale magnetic fields [e.g., Chapter 16 of Choudhuri, 1998].

by the Courant-Friedrichs-Lewy condition [e.g., [Anderson et al., 2009](#)] that varies significantly between the regions. The location of the boundary between subregions was chosen to satisfy the condition that the flow becomes supersonic and super-Alfvénic before the boundary. Consequently, the inner region is independent of the solution in the outer region, since no signals can travel toward the sun in the outer region. Steady-state solutions are obtained in the inner region by time relaxation, starting from an initial state composed of either a Parker-type flow in a dipole magnetic field [[Usmanov and Goldstein, 2003](#)] or derived from synoptic solar magnetograms for different solar rotations [[Usmanov et al., 2014](#)]. The boundary conditions for the outer region are extracted from the inner region solution, and steady state solutions are obtained by time relaxation. The typical integration time in the inner region is 48 hours, while in the outer region it is 600 hours.

Solving the magnetohydrodynamic equations in spherical coordinates is complicated due to the geometrical singularity on the polar axis [e.g., [Roache, 1976](#)]. We employ a composite grid [[Usmanov, 1996](#); [Usmanov et al., 2012](#)] consisting of three overlapping spherical fragments, and a suitable bicubic interpolation scheme. This approach allows us to avoid the singularity and the shrinking of the grid cells along the azimuthal direction as one approaches the poles. To increase the grid resolution in the region close to the Sun, we use a logarithmic transformation of the radial coordinate r to $r' = \ln(r/r_0)$, where $r_0 = 1 R_\odot$ [[Usmanov, 1993](#)]. Assuming a constant grid spacing $\Delta r'$, Δr increases linearly as a function of r . In the inner region the grid resolution therefore increases from $\sim 0.01 R_\odot$ at the coronal base to $\sim 0.3 R_\odot$ at the outer boundary of $30 R_\odot$. The outer region grid spacing increases from 0.3 to $9.6 R_\odot$. The angular spacing is taken to be 1.5° in both regions.

Our numerical method employs the Central Weighted Essentially Non-Oscillatory (CWENO) scheme [[Kurganov and Levy, 2000](#)]. CWENO is a spatially third-order,

Table 4.2: Boundary values used in the initial state for sample run

Symbol	Description	Value
N_0	proton number density in the initial state at $1 R_\odot$	$8 \times 10^7 \text{ cm}^{-3}$
T_0	electron and proton temperature in the initial state at $1 R_\odot$	$1.8 \times 10^6 \text{ K}$
B_0	magnetic field strength of dipole at $1 R_\odot$	12 G
δv_0	driving amplitude of fluctuations in the initial state at $1 R_\odot$	35 km s^{-1}
σ_{c0}	normalized cross helicity in the initial state	0.8
λ_0	correlation scale of turbulence in the initial state at $1 R_\odot$	$0.015 R_\odot$

semi-discrete method that employs a piecewise polynomial reconstruction and smoothness indicators. For the time evolution, the Strong Stability-Preserving (SSP) Runge-Kutta discretizations [Gottlieb et al., 2001] of second, third, and fourth order of accuracy are implemented. To maintain the $\nabla \cdot \mathbf{B} = 0$ constraint, the code implements the 8-wave method of Powell [1994], which adds source terms proportional to $\nabla \cdot \mathbf{B}$ to the momentum and induction equations. The simulation codes are written using Message Passing Interface (MPI) and optimized for running on distributed memory parallel clusters.

The boundary and initial conditions used in different runs will be specified at appropriate points in the remainder of this thesis. In the next section, we present sample solutions with boundary and initial conditions specified in Table 4.2. The solar source dipole is taken to be tilted by 10° relative to the solar rotation axis, representing nominal solar minimum conditions [e.g., Owens and Forsyth, 2013]. Note that these numerical values are observationally motivated, and are fine-tuned to yield solutions that match near-Earth observations.

Before presenting the sample results, we note that some of the applications in the forthcoming chapters use a previous version of the simulation in which the MHD equations are solved with a WKB Alfvén wave model in the region $1 - 45 R_\odot$. Appendix

C carries a brief description of this model. The use of the older model will be indicated at appropriate points.

4.7 Sample Solutions

In Figure 4.1 we show inner-region ($1 - 30 R_{\odot}$) results from a simulation employing a solar dipole tilted by 10° relative to the solar rotation axis. Figure 4.2 shows results from the outer region ($30 R_{\odot} - 5 \text{ au}$). Meridional planes at azimuthal angle (heliolongitude) $\phi = 0.75^{\circ}$ are displayed, showing the variation of the solutions in the radial and polar (heliolatitudinal) directions. The radial evolution of selected fields is shown in Figure 4.3.

In the forthcoming chapters we will discuss several aspects of the solutions in greater detail, within the context of the specific problems under consideration. We remark here on some apparent features that can be seen in Figures 4.1, 4.2, and 4.3. First, the tilted dipole in combination with solar rotation produces the strikingly asymmetrical and *wavy* structure of the heliospheric sheet current sheet, where the radial magnetic reverses polarity [e.g., Smith, 2001]. One can also see the two-stream structure of the flow, with the high-density slow wind constrained to low heliolatitudes, and the fast wind flowing from polar regions.

The turbulence energy increases with radius, up to around $20 R_{\odot}$, accelerating and heating the wind (causing the temperature to fall slower compared with adiabatic expectations; see Section 1.1.3) in the process. The cross helicity is low in the equatorial slow wind region, while the correlation scale is large. This is because turbulence in the slow wind is more “aged” [Matthaeus et al., 1998] compared with the more Alfvénic fast wind at higher heliolatitudes. The increase of the correlation scale with heliocentric distance is related; as the turbulence develops, it begins to involve larger scales in the cascade. This behavior is reminiscent of the evolution of the spectra in Figure 1.5, where the breakpoint frequency shifts to lower values with increasing distance. Figure 4.3 shows that a higher coronal base temperature weakens the turbulence and acceleration of the wind, due to shallower density gradients.

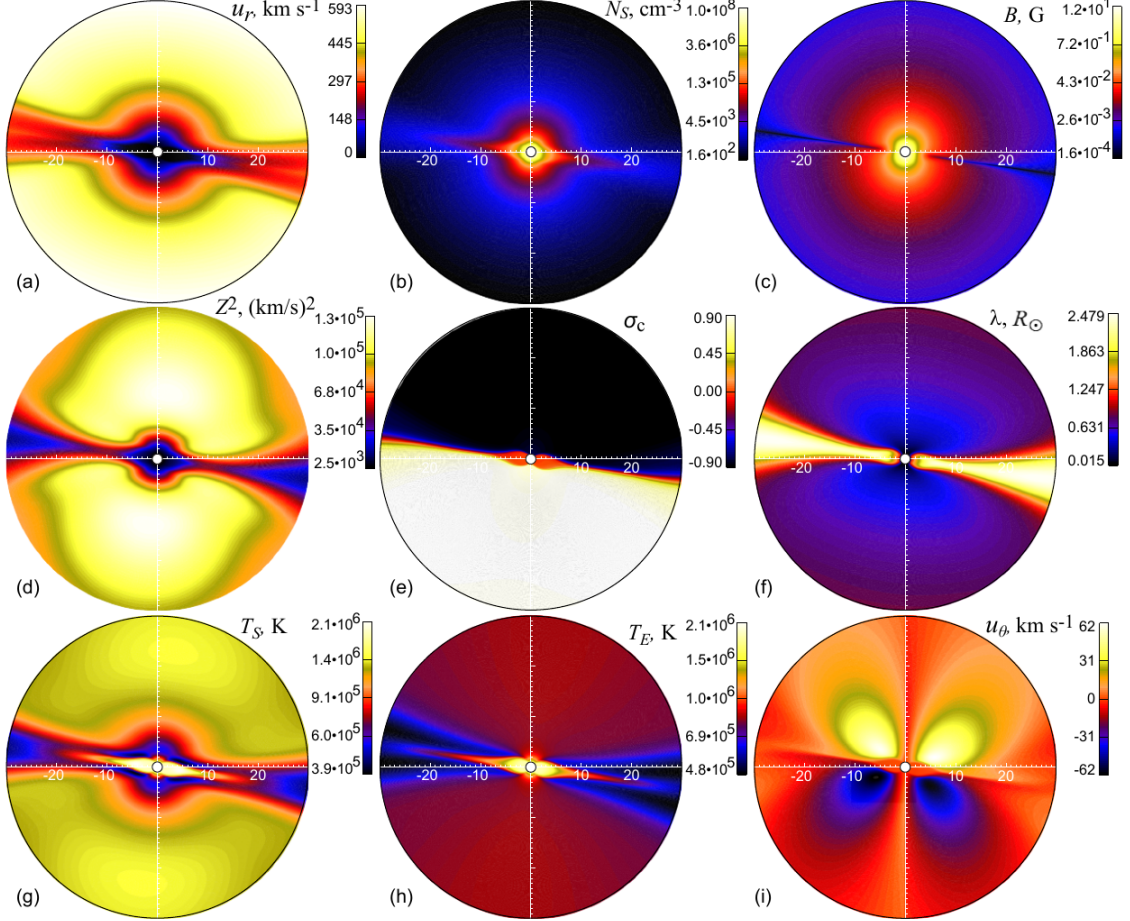


Figure 4.1: Inner-region ($1 - 30 R_{\odot}$) results in the meridional plane at heliolongitude $\phi = 0.75^{\circ}$, from a simulation employing a solar dipole tilted by 10° relative to the solar rotation axis. The fields shown are: (a) radial velocity u_r , (b) proton density N_S , (c) magnetic field magnitude B , (d) turbulence energy density Z^2 , (e) cross helicity σ_c , (f) correlation scale of the fluctuations λ , (g) proton temperature T_S , (h) electron temperature T_E , and (i) meridional velocity u_{θ} [Usmanov et al., 2018].

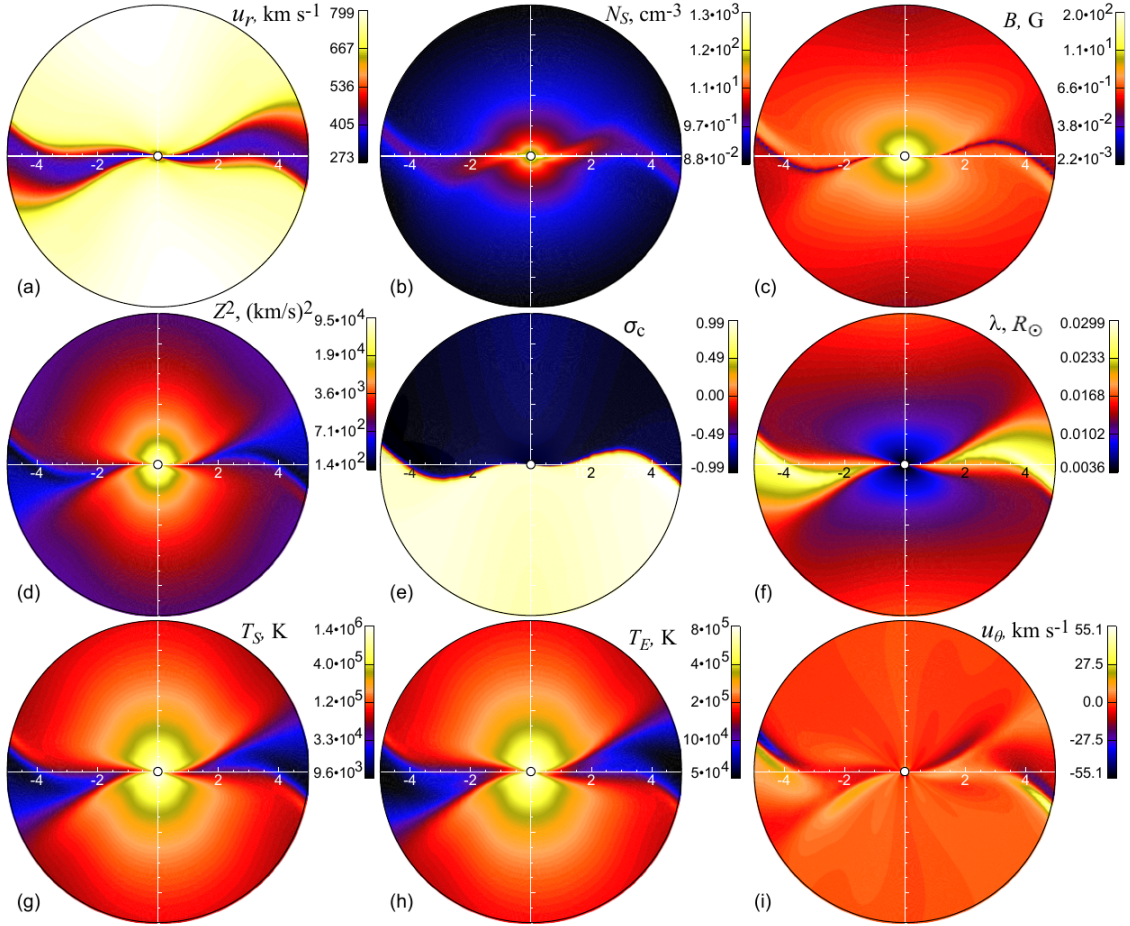


Figure 4.2: Description follows from Figure 4.1, with a view of the outer region ($30 R_\odot - 5 \text{ au}$) [Usmanov et al., 2018].

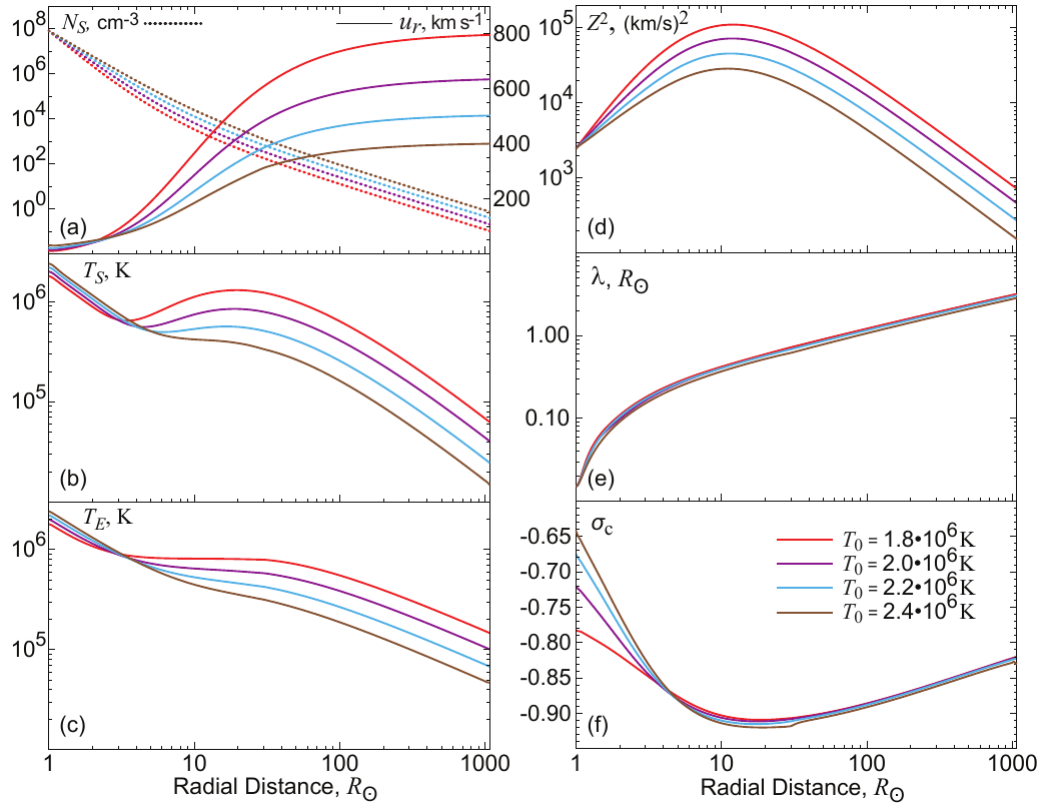


Figure 4.3: Radial profiles along the pole for varying coronal base temperature T_0 . The fields shown are (a) radial velocity u_r , (b) proton temperature T_S , (c) electron temperature T_E , (d) turbulence energy density Z^2 , (e) correlation scale of the fluctuations λ , and (f) cross helicity σ_c [Usmanov et al., 2018].

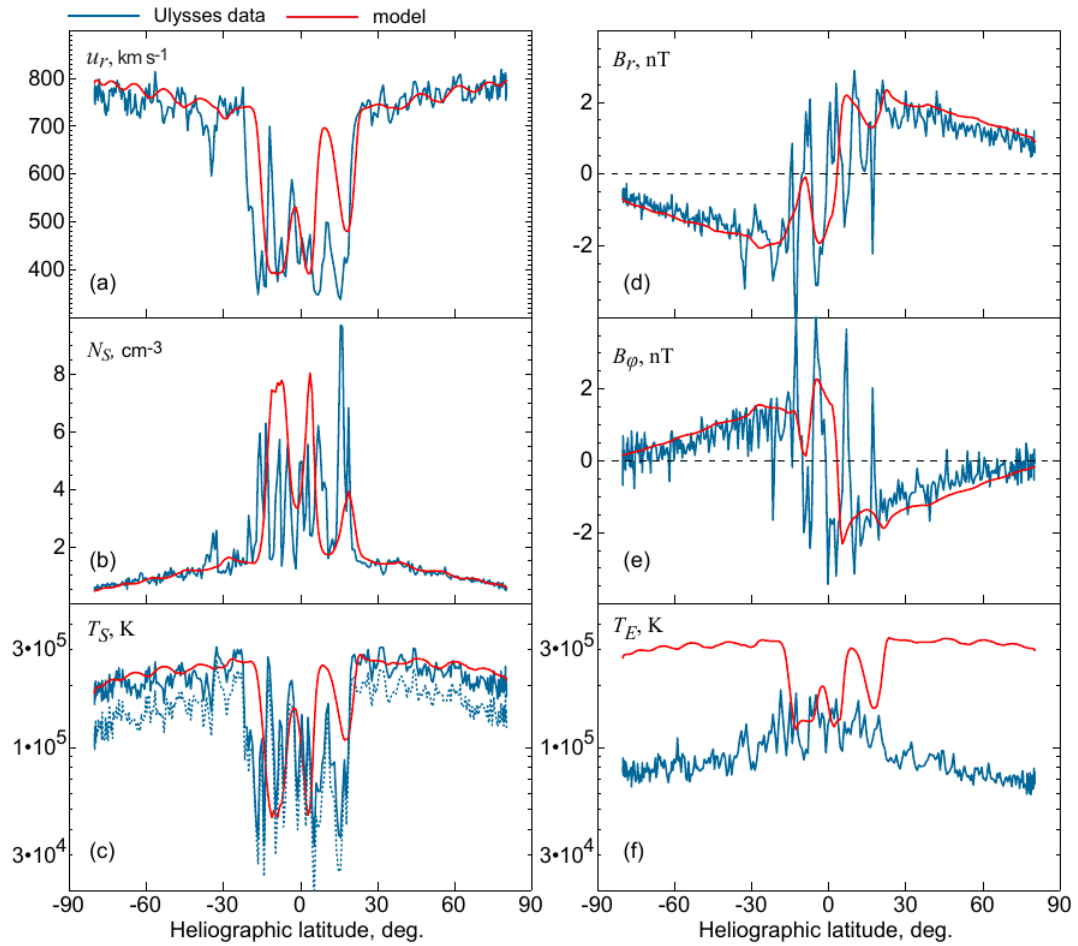


Figure 4.4: Simulated profiles (red) for a source magnetic dipole on the Sun tilted by 10° (with respect to the solar rotation axis) versus *Ulysses* daily averages of plasma and magnetic field parameters measured during the first fast latitude transit of (Sep 13, 1994 to July 31, 1995). The parameters shown are: (a) the radial velocity u_r , (b) the number density of solar wind protons N_S and (c) their temperature T_S , (d) the radial B_r and (e) the azimuthal B_ϕ magnetic field, and (f) the electron temperature T_E . Two estimates of the proton temperature measured by *Ulysses*, “T-large” and “T-small”, are shown by solid and dotted lines, respectively [Usmanov et al., 2018].

The solar wind model introduced in this chapter has been well-tested and performs well with several comparisons with spacecraft observations [Usmanov et al., 2011, 2012, 2014; Airapetian and Usmanov, 2016; Usmanov et al., 2016a, 2018]. A comparison of the model results with *Ulysses* data is shown in Figure 4.4.⁵ The simulations therefore provide us with a *model heliosphere* that can be used to study the problems discussed in Section 1.1.7. The first problem we consider is a study of the *collisional age* of the solar wind, presented in the next chapter.

⁵ Further comparisons with observations will be presented in the coming chapters.

Chapter 5

COLLISIONAL AGE OF THE SOLAR WIND

5.1 Introduction

Although the solar wind plasma is frequently described as collisionless, it is better regarded as weakly collisional, since there is extensive observational evidence for the role played by collisions in regulating various kinetic processes. For example, temperature anisotropies [Marsch, 2006] are not as completely developed as expected for a purely collisionless expansion. Recent observational surveys show that a simple local estimate of the number of binary Coulomb collisions [Kasper et al., 2008; Maruca et al., 2013] provides a convincing organization of a number of nonequilibrium kinetic plasma features. Here we develop improved estimations of this “collisional age” (defined precisely below) based on the global solar wind model presented in Chapter 4, which are compared with the simple formulation typically used in prior works. We also develop an analytical approximation and compare it with the standard local estimate and the improved estimate. The present formulations rely on plasma properties along the trajectory of a solar wind plasma element as it transits from the corona, and may prove useful in better understanding kinetic effects that should be observed by near-Sun missions such as *Parker Solar Probe (PSP)* and *Solar Orbiter*.¹

5.2 Background and Motivation

The role of Coulomb collisions in regulating the character of particle velocity distribution functions has been well established. Collisions isotropize cores of ion velocity distributions in slow and intermediate speed solar wind [Marsch and Goldstein,

¹ Parts of this chapter were published in Chhiber et al. [2016a].

1983], regulate the differential heating of protons and alpha particles [Feldman et al., 1974; Neugebauer, 1976; Klein et al., 1985], impact electron properties [Salem et al., 2003], and are ultimately responsible for conversion of ordered energy into heat through irreversible relaxation towards thermal equilibrium [e.g., Pezzi, 2017]. They are also relevant to the development of kinetic and exospheric models of the solar wind [Brandt and Cassinelli, 1966; Pierrard, 2010]. A parameter commonly employed in these studies is the *collisional age* (A_c) – a measure of the number of collisions experienced by the expanding solar wind plasma. It is defined as the ratio of the transit time of the solar wind (from the solar surface to the point of observation) to the mean time between Coulomb collisions τ_c . This measure broadly categorizes solar wind intervals based on an approximate estimate of the extent of collisional thermalization. Young wind ($A_c \ll 1$) is collisionless; when $A_c \gg 1$, the wind is collisionally old, and Coulomb relaxation effects a reduction of non-thermal features. Here we note that another useful index of collisionality is the Knudsen number [e.g., Scudder and Karimabadi, 2013; Scudder, 2015], $Kn = \lambda_{coll}/L$, where λ_{coll} is the mean free path between Coulomb collisions, and L a characteristic length of the system. Kn is more relevant for subsonic flows, and in Appendix 5.A we clarify the connection between the Knudsen number and the collisional age, and their validity in different regimes. Here we focus on supersonic flow of protons in the solar wind, where the collisional age is more appropriate.

Livi et al. [1986] calculated the collisional age based on Helios data, to identify domains of collisionality in the solar wind, concluding that the primary collisional domain is the heliospheric current sheet, where this age is largest. Griffel and Davis [1969] showed that a collisionless wind would result in extreme exospheric temperature anisotropies in ion distribution functions, but $A_c \approx 1$ is enough to reduce them to observed levels. This indicates that $A_c \sim 1$ is a natural limiting value to distinguish collisionless and collision-dominated areas. Kasper et al. [2008] find that for $A_c > 1$, non-thermal features are wiped out; hydrogen and helium temperatures are equalized, the ratio of proton temperatures parallel and perpendicular to the ambient magnetic field tends to one, and ion differential flow speed tends to zero. Further, even though

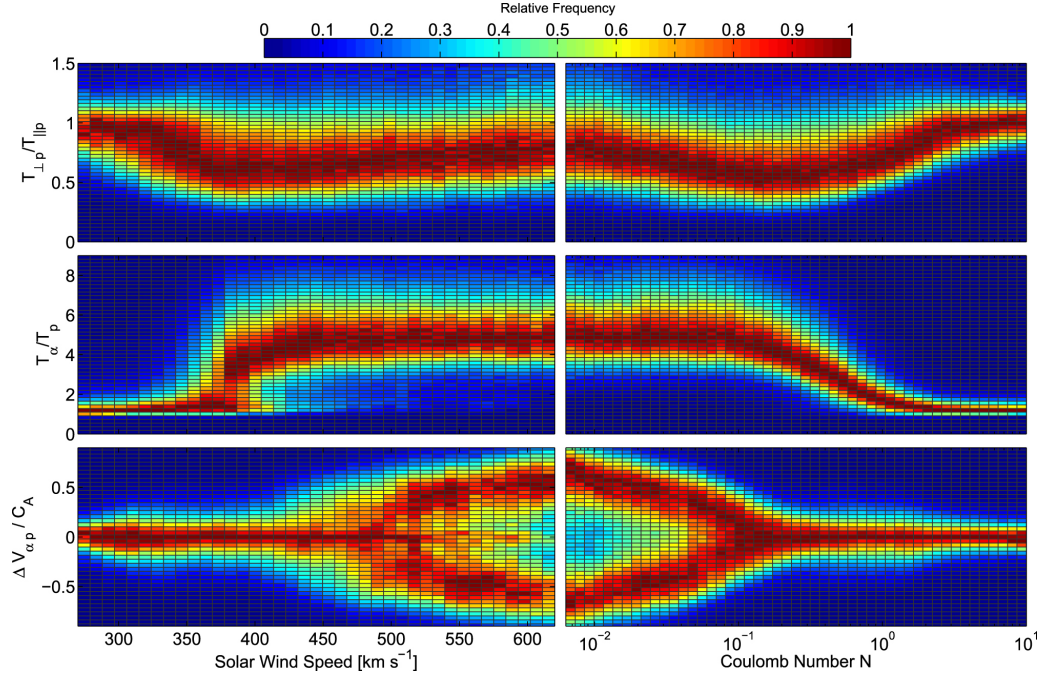


Figure 5.1: Two-dimensional histograms of distributions of $T_{\perp p}/T_{\parallel p}$, T_{α}/T_p , and $\Delta V_{\alpha p}/C_A$ as functions of solar wind speed (left) and Coulomb number N_C (right). While nonthermal solar wind is generally associated with high speeds, these distributions suggest that the occurrence frequency is really determined by the Coulomb number N_C (equivalent to the local collisional age defined by Equation 5.6). *Figure reproduced from Kasper et al. [2017] under the Creative Commons Attribution 3.0 licence.*

nonthermal features correlate with parameters like the number density, temperature, and solar wind speed, the correlation is stronger with A_c than with any individual parameter [Maruca et al., 2013]. This correlation is apparent in Figure 5.1, which compares the distributions of three markers of nonthermal behaviour – ratio of proton temperatures parallel and perpendicular to the magnetic field $T_{\perp p}/T_{\parallel p}$, ratio of α -particle to proton temperature T_{α}/T_p , and the differential velocity between α -particles normalized by the Alfvén speed $\Delta V_{\alpha p}/C_A$ – as a functions of both the solar wind speed and the collisional age [Kasper et al., 2017].

The local calculation of A_c gives useful results, but could be inaccurate, or even misleading, in some circumstances. The “age”, as a measure of the collisional *history*

of a particle, must depend on the path of a plasma parcel in the expanding solar wind, and this necessitates an *integral* formulation. The parameters that define A_c may vary along streamlines, and the total number of collisions experienced by a plasma parcel may not be well estimated by the outermost collision rate, at the position of observation. The possibility for ambiguity here is great, given that the rate of Coulomb collisions is highest in the lower solar atmosphere. Consequently, the age calculation is particularly sensitive to near-sun regions, and those contributions may influence the accuracy of the local one-point age estimate. This leads to the second issue – where do we start counting collisions? And which starting point corresponds to the local estimate that refers only to observations at one point? We address these questions constructively in the present study by computing the cumulative collisional age starting from various points in the solar atmosphere, employing data from our solar wind model (Chapter 4) to obtain the needed spatially varying parameters.

5.3 Three Formulations of Collisional Age

Consider a plasma parcel in the solar wind. Let the timescale of a proton-proton (p-p) collision be τ_c . The collisional age of the plasma parcel, i.e., the average number of collisions experienced by a typical particle within the parcel, between some initial time t_0 and the time of observation t , is defined as

$$A_c(t) \equiv \int_{t_0}^t \frac{dt'}{\tau_c(t')}. \quad (5.1)$$

With $u dt' = ds$, where u is the speed of the plasma along a streamline of the flow, and ds a line-element along the streamline, the age becomes

$$A_c(\mathbf{r}) = \int_{\mathbf{r}_0}^{\mathbf{r}} \frac{ds}{u(s)\tau_c(s)}, \quad (5.2)$$

where s denotes distance along the streamline, and \mathbf{r}_0 and \mathbf{r} denote the initial and final position of the streamline, respectively. τ_c is taken as [Spitzer, 1965]

$$\tau_c = \left(11.4 \frac{s}{\text{cm}^3 \text{ K}^{3/2}} \right) \left(\frac{T^{3/2}}{n} \right) \left(\frac{1}{\lambda} \right), \quad (5.3)$$

where T and n are the proton temperature and density, respectively, and λ is the Coulomb logarithm:

$$\lambda = 9.42 + \ln \left[\left(\frac{1}{\text{cm}^{3/2} \text{ K}^{3/2}} \right) \left(\frac{T^{3/2}}{n^{1/2}} \right) \right]. \quad (5.4)$$

We combine these equations to obtain

$$A_c(\mathbf{r}) = \kappa \times \int_{\mathbf{r}_0}^{\mathbf{r}} \frac{n(s)}{u(s)T^{3/2}(s)} \lambda(s) ds, \quad (5.5)$$

where $\kappa \equiv \left(8.73 \times 10^{-8} \frac{\text{m}^3 \text{ K}^{3/2}}{\text{s}} \right)$. In the following, we make the reasonable approximation that above $20 R_\odot$ the flow is radial. Below we evaluate Equation (5.5) by employing the spatially varying n , u , and T from the our solar wind model.

Observational estimates of the collisional age cannot employ the complete formula above, which requires information about the variation along streamlines of u , n , and T . We consider two other formulations of the age, one of which has been used in observational work, and a new analytical expression that we derive. We refer to the former age as A_{c1} , and the latter as A_{c2} .

Previous works [e.g., Livi et al., 1986; Kasper et al., 2008] have used the simple approximation

$$A_{c1}(r) = \frac{\tau_{exp1}}{\tau_c}, \quad (5.6)$$

that is, the age at a radial distance r from the sun is simply given by the ratio of the local expansion time (τ_{exp1}) to the local collision timescale, both calculated from the values of u , n , and T at the position r . The local expansion time is $\tau_{exp1}(r) = \frac{r}{u(r)}$, equivalent to the transit time from the origin to position r with constant velocity.

We expect this “one-point” equation for the *locally determined* collisional age to be potentially deficient, for the reasons discussed in the last section: the time scales change along the flow tubes, there are more collisions near the sun, and the local formulation makes no statement about a starting point for accruing collisions. We will see that our results confirm these expectations. Further, shear driving and inhomogeneities can influence the collision timescale [Scudder, 1992], and the local measure may fail to capture these effects. A path-dependent age implicitly incorporates some of these effects through variation in plasma parameters.

One may also derive a simple and approximate analytical expression for the collisional age, using observed power laws for the radial evolution of the density and the temperature, and a simple analytical model for the solar wind velocity. According to Parker’s coronal model (Section 2.1), we have, for large r [Hundhausen, 1972]

$$u(r) = 2u_c \sqrt{\ln \frac{r}{r_c}}, \quad (5.7)$$

where $u_c = \sqrt{2kT_c/m}$ and $r_c = (GM_\odot m)/(4kT_c)$. Here k is the Boltzmann constant, m the proton mass, G the gravitational constant ($6.67408 \times 10^{-11} \text{ m}^3 \text{ kg}^{-1} \text{ s}^{-2}$), M_\odot the solar mass, and T_c a model parameter that we may specify. The density and temperature power laws may be expressed as $n(r) = n_0 \left(\frac{R_0}{r}\right)^p$, and $T(r) = T_0 \left(\frac{R_0}{r}\right)^m$, where n_0 and T_0 are reference values of the density and the temperature respectively, at the position R_0 . Note that the analytic speed profile is derived from an isothermal model, and as such, is not fully consistent with the radially varying temperature. Nevertheless, it is an improvement over the constant speed assumption used in previous work, and leads to a simple and easy-to-use analytical formula for the collisional age. Using the scalings in Equation (5.5) yields

$$A_{c2}(r) = C \times \int_{r_0}^r \frac{1}{r'^{\alpha} \sqrt{\ln r'}} dr', \quad (5.8)$$

where r' denotes the position along a radial spoke, $C = 1.31 \times 10^7 \frac{\lambda n_0 R_0^\alpha r_c^{1-\alpha}}{2u_c T_0^{1.5}}$, and

$\alpha = p - 1.5m$. With $\alpha = 1$, the above integral has the exact solution

$$A_{c2}(r) = 2 \times C(\sqrt{\ln \tilde{r}} - \sqrt{\ln \tilde{r}_0}). \quad (5.9)$$

Here \tilde{r}_0 and \tilde{r} are the initial and final radial positions, respectively, that have been normalized to units of r_c . The slowly varying Coulomb logarithm λ is regarded as a constant and is calculated from values of n and T at R_0 . With $p = 2$ [Richardson et al., 1995], choosing $m = 0.67$ allows us to use this exact solution. The choice $m = 0.67$ is not unreasonable, since it lies between the two observed values of 0.5 [Richardson et al., 1995] and 0.74 [Hellinger et al., 2011], and we work with these, in view of the simplicity afforded by Equation (5.9).

5.4 Simulation Results

We use the model discussed in Chapter 4 with an older version of the coronal code that solves one-fluid, polytropic ($\gamma = 1.08$) solar wind equations with WKB Alfvén waves in the $1 - 45 R_\odot$ region (Appendix C). The input parameters at the coronal base are the same as those used in Usmanov et al. [2014]: the driving amplitude of Alfvén waves is set to 35 km s^{-1} , the initial density is $0.4 \times 10^8 \text{ cm}^{-3}$, and the initial plasma temperature is $1.8 \times 10^6 \text{ K}$. The magnetic field magnitude is assigned as the field strength of the untilted source dipole on the poles. This parameter is set to 16 G to match the magnitude of the heliospheric magnetic field observed by *Ulysses* [Usmanov et al., 2014].

We first briefly discuss the radial evolution of several relevant timescales: the p-p collision time (Equation 5.3); the solar wind expansion time τ_{exp1} ; and the time scale for transiting a Coulomb mean free path λ_{coll} , namely

$$\tau_{exp2} = \lambda_{coll}/u = v_{therm}\tau_c/u, \quad (5.10)$$

where $v_{therm} = \sqrt{\frac{2kT}{m}}$. Another timescale, the non-linear time, characterizes the turbulent evolution of the solar wind:

$$\tau_{NL} = \lambda_{corr}/Z, \quad (5.11)$$

where λ_{corr} is the correlation length, and Z^2 is twice the turbulent energy per unit mass. If the expansion timescales are shorter than the collision timescale, the expansion is weakly collisional, becoming collisionless when $\tau_{exp1}, \tau_{exp2} \ll \tau_c$. When the nonlinear time scale is much shorter than the collision timescale ($\tau_{NL} \ll \tau_c$), the turbulence evolves without significant influence of collisions.

Figure 5.2 shows the radial evolution, at a low-mid heliolatitude of 15° , of the above four timescales. The collisionality of the solar wind reduces drastically as one leaves the solar surface, and beyond $4 R_\odot$ the collision time scale is longer than either expansion time scale, and much longer than the nonlinear time. Outside of $\sim 10 R_\odot$, both expansion and nonlinear effects such as turbulence are operating in a relatively low collisionality regime. Figure 5.3 shows the scatter of the timescales with varying heliolatitude; the solar equator is represented by black, with the color of the lines turning red towards the pole. We see that mid-high latitude wind is less collisional than the dense and slow equatorial flow. The turbulence is weakest (large τ_{NL}) at 0° latitude, and increases in strength at mid-latitudes, which are sites of stream interactions between slow and fast wind.

The calculation of the collisional age using Equation (5.5) is obtained by numerical integration based on the 3D MHD simulation data. We first must decide on an initial point for the integration. The goal is to understand how collisions, in the weakly collisional solar atmosphere, extinguish kinetic effects such as temperature anisotropies [e.g., Maruca et al., 2013]. Consequently it makes sense to start counting these collisions after the wind exits the region of very high collision rate very close to the solar surface. The determination of a ‘‘critical level’’ above which collisions are assumed to be weak is also required in the construction of exospheric models of the solar wind.

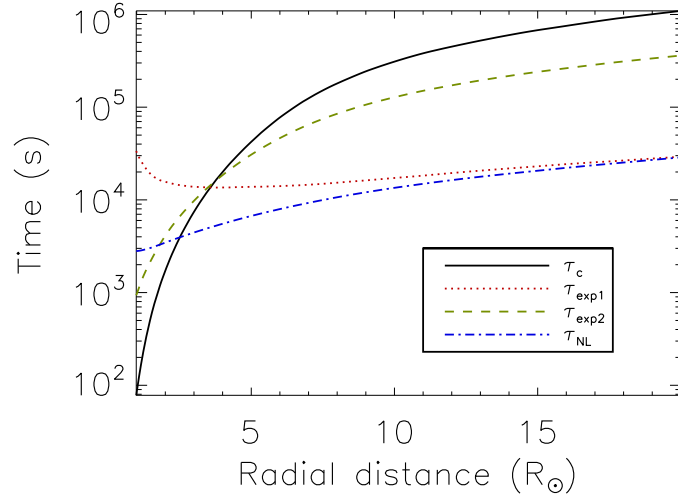


Figure 5.2: Timescales as a function of radial distance, at 15° heliolatitude: collision timescale τ_c , expansion timescales τ_{exp1} and τ_{exp2} as defined in the text; nonlinear timescale τ_{NL} .

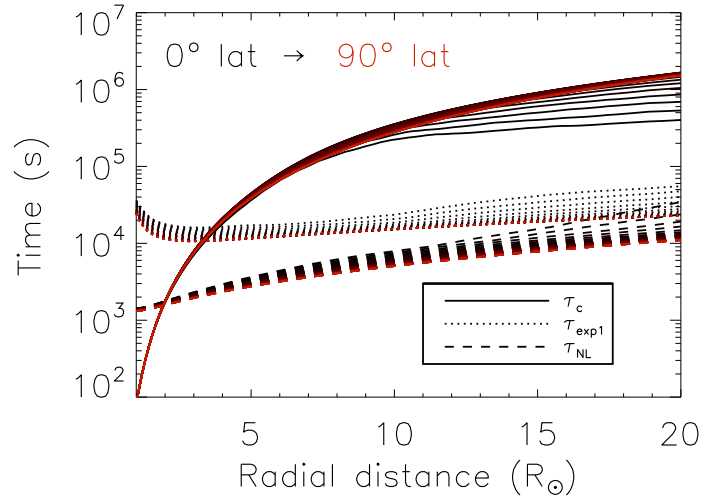


Figure 5.3: Scatter of the timescales with varying heliolatitude; the solar equator is represented by black, with the color of the lines turning red towards the pole.

One definition [Jeans, 1921] takes the height above the sun from which $1/e$ of fast particles would escape without further collision as the critical level. Depending on the energy of particles, the critical level may range from 1 to $7 R_{\odot}$ [Brandt and Cassinelli, 1966]. In our numerical model, between 2 and $3 R_{\odot}$ there is a sharp increase in the slope of the density as one approaches the sun. Furthermore, the location of the sonic point in our simulation is around $3 R_{\odot}$. Therefore, we identify $3 R_{\odot}$ as a preferred minimum starting point for integration of the total collisional age, noting that this is near the sonic point, and not far from the (transition) region where collisionality decreases rapidly [e.g., Kasper et al., 2017].

For our main results, we compare the three formulations of the collisional age described in Section 5.3. Figure 5.4 shows the radial evolution of the ages calculated at heliolatitudes of 0° and 55° , in order to represent latitudes ranging from low to high. For the numerically integrated age, A_c , we show the age profile using several different initial points (r_0) for the integration. As r_0 is moved outward from the transition region boundary ($3 R_{\odot}$), there is a significant drop in the collisional age because the high collisionality found near the Sun is not included. Figure 5.4 also shows the one-point collisional age A_{c1} , which is very high when evaluated at lower radial positions because the local collision-times are small in that region. But at higher r , the point-wise calculation does not “see” the collisions experienced by the plasma at lower r , and A_{c1} falls to lower values. Note that the integrated age (A_c) agrees well with the locally computed age (A_{c1}) if the initial position for the integration is at sufficiently large radial distance. But if one is interested in the number of collisions starting from the transition region, or even starting from $10 R_{\odot}$, then the local formulation gives a significant underestimate, of about an order of magnitude, for both latitudes shown in Figure 5.4.

For the calculation of the analytical formula A_{c2} (Equation 5.9), we take the reference position, R_0 , at 1 A.U., and take n_0 and T_0 to be the values of density and temperature respectively at 1 A.U. from the simulation data. We use $T_c = 2.5 \times 10^6$ K. We see that compared to the local estimate, the analytical formula for the age is closer

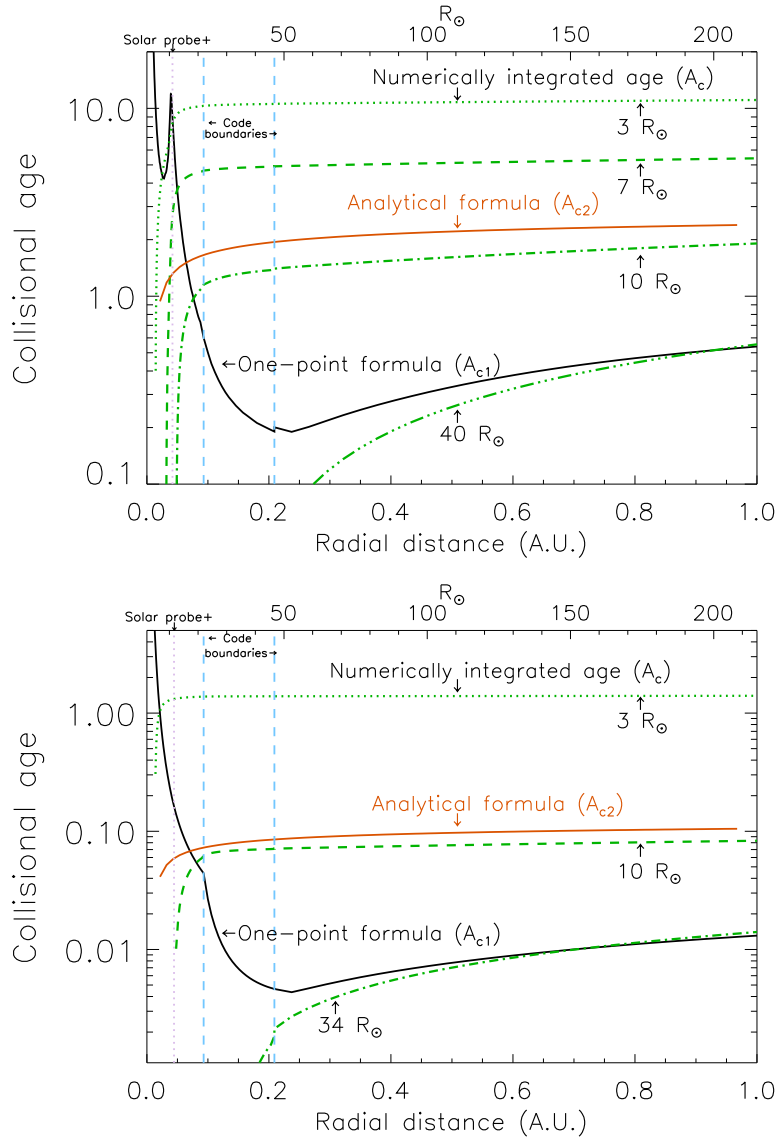


Figure 5.4: Comparison of A_c , A_{c1} , and A_{c2} at (top) 0° and (bottom) 55° heliolatitude. Dotted-dashed lines in green represent A_c , the numerically integrated age (Equation 5.5) for different initial positions. Solid black line is A_{c1} , the age computed using the point-wise formula Equation (5.6). Solid red line is A_{c2} , the analytical formula in Equation (5.9). The vertical dotted purple line is the approximate perihelion of *PSP*, $9 R_\odot$. The two vertical dashed blue lines mark the outer boundaries of the “inner region” and the “intermediate region” in the simulation (Appendix C).

to the “fully” integrated numerical calculation. Beyond $20 R_{\odot}$ the analytic formula age lies between the fully integrated ages computed with lower boundaries positioned somewhere between $3 R_{\odot}$ and $10 R_{\odot}$ for all latitudes computed. Interpolating between the illustrated curves in Figure 5.4 (top), one sees that the analytical approximation gives an age very close to the integrated age when the integration is started around $9 R_{\odot}$ at 0° latitude. The analytical formula may therefore be used as a form of correction to the locally computed age (A_{cl}), that must necessarily be used when working with spacecraft data.

Comparing the top and bottom panels of Figure 5.4, we see that the collisional age in the equatorial region is an order of magnitude larger than the age in the polar regions. The heliospheric current sheet region is therefore the collision-dominated domain of the solar wind, in agreement with Livi et al. [1986]. This finding complements Figure 5.5, which shows meridional planes from a simulation with the source dipole tilted by 30° relative to the solar rotation axis. The left (right) panel of this figure shows A_c with the initial integration point r_0 at $7 R_{\odot}$ ($44 R_{\odot}$). Evidently, if we count the collisions that occur close to the Sun (Figure 5.5(a)), then the collisionally “oldest” plasma is confined to a narrow beam that is much more collisional than the surrounding wind. This feature is “washed-out” in Figure 5.5(b), which suggests a general region of weak collisionality at low and mid latitudes. This comparison indicates that a calculation that doesn’t account for the high collisionality close to the Sun may misleadingly lump collisionally old plasma with plasma that has not been thermalized by collisions.

A possible example of this effect can be seen in the first panel in the right column of Figure 5.1, which gives the impression that a substantial fraction of the data has $T_{\perp p}/T_{\parallel p} \sim 1$ and a *low* collisional age, when the collisional age is computed using the local approximation (5.6). It is possible that this section of the data is from the hypothetical collisionally old “beam” seen in Figure 5.5, but the local measure of the age at *Wind*’s location underestimates its collisionality. We acknowledge that this point is speculative, and we plan to investigate it more closely in future work.

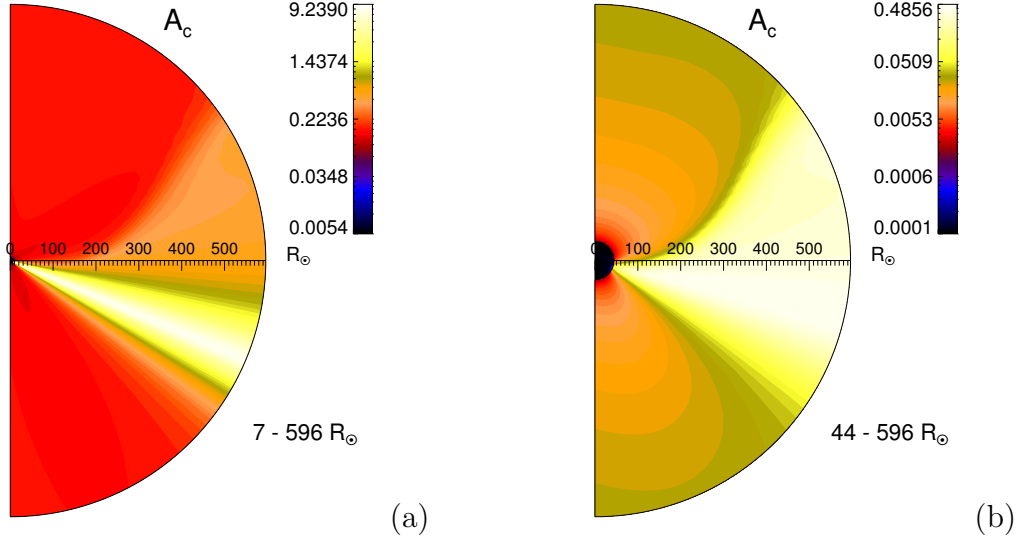


Figure 5.5: Meridional planes from a 30°-tilted-dipole simulation showing the numerically integrated collisional age A_c with (a) $r_0 = 7 R_\odot$ and (b) $r_0 = 44 R_\odot$.

5.5 Conclusions

We have examined three formulations of collisional age, i.e., number of Coulomb collisions experienced by a proton in a plasma parcel as it transits to the position of observation. The most complete of these formulations integrates the collision rate along a plasma trajectory that leads to a position of observation. This version, however, requires knowledge of plasma properties (density, temperature, and velocity) along this entire path; here the required integrations are carried out using data from our global solar wind simulation code. One finds that the results depend strongly on where the integration is begun, in view of the much higher rate of collisions found close to the sun. The second formulation of collisional age is the traditionally used estimate that relies only on local, one-point plasma properties. It gives qualitatively good answers, and quantitative agreement with the integrated age if the inner boundary of integration is far from the sun, outside of $20 R_\odot$, i.e. beyond the expected position of the trans-Alfvénic region. The third version of collisional age we examined is an analytical approximation based on isothermal solar wind theory and empirical fits to density and temperature profiles. The analytical approximation works well to give agreement with

the integrated age when the inner integration boundary is around 5 to 9 R_{\odot} at the latitudes we examined. As such the analytic estimate provides a simple way to correct the local approximation, and to provide an age estimate closer to what is obtained through a full integration, which requires 3D data. These results may be useful in spacecraft data analysis when collisionality needs to be estimated, and in particular in planning for the soon-to-be-launched *PSP* and *Solar Orbiter* missions.

APPENDIX

5.A Collisional Age vs Knudsen Number

We investigate the validity of the collisional age versus the Knudsen number (Kn) as a measure of the collisionality of a fluid. The key issue is whether a particle samples an inhomogeneity (at spatial scale R) prior to experiencing a collision, for mean free path λ_{coll} . The time for a collision is $\tau_c = \lambda_{coll}/v_{therm}$, where v_{therm} is the thermal speed of the particle. The time for sampling the inhomogeneity is estimated as $T = R/(u + v_{therm})$, where u is the large-scale flow speed. Then the number of collisions is

$$T/\tau_c \rightarrow \begin{cases} R/u\tau_c = A_{c1}, & \text{if } u \gg v_{therm}, \\ R/v_{therm}\tau_c = 1/Kn, & \text{if } u \ll v_{therm}. \end{cases} \quad (5.12)$$

Therefore, for supersonic flow ($u \gg v_{therm}$), the collisional age is the correct measure, while for subsonic flow ($u \ll v_{therm}$), the Knudsen number is more appropriate. Indeed, Kn is the more relevant number for solar wind electrons, which are subsonic [Livi et al., 1986]. In this work, we discuss proton collisionality in the expanding solar wind, and hence our focus is on the collisional age.

5.B Turbulence Age of the Solar Wind

The dimensionless age of turbulence, in units of the non-linear time (τ_{NL}), can be defined analogously to Equation (5.1):

$$A_t \equiv \int_{t_0}^t \frac{dt'}{\tau_{NL}(t')} = \int_{t_0}^t \frac{Z(t')}{\lambda_{corr}(t')} dt' = \int_{\mathbf{r}_0}^{\mathbf{r}} \frac{Z(s)}{\lambda_{corr}(s)u(s)} ds. \quad (5.13)$$

This quantity measures the state of dynamical evolution of turbulence in the expanding solar wind [Matthaeus et al., 1998]. Meridional planes comparing this quantity with the

collisional age A_c are shown in Figures 5.B.1 and 5.B.2 for an untilted dipole simulation. The initial point for integration is taken at $45 R_\odot$, and therefore the collisional age is underestimated in these preliminary figures.

The influence of variation in turbulence level at the inner boundary is shown in Figure 5.B.1, which indicates that the turbulence ages faster with increased fluctuation energy at the inner boundary, while the collisional age decreases (possibly due to increased heating and acceleration of the wind). Figure 5.B.2 shows that the turbulence is most aged at low latitudes where strong shearing interactions between slow and fast streams can provide a source of driving [Roberts et al., 1992; Breech et al., 2008; Usmanov et al., 2014]. A detailed study of turbulence age in the solar wind, with comparisons of different models, is a topic for future work.

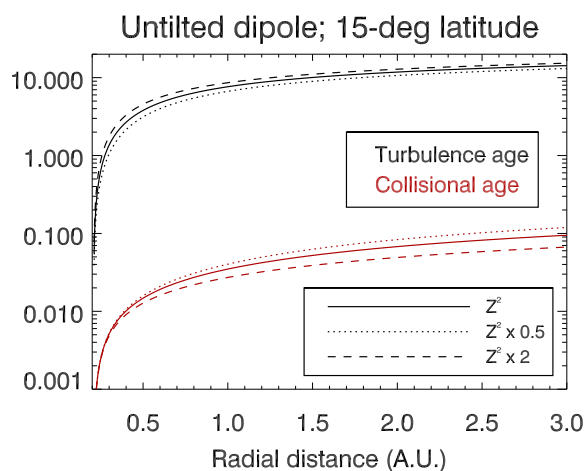


Figure 5.B.1: Radial evolution of turbulence (black curves) and collisional (red curves) ages at 15° heliolatitude, computed from an untilted dipole simulation. The initial point of integration is taken at $45 R_\odot$; The dashed (dotted) curves represent solutions with turbulence levels doubled (halved) relative to a reference value (solid curve).

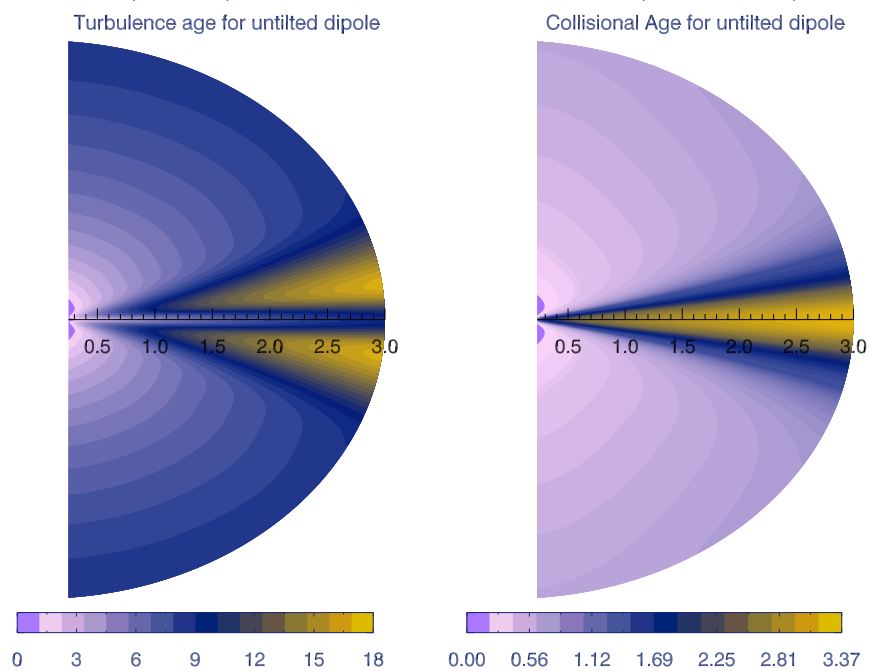


Figure 5.B.2: Meridional plane variation computed using the same parameters as in Figure 5.B.1.

Chapter 6

COSMIC RAY DIFFUSION COEFFICIENTS THROUGHOUT THE INNER HELIOSPHERE

6.1 Introduction

The interaction of energetic particles with the solar wind is a topic of wide interest in space physics and astrophysics. Several varieties of charged particles populate the heliosphere, including energetic particles originating at the Sun (solar energetic particles, or SEPs) and galactic cosmic rays (GCRs) that enter the heliosphere uniformly and nearly isotropically from the outside [Kunow et al., 1991]. These cosmic rays (CRs) are strongly guided and scattered by the solar wind and the turbulent fluctuations that transport with it [Parker, 1956, 1964; Jokipii, 1966]. As such, the study of the origin and transport of cosmic rays is an important problem in heliospheric physics, with implications ranging from space weather and exploration to fundamental space plasma physics [Jokipii, 1971; Fisk, 1979; Kunow et al., 1991]. The effects of these energetic particles on the health of astronauts [Parker, 2005] and the well-being of electronic components in spacecraft [Tylka et al., 1997] are an immediate concern. In addition, the accuracy with which we can understand CR propagation also provides a testbed for energetic particle transport in numerous space and astrophysical applications [Kulsrud and Pearce, 1969; Dröge, 2003]. The solar wind provides us with an opportunity to observe, at close range, the behavior of energetic particles in random, turbulent magnetic fields [Bruno and Carbone, 2013]. Such fields are ubiquitous in astrophysical systems [Candia and Roulet, 2004], and the insights we glean from studies of CRs in the heliosphere can potentially find application elsewhere in the universe [e.g., Subedi et al., 2017]. Finally, observations of cosmic rays can also serve as probes

into solar activity and solar wind structure, as CR variations are seen to be correlated with solar and geomagnetic activity [Snyder et al., 1963].

Theories of the modulation of cosmic rays in the heliosphere attempt to explain the observed temporal and spatial variation in their spectra [Fisk, 1979; Potgieter, 2013], and for that purpose, require a knowledge of the cosmic ray diffusion tensor. In fact, one of the key challenges in solving the Parker CR transport equation [Parker, 1965a] is the inadequate knowledge of the spatial, temporal, and rigidity dependence of the components of the diffusion tensor. In turn, the specification of this tensor through the heliosphere requires an understanding of two topics. First, a theoretical understanding of the diffusion process itself is needed, which would lead to predictions of the structure of the diffusion tensor itself. Equally important is the knowledge of the large scale flows and electromagnetic fields in the plasma, and the distribution of background solar wind turbulence in which the particles are scattered. The present approach permits three dimensional, and (in principle) time-varying calculation of all three of these properties (diffusion tensor, large-scale flow, large-scale electromagnetic field) to be computed in a single model.

The formal structure of the diffusion tensor involves diagonal components corresponding to diffusion parallel and perpendicular to the interplanetary magnetic field (IMF), as well as off-diagonal components describing perpendicular drifts [e.g., Moraal, 1976; Minnie et al., 2007]. While quasi-linear theory [Jokipii, 1966] extended to include time-dependent and non-linear corrections [Goldstein, 1976; Bieber et al., 1994; Dröge, 2003] provides a relatively good accounting of parallel diffusion, theories of perpendicular diffusion have faced the challenge of accounting for non-linear effects such as transfer of particles across field lines, backscatter from parallel diffusion, and field-line random walk [Jokipii, 1966; Giacalone and Jokipii, 1999]. The non-linear guiding center (NLGC) theory [Matthaeus et al., 2003] accounts for the above,¹ and is further

¹ See also Shalchi [2009].

improved by the random ballistic interpretation of [Ruffolo et al. \[2012a\]](#). In the current work we focus on the parallel and perpendicular and diffusion coefficients; the drift motion could be a topic for future work.

Since turbulent fluctuations are responsible for scattering CRs, the diffusion theories mentioned above typically involve turbulence parameters such as the energy of the random magnetic fluctuations and correlation scales. Our strategy for evaluating the CR diffusion coefficients through the inner heliosphere consists of two steps: first, specification of the relevant turbulence parameters based on a global solar wind model, and second, evaluation of the CR diffusion coefficients using the specified heliographic distribution of turbulence. For the first step, we deduce turbulence parameters from the model described in Chapter 4. Once these are specified through the model heliosphere, for the second step of our calculation, we use, as a starting point, fairly standard, well-tested formalisms for parallel and perpendicular diffusion coefficients – quasi-linear theory [[Jokipii, 1966](#); [Bieber et al., 1995](#); [Zank et al., 1998](#)] to compute the parallel component of the diffusion tensor, and the random ballistic decorrelation [RBD; [Ruffolo et al., 2012a](#)] interpretation of NLGC theory for perpendicular diffusion.

Previous studies of the heliographic dependence of the CR diffusion coefficients include work based on both WKB models for Alfvén waves [[Völk et al., 1974](#); [Morfill and Voelk, 1979](#)], and models for strong turbulence [[Bieber et al., 1995](#); [Zank et al., 1998](#); [Pei et al., 2010](#)]. The present work builds on these studies, but also makes some significant departures, motivated and enabled by recent advances in diffusion theory and sophistication of solar wind simulations. The major points of departure from previous work are listed below:

1. We use a fully 3D global simulation of the solar wind that provides us with a reliable and self-consistent model heliosphere. Previous work has used one-dimensional (1D) radial evolution models with spherical symmetry, with shear-driving effects included through a model [[Zank et al., 1998](#); [Pei et al., 2010](#)]. Thus, while examining latitudinal dependence of the diffusion tensor, these studies implicitly assume that they

are far from regions with significant latitudinal gradients. In contrast, three dimensionality improves the physical authenticity of the simulation by explicitly including shear-driving effects on the flow across latitudes, and leads to improved data-visualization through two-dimensional (2D) contour plots. A similar 3D approach has been recently used in [Guo and Florinski \[2016\]](#) to study the propagation of GCRs from 0.3 AU to the termination shock.

2. The computation of the CR diffusion tensor requires specification of the background solar wind speed, and the underlying large-scale heliospheric magnetic field. Previous work [[Bieber et al., 1995](#); [Zank et al., 1998](#); [Pei et al., 2010](#)] used a radially constant solar wind speed with some latitudinal variation, and a Parker-spiral type magnetic field model. However, the use of a prescribed model for the background fields has been found inadequate [[Reinecke et al., 1997](#)], and instead we use the large-scale, resolved flow from our MHD-RANS simulation. This provides a complete specification of the background large-scale fields, with spatial variation that has been found to agree well with observations [[Usmanov et al., 2014](#)].

3. We examine the diffusion coefficients at radial distances between $2 R_{\odot}$ and 3 AU, where R_{\odot} denotes a solar radius. We are not aware of any other similar study that has probed regions this close to the sun, which are of prime interest for SEP propagation, space weather, and for upcoming spacecraft missions, including *Parker Solar Probe (PSP)*.

4. A magnetic dipole with its tilt (relative to the solar rotation axis) varying through the solar activity cycle is a first and rough approximation for the solar magnetic field [[Babcock, 1961](#)]. We examine the effect of changing the tilt of the source solar dipole by using simulations with a dipole untilted with respect to the solar rotation axis, and a dipole with 30° tilt, in contrast to previous work employing axisymmetric solar wind parameters [[Zank et al., 1998](#); [Pei et al., 2010](#)]. The tilt of the solar dipole and the warping of the heliospheric current sheet [[Smith, 2001](#)] indicate high levels of solar activity [[Heber and Potgieter, 2006](#)], which is a factor of interest since CR intensity is anticorrelated to solar activity levels [[Forbush, 1954](#); [Fisk, 1979](#)]. We note

here that previous work that examined the effect of solar activity on CR-intensity variation [Jokipii and Kota, 1995] did not include turbulence modeling, and here we examine how varying turbulence levels influence the diffusion coefficients.

5. The perpendicular diffusion coefficient has been previously evaluated using the so-called “BAM” model [Bieber and Matthaeus, 1997] by Zank et al. [1998], and the NLGC theory by Pei et al. [2010] and Zank et al. [2004]. Recently, the NLGC theory has been reinterpreted by Ruffolo et al. [2012a], and their RBD theory yields a significantly improved agreement with numerical experiments for magnetic fluctuation amplitudes comparable to the large-scale magnetic field. This makes it very well suited for application to the solar wind, where the IMF includes a strong fluctuating component [Belcher et al., 1969; Marsch, 1991], and we use the RBD theory to derive a new expression for the perpendicular diffusion coefficient.

6. With the above improvements, the present approach departs significantly from both SEP studies [e.g., Zhang et al., 2009] and GCR modulation studies [e.g., Engelbrecht and Burger, 2013] that have used relatively simplified assumptions in one or more of the above categories, such as semiempirical diffusion coefficients and simple scalings with magnetic field magnitude.

The outline of this chapter is as follows: we describe the form of the CR diffusion tensor in Section 6.2, and briefly discuss the turbulence model and the simulation in Section 6.3. Section 6.4 presents the heliographic distribution of the diffusion coefficients. In Appendix 6.A we briefly describe how other types of diffusion coefficients might be estimated using similar approaches.²

6.2 Cosmic Ray Diffusion Tensor

The CR diffusion tensor, κ_{ij} , describes the scattering of CRs by random fluctuations in the IMF. It may be expressed as [Parker, 1965a; Jokipii and Parker, 1970]

² The contents of this chapter were published in Chhiber et al. [2017a].

$$\kappa_{ij} = \kappa_{\perp} \delta_{ij} + \frac{B_i B_j}{B^2} (\kappa_{\parallel} - \kappa_{\perp}) + \epsilon_{ijk} \kappa_A \frac{B_k}{B}, \quad (6.1)$$

where \mathbf{B} is the mean IMF, δ_{ij} is the Kronecker delta, and ϵ_{ijk} is the Levi-Civita symbol. This work presents calculations of κ_{\parallel} and κ_{\perp} , which are the diagonal components of the diffusion tensor parallel and perpendicular, respectively, to the mean IMF.

The present work does not calculate κ_A , which can describe particle drifts under the influence of large-scale gradients and curvature in the IMF. Our results are directly relevant to the outward propagation of SEPs, for which κ_{\parallel} and κ_{\perp} are needed to describe how the SEP distribution spreads in the parallel and perpendicular directions, whereas over the short time scale of the SEP outflow the drifts may mainly shift the lateral distribution over a small angle. The lateral distribution of particle injection is often unknown, and the effects of drifts are often neglected, though [Marsh et al. \[2013\]](#) argue that they should be considered. Both diffusion and drifts are considered to be important to the modulation of GCR with the solar cycle and the small gradients in GCR density [[Moraal, 1976](#); [Jokipii and Thomas, 1981](#)], though these processes take place over a wider region than considered in the present work ($r \leq 3$ AU).

We shall also examine the radial diffusion coefficient

$$\kappa_{rr} \equiv \kappa_{\parallel} \cos^2 \Psi + \kappa_{\perp} \sin^2 \Psi, \quad (6.2)$$

which is of particular relevance to models of solar modulation of CRs. Here, Ψ is the “winding” angle between the IMF and the radial direction. Following previous work, we define mean free paths, $\lambda_{\parallel, \perp}$, that are equivalent to the diffusion tensor through

$$\lambda_{\parallel, \perp} \equiv 3\kappa_{\parallel, \perp}/v, \quad (6.3)$$

where v is the particle speed.

We note that in the present work we use the large-scale flow from our simulation to specify B and Ψ as spatially varying fields through the 3D heliosphere. This is in

contrast to previous studies [Bieber et al., 1995; Zank et al., 1998; Pei et al., 2010], where B and Ψ were specified through a Parker-type model and a radially constant solar wind speed (to compute Ψ). However, the features of the IMF have a major influence on CR transport, and a Parker-type field is an oversimplification, particularly at high heliolatitudes.³ Moreover, the use of a-priori prescribed background fields in modulation studies has been held responsible for restricting the diffusion tensor to values that preclude agreement of models with observations [Reinecke et al., 1997], and the present work makes a significant improvement in this regard.

6.2.1 Parallel Mean Free Path

In determining the parallel mean free path (mfp), the turbulence “geometry”, i.e., the distribution of energy over parallel and perpendicular wavevectors (Section 3.3.1), is a controlling factor. Observations [Bieber et al., 1994] show that a pure “slab” model of heliospheric turbulence [Jokipii, 1966] underestimates the parallel mfp. In the slab model, the magnetic fluctuations are polarized perpendicular to the mean field and their wave-vectors are parallel to the mean field. Bieber et al. [1994] find that a composite model with a dominant 2D part (fluctuations and their wave-vectors both perpendicular to the mean field) and a minor slab part provides a better approximate parametrization of the turbulence and an improved description of the observed mean free paths. Furthermore, theoretical studies and observations [Matthaeus et al., 1990; Zank and Matthaeus, 1992, 1993; Bieber et al., 1996; Ghosh and Goldstein, 1997] suggest that around 80% of magnetic fluctuation energy in the inertial range should reside in the 2D component, with the rest in the slab component.

In the following, we take the z -component along the mean field. Considering parallel diffusion first, we note that in quasilinear theory the 2D fluctuations are effectively invisible to CRs resonating with the turbulence as they move along the magnetic

³ See Heber and Potgieter [2006] for an overview of suggested modifications to the Parker field.

field, and the scattering by slab fluctuations (assumed to be axisymmetric) is described by the parallel mfp [Zank et al., 1998]

$$\lambda_{\parallel} = 6.2742 \frac{B^{5/3}}{\langle b_s^2 \rangle} \left(\frac{P}{c} \right)^{1/3} \lambda_s^{2/3} \times \left[1 + \frac{7A/9}{(1/3 + q)(q + 7/3)} \right], \quad (6.4)$$

where

$$A = (1 + s^2)^{5/6} - 1, \quad (6.5)$$

$$q = \frac{5s^2/3}{1 + s^2 - (1 + s^2)^{1/6}}, \quad (6.6)$$

$$s = 0.746834 \frac{R_L}{\lambda_s}, \quad (6.7)$$

and a model 1D Kolmogorov spectrum is assumed, with a power spectrum of the form $\tilde{P}(k_{\parallel}) \propto (1 + k_{\parallel} \lambda_s)^{-5/6}$. Here c is the speed of light, $R_L = P/Bc$ the particle Larmor radius, $\langle b_s^2 \rangle$ the variance of the slab geometry fluctuation, $P \equiv \tilde{p}c/Ze$ the particle rigidity (\tilde{p} and Ze are the particle momentum and charge, respectively), k_{\parallel} is the wave vector parallel to the mean field, and λ_s the correlation length for slab turbulence. Equation (6.4) is valid at rigidities ranging from from 10 MV to 10 GV [Zank et al., 1998]. At larger heliocentric distances, the fractional term in braces becomes significant due to high-rigidity particles resonating with fluctuations in the energy containing range instead of the inertial range. This is discussed further below in the context of rigidity dependence of the mfps (Section 6.4.4).

6.2.2 Perpendicular Mean Free Path

Perpendicular diffusion is often not considered as important as parallel diffusion in energetic particle studies, because it is usually inferred that $\lambda_{\perp} \ll \lambda_{\parallel}$ [Palmer, 1982]. However, Dwyer et al. [1997] found that for strong particle enhancements related to

corotating interaction regions, $\lambda_{\perp}/\lambda_{\parallel}$ rose to ~ 1 in the fast solar wind stream arriving after the stream interface. Using data from the *Ulysses* spacecraft during the SEP event of 2000 Jul 14, [Zhang et al. \[2003\]](#) inferred $\lambda_{\perp}/\lambda_{\parallel} \approx 0.25$. Our 3D model inner heliosphere provides an opportunity to examine the domains where perpendicular diffusion can be comparable with parallel diffusion.

Quasi-linear theory [[Jokipii, 1966](#)] provides a physically appealing description of perpendicular diffusion in terms of the diffusive spread of magnetic field lines, with the gyrocenters of charged particles following the field lines. Other approaches have considered the relationship between κ_{\perp} and κ_{\parallel} [[Axford, 1965](#); [Gleeson, 1969](#)], and applied the Taylor–Green–Kubo formulation [[Bieber and Matthaeus, 1997](#), “BAM”] to the problem. However, the field-line-random-walk (FLRW) approach [[Jokipii, 1966](#)] overestimates the strength of the diffusion, while BAM predicts diffusion that is weaker than that observed in numerical experiments [[Giacalone and Jokipii, 1999](#); [Mace et al., 2000](#)]. The NLGC theory [[Matthaeus et al., 2003](#)] accounts for both the random walk of the field lines and the influence of parallel scattering, and shows good agreement with both observations [[Bieber et al., 2004](#)] and simulations, with the NLGC results bracketed by the FLRW and BAM results [[Matthaeus et al., 2003](#)].

Recent work [[Ruffolo et al., 2012a](#)] has reinterpreted NLGC by replacing the diffusion of gyrocenter trajectories with a random ballistic decorrelation (RBD), where the guiding-center motion is approximated as ballistic (i.e., with constant velocity) between scattering events. The RBD-modified theory agrees with numerical simulations over a wider range of fluctuation amplitudes than the original NLGC, specifically for fluctuations comparable in size to the large-scale field. This makes it particularly suited for application to the solar wind [[Belcher et al., 1969](#); [Marsch, 1991](#)]. Other improvements to NLGC have also been developed [see, e.g., [Shalchi, 2009](#)].

The phenomenon of “backtracking” due to parallel scattering causes a particle to reverse its motion along the field line, thus retracing its steps over a certain time-span. This leads to a negative v_x -correlation (v_x is a component of the particle’s velocity perpendicular to the mean field), which results in a reduction in the running

perpendicular diffusion coefficient [see, e.g., [Shalchi, 2009](#)]. With this backtracking correction, RBD yields the following perpendicular diffusion coefficient [see [Ruffolo et al., 2012a](#)]:

$$\kappa_{\perp} = \frac{a^2 v^2}{6B^2} \sqrt{\frac{\pi}{2}} \int_0^{\infty} \frac{S_2(k_{\perp}) \text{Erfc}(\alpha) 2\pi k_{\perp} dk_{\perp}}{k_{\perp} \sqrt{\langle \tilde{v}_x^2 \rangle}}, \quad (6.8)$$

where $a^2 = 1/3$, v is the particle speed, \tilde{v}_x is the x -component of the guiding-center velocity, S_2 is the 2D axisymmetric turbulent fluctuation spectrum, Erfc is the complementary error function, and k_{\perp} is the component of the wave-vector perpendicular to the mean magnetic field. We also have

$$\alpha = \frac{v^2}{3\kappa_{\parallel} k_{\perp} \sqrt{2\langle \tilde{v}_x^2 \rangle}}, \quad (6.9)$$

and

$$\langle \tilde{v}_x^2 \rangle = \frac{a^2 v^2 b^2}{6B^2}, \quad (6.10)$$

where b^2 is the combined variance of the 2D and slab magnetic fluctuations: $b^2 = \langle b_2^2 \rangle + \langle b_s^2 \rangle$. Note that in Equation (6.8), the slab turbulence spectrum does not appear. This is because we follow the suggestion by [Shalchi \[2006\]](#) that the direct contribution of the slab component to perpendicular transport is subdiffusive, and therefore the slab term should not contribute to Equation (6.8). This hypothesis has been supported by simulations [[Ruffolo et al., 2012a,b](#)], and accordingly, has been adopted in the present work as well. Slab fluctuations can, however, still influence κ_{\perp} through κ_{\parallel} , which appears in Equation (6.9) for α , and $\langle \tilde{v}_x^2 \rangle$.

The 2D power spectrum may be expressed as a power law [[Matthaeus et al., 2007](#)]

$$S_2(k_{\perp} \leq 1/\lambda_2) = C_2 \langle b_2^2 \rangle \lambda_2^2 (\lambda_2 k_{\perp})^p, \quad (6.11)$$

$$S_2(k_{\perp} > 1/\lambda_2) = C_2 \langle b_2^2 \rangle \lambda_2^2 (\lambda_2 k_{\perp})^{-\nu-1}, \quad (6.12)$$

where λ_2 is the 2D correlation scale, C_2 is a normalization constant, $\langle b_2^2 \rangle$ is the variance

of the 2D turbulent fluctuations, and p is a power index that takes on integral values that correspond to different power spectra. We assume a Kolmogorov spectrum in the inertial range by taking $\nu = 5/3$. From the requirement that $\langle b_2^2 \rangle = 2\pi \int_0^\infty S_2(k)k dk$, we get

$$C_2 = \frac{(\nu - 1)(p + 2)}{2\pi(p + \nu + 1)}. \quad (6.13)$$

Note that the inertial range ($k_\perp > 1/\lambda_2$) behavior is described by a conventional power law, and p only determines the long-wavelength properties of the spectrum. The spectral behavior of interplanetary magnetic fluctuations at long wavelengths is not well determined from single point measurements [Matthaeus et al., 2016b], and there are ambiguities surrounding the question of whether the observed structures are spatial or temporal in origin. The observations of “ $1/f$ ” noise at low frequencies also complicate matters [Matthaeus and Goldstein, 1986]. All values of $p \geq -1$ yield power spectra that give rise to a finite energy, but these spectra may be differentiated based on the characteristic length scales associated with them. In addition to the standard correlation scale [Batchelor, 1953], there is a distinct scale, called the ultrascale, which is of importance in applications of 2D turbulence [Matthaeus et al., 2007, and references therein]. The ultrascale is so named because it is generally larger than the correlation scale, and it may be interpreted as a typical size of an “island” of 2D turbulence [Matthaeus et al., 1999a] and as the perpendicular coherence length of the FLRW [Ruffolo et al., 2004].

We consider the following cases [Matthaeus et al., 2007]: $p = -1$ (infinite correlation scale and an infinite ultrascale), $p = 0$ (finite correlation scale but an infinite ultrascale), and $p \geq 1$ (finite ultrascale and finite correlation scale). The case $p = 2$ is of special interest since it corresponds to homogeneous turbulence. Each of the above possibilities is realizable as each yields a finite energy. However, unlike the correlation scale, the values taken by the ultrascale in space and astrophysical plasmas are not well known, and there is a paucity of established methods to measure it [for a proposed

technique see [Matthaeus et al., 2007](#)]. Therefore, it is of interest to examine the dependence of the diffusion coefficients on p . If there is a marked differentiation between the mfps computed for different cases, then observations of the mfps may be used to infer constraints on the ultrascales prevailing in the heliospheric plasma.

To finally obtain an expression for the perpendicular mean free path, we use Equations (6.11) and (6.12) in Equation (6.8) and set $\nu = 5/3$ to get

$$\begin{aligned}
\lambda_{\perp} = \mathcal{F}_1 \left\{ \frac{\lambda_2^{-2/3}}{5\mathcal{F}_2^{5/3}\sqrt{\pi}} \left[3\sqrt{\pi}\mathcal{F}_2^{5/3}\lambda_2^{5/3}\text{Erfc}(\mathcal{F}_2\lambda_2) \right. \right. \\
+ \Gamma\left(\frac{1}{3}\right) - 3\Gamma\left(\frac{4}{3}, \mathcal{F}_2^2\lambda_2^2\right) \left. \right] \\
+ \delta_{p,-1}\lambda_2 \left[\mathcal{F}_2\lambda_2 \frac{2}{\sqrt{\pi}} {}_2F_2\left(\frac{1}{2}, \frac{1}{2}; \frac{3}{2}, \frac{3}{2}; -\mathcal{F}_2^2\lambda_2^2\right) \right. \\
- 0.981755 - \log(\mathcal{F}_2\lambda_2) \left. \right] \\
+ (1 - \delta_{p,-1})\frac{\lambda_2}{p+1} \left[\text{Erfc}(\mathcal{F}_2\lambda_2) \right. \\
\left. \left. - \frac{\mathcal{F}_2\lambda_2}{\sqrt{\pi}} E_{\frac{p}{2}+1}(\mathcal{F}_2^2\lambda_2^2) \right] \right\}, \tag{6.14}
\end{aligned}$$

where

$$\mathcal{F}_1 = \sqrt{\pi^3}C_2 \frac{v\langle b_2^2 \rangle a^2}{B^2\sqrt{2\langle \tilde{v}_x^2 \rangle}}, \tag{6.15}$$

and

$$\mathcal{F}_2 = \frac{v}{\lambda_{\parallel}\sqrt{2\langle \tilde{v}_x^2 \rangle}}. \tag{6.16}$$

In Equation (6.14), Erf is the error function, Γ is the gamma function, ${}_2F_2$ is a hypergeometric function, $E_{\frac{p}{2}+1}$ is the generalized exponential integral function, and the Kronecker delta function is used as a switch between the four values of p . C_2 depends on the value of p , as can be seen from Equation (6.13). Note that in the corresponding NLGC result [\[Pei et al., 2010\]](#), an implicit method is required to obtain λ_{\perp} , in contrast to the RBD result, which is an explicit solution for λ_{\perp} .

6.3 Solar Wind Model

Equations (6.4) and (6.14) require specification of the large-scale IMF, and the magnetic fluctuation energies and correlation lengths for both slab and 2D turbulence. For this purpose, we use the solar wind model described in Chapter 4, with the region from the coronal base to $45 R_{\odot}$ modeled using the WKB Alfvén wave approach described in Appendix C. In our calculations, we have used the following input parameters at the coronal base: the driving amplitude of Alfvén waves is set to 35 km s^{-1} , the initial density is $0.4 \times 10^8 \text{ cm}^{-3}$, and the initial plasma temperature is $1.8 \times 10^6 \text{ K}$. The magnetic field magnitude is assigned as the field strength of the source magnetic dipole on the poles. This parameter is set to 16 G to match the magnitude of the heliospheric magnetic field observed by Ulysses.

For our purposes here, we extract from the outer region simulation ($45 R_{\odot} - 3 \text{ AU}$) the mean magnetic field, \mathbf{B} , the fluctuation energy, Z^2 (defined below), and the correlation length for the turbulence, λ . Here,

$$Z^2 = \langle v'^2 + b'^2 \rangle, \quad (6.17)$$

is twice the turbulent energy per unit mass, defined in terms of the velocity and magnetic field fluctuations, \mathbf{v}' and \mathbf{B}' , respectively. The amplitude of magnetic fluctuations has been normalized to Alfvén units using $\mathbf{b}' = \mathbf{B}'(4\pi\rho)^{-1/2}$, where ρ is the mass density. To extend our calculation closer to the sun, we use data from the inner ($1 - 20 R_{\odot}$) and intermediate ($20 - 45 R_{\odot}$) regions, where the simulation does not have a turbulence model for Z^2 and λ (Appendix C). Here we use the the WKB Alfvén wave energy density \mathcal{E} as a proxy for the turbulent fluctuation energy, via $Z^2 = 2\mathcal{E}/\rho$. To get an approximation for the correlation scale in these regions, we use the hypothesis from [Hollweg \[1986\]](#) that the correlation length varies as the distance between magnetic field lines, which in turn depends on the field strength [[Spruit, 1981](#)], so that $\lambda \propto B^{-1/2}$. We set the constant of proportionality such that λ at the boundaries of the intermediate and outer regions matches.

To proceed with the calculation of the mfps, some assumptions must be made in order to relate the correlation scale of our turbulence model (λ) to the slab and 2D correlation scales in Equations (6.4) and (6.14), respectively. First, we note that the turbulent fluctuations in our model are primarily transverse to the mean magnetic field (see Section 4.4), and thus identify the correlation scale of 2D turbulence to be equal to the correlation scale of our turbulence model, so that $\lambda_2 = \lambda$. Observational studies [Osman and Horbury, 2007; Weygand et al., 2009, 2011] indicate that the slab correlation scale is about a factor of two larger than the 2D correlation scale, and accordingly, we assume $\lambda_s = 2\lambda_2$. In our approximate treatment, we assume in effect that the magnetic and velocity correlation functions are structurally similar [Zank et al., 1996], so that the magnetic correlation length is found to be equal to the single correlation scale that we follow dynamically. In the inner heliosphere where the cross helicity is large, it becomes advantageous to employ a two correlation length theory [Matthaeus et al., 1994a; Wan et al., 2012b; Zank et al., 2012, 2017], as has been implemented by, e.g., Adhikari et al. [2017], Zhao et al. [2017], and Zhao et al. [2018].

To approximate the energy in slab and 2D magnetic fluctuations, we first convert Z^2 to B'^2 using Equation (6.17):

$$\langle B'^2 \rangle = \frac{Z^2}{r_A + 1} 4\pi\rho, \quad (6.18)$$

where $r_A = \langle v'^2 \rangle / \langle b'^2 \rangle$ is the Alfvén ratio. An accurate dynamical model for r_A is desirable, but must include complications such as non-local effects [e.g., Grappin et al., 1983; Matthaeus et al., 1994a; Hossain et al., 1995]. At present we maintain a simpler approach, and take r_A to have a value of 1 in the inner and intermediate regions ($1-45 R_\odot$), and a value of 1/2 for heliocentric distances larger than $45 R_\odot$. These values are motivated by spacecraft observations [Tu and Marsch, 1995], but we recognize that attempts have been made to treat r_A dynamically [Grappin et al., 1983; Marsch and Tu, 1989; Tu and Marsch, 1990; Matthaeus et al., 1994a; Yokoi and Hamba, 2007; Zank et al., 2012]. See especially the comparison with observations by Adhikari et al. [2015]

and [Zank et al. \[2017\]](#).

Next, recalling the assumption that the magnetic fluctuations have a dominant 2D component with a small slab contribution, and following observations [[Matthaeus et al., 1990](#); [Bieber et al., 1994](#)] that find the ratio of the 2D and slab energies to be 80% to 20%, we use

$$\frac{\langle b_s^2 \rangle}{\langle b_2^2 \rangle} = \frac{20}{80} = 0.25 \quad (6.19)$$

to compute the slab and 2D fluctuation energies from Equation (6.18) and $\langle b_2^2 \rangle + \langle b_s^2 \rangle = \langle B'^2 \rangle$. In recent work by [Hunana and Zank \[2010\]](#) and [Zank et al. \[2017\]](#), refinements to this simplified perspective on the breakdown of the slab and 2D fluctuation energies are discussed. In particular, [Zank et al. \[2017\]](#) solve separate equations for the slab and 2D energies with a simplified IMF and background solar wind flow. They find that the evolution of the two components is markedly different in the outer heliosphere (beyond ~ 3 AU), where driving by pickup ions leads to an increase in the slab component's energy, while the energy of the 2D component continues to decrease with heliocentric distance. Their results show, however, that the radial evolution of slab and 2D energies is not too dissimilar below 3 AU. Similar results are presented by [Oughton et al. \[2011\]](#) using their two-component model. Therefore, for the purposes of our present work, where we focus on the inner heliosphere, our simple decomposition of $\langle B'^2 \rangle$ into slab and 2D components, using the constant ratio expressed in Equation (6.19), seems appropriate. Studies of CR diffusion in the outer heliosphere undoubtedly benefit from using a two-component turbulence transport model [[Zhao et al., 2017, 2018](#)]. A detailed assessment of different transport equations for turbulence is beyond the scope of this work.

6.4 Simulation Results

6.4.1 Solar Wind Model Results

We begin our presentation of the results with a discussion of the core fields from the simulation – B , λ , and Z^2 – which are the ingredients that go into our calculation of

the diffusion coefficients. Figure 6.1 shows the radial evolution of the turbulence energy and the turbulence correlation scale from our model with an untilted dipole source. The data are for a 7° heliolatitude, which we take to be the broadly-defined ecliptic region. Also shown are observational results from *Voyager 2*, *Helios*, and the National Space Science Data Center (NSSDC) Omnitape dataset, indicating a reasonable agreement with the simulation results. The observational data for Z^2 and λ are from Zank et al. [1996] and Smith et al. [2001], respectively. Note that the observations are for various times in the solar cycle, and are shown here for general context only. The dashed vertical lines in Figure 6.1 represent the boundaries of the different simulation regions, with red marking the inner-intermediate region boundary at $20 R_\odot$, and blue marking the intermediate-outer region boundary at $45 R_\odot$, respectively. Note that we present results for $r > 2 R_\odot$ (r is the radial distance measured from the solar center), even though the inner boundary of the inner region simulation is at $1 R_\odot$. The parallel mfp acquires extremely large values (> 10 AU) in the region very close to the solar surface, due to the large values of B prevailing there. These large values of λ_{\parallel} are not of physical relevance and present problems for visualization, and we therefore restrict our results to $r > 2 R_\odot$.

Figure 6.2 shows the distribution in the meridional plane of the three ingredients – B , Z^2 , and λ – for a simulation with an untilted source dipole. The figures on the left are from the inner and intermediate regions ($2 - 45 R_\odot$), and the ones on the right are from the outer region ($0.21 - 3$ AU). For a detailed discussion of these simulation results, we refer the reader to Usmanov et al. [2000] and Usmanov et al. [2014]. We note here that the magnetic field results agree well with Ulysses observations [see Figure 8 of Usmanov et al., 2014], with the field vanishing at the heliospheric current sheet (HCS) at 0° heliolatitude. The turbulence correlation scale increases with heliocentric distance, as is well known from observations [Tu and Marsch, 1995]. The turbulence energy increases on moving from the ecliptic plane towards higher heliolatitudes because of shear interactions between slow (low latitude) and fast (high latitude) wind [See, e.g., Breech et al., 2008]. In the following subsections, we will

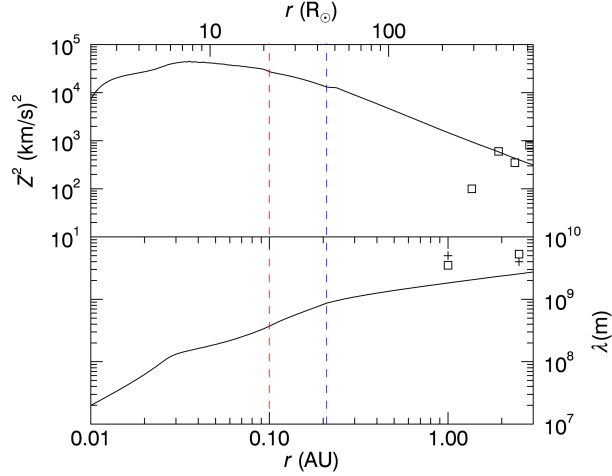


Figure 6.1: Model results near the ecliptic plane, for a run with an untilted solar dipole, are compared with observational data from *Voyager 2*, *Helios*, and the NSSDC Omnitape. The Z^2 data are from Zank et al. [1996], and the λ data are from Smith et al. [2001]. The solid lines are from our simulations. The different symbols represent different methods of calculation. The dashed vertical lines represent the boundaries of the different simulation regions, with red marking the inner-intermediate region boundary at $20 R_{\odot}$, and blue marking the intermediate-outer region boundary at $45 R_{\odot}$, respectively. Note that the observations are for various times in the solar cycle, and are shown here for general context only.

discuss how these distributions influence the behaviour of the diffusion length-scales.

6.4.2 Radial Evolution of Mean Free Paths

In Figure 6.3 we show the radial evolution of the parallel, perpendicular, and radial mfps (black, red, and blue lines, respectively) in the ecliptic region (Figure 6.3(a)) and near the solar rotation axis 86° heliolatitude, Figure 6.3(b), for an untilted source dipole. Also shown is the ratio of the perpendicular mfp to the parallel mfp (green lines). The solid, dotted, dashed, and dash-dotted lines correspond to $p = -1, 0, 1$, and 2 , respectively, and the mfps are computed for protons with rigidity equal to 445 MV, corresponding to a kinetic energy of 100 MeV. Here we would like to remind the reader that our turbulence parameters (Z^2 and λ) in the region $1 - 45 R_{\odot}$ are not from the turbulence model, but are calculated using the approximations detailed in Section 6.3.

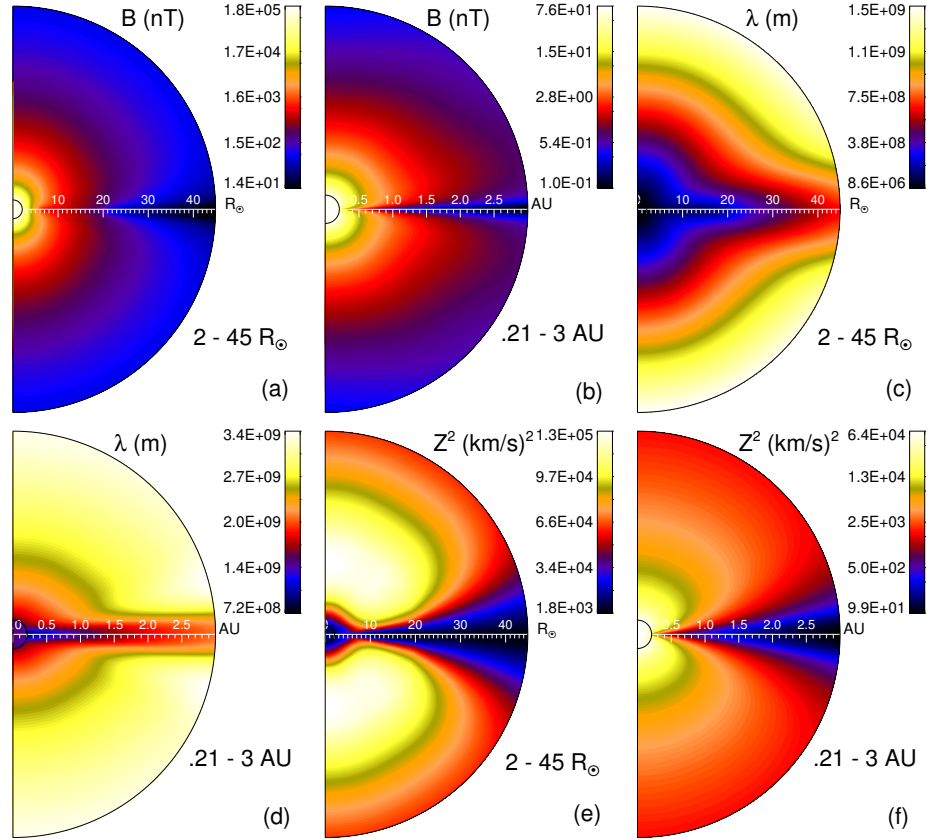


Figure 6.2: Contour plots of the heliospheric magnetic field (B), the turbulence correlation scale (λ), and the turbulence energy (Z^2) in the meridional plane for an untilted solar dipole. The figures on the left cover $2 - 45 R_{\odot}$, and the ones on the right cover $0.21 - 3$ AU ($45 - 645 R_{\odot}$).

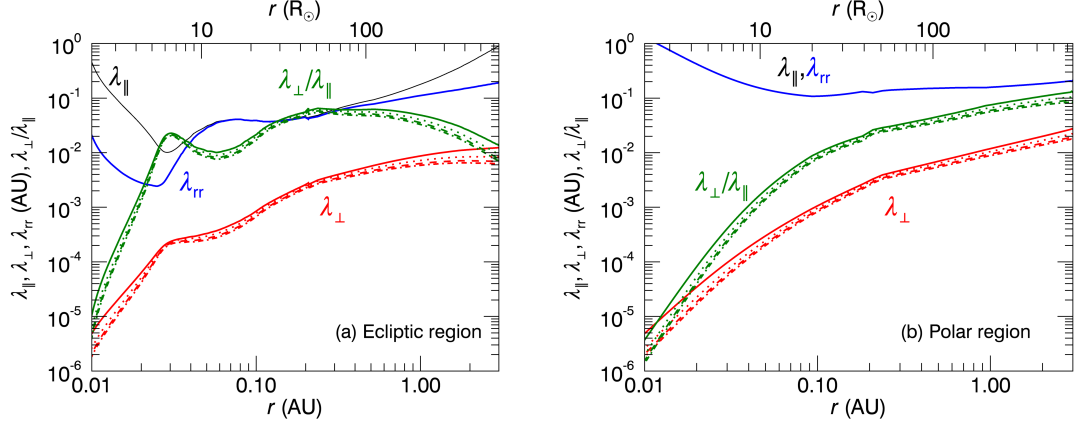


Figure 6.3: Radial dependence of the parallel (black), perpendicular (red), and radial (blue) mfps (a) near the ecliptic plane (7° heliolatitude) and (b) near the pole (86° heliolatitude). Also shown is $\lambda_\perp/\lambda_\parallel$ (green). The solid lines are for $p = -1$, the dotted lines for $p = 0$, the dashed lines for $p = 1$, and the dash-dotted lines for $p = 2$. Proton rigidity is 445 MV (100 MeV kinetic energy). Note that the curves for λ_\parallel and λ_{rr} coincide in (b).

As such, these results represent a preliminary attempt at mapping the diffusion length scales in a region that will soon be investigated by upcoming spacecraft missions such as *PSP*. We plan a follow-up work where we use our new coronal turbulence model (Chapter 4) to compute the diffusion coefficients.

Near the ecliptic plane (Figure 6.3(a)), as one moves outward from the solar surface, the increasing strength of the turbulence energy (see Figure 6.1) leads to a sharp decrease in λ_\parallel in the region $2 - 5 R_\odot$, with the rapidly decreasing IMF reinforcing this behaviour. In this region, $\lambda_\parallel \propto r^{-3.46}$, and there is a corresponding increase in λ_\perp ($\propto r^{3.55}$ for $p = -1$ and $\propto r^{4.34}$ for $p = 2$). Since the IMF has a significant meridional component here, the large winding angle (Ψ) between the radial direction and the IMF leads to λ_\perp having an influence on the radial mfp (see Equation 6.2), with $\lambda_{rr} \propto r^{-1.97}$. From $0.03 - 3$ AU, λ_\parallel mostly increases as $r^{0.82}$, and λ_\perp as $r^{0.79}$. From 0.1 to 3 AU, Ψ is once again large because of the increased azimuthal component of the IMF, and λ_\perp reduces the radial mfp, with $\lambda_{rr} \propto r^{0.53}$. Observational studies for $r < 3$ AU have found $\lambda_{rr} \propto r^b$ with b ranging from $0.4 - 0.7$ [Beeck et al., 1987]. Note that

the radial mfp depends on the value of p (through λ_{\perp}), but the λ_{rr} curves for different p coincide.

Moving on to the radial evolution of the mfps in the polar region, Figure 6.3(b) shows that the radial mfp is completely dominated by λ_{\parallel} . This is because the IMF is near radial at the poles, with a very small winding angle. At the poles, $\lambda_{rr} \propto r^{-1.1}$ until 0.1 AU, after which it remains nearly constant, with identical behavior exhibited by λ_{\parallel} . From $2 R_{\odot} - 0.2$ AU, $\lambda_{\perp} \propto r^{2.10}$ for $p = -1$ and $\lambda_{\perp} \propto r^{2.34}$ for $p = 2$. From 0.2 – 3 AU, $\lambda_{\perp} \propto r^{0.78}$ for $p = -1$ and $\lambda_{\perp} \propto r^{0.69}$ for $p = 2$.

Figure 6.4 shows the effect of a source dipole with a 30° tilt when one encounters the heliospheric current sheet (HCS) at around 1 AU: λ_{\parallel} goes through a sudden dip of almost two orders of magnitude, while λ_{\perp} has a corresponding increase of around an order of magnitude. (the radius where the HCS crosses our chosen heliolatitude of 7° depends on our choice of the azimuthal angle for which we plot results as a function of radius.) The vanishing mean magnetic field and non-vanishing turbulence amplitude at the HCS explain this behaviour, which will be further illustrated in the next subsection discussing the 2D variation of the mfps in the meridional plane. We note from Figures 6.3 and 6.4 that the ratio $\lambda_{\perp}/\lambda_{\parallel}$ stays between 0.1 and 0.01 for most of the inner heliosphere, but it exceeds unity at the HCS. Keeping in mind that the current sheet is a singular region in our simulation, in its vicinity the fields do possess physically realizable values. Therefore we may stress the fact that similarly large values of $\lambda_{\perp}/\lambda_{\parallel}$ have been observed [Dwyer et al., 1997; Zhang et al., 2003]. We will come across these domains of significant perpendicular diffusion once again in the meridional plane contours in Section 6.4.5, below.

In the results presented so far the choice of the long wavelength spectral index p does not significantly alter the mfps, with λ_{\perp} for $p = -1$ generally not more than a factor of two larger than λ_{\perp} for $p = 2$. Referring to the discussion in Section 6.2.2, this result indicates a rather weak dependence of the mfps on the ultrascale (via different p values). The exception appears very close to the solar surface ($2 R_{\odot}$) in Figure 6.3, where the perpendicular mean free path for the $p = -1$ case is several times larger than

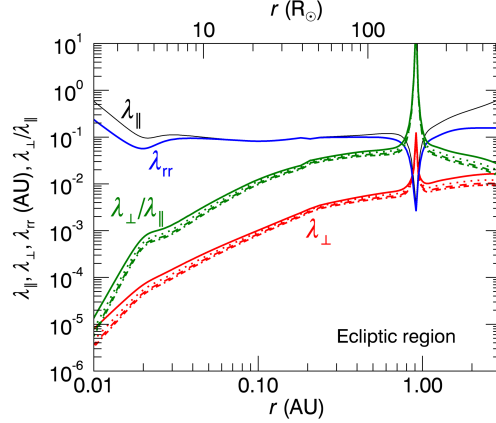


Figure 6.4: Radial dependence of the parallel (black), perpendicular (red), and radial (blue) mfps near the ecliptic plane (7° heliolatitude), with a solar dipole having a 30° tilt. For our particular choice of azimuthal angle (26°), an HCS crossing occurs at 0.8 AU. Also shown is $\lambda_\perp/\lambda_\parallel$ (green). The solid lines are for $p = -1$, the dotted lines for $p = 0$, the dashed lines for $p = 1$, and the dash-dotted lines for $p = 2$. Proton rigidity is 445 MV (100 MeV kinetic energy).

that for the $p = 2$ case. This behaviour may be probed further in simulations with improved coronal turbulence models that are more reliable at such small heliocentric distances. In the following results, unless specified otherwise, we will choose $p = 2$, which corresponds to homogeneous turbulence.

In Figure 6.5 we examine the effect of varying the turbulence energy amplitude at the inner boundary ($45 R_\odot$) of the outer region of the simulation, again for 100 MeV protons. Such variation may arise due to solar activity. The solid lines represent a standard Z^2 specified at the inner boundary, and dashed and dotted lines represent simulations performed with double and half of this standard value specified at the inner boundary, respectively. In the ecliptic region (7° heliolatitude), Figure 6.5(a) indicates, as expected, that an increasing turbulence level leads to a decrease in λ_\parallel (and consequently λ_{rr}). The stronger turbulence increases λ_\perp in proportion to Z , and therefore increases the extent to which particles may diffusively penetrate the heliosphere. Comparing Figures 6.5(a) and 6.5(b), it is interesting to note that in

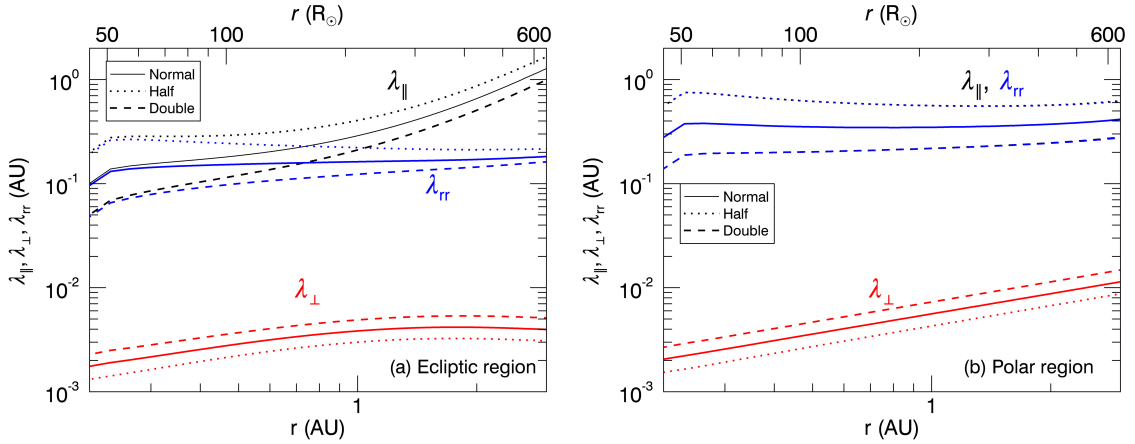


Figure 6.5: Radial dependence of the parallel (black), perpendicular (red), and radial (blue) mfps (a) near the ecliptic plane (7° heliolatitude) and (b) in the polar region (86°), for varying turbulence amplitudes, with $p = 2$. The dashed and dotted lines represent simulations with the turbulence energy (Z^2) at the inner boundary of the outer region ($45 R_\odot$) doubled and halved, respectively, relative to a standard level. See text for more details. Note that the curves for λ_{\parallel} and λ_{rr} coincide in (b).

the ecliptic region, varying turbulence at the inner boundary leads to an effect on λ_{\parallel} that becomes less pronounced with radial distance. This is not the case in the polar regions with fast wind, however, where the turbulence is less “aged” compared with low latitudes [Matthaeus et al., 1998].⁴ Stream interactions near the ecliptic plane reduce the turbulence at a faster rate compared to the rate in the polar regions far from such shearing interactions.

We end this subsection by comparing our solutions in the ecliptic plane with “consensus” constraints on observations [Palmer, 1982; Bieber et al., 1994]. Based on information compiled from several sources, the Palmer consensus finds that for particles in the rigidity range $0.5 - 5000$ MV, $\lambda_{\parallel} = 0.08 - 0.3$ AU. We note here that the values for the mfps obtained by fitting observational data may depend on the model used; Reames [1999] reviews some such results and suggests a higher parallel mfp of ~ 1 AU. Our λ_{\parallel} for a 100 MeV proton at 1 AU varies from $0.29 - 0.40$ AU, and fits the consensus

⁴ See Section 5.B.

Table 6.1: Parallel mfps in AU for 100 MeV protons at in the ecliptic region at 1 AU. B1, B2, and B3 are from [Breech et al. \[2008\]](#); P1 and P2 are from [Pei et al. \[2010\]](#); Cases 1 - 3 are our solutions for varying turbulence levels. Note that our calculation of λ_{\parallel} is independent of p .

p	B1	B2	B3	P1	P2	Case 1	Case 2	Case 3
-1	2.92	6.86	1.64	0.92	0.47			
0	2.33	5.49	1.31	0.74	0.38	0.29	0.21	0.40
1	2.14	5.03	1.20	0.68	0.35			
2	2.04	4.80	1.15	0.64	0.33			

range well. Our solutions are smaller than the values from [Breech et al. \[2008\]](#) and [Pei et al. \[2010\]](#), which we list in Table 6.1, along with our results. Here, cases 1, 2, and 3 refer to standard, doubled, and halved turbulence levels, as described above. Note that unlike our calculation of λ_{\parallel} , the calculations from [Breech et al. \[2008\]](#) and [Pei et al. \[2010\]](#) depend on the value of p .

Our improved agreement with the Palmer consensus range may be attributed to two improvements in modeling: (1) Here B is a spatially varying field computed dynamically from a self-consistent 3D model, in contrast to the Parker-type model used in [Breech et al. \[2008\]](#) and [Pei et al. \[2010\]](#); (2) The effect of shear interactions is computed self-consistently in our turbulence model [[Usmanov et al., 2014](#)], unlike in [Breech et al. \[2008\]](#) and [Pei et al. \[2010\]](#), where a shear-driving parameter is employed.

6.4.3 Latitudinal Evolution of Mean Free Paths

Figure 6.6 shows the variation of mfps with latitude at different heliocentric distances for an untilted solar dipole. We see from Figure 6.6(a) that, in general, λ_{\parallel} (solid lines) increases by almost an order of magnitude as one leaves the solar equatorial plane and moves to higher latitudes, and assumes a near constant value as one approaches the polar regions. The opposite behaviour is seen for λ_{\perp} (dashed lines), which decreases on moving away from the equatorial plane. This is a combined result of the increase in the IMF strength and the correlation scale of the turbulence (λ)

while moving away from the solar equatorial plane (i.e., away from the HCS), and the increase in the turbulence energy due to shear-interactions between slow and fast solar winds. We note that very close to the sun ($4 R_{\odot}$, black line), λ_{\parallel} first decreases with latitude as one leaves the equatorial plane, then increases at higher latitudes, to values larger even than those seen at larger heliocentric distances. This behavior is because of the IMF increasing monotonically with latitude, close to the sun. At larger distances, the IMF plateaus with increasing latitude, and from 1 AU onwards it decreases in the polar regions (See Figure 6.2). Thus, particles experience less scattering in polar regions close to the sun. This also explains the latitudinal variation of λ_{\perp} at $4 R_{\odot}$.

Figure 6.6(b) shows the increase in λ_{rr} as one moves towards the polar regions, and illustrates once again the fact that while λ_{rr} is affected by λ_{\perp} very close to the sun at low latitudes, near the polar regions it follows the trend set by λ_{\parallel} . Figure 6.6(c) shows that the ratio of λ_{\perp} to λ_{\parallel} decreases as one leaves the solar equatorial plane (i.e., away from the HCS), with the perpendicular mfp staying 1–2 orders of magnitude below the parallel mfp, except very close to the sun ($4 R_{\odot}$, black line) where it becomes 3 orders of magnitude smaller because of the low turbulence levels in that region. We will examine the latitudinal dependence of the mfps once again in meridional plane figures in Section 6.4.5, below.

6.4.4 Rigidity Dependence of Mean Free Paths

In Figure 6.7 we plot the rigidity (P) dependence of mfps for protons at different radial distances in the ecliptic and polar regions. Below 1 AU, $\lambda_{\parallel} \propto P^{0.33}$ for all rigidities considered here ($10 - 10^4$ MV). Above 1 AU there is a steepening of the slope for rigidities larger than 10^3 MV. As noted in Section 2.1, this is due to high energy particles resonating with turbulent fluctuations in the energy containing range instead of the inertial range. As the IMF (B) decreases with heliocentric distance, a high rigidity particle's Larmor radius ($R_L = P/Bc$) may become resonant with the correlation scale of the turbulence (λ_s). When $R_L/\lambda_s \gg 1$, the expression in braces in Equation (6.4) scales with rigidity as $P^{5/3}$, and we have $\lambda_{\parallel} \propto P^2$ instead of $\lambda_{\parallel} \propto P^{1/3}$.

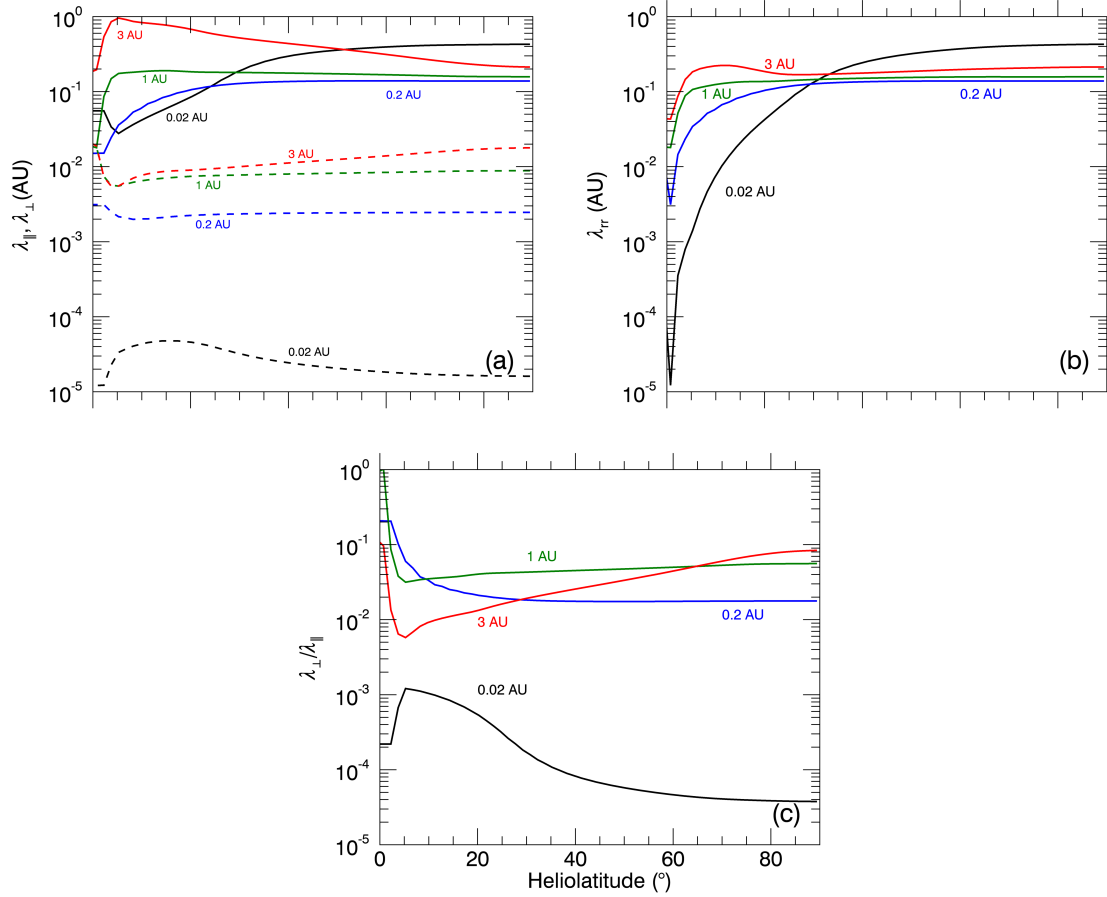


Figure 6.6: The top panel (a) shows the latitudinal dependence of parallel (solid lines) and perpendicular (dashed lines) mfps. The middle (b) and bottom (c) panels show the latitudinal variation of λ_{rr} and $\lambda_{\perp}/\lambda_{\parallel}$, respectively. All panels are for an untitled solar dipole and $p = 2$. Black, blue, green, and red lines represent radial distances of 0.02, 0.2, 1, and 3 AU (4, 45, 215, and 645 R_{\odot}), respectively. Proton rigidity is 445 MV (100 MeV kinetic energy).

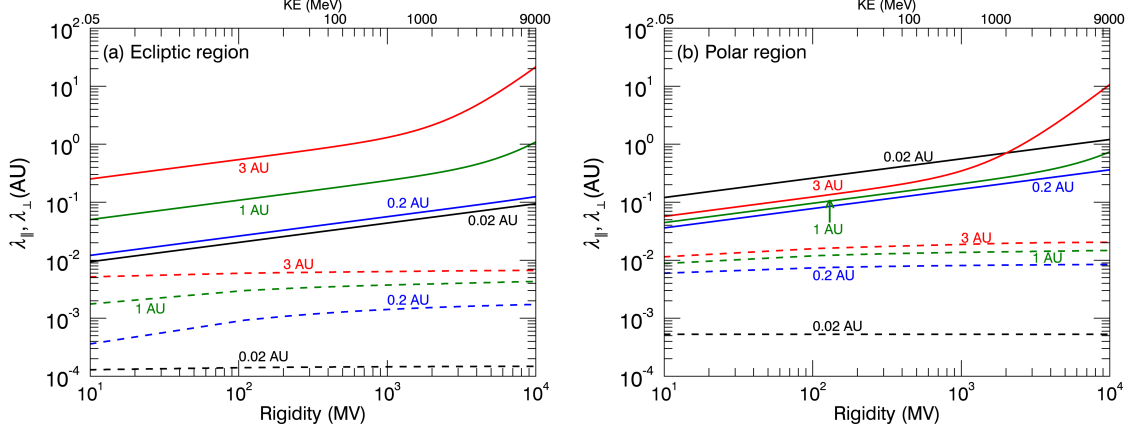


Figure 6.7: Rigidity dependence of λ_{\parallel} (solid line) and λ_{\perp} (dashed line), (a) near the ecliptic plane (7° heliolatitude), and (b) in the polar regions (86° heliolatitude), for an untilted solar dipole and $p = 2$. Black, blue, green, and red lines represent radial distances of 0.02, 0.2, 1, and 3 AU (4, 45, 215, and $645 R_{\odot}$), respectively.

Indeed, for rigidities $\sim 10^4$ MV we find that $\lambda_{\parallel} \propto P^{1.2}$ at 1 AU and $\lambda_{\parallel} \propto P^{1.8}$ at 3 AU.⁵ Our results agree well with the observations shown in Bieber et al. [1994], with power indices ranging from 0.2 to 0.56 for a number of solar events where rigidity ranges from 10 to 10^3 MV. Our results also agree with the theoretical and numerical findings in Bieber et al. [1994] and Pei et al. [2010].

In general, λ_{\perp} shows lower variation with rigidity. In the polar regions λ_{\perp} stays nearly constant with rigidity. This behavior is consistent with the Bieber et al.'s [2004] finding that NLGC predicts a very weak rigidity dependence; they note that this is supported by observations for rigidities between $10^2 - 10^4$ MV. Note that the rigidity profiles of λ_{\parallel} and λ_{\perp} that we derive from simulation results and diffusion theories are quite different from some that have been employed in the literature to model solar modulation of Galactic cosmic rays [e.g., see Figure 12 of Vos and Potgieter, 2015].

⁵ See also the discussion on the effect of pickup ion driven turbulence on high-rigidity particles in the outer heliosphere in [Zank et al., 1998, Section 4].

6.4.5 Meridional Plane Contours of Mean Free Paths

In this section, we describe the variation of λ_{\parallel} , λ_{\perp} , λ_{rr} , and $\lambda_{\perp}/\lambda_{\parallel}$ in meridional planes for 100 MeV protons, complementing results of the previous sections. Figure 6.8 shows results from a simulation with a source magnetic dipole that is untilted with respect to the solar rotation axis. It is clear that at the HCS, with its vanishing magnetic field, perpendicular diffusion is comparable to parallel diffusion in most of the inner heliosphere, with λ_{\perp} and λ_{\parallel} both around 0.01 AU. In the broader ecliptic plane, however, λ_{\parallel} remains 1-2 orders of magnitude above λ_{\perp} , varying from 0.01 to almost 1 AU within a radial distance of $10 R_{\odot}$ to 3 AU, while λ_{\perp} increases from ~ 0.0001 to 0.01 AU. As noted in the 1D plots, very close to the sun λ_{\parallel} experiences a dramatic increase to a value of 1 AU due to the weak turbulence and strong magnetic field prevailing there. We also see that at radial distances of 1.5 – 3 AU, λ_{\parallel} is a few times larger at lower latitudes, compared to values in polar regions. This is because the IMF decreases and the turbulence energy increases with latitude at these radial distances, leading to a reduction in parallel diffusion in the polar regions, and a corresponding increase in perpendicular diffusion. This can also be seen in Figure 6.8(h) showing contours of $\lambda_{\perp}/\lambda_{\parallel}$, which increases by nearly one order of magnitude from low latitudes to the poles. The radial mfp increases uniformly with heliocentric distance at lower latitudes, but is dominated by λ_{\parallel} in polar regions, because of the small winding angle between the IMF and the radial direction here. This leads to λ_{rr} acquiring a nearly constant value of around 0.2 AU in polar regions beyond 2 AU.

Figure 6.9 shows contour plots for mfps in the meridional plane at azimuthal angle equal to 26° , for a simulation with a source magnetic dipole that is tilted by 30° with respect to the solar rotation axis. In this case, solar rotation produces an asymmetrical magnetic field structure, which has a striking effect on the diffusion parameters, with the displacement of the current sheet from the ecliptic plane modifying their distribution at low latitudes. Note that the blob-like structures in Figures 6.9(f) and 6.9(h) arise due to grid points coinciding with the HCS. The rapid decrease in the magnitude of the IMF near the HCS leads to the formation of the blob contours

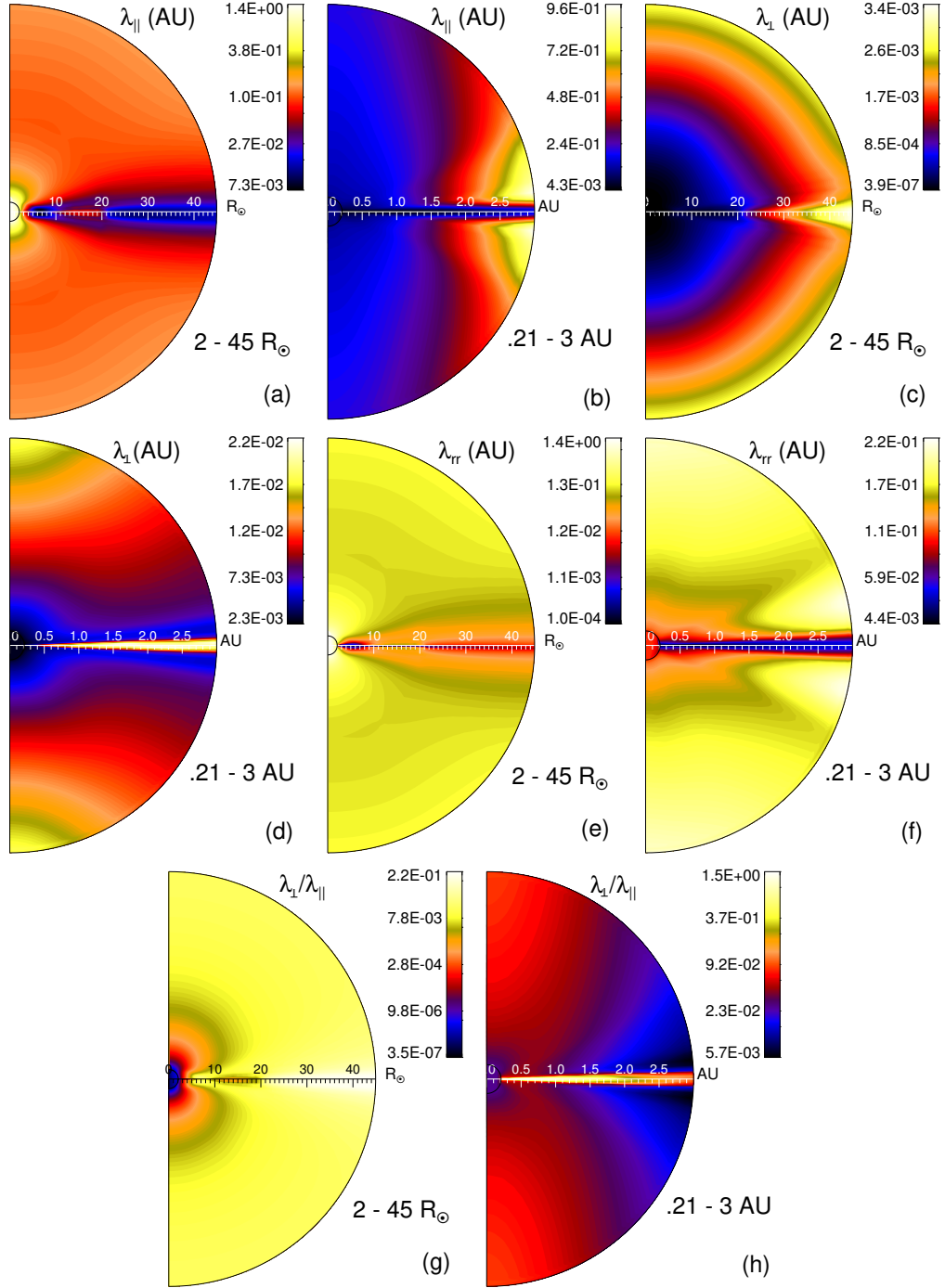


Figure 6.8: Contour plots in the meridional plane of mfps, with a solar dipole that is untilted with respect to the solar rotation axis. The inner and intermediate regions ($2 - 45 R_{\odot}$) and the outer region ($0.21 - 3$ AU, or $45 - 645 R_{\odot}$) are shown separately. Proton rigidity is 445 MV (100 MeV kinetic energy) and $p = 2$.

around grid points where B vanishes. This effect is not seen in Figure 6.8 from the untilted dipole simulation; in this case the HCS lies at 0° heliolatitude, where no grid points are present, by construction.

As noted previously in Section 6.2.2, observations indicate that the ratio $\lambda_\perp/\lambda_\parallel$ may approach, and even exceed unity. In our simulation, this happens in the HCS. The basic features described above for the untilted dipole are still present in this case, but are now organized with respect to the tilted HCS. During periods when solar activity levels are high, the warped current sheet is spread out across a larger portion of the heliosphere (Figure 6.9) compared with the low-activity case (untilted dipole, Figure 6.8), and the HCS is thus more likely to influence CRs.

6.5 Conclusions and Discussion

We have presented a detailed analysis of the diffusion coefficients for cosmic ray transport in the inner heliosphere. The purpose is to use a well-tested, fully 3D global simulation of the solar wind, with turbulence modeling, to obtain the heliospheric distribution of the large-scale heliospheric magnetic field, the energy in the turbulent fluctuations, and the correlation scale of the turbulence. This distribution has been coupled with a quasi-linear theory for parallel diffusion, and the recent random ballistic decorrelation interpretation of the non-linear guiding center theory for perpendicular diffusion. The present work extends previous studies on the heliospheric diffusion of cosmic rays by Bieber et al. [1995], Zank et al. [1998], and Pei et al. [2010], but has a stronger focus on the inner heliosphere, with the inner boundary of our simulations at $1 R_\odot$. Recent complementary work [Guo and Florinski, 2016] carries out similar computations of diffusion coefficients for the outer heliosphere.

We find that at the heliospheric current sheet λ_\perp can be greater than λ_\parallel , but usually λ_\parallel is 1–2 orders of magnitude larger through most of the inner heliosphere. Very close to the sun ($2 R_\odot$), the strong IMF leads to a large value of λ_\parallel (~ 0.5 AU), which initially decreases for several solar radii before increasing with radial distance at low to intermediate latitudes, and becomes nearly constant at the polar regions. λ_\perp

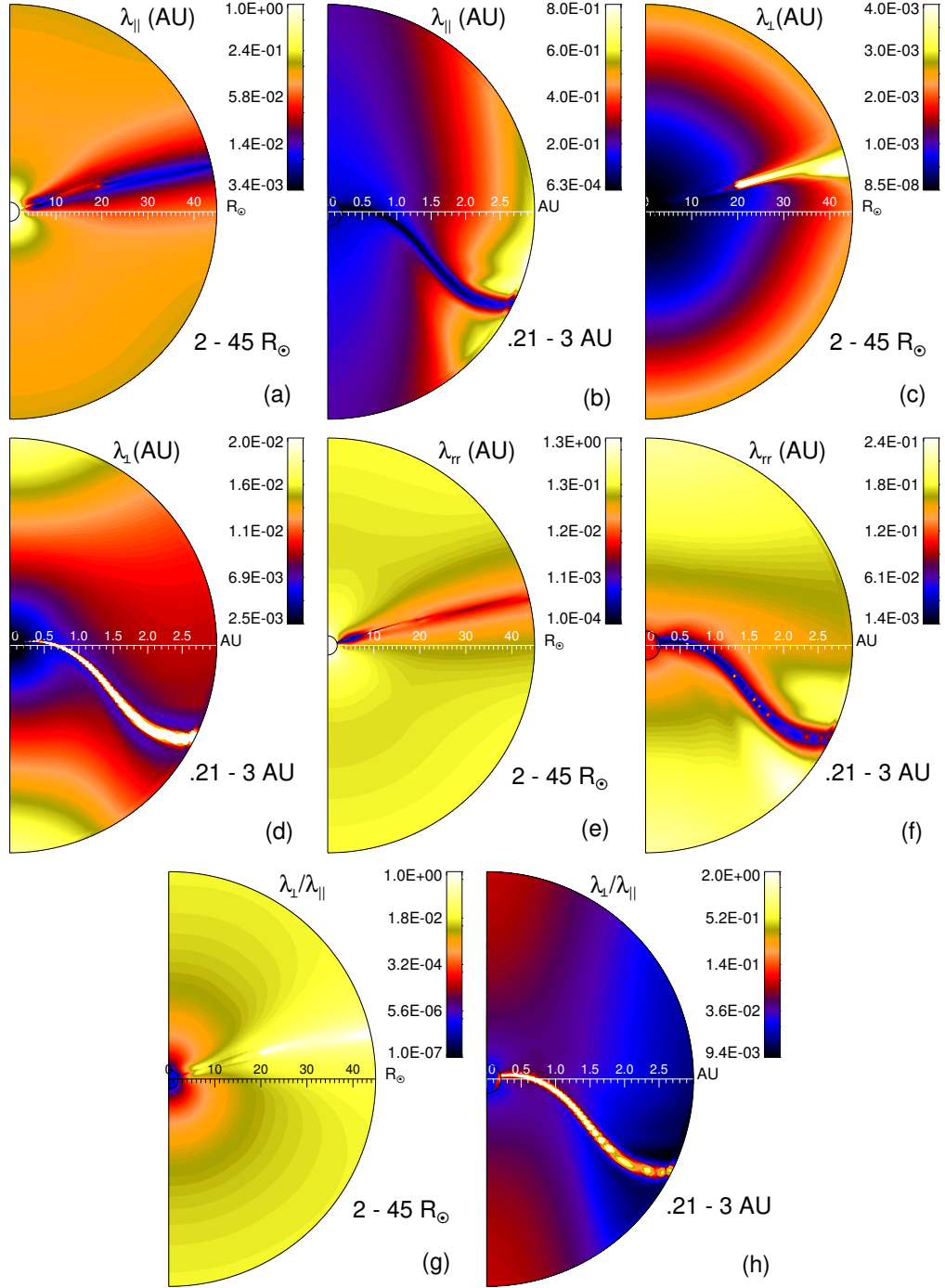


Figure 6.9: Contour plots of mfps in the meridional plane with azimuthal angle of 26° , with a solar dipole tilted 30° with respect to the solar rotation axis. The inner and intermediate regions ($2 - 45 R_\odot$) and the outer region ($0.21 - 3 \text{ AU}$, or $45 - 645 R_\odot$) are shown separately. Proton rigidity is 445 MV (100 MeV kinetic energy) and $p = 2$.

increases with heliocentric distance throughout the inner heliosphere, and is larger in the polar regions compared to low latitudes. λ_{rr} is dominated by λ_{\parallel} through most of the inner heliosphere. However, λ_{\perp} does affect λ_{rr} in parts of the near-ecliptic region. Our estimations of λ_{\parallel} near the ecliptic plane at 1 AU show good agreement with the Palmer consensus range of 0.08 – 0.3 AU.

At heliocentric distances below 1 AU, we find that the parallel mfp varies with rigidity as $P^{0.33}$ for all rigidities considered here ($10 - 10^4$ MV). Above 1 AU, highly energetic particles begin to resonate with turbulent fluctuations in the energy containing scales, and the rigidity dependence of λ_{\parallel} steepens. The perpendicular mfp is weakly dependent on rigidity. Our results on the rigidity dependence of mfps are consistent with observations.

The mfps are found to be weakly dependent on the type of power spectrum used to represent the large scale fluctuations. This suggests that any attempts to use spacecraft observations of mfps to infer constraints on the ultrascale would be challenging. The effects of solar activity (via a tilted solar dipole and variations of turbulence levels) are also studied, with increased activity leading to stronger perpendicular diffusion and weaker parallel diffusion. This interpretation has been supported by the recent findings of [Zhao et al. \[2018\]](#).

The model we have adopted for turbulence transport has been thoroughly studied and tested [[Breech et al., 2008](#)]. More elaborate models, with more transport equations (and more free parameters) are available [[Zank et al., 2012](#)]. In particular, these models include extensions such as dynamically variable residual energy, separate transport equations for slab and 2D fluctuations, and as many as three distinct dynamically evolving correlation lengths [[Oughton et al., 2011](#); [Zank et al., 2017](#)]. For the present we forgo the associated additional complication and rely on the present model’s ability to account very well for a variety of observations [[Usmanov et al., 2011, 2012, 2014](#)].

We also remark that the turbulent fluctuations we follow dynamically are the

quasi-two-dimensional fluctuations that we assume are energetically dominant. A variety of studies [Matthaeus et al., 1990; Zank and Matthaeus, 1993; Bieber et al., 1994, 1996] are consistent with dominance by quasi-2D turbulence in solar wind turbulence. In the present approach we assumed that the quasi-slab component of the fluctuations, which represent perhaps 20% of the total fluctuation energy, are a constant fraction of the turbulence energy. Useful extensions have been presented by Oughton et al. [2011]; Zank et al. [2017] that adopt somewhat different approaches with the common goal of independently transporting both 2D and slab-like fluctuations. As noted above, these models find that the radial evolution of 2D and slab fluctuation energies is not too dissimilar in the inner heliosphere, and therefore our decomposition of the total turbulence energy into slab and 2D components using a constant ratio appears reasonable. These models also show that in the outer heliosphere (above 3–4 AU), the energy in the slab fluctuations increases with heliocentric distance due to driving by pickup ions, while the 2D fluctuation energy continues to decrease. As such, studies of CR diffusion in the outer heliosphere would undoubtedly benefit from using a two-component turbulence transport model [see Zhao et al., 2017, 2018].

Such models have been implemented [Wiengarten et al., 2016; Shiota et al., 2017], with many differences relative to the present model. For example, the Shiota et al. [2017] model has a more elaborate transport formalism, as described above, but neglects the impact of turbulence on the background flow and relies on ad-hoc shear terms instead of fully coupling to the large-scale solar wind solutions. In contrast, we employ a dynamic eddy-viscosity model (Section 4.5) to achieve this coupling. Clearly no model at present is a complete treatment, and there are advantages and trade-offs in various approaches. We hope to advance our own model with additional refinements in the near future.

We anticipate that 3D calculations of the CR diffusion coefficients in the way we have demonstrated here, employing large scale solar wind solutions with turbulence transport and turbulence modeling, will become increasingly important for realistic energetic particle transport calculations in the future. We also note that related types

of diffusion coefficients, such as drag or self-diffusion, may be similarly estimated using adaptations of the above approach, as described briefly in the [Appendix](#). Studies of phenomena such as shock-ensembles and super-events [[Mueller-Mellin et al., 1986](#); [Kunow et al., 1991](#)], where several shocks merge to influence energetic particle transport at widely separated locations, would benefit enormously from such 3D studies in model heliospheres. Our findings of domains where $\lambda_{\perp}/\lambda_{\parallel} \geq 1$ may be used to further study the effects of significant perpendicular diffusion, which has been seen to reduce the SEP flux and make it more uniform [[Zhang et al., 2009](#)]. Additional development at the MHD level will be needed to utilize this kind of tool for explaining observed SEP events associated with transient phenomena such as flares, CMEs and interplanetary shocks [[Ruffolo et al., 2006](#); [Dröge et al., 2016](#); [Agueda and Lario, 2016](#)]. In the present paper we have not undertaken specific calculations employing the diffusion coefficients we obtained using a global model; this is deferred to future work. We anticipate that this approach will be useful in understanding *PSP* observations of energetic particles near the Sun.

As we have now demonstrated that such an approach can provide detailed three dimensional information concerning both MHD transport and particle mean free paths, it becomes clear that what will be needed are improved methods for driving this kind of model with more sophisticated and detailed solar observations [e.g., [Zhao et al., 2018](#)]. Future work could also investigate the influence of drifts on CR modulation. To facilitate use of the present data from this model for particle transport calculations of relevance to the current generation energetic particle and Space Weather studies, we have uploaded as Supplementary Material the 3D grids of the diffusion coefficients that were described here [[Chhiber et al., 2017b](#)].

APPENDIX

6.A Turbulent Drag Coefficient

Here we present an estimation of a general turbulent diffusion coefficient that is based on Taylor’s formulation of the problem [Taylor, 1922]. The diffusion coefficient for the passive transport of any quantity in a turbulent neutral fluid may be approximated by [Choudhuri, 1998]

$$D_T \approx \frac{1}{3} \langle v^2 \rangle \tau_{\text{cor}}, \quad (6.20)$$

where $\langle v^2 \rangle$ is the mean square turbulent velocity and τ_{cor} is the correlation time of the turbulence. By assuming $\langle v^2 \rangle \sim Z^2$, and defining the turbulence correlation length $\lambda \sim Z\tau_{\text{cor}}$, we rewrite the above equation as

$$D_T \propto Z\lambda. \quad (6.21)$$

Note that any standard diffusion coefficient, drag coefficient, eddy viscosity, or other similar quantity can be expressed in a form similar to Equation (6.21), i.e., as a product of a characteristic velocity and a length scale [see, e.g., Tennekes and Lumley, 1972].

In Figure 6.A.1 we show contour plots for D_T in the meridional plane, computed from a simulation with a solar dipole that is untilted with respect to the solar rotation axis. We may interpret D_T as a turbulent drag coefficient, which is of relevance to the propagation of CMEs in the solar wind. At high heliolatitudes, the drag coefficient increases from the solar surface to 0.5 AU, and then gradually decreases. Notably, at heliocentric distances smaller than 0.5 AU, D_T increases by an order of magnitude in moving from the ecliptic to polar regions. This implies that a CME would be “channelled” to lower latitudes as it propagates through the inner heliosphere. Applications

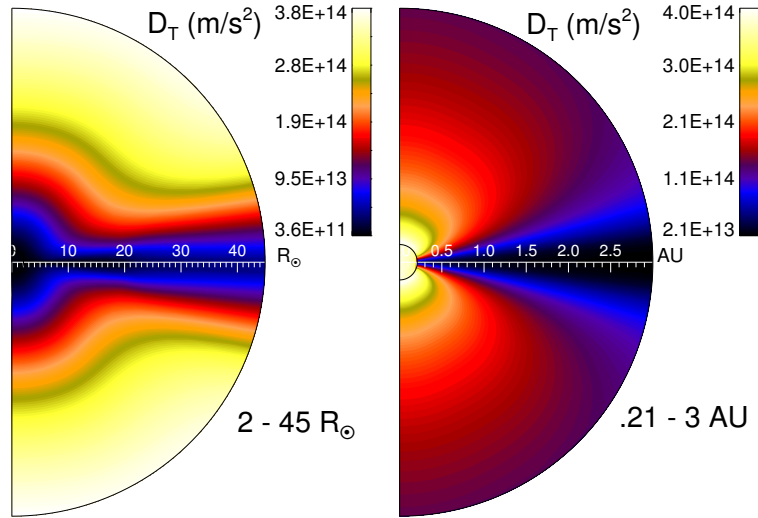


Figure 6.A.1: Turbulent drag coefficient computed from a simulation with a solar dipole that is untilted with respect to the solar rotation axis. The inner and intermediate regions ($2 - 45 R_{\odot}$) and the outer region ($0.21 - 3$ AU, or $45 - 645 R_{\odot}$) are shown separately.

involving these more general approximations to diffusion processes may also be enabled by the approach described in this chapter.

INTERLUDE I

In the preceding two chapters we used our solar wind model to study the collisional age of the solar wind and to compute cosmic ray diffusion coefficients throughout the inner heliosphere – two problems that were somewhat independent of each other, but provided examples of the application of our simulations to specific space physics problems that involve the interplay of large-scale flow and smaller-scale turbulent fluctuations. The next two chapters share the common motif of having been partly motivated by recent observations [DeForest et al., 2016] that have been interpreted as the manifestation of onset of large-scale turbulence in the young solar wind. These remote sensing observations hint at the role played by certain *critical surfaces* where the corona undergoes a transition from a regime where the magnetic field controls the flow, to a hydrodynamically dominated regime where more isotropic large-scale motions are possible. We will use our simulations to localize these critical surfaces and investigate the flow in propinquitous regions, and make direct comparisons with observations. We will also develop estimates of the largest scales across which solar wind fluctuations can have a causal effect (Section 7.A), and provide contextual predictions for the soon-to-be-launched *Parker Solar Probe* mission.

Chapter 7

WEAKENED MAGNETIZATION AND ONSET OF LARGE-SCALE TURBULENCE IN THE YOUNG SOLAR WIND — COMPARISONS OF REMOTE SENSING OBSERVATIONS WITH SIMULATION

7.1 Introduction

Analysis of *STEREO* imaging observations by [DeForest et al. \[2016\]](#) (henceforth D16) describes the initiation of turbulence in the young solar wind in solar minimum conditions. The typical striated, radially elongated patterns of scattered light that are characteristic of the corona give way, with increasing separation from the sun, to more isotropic patterns at distances of a few tens of solar radii. These were interpreted as the incipient dynamical effects of the super-Alfvénic solar wind, which at these distances, become less impeded due to the weakening magnetic field and the increase of the plasma beta (gas pressure/magnetic pressure). Here we provide support for this interpretation, employing magnetohydrodynamic (MHD) simulation of the corona and solar wind. The simulation results provide more detailed expectations for locations of the Alfvén critical surface and the first plasma beta unity surface moving outward into the dynamically active solar wind. A similar approach can provide context for the upcoming *Parker Solar Probe* (PSP) and *Solar Orbiter* missions, which will explore this transition in the inner heliosphere.¹

7.2 Background

A striking feature of solar coronal observations is the visible *anisotropy* of the images. This is evident in white light images [e.g., [Bird and Edenhofer, 1990](#)] wherein anisotropic features emanate from coronal holes, and striated features are suggestive

¹ The contents of this chapter were published in [Chhiber et al. \[2018c\]](#).

of open magnetic field lines. An immediate inference is that various physical quantities admit stronger gradients in directions *across* striations and weaker gradients *along* striations. This is entirely consistent with the standard view that the corona is magnetically dominated, while theory also shows that a strong magnetic field induces a similar perpendicular anisotropy [Robinson and Rusbridge, 1971; Shebalin et al., 1983; Oughton et al., 1994; Oughton et al., 2015]. The coronal magnetic field and density both decrease rapidly with altitude, but the plasma beta throughout the lower corona is presumably less than unity. The sonic point, where the wind speed exceeds the sound speed, is often predicted to be in the range of $2 - 5 R_{\odot}$ [Kopp and Holzer, 1976; McKenzie et al., 1995; Habbal et al., 1995; Cranmer et al., 2007; Verdini et al., 2010]. Some spectroscopic studies [e.g., Giordano et al., 2000] find that the wind speed is larger than 100 km s^{-1} within $2 R_{\odot}$, although these predictions are mainly applicable to coronal hole regions. At low latitudes the sonic point may lie as far as $7 - 20 R_{\odot}$ [Lotova et al., 1997]. In general, low plasma beta and sub-Alfvénic flow favor a corona that is strongly structured by the magnetic field.

Shifting attention to near Earth at 1 AU, spacecraft observe a highly super-Alfvénic solar wind with variable plasma beta (β), hovering mostly near unity [e.g., Bavassano et al., 1997]. Magnetic clouds [Klein and Burlaga, 1982] that may have $\beta \ll 1$ are exceptions, but these occur relatively infrequently except at solar maximum. Therefore at some position between the corona and Earth orbit, the typical dominance of the magnetic field is lost, and one might expect that the spatial structuring and associated anisotropy is also diminished.

The region where this transition might occur may be estimated in at least two ways. First, there is the point (or region) at which the accelerating solar wind speed becomes equal to the Alfvén speed. In symmetric, one dimensional models this is called the Alfvén critical point; we designate it as the Alfvén surface. Here the magnetic field pressure can no longer overcome the inhomogeneities in ram pressure of the solar wind. Above the Alfvén surface, low frequency wave modes no longer propagate inward toward the Sun in the Sun’s inertial frame, and the plasma therefore becomes causally

disconnected from the corona itself, even as the corona continues to influence the solar wind. Frozen-in field lines cannot retract into the Sun from beyond the Alfvén surface, while reorganization of the plasma above this surface cannot (in MHD) affect the corona, as there is no way for the information to propagate down to the corona.²

Another region of interest is found by moving outwards and seeking the first position at which mechanical pressure equals or exceeds magnetic pressure – this is the “first $\beta = 1$ surface” or simply the $\beta = 1$ surface. The location of these surfaces depends on parameters such as boundary conditions at the photosphere or transition region, but importantly, also on the 3D structure of the wind. Normally one anticipates that the Alfvén surface lies outside the sonic point, the $\beta = 1$ surface lies still farther outward than the Alfvén surface.

7.3 Insights from *STEREO* Heliospheric Imaging

We make use of the published D16 analyses of image sequences collected by the inner Heliospheric Imager instrument onboard the *Solar-Terrestrial Relations Observatory* (*STEREO*/HI1) in December 2008. These images cover apparent distances of approximately 4 to 100 R_{\odot} from the center of the Sun, spanning the transition from the ordered magnetic field-dominated coronal conditions to the more turbulent and less ordered large-scale wind. D16 describes the observation and techniques to extract evolving structure from the images, leading to a novel quantification of the clear textural shift in the apparent structure of the corona and solar wind in this altitude range. D16 also provides more detailed discussion of observational factors such as the superposition of scattering positions that contribute to the image seen in the plane of the sky.

For present purposes, the central conclusion of D16 is that an evolution towards isotropy begins to occur within the spatial range of these images. The onset of this evolution appears at length scales somewhat larger than reasonable extrapolations of

² The role of Alfvén modes is emphasized here; magnetosonic modes (Section 2.2.3) are a secondary issue since these are presumably a minor ingredient due to damping [Barnes, 1966].

the observed correlation scale at 1 AU to the relevant regions near 0.2 AU. Their interpretation is that this is the onset of nonlinear turbulent couplings at the largest possible scales in the nascent solar wind.

The region in which this more isotropic behavior might begin to be seen is likely prescribed by several simple physical inequalities. First the magnetic field must not be so strong that it can overcome the largest potentially isotropizing force, the differential ram pressure due to shearing interactions between neighbouring wind streams [e.g., [Breech et al., 2008](#)]. Therefore this isotropization is expected to be *at least* at the distance at which $\rho U^2/2 > B^2/8\pi$ (density ρ , magnetic field strength B , solar wind speed U), which is equivalent to the condition that the wind speed exceeds the Alfvén speed, $U > V_A$. Second, gradients of mechanical (thermal) pressure exert a dynamical influence towards isotropy in the absence of a strong magnetic field, as in a hydrodynamic regime. Thus we also expect that $P \simeq B^2/8\pi$ provides conditions favorable for mechanical pressure to offset or even overcome the magnetic pressure. The former condition is that we look beyond the Alfvén critical point, while the latter indicates that the plasma beta be not too low ($\beta = 8\pi P/B^2 \simeq 1$) and that we look beyond the first unity beta surface. Both of these conditions favor an evolution towards isotropy.

A third condition is somewhat more subtle but equally important. That is, given that the above two conditions are adequately met, the length scales at which structures begin to isotropize should be causally related [[Chhiber et al., 2016b, 2018b](#)] within the relevant dynamical framework. Since we are considering fairly large scales here, the appropriate reference frame is compressible MHD. Therefore if an Alfvén wave is to participate in affecting isotropization at length scale ℓ , then a suitable duration of time must be available, namely the wave transit time of distance ℓ . Similarly, if the influence of gas pressure is to come into play, a time duration of the sound crossing time of distance ℓ is needed. For turbulence effects such as vortex turnover to become involved, the expectation is that an eddy turnover time at scale ℓ is required. For the present, we anticipate that the isotropization scale may be related to the correlation scale of the turbulence, and make further remarks in the Discussion section (7.6) and

in Appendix 7.A.

3D MHD modeling, given a set of reasonable assumptions on boundary data, provides all parameters needed to locate the positions of Alfvén and $\beta = 1$ surfaces, thus providing physically motivated context for interpreting the remote sensing observations. We now briefly describe the simulation used here for a direct comparison with the D16 *STEREO* images.

7.4 Solar Wind Model

To obtain 3D numerical solutions for solar wind conditions in the inner heliosphere during the relevant time period (December 2008), we employ the solar wind model described in Chapter 4. It is worth remarking on the appropriateness of using the MHD-RANS approach in this study. The *STEREO* images we wish to compare with simulations span a distance of around 0.3 AU, or 50 million km, in two dimensions. Global simulation is required to map the critical surfaces at such large scales, but computational constraints do not allow simultaneous resolution of the small scales where the inertial range of solar wind turbulence resides (see Section 1.1.6). Our subgrid turbulence model provides a way to include dynamical coupling between large scale fields and turbulence in a self-consistent manner. Furthermore, the spatial resolutions of the simulation (~ 1.5 Gm at 0.2 AU) and the *STEREO* images ($\sim 0.5 - 2.5$ Gm) are similar, making comparison apt.

7.5 Results

The comparisons shown here between *STEREO* observations and global heliospheric MHD solutions are based on two runs of the simulation: in the first case (Run I) we employ an untilted dipole magnetic field at the inner boundary. The dipole strength is set to 12 G to match the magnitude of the heliospheric magnetic field observed by *Ulysses* in January 2008. In the second case (Run II) the MHD code is driven by a magnetic field at the base obtained from a December 17, 2008 – January 13, 2009 (CR 2078) magnetogram published by Wilcox Solar Observatory. These are simple

but appropriate conditions given that 2008 is in deep solar minimum. Therefore one expects the solar magnetic field to have definite large scale polarity, and to be well approximated as a dominant dipole, plus corrections. The simulation domain extends from the coronal surface at $1 R_{\odot}$ to 3 au. Runs I uses the turbulence transport model described in Chapter 4 in the full domain, while runs of type II use the WKB model described in Appendix C for the region between the coronal surface and $45 R_{\odot}$. The output of this model is then used as an initial condition for the turbulence transport model. Other coronal base parameters are identical in both runs: the amplitude of Alfvén waves is 35 km s^{-1} , the density is $0.4 \times 10^8 \text{ cm}^{-3}$, and the plasma temperature is $1.8 \times 10^6 \text{ K}$. Further details may be found in Usmanov et al. [2014]. Figure 7.1 compares Run II with *Ulysses*' fast latitude scan during 2007 – 2008, indicating good overall agreement.

Figures 7.2 and 7.3 depict meridional plane density maps for these simulations, at two different scales – a close-up ($1 - 30 R_{\odot}$), and a larger scale view. The meridional planes are at arbitrary longitude, since the results are near axisymmetric. A highly processed *STEREO* image (Figure 1 from D16) is also shown. Note that D16 use a coordinate system based on helioprojective latitude and longitude, and we use a factor of $3.8 R_{\odot}$ per degree to convert helioprojective coordinates to the heliocentric distances shown in Figures 7.2 and 7.3. The simulation panels show the variation in heliolatitude θ of the sonic critical surface $r_s(\theta)$, the Alfvén critical surface $r_A(\theta)$, and the $\beta = 1$ surface $r_{\beta}(\theta)$, as described below. Operationally the Alfvén critical surface is defined by the set of points, scanning outward, at which the solar wind speed first exceeds the Alfvén speed $V_A = B/\sqrt{4\pi\rho}$, where ρ is the proton mass density. Similarly, the sonic surface is defined by the set of points, scanning outwards from the sun, at which the wind speed becomes larger than the sound speed $c_s = \sqrt{\gamma P/\rho}$. Here γ is the polytropic index and P is the sum of proton and electron pressures. The first $\beta = 1$ surface is identified as the set of points, scanning outward, at which $\beta = 1$ is first encountered.

The simulation results in Figures 7.2 and 7.3 show the general expansion of the wind and a higher density streamer belt region extending along the heliospheric

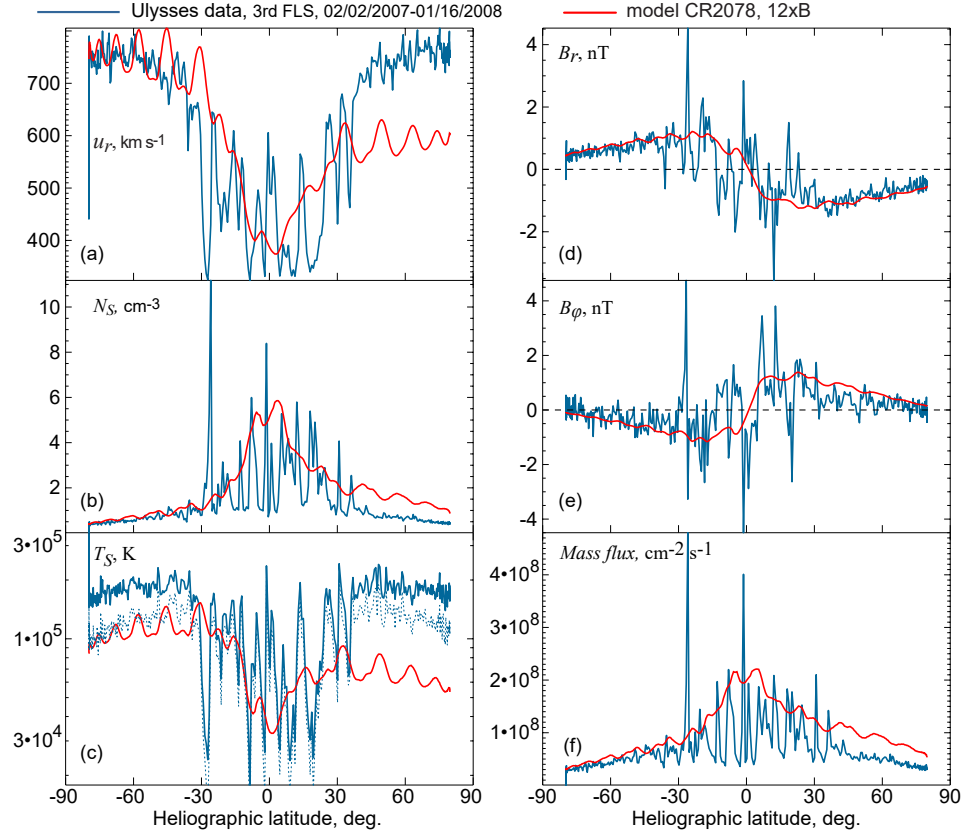


Figure 7.1: Data from *Ulysses*' fast latitude scan during 2007 – 2008 compared with Run II.

current sheet. As expected, the untilted dipole (Figure 7.2) produces a less complex wind. At almost all angles the sonic, Alfvén, and beta surfaces are ordered such that $r_\beta \gg r_A \gg r_s$. However, near the current sheet the beta surface dramatically dips towards lower altitudes, as the magnetic field strength attains very low values. In the magnetogram-driven run, the beta and Alfvén surfaces are notably less symmetric, and lie much closer to the sun. This is because the complex magnetic field topology in the magnetogram run impedes the outward flow [Réville et al., 2015]. The locations of the sonic and Alfvén surfaces are generally consistent with observations [Lotova et al., 1997; DeForest et al., 2014] and modeled predictions [Cranmer et al., 2007; Verdini et al., 2010].³

³ We examine the sonic and Alfvén surfaces in more detail in Chapter 8.

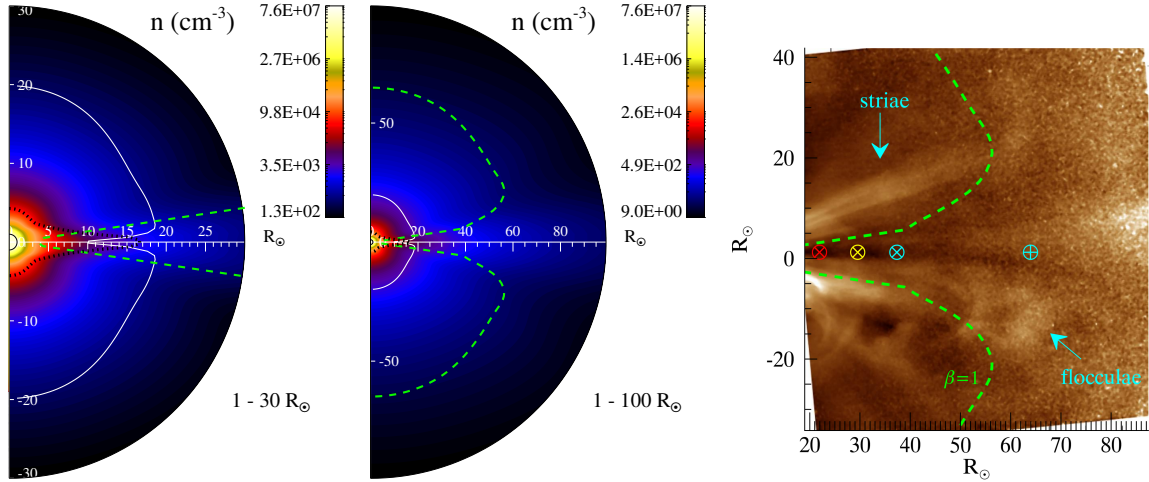


Figure 7.2: Left and center: Contours of proton density in a meridional plane from Run I (untilted dipole). Dotted black, solid white, and dashed green curves show sonic, Alfvén, and $\beta = 1$ surfaces. Right: Surfaces computed from the model superimposed on a processed *STEREO* image from Dec 16, 2008. *Helios* perihelion is shown as ‘ \oplus ’; first three perihelia of PSP are shown as ‘ \otimes ’.

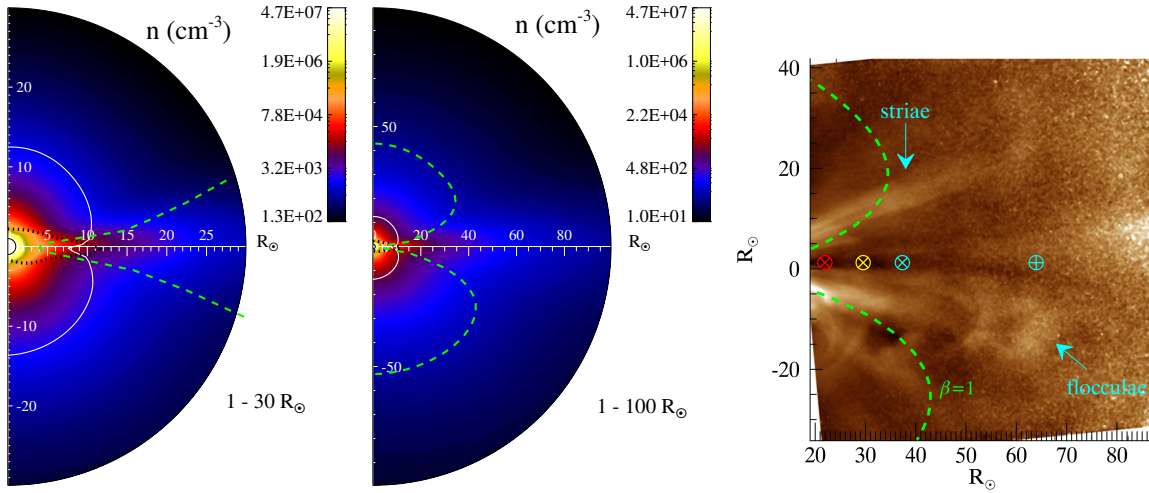


Figure 7.3: Left and center: Contours of proton density in a meridional plane from Run II (Dec 2008 magnetogram). Right: Surfaces computed from the model superimposed on a processed *STEREO* image from Dec 16, 2008. Description of curves and symbols follows Figure 7.2.

In the right-most panels of Figures 7.2 and 7.3, the beta unity surfaces derived from the simulations are superposed on an image from D16. It is apparent that the region above r_β is well associated with onset of dynamical activity as described by D16. The correspondence of observed activity with the position of these curves in the simulations is not precise, nor would one expect it to be. Nevertheless, it is of interest to note that outside of the Alfvén critical distances, and even prior to the unity beta surfaces, some dynamical activity is already evident. The “striation” begins to give way to “foculation” past the $\beta = 1$ surface obtained from the simulations, thus supporting the interpretation advanced by D16.

To complete an examination of the D16 interpretation of the *STEREO* images, we compute second order structure functions [e.g., Panchev, 2016] of the magnetic field \mathbf{B} ,

$$S(\mathbf{s}) = \langle |\Delta\mathbf{B}(\mathbf{s})|^2 \rangle, \quad (7.1)$$

as a function of vector spatial lag \mathbf{s} . The magnetic vector increment is defined as $\Delta\mathbf{B}(\mathbf{s}) = \mathbf{B}(\mathbf{x} + \mathbf{s}) - \mathbf{B}(\mathbf{x})$, and $\langle \dots \rangle$ denotes an average over a suitable sample of points in the simulation domain. The lag \mathbf{s} is taken to be in either the radial (S_{radial}), or the polar (S_{polar}) direction within a meridional plane.

Figure 7.4 shows these structure functions computed at increasing heliocentric distances (20 – 60 R_\odot) from the magnetogram based simulation. Spatial lags are computed up to about 14 R_\odot (10 Gm), and averaging is performed in the meridional plane over a range of latitudes from low to intermediate, following D16. Further averaging is performed over longitude. The last panel of Figure 7.4 shows the ratio $S_{\text{polar}}/S_{\text{radial}}$ for a range of heliocentric distances. It is apparent that polar variations (transverse to flow) are greater than the radial variations at the smaller heliocentric distances shown. However, there is a systematic trend with increasing heliocentric distance of the ratio to decrease towards unity. This signifies an evolution towards isotropy in this region, at the scales we are examining. Again, this is fully consistent with the structure function

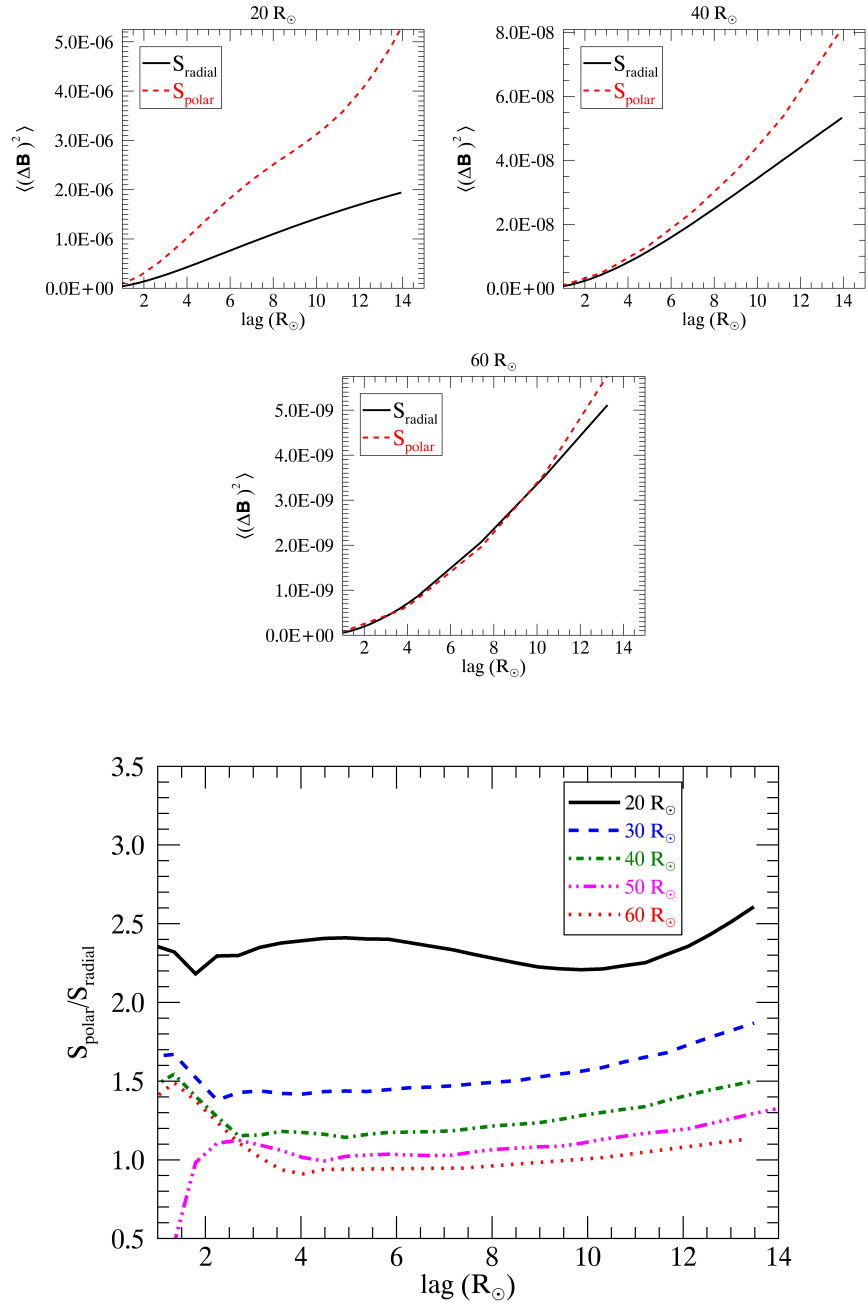


Figure 7.4: Top: Structure functions of magnetic field from Run II at $20 - 60 R_{\odot}$. Black (red) solid (dashed) curve represents lag in the radial (polar) direction. Bottom: Ratio of polar structure function to radial structure function, computed at different heliocentric distances. A clear trend towards isotropization with increasing distance is evident.

calculations given by D16 based on *STEREO* remote sensing data.⁴

7.6 Discussion and Conclusions

The present chapter complements the observations of D16 by providing some quantitative, if approximate, *context* from simulations. We have employed a steady state simulation, equivalent to a time average, using standard solar minimum parameters and boundary values corresponding to the solar epoch examined by D16. Our identification of the $\beta = 1$ and Alfvén critical surfaces in the simulations and comparison with the D16 observations serves several unique purposes: First, it provides in effect a direct test of the physical interpretation of the images as given by D16, namely that the observed transition represents the earliest manifestation of large scale interplanetary turbulence, enabled by weakened magnetization and relative strengthening of hydrodynamic influence on the flow as it passes the Alfvén and first beta unity surfaces [see also [Kasper et al., 2017](#)].

Second, this comparison provides a certain level of general calibration of the remote sensing observations, in a region as yet unexplored by in-situ spacecraft, pending the *PSP* and *Solar Orbiter* missions. It offers a first look at inter-calibration of simulation results and *STEREO*/HI1 observations, which we may refine in future analogous applications.

We emphasize that the comparison of the observations and the simulations is not claimed to be exact or detailed. The Reynolds-averaged solution for the resolved (or mean) field includes effects of fluctuations that are averaged over, even though they modify the properties of the resolved solutions through the density, momentum, energy and magnetic field (Chapter 4). However, such fluctuations are not explicitly represented in the solutions depicted, e.g., in Figures 7.2 and 7.3, which lack detail compared to the *STEREO* image also due to the simplified boundary conditions that are employed and the fact that the simulations are driven to a steady state.

⁴ Note that D16 computed structure functions by averaging over a 15 day interval of *STEREO* data, which makes them suitable for comparison with structure functions from our steady state simulations.

The current contextual discussion may readily be extended to other observations, both existing and anticipated. For example, *Helios* observations [e.g., Tu, 1988; Bruno and Carbone, 2013], indicate a spectral break point between shallower frequency (f) spectra and the familiar “ $f^{-5/3}$ ” Kolmogorov-like spectrum that characterizes strong turbulence (see Figure 1.5). This break point moves towards lower frequencies at larger heliocentric distances. At the perihelion of *Helios*’ orbit (0.29 AU)⁵ the break point is observed to be at about 7×10^{-3} Hz in fast (~ 700 km s⁻¹) solar wind. This corresponds to a maximum in-situ generated correlation length of about 0.1 Gm. In contrast, *Helios* perihelion data in the slow wind shows no resolved break point. So the break must be below 10^{-5} Hz. At 300 km s⁻¹ this implies a much longer correlation length. The distance 0.29 AU appears within the range of interest in Figures 7.2 and 7.3. For the simplified simulations we present, the fast wind period would notionally correspond to a position at 0.29 AU that is slightly above or below the heliospheric current sheet region. The slow wind interval would correspond to the current sheet region as an extension of the streamer belt. We note that the 0.1 Gm correlation scale implied by the *Helios* fast wind break point is below the grid resolution (~ 1.5 Gm at 0.2 AU) of the simulation and also subgridscale in the *STEREO* observations, which have an effective spatial resolution of $\sim 0.5 - 2.5$ Gm. This is consistent with estimates made in D16 which indicate that the early onset of nonlinear turbulence dynamics indicated by the observed fading of the *striae* occurs at very large scales (around a few Gm); indeed, scales that are larger than the correlation scales extrapolated inward from near Earth orbit. In Appendix 7.A we estimate the largest length-scales over which turbulence can have a causal effect in the expanding solar wind, and we compare this *causality scale* with the correlation scale and the spatial scale of the *focculae*.

Finally, we anticipate that the *PSP* mission to be launched in 2018 will also probe this critical region, and will provide ground truth in-situ observations. For

⁵ A nominal position of Helios at perihelion is suggested in Figure 7.3 by a ‘ \oplus ’ symbol.

further context, the perihelia for *PSP* in its first several orbits [Fox et al., 2016] are demarcated with ‘ \otimes ’ symbols in Figure 7.3. We emphasize that this comparison of observations and simulations in the region within 0.2 AU provides an additional data point for studies of radial evolution of turbulence parameters, that can be employed in numerical studies and interpretations of observations in the future.

APPENDIX

7.A Range of Influence of Turbulence in Solar Wind Fluctuations: Estimating a Causality Threshold

7.A.1 Introduction

Plasma dynamics proceeds through local dynamical interactions, and therefore when the complete system is treated explicitly, the influence of the physical state at any point at a specified time spreads to regions near that point at finite propagation speeds. This influence may spread due to wave modes, shocks, convection, collisions, and so on, each of which may have its own preferred speeds, anisotropies and distribution of speeds. The finite speed of propagation of all such these signals implies a time-dependent finite “*region of influence*” (ROI) around any point, which demarcates the range of causal influence by plasma processes. In certain models the finite propagation speeds of some signals are ignored or “ordered out” of the problem – a prominent example being incompressible flows in which the compressional wave speed may be treated as infinite, and its effects are replaced by a constraint [e.g., Chapter 4 of [Choudhuri, 1998](#)]. On the other hand for certain practical applications, finite propagation speeds, which introduce a “*causality threshold*” should not be ignored. The problem is analogous to the causality limit set by the light cone in relativity [e.g., [Hartle, 2003](#)], except that we are concerned with various slower signal propagation speeds in plasmas. When turbulence and expansion are included in models, questions related to the ROI become impractical to answer with precision, and estimation is required.

The basic idea is elementary – in a homogeneous medium in which a maximum propagation speed V can be identified, and the maximum distance over which a causal influence may be felt after a time t is just $L = Vt$. This might apply to homogeneous

(MHD) with V the fast magnetosonic speed, or in classical electrodynamics where a retarded potential is introduced and V is the light speed [e.g., [Jackson, 1975](#)]. However, in the solar wind the importance of understanding the region of influence (or causality threshold) and properly taking it into account is even more important due to the ubiquitous presence of expansion, the presence of several important wave speeds, and the presence of a generally unresolved fluctuating plasma fluid velocity.⁶

7.A.2 A Simple Estimate of the Causality Threshold

If the resolved (large scale) velocity \mathbf{U} is uniform and constant, the situation is illustrated in the first panel of [Figure 7.A.1](#). In this case the line segment connecting the two convecting points $\overline{PP'}$ has constant magnitude ℓ_0 . If the r.m.s turbulence speed is u' , then $L(\tau)$, the distance the turbulent signal travels in time τ , under the assumption that the velocity remains coherent, is just $L(\tau) = u'\tau$. Conversely if we specify L then the associated time is $\tau(L) = L/u'$. One might allow for the variability in u' by making it time dependent, so that $L(\tau) = \int^\tau dt' u'(t')$. If the further refinement of a spatial dependence in u' is allowed, then the problem will require a statistical treatment. For the simple coherent velocity case, the range of influence is not limited, but becomes arbitrarily large at large times.

If one considers a fixed $L = \lambda$, the correlation length of the turbulence, then the time to influence a distant point separated by L is just

$$\tau(\lambda) = \lambda/u' \equiv \tau_{nl}, \quad (7.2)$$

which is the nonlinear time, or eddy turnover time, of the turbulence.

In the expanding solar wind, the effective distance over which the turbulent signal can effectively propagate information in a medium such as the solar wind is influenced by, or even limited by, the expansion. The case of uniform expansion is illustrated in the second panel of [Figure 7.A.1](#). If points P and P' move along radial

⁶ The material in this Appendix is being prepared for publication in [Chhiber et al. \[2018b\]](#).

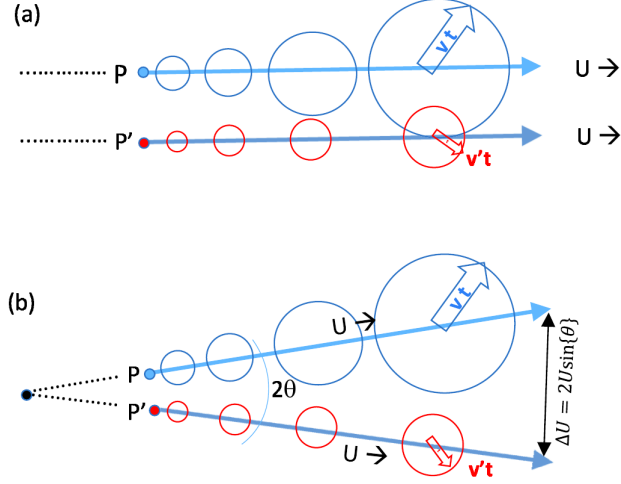


Figure 7.A.1: (a) Diagram of homogeneous case. (b) Diagram of expanding case with constant radial speed U . The turbulent speeds associated with the points P and P' are labeled v and v' , respectively. The expanding circles indicate the region of causal influence of turbulence.

trajectories at the same speed and at the same radial distance separated by angle 2θ , then it is clear that their separation in the direction perpendicular to radial is increasing. The speed of this receding motion is $\Delta U = 2U \sin \theta$. If $\Delta U > u'$ then the turbulence signal will never pass between points P and P' .

It is clear that solar wind expansion places an effective limit on signal propagation by turbulence. We consider a uniform radial expansion at constant speed U as a first approximation. The convection time to a radial position R is $\tau_{con} = R/U$. The expansion (or dilation) time is $\tau_{exp} = 1/\nabla \cdot \mathbf{U} = R/(2U_r)$, where U_r is the radial velocity of the solar wind. These two time-scales are essentially the same for the uniform constant speed expansion, but in general may be quite different.

The expansion/convection time-scale is associated with signal propagation due to large scale inhomogeneities, which compete with turbulent fluctuations to influence the dynamics of solar wind expansion. The time taken by a turbulent signal, travelling

with speed u' , to cover a distance L , is

$$\tau_{turb}^L = L/u'. \quad (7.3)$$

L is the distance an isolated turbulent signal would be able to traverse, if it remained coherent during the traversal. The effective distance over which the turbulent signal can effectively propagate information in the solar wind is, however, limited by the solar-wind expansion. Before we examine this limit, we note the connection between τ_{turb}^L and the canonical nonlinear time-scale of solar wind turbulence τ_{nl} : when $L = \lambda$, where λ is the correlation length of the turbulence, then,

$$\tau_{turb}^L(L = \lambda) = \lambda/u' \equiv \tau_{nl}. \quad (7.4)$$

We now evaluate the limit that the solar wind expansion places on effective signal propagation by turbulence. For a turbulent fluctuation to have an influence over a distance L , it must travel at least as fast as the expansion signal; that is, $\tau_{exp} \geq \tau_{turb}^L$, and the equality defines the maximum distance over which the turbulence may have a causal effect. This *causality threshold* for the turbulence (or *turbulence range of influence*) L_T is thus defined as

$$L_T = \frac{u'}{U} R = u' \tau_{exp}, \quad (7.5)$$

for the case of a constant speed uniform radial expansion.

In a more general case, the large scale stress tensor $\nabla_i U_j$ can contain both symmetric and antisymmetric parts, and the full description of the local properties of the large scale flow will involve expansion, shear, and vorticity. In these more complex circumstances, evaluation of the likelihood of communication between points P and P' will need to consider the orientation of the line segment relative to the large scale gradients. Some progress in tracking the communication between material elements can be achieved by considering an analytical formulation (see Equation 7.6 below).

Another approach (see following section) is to follow the position of fluid elements in large-scale (e.g., MHD) simulations. We will estimate the turbulence ROI using our solar wind model in the next section.

If the line segment $\delta\ell = \overline{PP'}$ is small compared to the scale over which the large scale velocity varies substantially, it is elementary to show that the line segment obeys the equation

$$\frac{\partial\delta\ell}{dt} + \mathbf{U} \cdot \nabla\delta\ell = \delta\ell \cdot \nabla\mathbf{U} \quad (7.6)$$

The right hand side involves the strain tensor of the resolved velocity U . This line-stretching formalism is useful when large-scale expansion and shear is superposed on the propagation of information due to unresolved turbulent motions.

7.A.3 Numerical Estimates from Simulations and Observations

To obtain numerical estimates for the turbulence ROI, we extract from our untilted dipole simulation the radial speed of the solar wind U , the fluctuation energy Z^2 , and the correlation length for the turbulence, λ . We estimate the velocity of turbulent fluctuations as $u' = Z$.

In Figure 7.A.2 we show the radial evolution of various quantities, in the ecliptic plane. In addition to the turbulence ROI L_T (Equation 7.5) and the correlation scale of the fluctuations λ computed from our solar wind models, we also show the result of a least-squares fit to solar wind spacecraft data [Ruiz et al., 2014] that yields the power law $\lambda(r) = 0.89(r/1 \text{ AU})^{0.43} \times 10^6 \text{ km}$.

To compare our model estimate of L_T with observations, we extract measured values of Z^2 from Pei et al. [2010], who use observational data from from *Voyager 2*, *Helios*, and the National Space Science Data Center (NSSDC) Omnitape dataset. To estimate L_T from these data, we assume a constant low-latitude solar wind speed of 400 km s^{-1} , and show the results as black diamonds in Figure 7.A.2.

These results indicate that the turbulence ROI is roughly an order of magnitude larger than the correlation scale of turbulent fluctuations. This finding is confirmed by Figure 7.A.3, which shows meridional planes from the untilted dipole simulation. Note

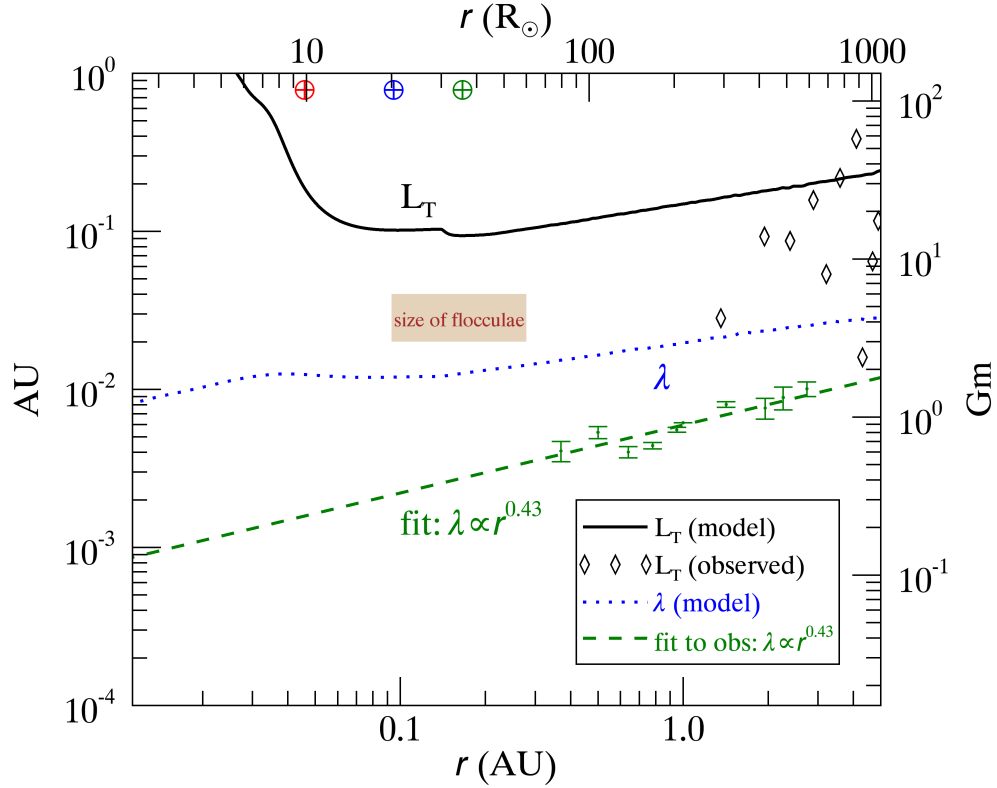


Figure 7.A.2: Radial evolution of the turbulence region of influence L_T (solid black line) and the correlation scale λ (dotted blue line) computed from the simulation in the ecliptic plane. The dashed green line shows a least-squares fit to solar wind spacecraft data [Ruiz et al., 2014] that yields the power law $\lambda(r) = 0.89(r/1 \text{ AU})^{0.43} \times 10^6 \text{ km}$. The black diamonds represent L_T computed from spacecraft measurements. The tan-colored bar indicates the region where the flocculation is observed in *STEREO* images (Figure 7.2), and the approximate size of the flocculae (3 – 6 Gm). The radial locations of the innermost three perihelia of the *PSP* are shown as \oplus .

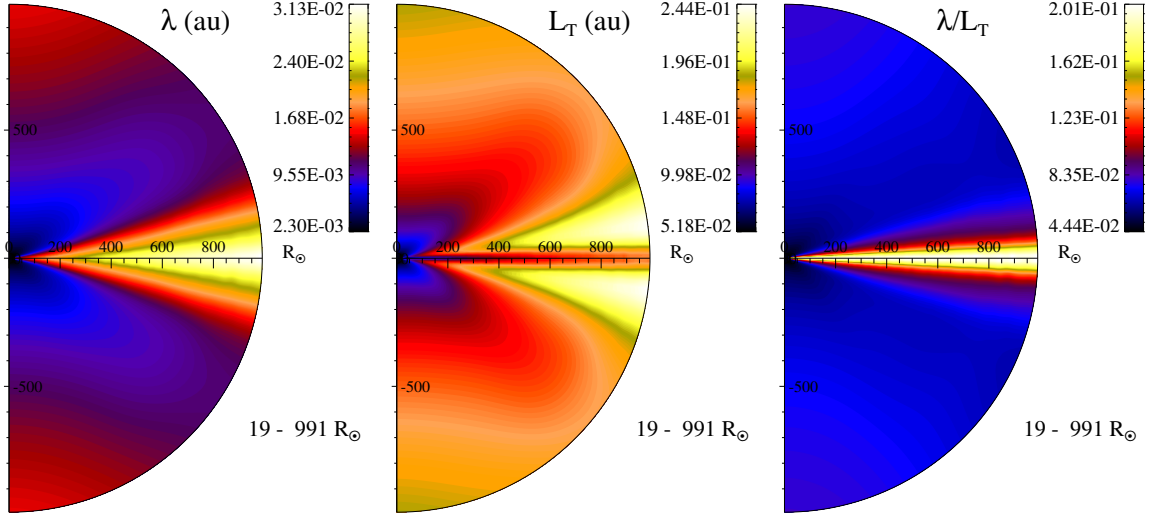


Figure 7.A.3: Meridional plane contours of the correlation scale λ , the turbulent ROI L_T , and their ratio λ/L_T .

that the ROI is largest at the low latitudes where shearing between fast and slow wind streams strengthens the turbulence.

The estimates shown in Figures 7.A.2 and 7.A.3 are based on Equation (7.5), but we can also use the simulation to directly compute the turbulent ROI of two points in the expanding solar wind, as depicted in schematic form in Figure 7.A.1. Figures 7.A.4 – 7.A.7 offer examples of this approach, discussed in detail below. These figures show contours of the radial velocity of the solar wind; a close-up view spanning $20 - 200 R_\odot$ and a larger-scale view spanning $20 R_\odot - 5 \text{ au}$ are shown.

In Figures 7.A.4 – 7.A.6, the circles represent an estimate of the expanding region of influence of turbulent fluctuations, starting from $20 R_\odot$ (above the Alfvén point). The radius of each circle is calculated as follows: first the time taken by the solar wind to travel the distance between two consecutive points (centers of circles shown) is estimated, assuming a solar wind speed that is the average of the speeds at the two points. Then we calculate the distance travelled by fluctuations in this time, at a speed given by $\sqrt{Z^2}$, where Z^2 is the turbulence energy at the center of the circle. This distance is added to the radius of the previous circle to compute a *cumulative*

measure of the extent of turbulence influence.

From Figure 7.A.4 we see that two points at heliolatitudes of 60° (red) and 35° (blue) are driven apart by expansion faster than they can influence each other via turbulence. Considering two points at heliolatitudes of 60° (red) and 40° (blue) (initial angular separation of 20°) in Figure 7.A.5, we now see that the regions of turbulent influence overlap marginally.

In the low-latitude case shown in Figure 7.A.6, two points with an initial separation of 25° are able to influence each other via turbulence, in contrast to the high-latitude case in Figure 7.A.4. This is consistent with Figure 7.A.3, and is expected due to the enhanced turbulent driving at low latitudes due to stream interactions [e.g., Roberts et al., 1992; Breech et al., 2008; Usmanov et al., 2014].

Finally, we consider the case of a turbulent signal propagating coherently with a constant speed equal to its initial speed at $20 R_\odot$. Compared with other heliocentric distances, the magnitude of turbulent fluctuations is highest near the Alfvén point (see Figure 8.6), so we expect this estimate of the ROI to be large. Indeed, Figure 7.A.7 suggests that two points with an initial angular separation of 30° lie within each other’s turbulent ROI, provided the initial signal stays coherent with a speed of $\sim 100 \text{ km s}^{-1}$.

7.A.4 Discussion

We have presented preliminary work on estimating a causality threshold for turbulent fluctuations in the expanding solar wind.⁷ To relate these results to the discussion in Section 7.6, we remind the reader of our interpretation of the flocculation observed in the *STEREO* images (Figures 7.2 and 7.3) as the onset of turbulence at large scales once the solar wind passes the first beta unity surface. One might expect the spatial size of these isotropic *flocculae* to correspond to the correlation

⁷ We note prior works that deal with aspects of the same issues [Matthaeus and Goldstein, 1986; Velli et al., 1989; Zhou et al., 1990; Mullan, 1990, 1991; Grappin et al., 1993; Wicks et al., 2013; Verdini and Grappin, 2015].

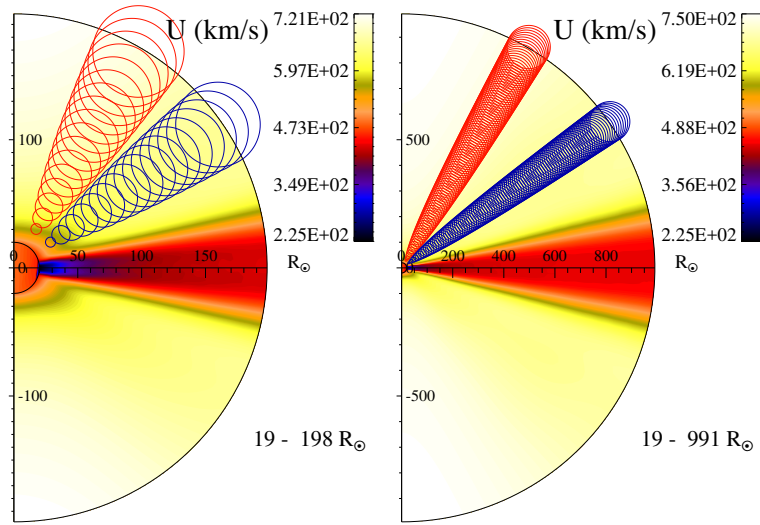


Figure 7.A.4: Meridional plane contours of solar wind speed; circles represent an estimate of the expanding region of influence of turbulent fluctuations, starting from $20 R_{\odot}$ (above the Alfvén point). The red (blue) circles represent the ROI of a point at 60° (35°) heliolatitude.

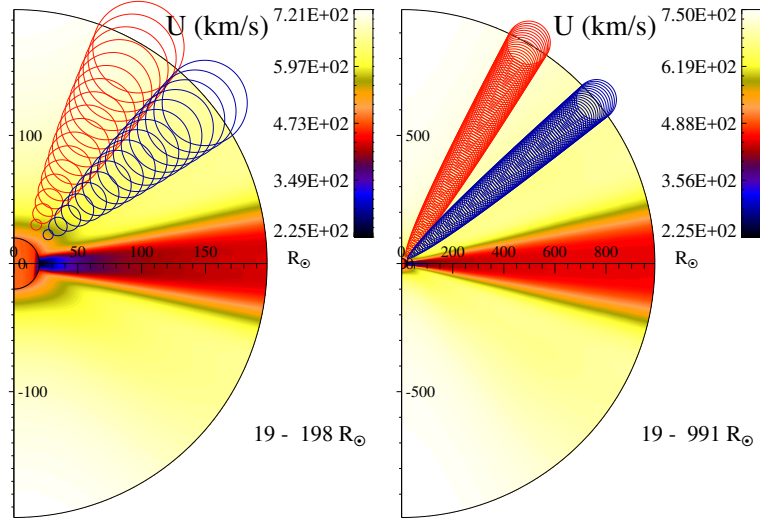


Figure 7.A.5: Meridional plane contours of solar wind speed; circles represent an estimate of the expanding region of influence of turbulent fluctuations, starting from $20 R_{\odot}$ (above the Alfvén point). The red (blue) circles represent the ROI of a point at 60° (40°) heliolatitude.

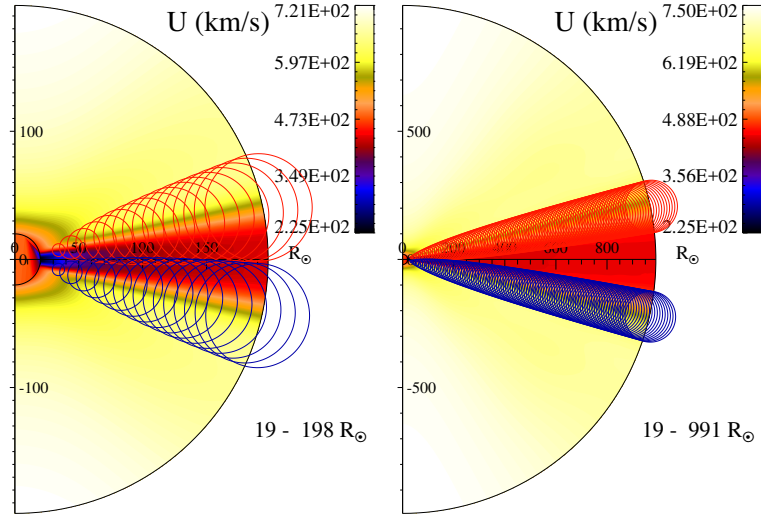


Figure 7.A.6: Meridional plane contours of solar wind speed; circles represent an estimate of the expanding region of influence of turbulent fluctuations, starting from $20 R_{\odot}$ (above the Alfvén point). The red (blue) circles represent the ROI of a point at a low heliolatitude of 12° (-13°). The two points with an initial angular separation of 25° may influence each other via turbulence, in contrast to the high-latitude case in Figure 7.A.4.

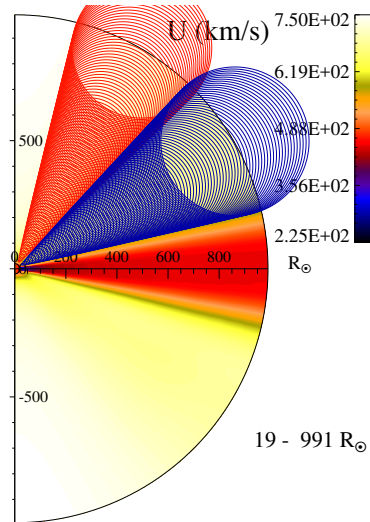


Figure 7.A.7: Here we assume that the turbulent speed of propagation stays constant with heliocentric distance. At the Alfvén point, this speed is $\sim 100 \text{ km s}^{-1}$. The red and blue points lie at heliolatitudes of 60° and 30° , respectively.

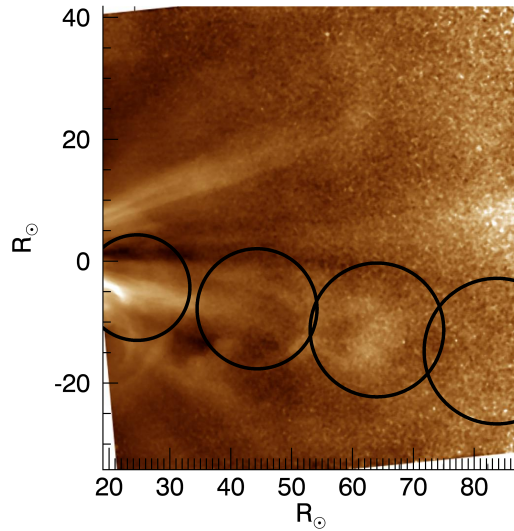


Figure 7.A.8: Turbulence ROI from the simulation superposed on a *STEREO* image showing the development of flocculation.

scale of the turbulence, which can be thought to represent the largest “eddies” in the system. However, the *focculae* are observed to be an order of magnitude *larger* than than extrapolations of the measured correlation scale to the region of interest (Figure 7.A.2). Nevertheless, our estimates of the region of influence of the turbulence are *also* roughly an order of magnitude larger than the correlation scale. This is consistent with the interpretation that the observed dynamics are manifestations of turbulent mixing at the largest possible scales permitted in the expanding solar wind. This hydro-like mixing is possible only after the controlling influence of the solar magnetic field has diminished, past the Alfvén and first beta unity surfaces, and the turbulence has had some time to “age” (Section 5.B). In Figure 7.A.8, we superpose circles representing the turbulence ROI (Equation 7.5) on a *STEREO* image; the *focculae* are evidently comparable in size to the ROI.

The concept of a finite ROI that limits the causal influence of solar wind fluctuations is of relevance to several areas of solar wind studies. We end this appendix with a brief discussion of the implications of a finite ROI for turbulent fluctuations in

the expanding solar wind.

First, the time series of observations made by a single spacecraft in the solar wind is often interpreted as a function of the spatial coordinate varying in the flow direction. This “frozen-in flow” (or Taylor) hypothesis [Taylor, 1938] permits frequency spectra to be interpreted as wavenumber spectra. Furthermore the properties of the wavenumber spectrum such as its possible powerlaw dependence on wavenumber, are typically construed as consequences of local turbulent activity. Notably the spectrum is related formally by a Fourier transform to a spatial correlation function, reflecting correlations associated with a turbulent cascade (Appendix B.3.1). The underlying assumption is that the relevant dynamical speeds, usually MHD speeds, are small compared to the bulk solar wind speed. When the dynamical speeds are small the Taylor hypothesis may formally become a better approximation⁸ but the rate at which MHD-mediated information spreads, compared to the solar wind speeds, also becomes slower in that same limit. Therefore, it is intuitively clear that there must be a maximum time-lag for which such a correspondence is meaningful in terms of dynamically generated correlations. That is, for sufficiently long time lags, the observed spectra and correlations are related to time dependence at the source, and not spatial structure influenced by in-situ MHD activity. This limit has direct consequences for observational analyses [e.g., Matthaeus and Goldstein, 1986], but is not always taken into account [Velli et al., 1989; Zhou et al., 1990].

Second, a limited range of influence can impact global or regional heliospheric numerical computations (or similar astrophysical computations) that adopt turbulence modeling methods (Section 3.2). This is particularly clear when approximating unresolved MHD fluctuations through an eddy viscosity. Such averaged dynamical terms

⁸ It is clear however that there are specific models for which the Taylor hypothesis is clearly invalid, such as whistler waves with phase speed greater than the wind speed. When wave speeds (including the Alfvén speed) become large, the standard Taylor hypothesis may require modification, as discussed, e.g., by Goldstein et al. [1986], Matthaeus [1997], and Klein et al. [2015]. For near-Sun conditions expected for the *PSP* mission, additional factors such as spacecraft speed may enter into modifications of the Taylor hypothesis (see Section 8.A). However, the present appendix does not consider these additional factors that influence applicability of the Taylor hypothesis.

appear in the momentum equation, just as a turbulent resistivity appears in the magnetic induction equation. In a Reynolds-averaging framework [e.g., [McComb, 1990](#)], *all* fluctuations are included in the eddy viscosity. However, for a time-varying system, the very large-scale fluctuations might span distances too large for relevant MHD scale signals to propagate in the available time. Arguably such fluctuations should not be included in the eddy viscosity or, in general, in the unresolved turbulence model (see [Appendix D](#)).

As a third example, consider the impact of causality considerations on the origin of the observed very low frequency fluctuations in the so-called “ $1/f$ ” range [[Matthaeus and Goldstein, 1986](#)]. Can these fluctuations emerge due to in-situ interplanetary dynamics? Should the energy in these fluctuations be included in the large-scale reservoir of energy that actively drives the smaller scale inertial range cascade [see also [Wicks et al., 2013](#)]? It turns out that a similar issue arises in a very different theoretical context when one develops an interpretation of time-domain third-order and higher-order statistics [[Sorriso-Valvo et al., 1999](#); [MacBride et al., 2008](#); [Marino et al., 2012](#)] in terms of spatial lags. In this case the very large spatial lags might need to be excluded in estimating the local cascade rate if the causality limits are exceeded.

More detailed studies of the ROI/causality-threshold are ongoing; in these, we aim to quantitatively address the issues discussed above.

Chapter 8

CONTEXTUAL PREDICTIONS FOR PARKER SOLAR PROBE: CRITICAL SURFACES AND REGIONS

8.1 Introduction

The *Parker Solar Probe* (*PSP*) mission [Fox et al., 2016] is scheduled for a summer-2018 launch, with the goal of exploring for the first time regions of solar wind that are of crucial importance in establishing the heliosphere. While approaching the Sun closer than any prior spacecraft, *PSP* will provide unprecedented high-resolution measurements of the solar corona and the young solar wind, with its main objectives being discovery of the structure and dynamics of the coronal magnetic field and the processes that heat and accelerate the wind and accelerate and transport energetic particles. As the *PSP* makes its high resolution in-situ measurements, a knowledge of the large-scale environment within which these observations exist is of vital importance. This global context may be provided by remote sensing [Bird and Edenhofer, 1990; Vourlidas et al., 2016] and global simulation. The present chapter constitutes the first¹ of a planned series of papers focused on contextual predictions for *PSP* using global simulations of the solar wind.

The transition of the solar corona into the solar wind is accomplished by several dynamical changes in the nature of the flow. The inner corona is magnetically structured, subsonic, and sub-Alfvénic, but as the solar plasma flows out from the corona into the young solar wind, it transforms into a supersonic and super-Alfvénic flow that is dominated by hydrodynamics. As discussed in the preceding chapter, this transition may coincide with the onset of large-scale turbulence [DeForest et al., 2016; Chhiber

¹ Chhiber et al. [2018d]

et al., 2018c,b], and mark the outer boundary of a zone of preferential ion heating [Kasper et al., 2017].

Useful markers that characterize this transition are the sonic critical surface, the Alfvén critical surface, and the first $\beta = 1$ surface (the plasma- β is the ratio of gas to magnetic pressure). In particular, when the flow speed U exceeds the Alfvén speed V_A , the magnetic field rigidity can no longer enforce plasma co-rotation [Weber and Davis, 1967], or overcome the differential ram pressure due to shearing interactions between neighbouring wind streams. And when the plasma- β increases above unity, gradients in the plasma (thermal) pressure may displace the magnetic field and more isotropic motions are possible [Chhiber et al., 2018c]. The region in which these two crucial conditions, $U > V_A$ and $\beta \sim 1$, are attained becomes in effect the region where the corona gives up control of the solar plasma, and the solar wind as an independent entity is born.

In this chapter we employ well-tested global magnetohydrodynamic (MHD) simulations of the solar wind [Usmanov et al., 2011, 2012, 2014, 2016a,b; Chhiber et al., 2017a, 2018c; Usmanov et al., 2018], that are self-consistently coupled with a turbulence transport model (Chapter 4), to study and characterize this region of transitions and to make contextual predictions for the *PSP* mission.² We incorporate the effects of long-term solar variability [Cane et al., 1999; Owens and Forsyth, 2013] by varying magnetic source dipole tilts and employing magnetogram-based boundary conditions. The simulation results are compared with a variety of remote sensing observations, demonstrating how the two approaches may be combined to gain insights regarding large scale heliospheric conditions in this region. Global simulation and remote sensing thus generate mutual support, and in turn, provide valuable context for the finer details that emerge from in-situ measurements. Subsequent papers in this series on contextual predictions for *PSP* will focus on turbulence properties along the spacecraft’s trajectory, on modifications of Taylor’s hypothesis for *PSP* [Matthaeus, 1997;

² Note that our use of “transition” here should not be confused with the well-known transition region that lies just above the chromosphere [e.g., Cranmer et al., 2007].

[Klein et al., 2015](#)], and on solar wind azimuthal flow.

This chapter is organized as follows: In Section 8.2 we provide background on critical surfaces and physically distinct regions of the inner wind, discussing recent work that motivates the present study. An overview of the *PSP* trajectory is provided in Section 8.3. Results are presented in Section 8.4, including comparisons of model output with remote sensing observations and contextual predictions along the *PSP* trajectory. We conclude with discussion in Section 8.5. An appendix (8.A) presents preliminary results on predictions for the turbulence environment encountered by the *PSP*, including an evaluation of the validity of the Taylor frozen-in hypothesis.

8.2 Theoretical and Observational Background

A mathematical discussion of a critical point of a system of ordinary differential equations may be found in standard texts [e.g., [Boyce et al., 1969](#)]. At such a point (also known as an *equilibrium point*), the solution is not uniquely determined, and an appeal must be made to physical effects outside the local mathematics, such as boundary conditions. Two such points are frequently discussed within the context of the solar wind – the sonic and Alfvénic critical points, where the flow speed equals the sound speed and the Alfvén speed, respectively.

One encounters the notion of a critical point in even the simplest, spherically symmetric, stationary and isothermal model of the solar wind (Section 2.1). As additional physical effects are added to a solar wind model, the mathematical structure of the equations changes, and with it the nature of the critical point. For instance, including electrons in a two-fluid model would introduce two sound speeds and two possible critical points. As we will see in Section 8.4, inclusion of the electron pressure in a two-fluid model shifts the location of the sonic point to a slightly greater heliocentric distance. Therefore, the “singular” aspect of a critical point is of limited physical relevance and it is questionable whether spacecraft data may be used to localize a definite critical point.

Nevertheless, from a physical perspective, these points (which become *critical surfaces* in a three-dimensional context) imply the existence of separate regions in the solar wind which are dominated by different physical effects. For instance, counterpropagating Alfvénic fluctuations may effectively generate turbulence in the inner corona [Matthaeus et al., 1999b], but above the Alfvén critical surface the population of inward propagating modes is diminished [Bruno and Carbone, 2013], and Alfvén wave collisions are no longer an efficient mode of turbulence production [Verdini and Velli, 2007]. The Alfvén surface also effects a separation of coronal regions having different angular flow properties; below this surface, the torque produced by the magnetic field is sufficiently strong to transfer angular momentum and produce a corotation of the coronal wind with the sun, while above the critical surface the azimuthal velocity of the solar wind drops rapidly with distance [Weber and Davis, 1967].

In addition to the demarcation of different regions by critical surfaces, the general vicinity of the surfaces may be a site of interesting physics, such as enhancement in turbulent fluctuations [Lotova et al., 1985]. These surfaces also signify the point beyond which MHD wave modes are unable to communicate upstream, because above the sonic (Alfvénic) critical surface the speed of propagation of information by sonic (Alfvén) modes is smaller than the speed of their advection downstream by the wind. Further, signatures of different coronal and solar phenomena may be evident in the location and morphology of critical surfaces, and may manifest in their temporal and spatial variability [Grail et al., 1996; Lotova et al., 1997].

Recent observations by DeForest et al. [2016] and the subsequent numerical investigations by Chhiber et al. [2018c] (described in detail in Chapter 7) provide additional *current* motivation for the present study. Making use of highly processed *STEREO* images from December 2008, DeForest et al. [2016] found a textural shift in the solar wind flow between heliocentric distances of 20 – 80 R_{\odot} . The images revealed that radially aligned, “striated” patterns gave way to more isotropic structures, termed “*focculae*”, at distances of a few tens of solar radii. Chhiber et al. [2018c] performed

global solar wind MHD simulations, representing nominal large-scale solar wind conditions at December 2008, and superposed plasma- β unity surfaces computed from these simulations on the *STEREO* images. They found that the observed textural shift occurred *above the first plasma- $\beta = 1$ surface*. The emerging interpretation states that as the solar wind passes into the region where $\beta \equiv 8\pi P/B^2 \geq 1$, mechanical pressure may overcome the organizing influence of the magnetic field B , thus enabling the observed isotropic motions, which may be triggered by hydrodynamic shearing between wind streams [e.g., [Roberts et al., 1992](#)]. A further point of interpretation (Section 7.A), consistent with the one above, is that the *floculae* may be a manifestation of solar wind fluctuations interacting at the largest scales that are causally related through turbulence in the expanding solar wind (Section 7.A).

The Alfvén and $\beta = 1$ surfaces discussed above may also be of significance to the phenomenon of preferential ion heating in the solar wind [e.g., [Marsch, 2006](#)]. Recently, [Kasper et al. \[2017\]](#) found evidence for a zone, extending from just above the transition region ($\sim 0.3 R_\odot$) to a distance of tens of solar radii, where α -particles are heated preferentially over protons. The outer boundary of this zone is likely associated with the Alfvén and $\beta = 1$ surfaces.

8.3 Sampling of the Three-dimensional Heliosphere by Parker Solar Probe

The preceding section serves to emphasize the importance and relevance of the critical surfaces. Yet, spacecraft missions hitherto have not sampled the critical surfaces in-situ, with the closest heliocentric distance of approach being *Helios*' perihelion at 0.29 au ($\sim 62 R_\odot$). *PSP* is all set to change this by spending “a total of 937 hours inside $20 R_\odot$, 440 hours inside $15 R_\odot$, and 14 hours inside $10 R_\odot$ ” over its 7-year nominal mission duration [[Fox et al., 2016](#)]. The spacecraft will most likely spend a very substantial amount of time under the first $\beta = 1$ surface, which is inferred to lie between 20 and $60 R_\odot$ [[DeForest et al., 2016](#); [Chhiber et al., 2018c](#)].³ According to

³ The location of the Alfvén and first unit beta surfaces may dip below $10 R_\odot$ at the heliospheric current sheet (HCS). It must be noted that global models are likely to overestimate the spatial extent

observations and models, the Alfvén surface lies between $\sim 10 - 30 R_{\odot}$ [Mullan, 1990; DeForest et al., 2014; Lotova et al., 1997; Cranmer et al., 2007; Verdini et al., 2010; Chhiber et al., 2018c], and the *PSP* could spend a substantial time under this surface as well. The sonic surface may lie below the *PSP*'s lowest perihelion at $9.86 R_{\odot}$, since coronal models often predict a location of $2 - 5 R_{\odot}$, although these predictions are applicably mainly to coronal hole regions. At low latitudes, the sonic point may lie as far as $20 R_{\odot}$ [Lotova et al., 1997].

Figure 8.1 shows a three-dimensional (3D) perspective of the *PSP* trajectory. The spacecraft ephemeris was extracted from a *NASA SPICE kernel*, and the trajectory is presented here in the Heliocentric Inertial (HCI) coordinate system [e.g., Fränz and Harper, 2002]. Here the *XY*-plane is defined by the Sun's equator of epoch J2000; the *+Z*-axis is parallel to the Sun's rotation axis of epoch J2000, pointing toward the Sun's north pole; the *+X*-axis is the ascending node of the Solar equatorial plane on the ecliptic plane of J2000; and the origin of the coordinate system is the Sun's center of mass. The *PSP* trajectory in 3D space is shown in red, while the blue curves represent projections of the 3D trajectory onto the *XY*, *XZ*, and *YZ* planes. The Earth (at time of launch) and the Sun are represented by the blue dot and the '*', respectively (not to scale). The trajectory shown includes all orbits in the 7-year nominal mission duration from 31st July 2018 to 1st September 2025.

As the *PSP* makes its high resolution in-situ measurements, a knowledge of the large-scale environment within which these observations exist is of vital importance. The large scales traversed by *PSP* orbits are illustrated strikingly in Figure 8.1, which serves to reinforce the appropriateness of large-scale global simulation (Chapter 4) for contextual predictions for the mission.

8.4 Results

The present chapter is based on analysis of two classes of simulation runs: (I) In the first case we employ a dipole magnetic field at the inner boundary, with the dipole

of the HCS due to their coarse resolution.

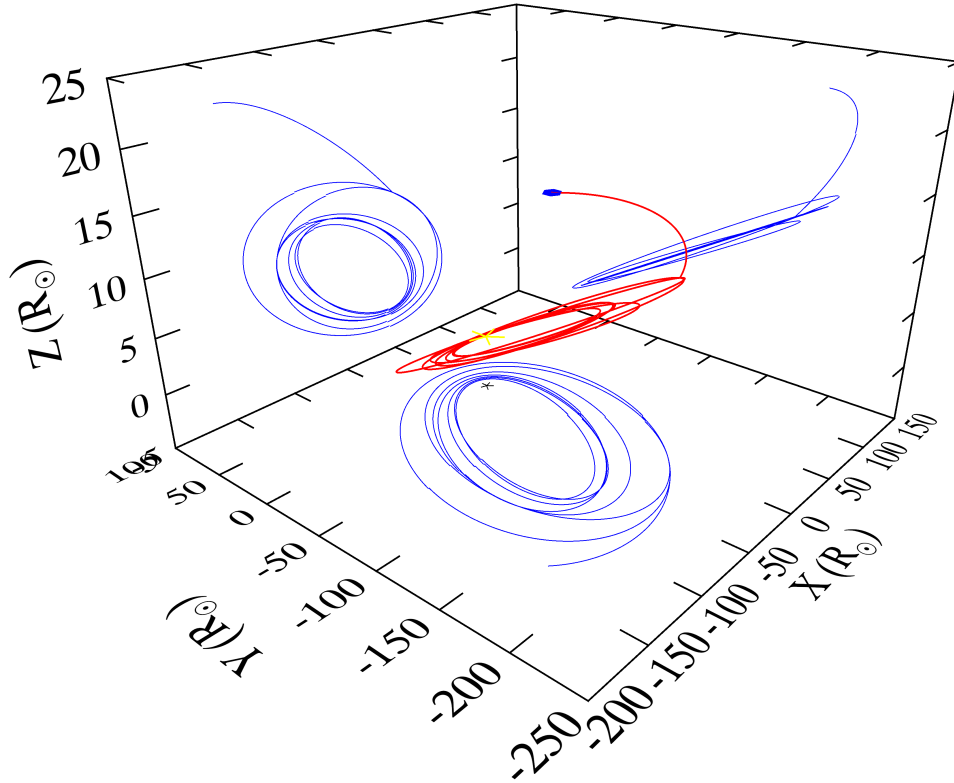


Figure 8.1: *PSP* trajectory in HCI coordinates (see text for details). The origin is the Solar center of mass and the XY -plane is the Solar equatorial plane. The red curves show the trajectory in 3D space and the blue curves are its projections onto the XY , XZ , and YZ planes. The ‘*’ symbol and blue dot represent the positions of the Sun and Earth, respectively.

tilted at angles of 0° , 5° , 10° , and 30° (Runs I-A, I-B, I-C, and I-D, respectively) to the solar rotation axis. A 60° run was also analyzed, but the results were found to be similar to the 30° simulation. The magnitude of the dipolar field is set to 12 G to match the magnitude of the heliospheric magnetic field observed by *Ulysses* in January 2008. This simple configuration has both open (near the pole of the dipole) and closed (near its equator) magnetic field geometry, and allows for simulation of both coronal-hole-like and streamer-like flows. This gives us a representation of the ambient, large-scale bimodal solar wind flow during periods of minimum solar activity [Cane et al., 1999; McComas et al., 2003; Usmanov and Goldstein, 2003; Owens and Forsyth, 2013]. (II) In the second case the MHD code is driven by a magnetic field at the base obtained from July 1989, July 1994, and December 2008 magnetogram data (Runs II-A, II-B, and II-C, respectively) published by the Wilcox Solar Observatory.

The simulation domain extends from the coronal surface at $1 R_\odot$ to 3 au. Runs of type I use the turbulence transport model described in Chapter 4 in the full domain, while runs of type II use the WKB model described in Appendix C for the region between the coronal surface and $45 R_\odot$. The output of this model is then used as an initial condition for the turbulence transport model. The following input parameters are specified at the coronal surface: the driving amplitude of Alfvén waves ($\sim 35 \text{ km s}^{-1}$), the density ($\sim 1 \times 10^8 \text{ particles cm}^{-3}$) and temperature ($\sim 1.8 \times 10^6 \text{ K}$). The magnetic field magnitude is assigned either using a source magnetic dipole on the Sun’s poles (with strength 12–16 G to match values observed by *Ulysses*) or from solar magnetograms. The input parameters also include the normalized energy difference σ_D , the fraction of turbulent energy absorbed by protons f_p , and the Kármán-Taylor constants α and β (see Table 4.1).

8.4.1 Surfaces: Meridional Plane Pictures

The significance of the sonic and Alfvén critical surfaces, as well as the first $\beta = 1$ surface, was discussed in Section 8.2. Operationally the Alfvén critical surface is defined by the set of points, scanning outward, at which the solar wind speed first

exceeds the Alfvén speed $V_A = B/\sqrt{4\pi\rho}$. Similarly, the sonic surface is defined by the set of points, scanning outwards from the sun, at which the total solar wind speed becomes larger than the sound speed $c_s = \sqrt{\gamma P_p/\rho}$. Here γ is the polytropic index and P_p is the proton pressure. Another definition of the sound speed is $c'_s = \sqrt{\gamma P/\rho}$, where $P = P_p + P_e$ includes the electron pressure P_e . We show the sonic surfaces computed using both these definitions to stress that the inclusion of various physical effects may change the location of the surface, and it is perhaps more appropriate to envision a transonic *region* [Lotova et al., 1997], rather than a highly localized surface. Nevertheless, at the fluid level of description P may be considered the more appropriate measure of pressure.

The plasma beta is also defined in two ways; in terms of the proton beta, $\beta_p = 8\pi P_p/B^2$, and in terms of the total electron plus proton beta, $\beta_{p+e} = 8\pi(P_p + P_e)/B^2$. The first $\beta = 1$ surface is identified as the set of points, scanning outward, at which $\beta = 1$ is first encountered. This is done in the analysis separately for proton beta and for total beta.

Figure 8.2 depicts the projection of these surfaces onto an arbitrarily selected meridional plane at 37° heliolongitude for Run I-C, a 10° tilt dipole driven case (Run I-A is axisymmetric). Unless specified otherwise, simulation data are plotted in the Heliographic Coordinate system [HGC, Fränz and Harper, 2002], in which Heliographic latitude is measured from the solar equator positive towards North, Heliographic longitude is defined in the direction of planetary motion, with the XY -plane defined by the solar equator of date.

The surfaces show a laminar appearance, and display a very organized ordering. For all latitudes well separated from the current sheet, the $\beta = 1$ surface is the most distant, with the Alfvén surface contained well within it, and the sonic surface(s) lower still, in the range $4 - 5 R_\odot$. The most dramatic feature is the rearrangement of the surfaces near the heliospheric current sheet region, an effect that can completely reverse the surface to an opposite ordering. In fact one can find a substantial region in which the $\beta = 1$ surface lies at lower radial distances than the Alfvén surface. There are

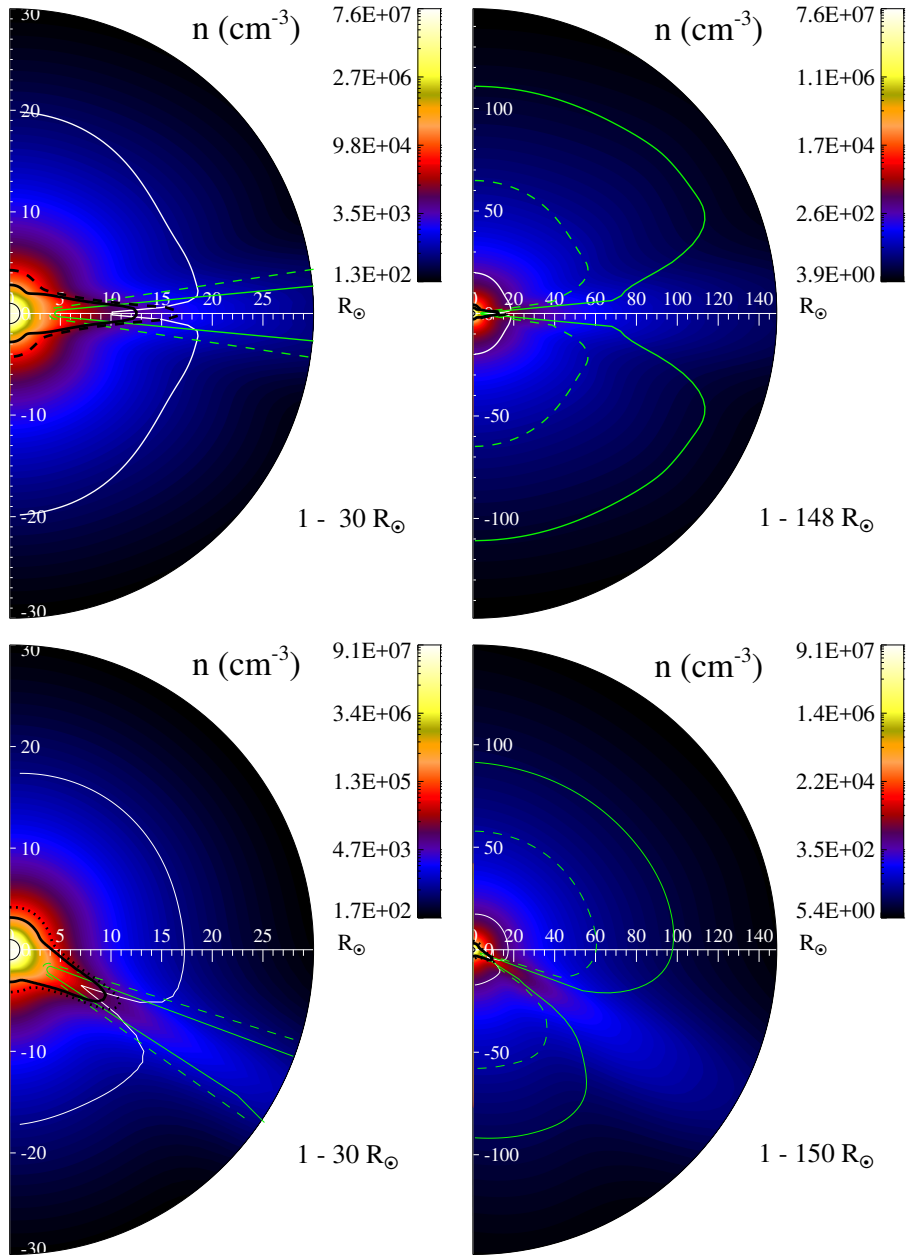


Figure 8.2: Meridional planes from untilted dipole Run I-A (top) and 30°tilted dipole Run I-D (bottom). The black curves show the sonic surface (solid line using c_s with just proton pressure and dashed line using c'_s which includes proton and electron pressures; see text), the white curve shows the Alfvén surface, and the green curves show the first unity β surface (solid line shows $\beta_p = 1$ and dashed line shows $\beta_{p+e} = 1$).

also regions, much smaller in these particular cases, in which the sonic surface is found at radial distances above the Alfvénic surface. In those small regions, the solar wind would have the somewhat anomalous character of being super-Alfvénic but subsonic. Alfvén wave pressure in such regions may be able to increase the mass flux of the resulting wind at higher radial distances [see [Leer et al., 1982](#)].

Before proceeding with further analysis, we want to emphasize that there are unavoidable limitations in this use of the simulations. A general and obvious comment is that our MHD solutions are based on simplified data that does not represent the actual boundary conditions corresponding to the solar wind during the *PSP* passage. More specifically, we emphasize that the discrete spatial resolution of the MHD model limits the thinning of the heliospheric current sheet (HCS). Therefore both the HCS, and the much wider plasma sheet surrounding it [[Winterhalter et al., 1994](#)], are expected to be broader in the simulation than in the actual solar wind. A rough estimation based on published data suggests that the real HCS may be a factor of ~ 5 thinner than what we report here. Nevertheless, within the resolution parameters of the code, the physics of the simulation is deemed to be accurate, so that, for example, the inversion of critical surfaces is expected to occur, albeit over a thinner region, in the solar minimum conditions seen in some *PSP* orbits.

8.4.2 Remote Sensing Context

We recall briefly the novel use of *STEREO* Heliospheric Imaging (HI) data by [DeForest et al. \[2016\]](#), which examined a series of images of the inner solar wind and argued, based on physical grounds, that the observed striation-flocculation transition occurred in the neighborhood of the first plasma- $\beta = 1$ surface. [Chhiber et al. \[2018c\]](#) employed MHD simulations, similar to those analyzed here, to provide confirming evidence of this interpretation (Figure 8.3). We revisit this analysis here. Figure 8.3 shows that the region in which the *striae* gives way to *focculae* is commensurate with the region in the simulation in which the first $\beta = 1$ surface is encountered, as the wind transitions from magnetic control to hydrodynamic control.

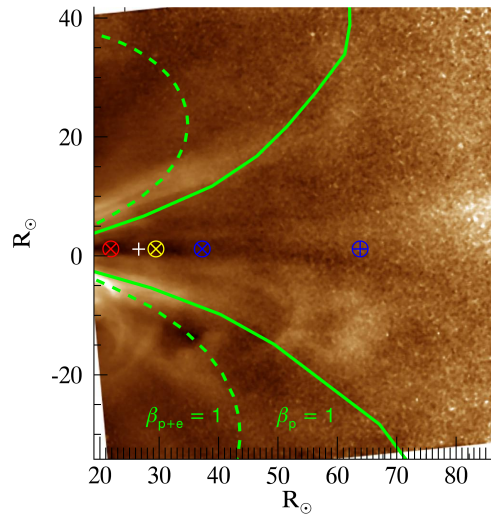


Figure 8.3: Green curves show the first unity beta surfaces (solid line for $\beta_p = 1$; dashed line for $\beta_{p+e} = 1$) computed from the model superimposed on *STEREO* image from DeForest et al. [2016]. White ‘+’ shows location of enhanced turbulence inferred by Lotova et al. [1985] (see Figure 8.6); *Helios* perihelion is shown as ‘ \oplus ’; the lowest three perihelia of the *PSP* are shown as ‘ \otimes ’.

Recently, [Kasper et al. \[2017\]](#) found evidence for a zone, extending from just above the transition region ($\sim 0.3 R_{\odot}$) to a distance of tens of solar radii, where α -particles are heated preferentially over protons. The lower boundary of this zone would likely be at the chromospheric transition region, where the plasma collisionality changes from strong to weak (see Chapter 5), thus permitting nonthermal physics to produce observed temperature anisotropies [e.g., [Marsch, 2006](#)]. It is conceivable that this zone of preferential heating ends at the first beta unity surface, since kinetic temperature anisotropies are generally associated with $\beta \lesssim 1$ [e.g., [Matteini et al., 2012](#)]. This zone should be detected by the *PSP* as it reaches below the first beta unity surface.

The location of the sonic critical surface as a function of latitude was estimated from scintillation data by [Lotova et al. \[1997\]](#). During solar minimum the surfaces were inferred to be relatively spherical, while at solar maximum the surfaces were of more irregular shape. Figure 8.4 shows the *Lotova* results and offers a comparison with sonic critical surfaces obtained from two MHD simulations – a solar minimum magnetogram and a solar maximum magnetogram. We note a reasonable qualitative similarity, especially regarding the oblateness at the poles during solar minimum and the spherical but jagged shape during solar maximum. These results suggest that variations in the morphology of the critical surfaces can be used to infer the state of solar activity.

Another look at the properties of the solar wind in the critical region is provided by reproducing the scintillation intensity data of [Lotova et al. \[1985\]](#) in Figure 8.6. For comparison we show the radial profiles of two parameters obtained with from an untilted dipole simulation (Run I-A). The parameters shown are the radial solar wind speed V_r and the turbulence energy density (per unit mass) Z^2 (Equation 4.20). The scintillation profile shows a feature in the range of $20 - 30 R_{\odot}$ that is interpreted as a region of enhanced turbulence, giving rise to enhanced radio scattering from density irregularities. Shaded regions in the plot indicate the range of radii at which the Alfvén and sonic surfaces are found in the ecliptic region in the simulation. The Figure also shows *PSP* perihelia for several orbits. We note that the scintillation feature lies very

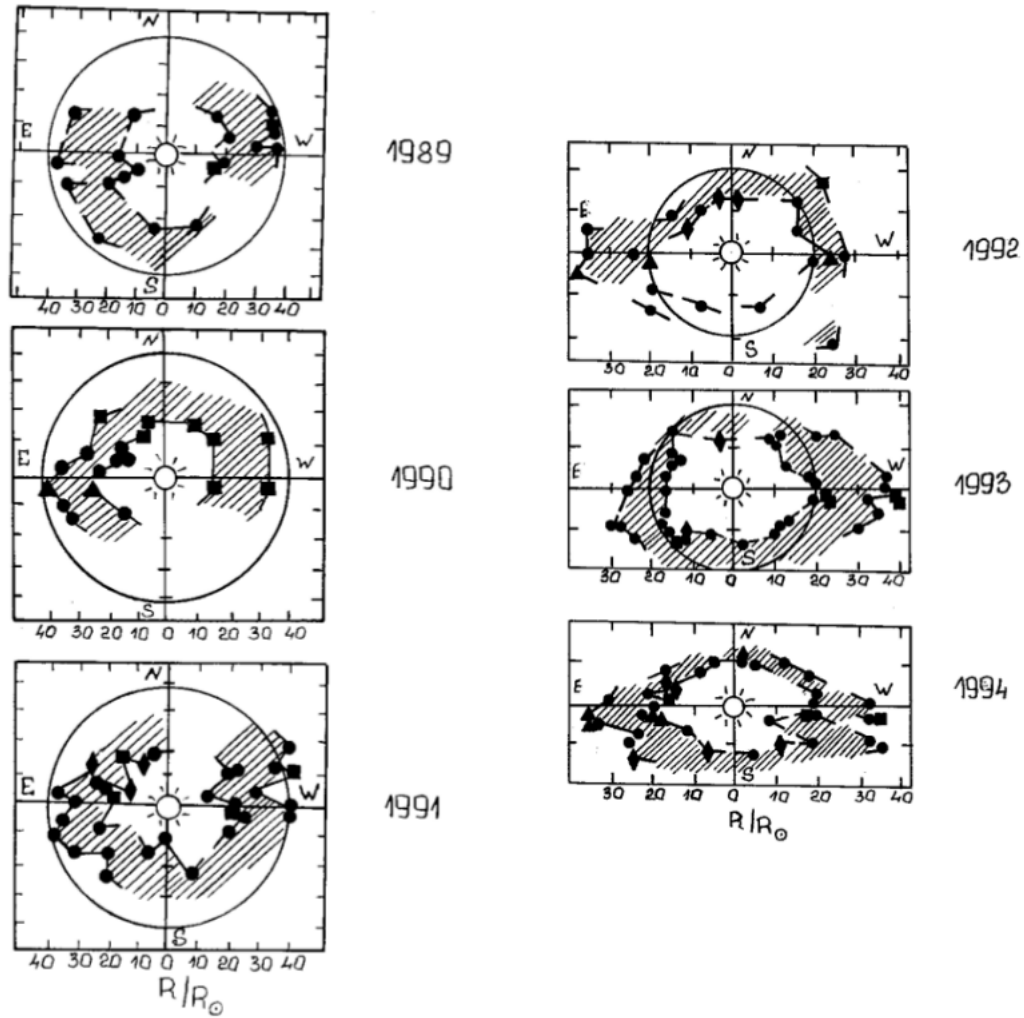


Figure 8.4: Transonic regions from [Lotova et al. \[1997\]](#), showing the transition from spherically symmetric but jagged morphology at solar maximum (1989), to oblateness at the poles during solar minimum (1994; see [Figure A.1](#)). *Figure reproduced from [Lotova et al. \[1997\]](#) with permission from [Springer Nature](#) (see [Appendix E](#)).*

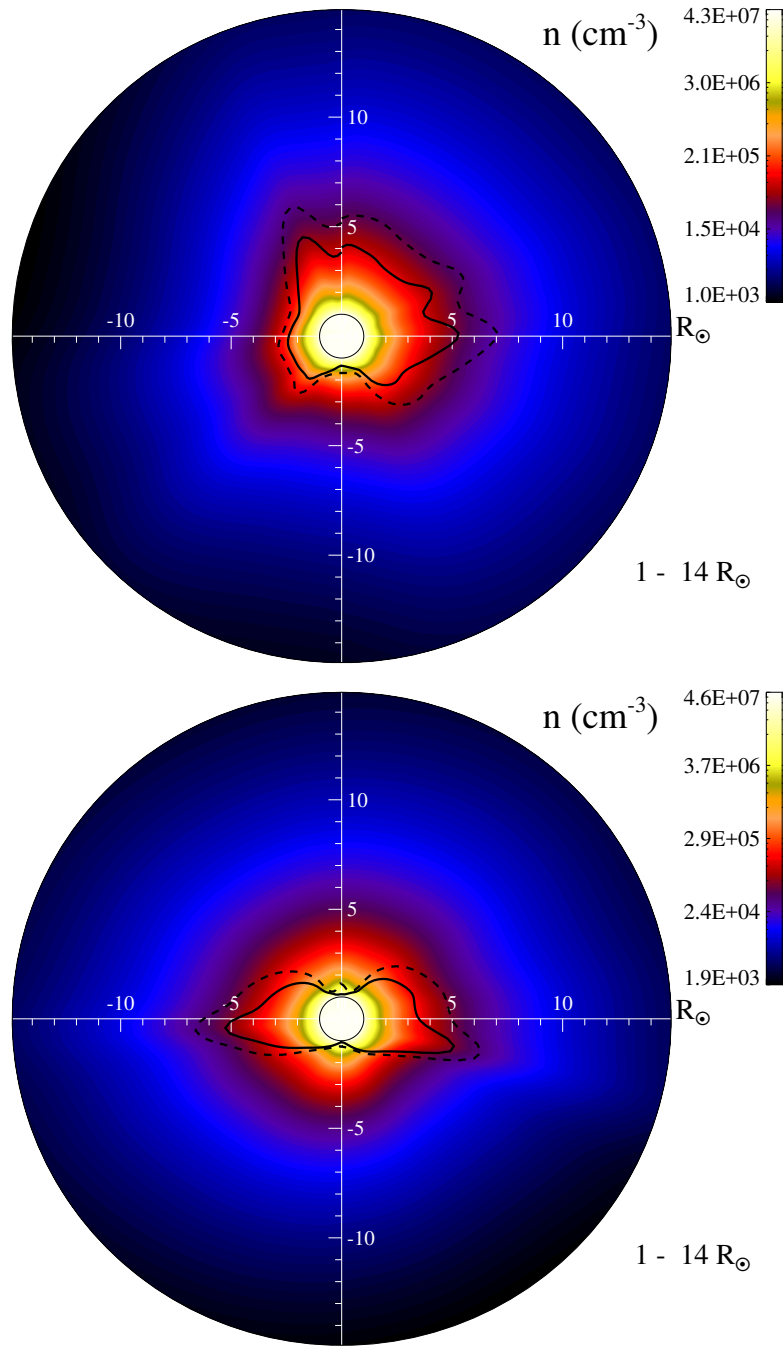


Figure 8.5: Sonic surfaces (solid line using c_s with just proton pressure and dashed line using c'_s which includes proton and electron pressures; see text) from Runs II-A and II-B, using solar maximum (July 1989) and solar minimum (July 1994) magnetograms, respectively. The transition from solar maximum to solar minimum is qualitatively consistent with the one seen in Figure 8.4.

close to the position of the maximum turbulence energy from the simulation, and is also close to the locations of the sonic and Alfvénic critical surfaces in the simulation. This enhancement in turbulence may be caused by the interactions of counter-propagating Alfvén waves [Matthaeus et al., 1999b]. The acceleration of the wind is also initiated in this region.

8.4.3 What *PSP* will see: Dipole-based Simulations

Using the *PSP* trajectory and a coordinate transformation to link it to the global MHD solution, one may graphically illustrate the relationship between the *PSP* orbit and the simulated heliospheric structure. Superposing the orbits on the simulation results should not be construed as a prediction, since the boundary data, even if compatible with projected future conditions, is necessarily imprecise. However this exercise does present a possible context for the *PSP* mission. Portraying this relationship is not trivial, because the critical surfaces rotate with the Sun (here, a steady state in that frame), while the *PSP* orbit traces a curve in three-space that does not precisely lie in a single plane in any inertial frame. (see Fig. 8.1).

To produce an illustrative comparison of the orbits and critical surfaces, we may choose to look at a sequence of (non-inertial) meridional planes that always contain the *PSP* orbit. In this frame the orientation of the solar dipole field rotates at a non-constant angular frequency. Figure 8.7 depicts such a sequence of meridional planes. The MHD simulation used for this illustration employed a 10° tilted dipole boundary condition (Run I-C), representing solar-minimum conditions likely to be sampled by the *PSP* in its early orbits. The position of *PSP* in each frame (during the 8th orbit; see Figure 8.9) is at the center of the yellow ‘+’ symbol. The times are chosen to correspond to *PSP* passing over a critical surface. The plots are labeled by time measured in days-from-launch. A video animation of these figures is available as Supplementary Material. An animation illustrating *PSP* crossings of critical surfaces in the final orbit, during solar-maximum conditions (Run II-A), is also available. A video animation of these figures is available [online](#).

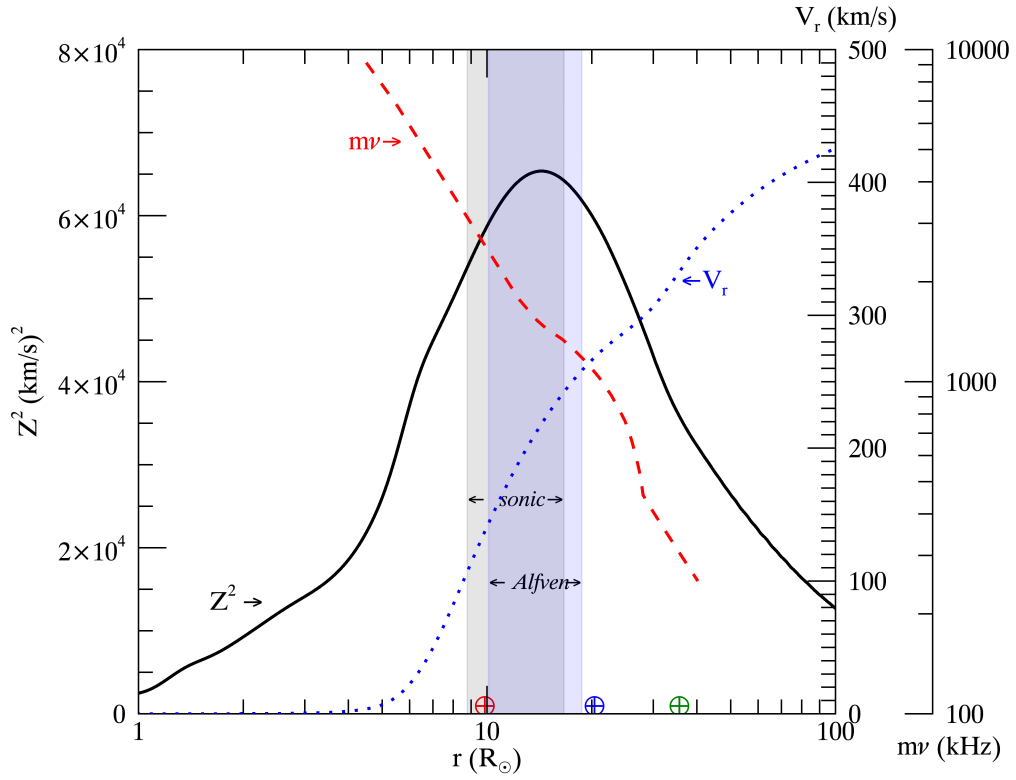


Figure 8.6: Enhanced scintillation ($m\nu$) region from the observations of [Lotova et al. \[1985\]](#), seen as a bump at $\sim 20 - 30 R_{\odot}$ in the dashed red curve. The radial solar wind speed V_r (dotted blue curve) and the turbulence energy density (per unit mass) Z^2 (solid black curve) from Run I-A are also shown, along with shaded bands representing the locations of the Alfvén (pale blue band) and sonic (grey band) surfaces in the ecliptic region of the simulation. The final three perihelia of the *PSP* are represented as \oplus symbols.

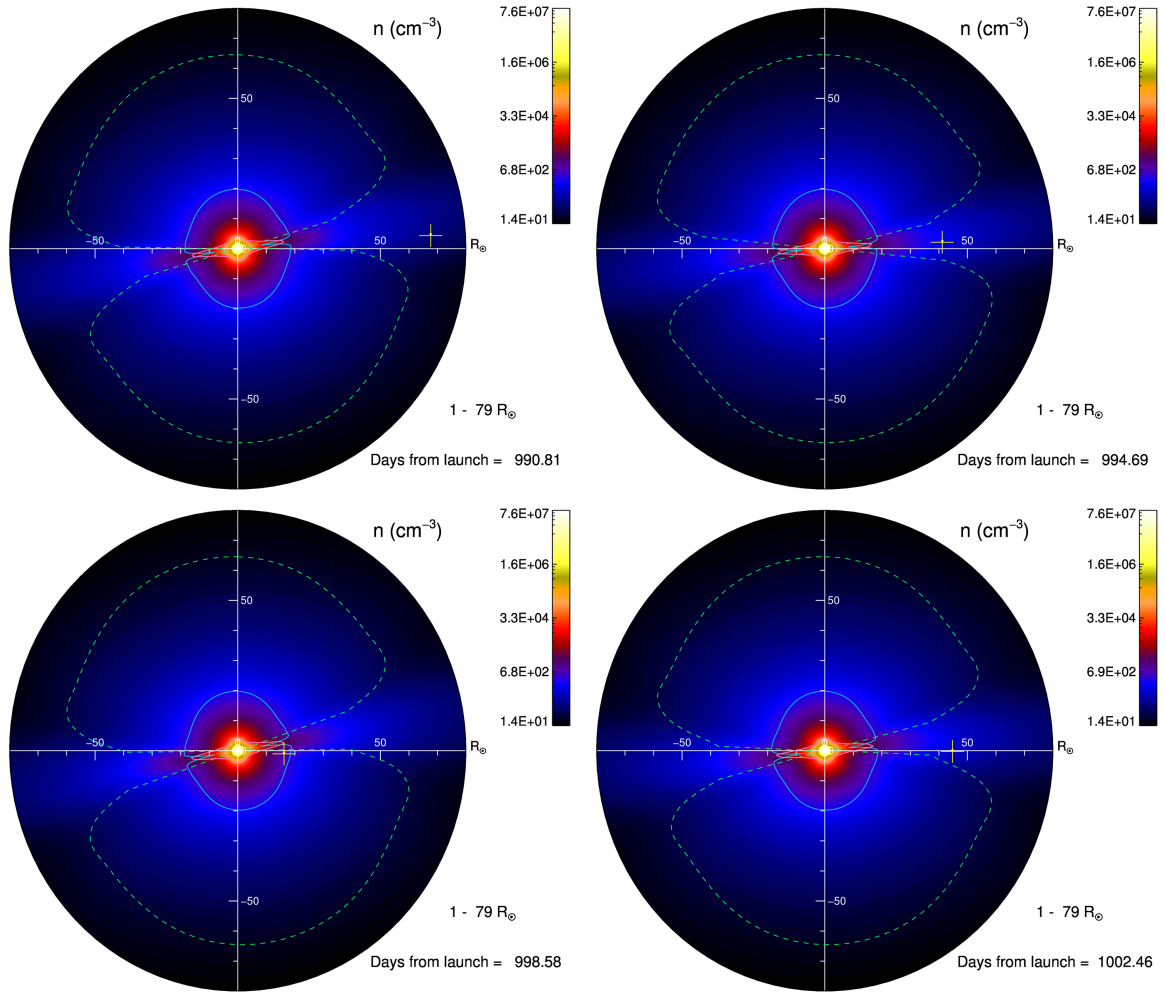


Figure 8.7: *PSP* crossings of the critical surfaces are illustrated by a sequence of meridional planes that contain the spacecraft trajectory. The 8th orbit is depicted in a 10° dipole simulation (Run I-C; see top panel of Figure 8.9), representing solar-minimum conditions. The sonic, Alfvén, and first (proton+electron) beta unity surfaces are depicted as solid pink, solid blue, and dashed green curves, which are superposed on contours of proton density. The *PSP* position is at the center of the yellow ‘+’ symbol. A video animation is available [online](#).

Another interesting way to visualize the relationship between the *PSP* orbit and the critical surfaces is to tally the time spent in each orbit within the $\beta = 1$ surface (henceforth β refers to the “two-fluid” plasma beta β_{p+e}), the Alfvén surface and the sonic surface. As a first example of this compilation, Figure 8.8 (top) shows the residence time within each of these regions, using the planned *PSP* orbits, for the case of a solar wind with untilted dipole boundary conditions. The upper section of the plot shows, as functions of time, the variation of orbital radial distances, as well as radial position of the critical surfaces at the angular position (heliolatitude and heliolongitude) of the *PSP*. This directly illustrates *PSP*'s penetration of the critical surfaces at various times.

Referring to the lower section that shows accumulated time within critical surfaces, for each orbit, we see that, beginning with orbit 8, this virtual *PSP* mission penetrates the Alfvén surface for 18 hours or more for all subsequent orbits to 25. Beginning with orbit 10, *PSP* spends between 15 and 40 hours in each plotted orbit below the predicted sonic surface. There are no orbits falling below the $\beta = 1$ surface. This set of predictions is somewhat anomalous due to the lack of dipole tilt, so that the orbits almost always fall in the (artificially wide) high- β current sheet region.

Figure 8.8 (bottom) shows a similar compilation done for a 5° dipole tilt run. We can see now, as would be expected, that the encounters with critical surfaces have a strong dependence on the dipole tilt angle, which translates into the degree of latitudinal excursion of the HCS. In fact, for this case the critical surface are frequently seen at larger heliocentric distances, with significant consequences for the sub-critical-surface residence times. We now see that the $\beta = 1$ surface is crossed relatively early, in orbit 4, during which the *PSP* remains inside that surface for more than 50 hours. The pattern of crossing the critical surfaces subsequently become more irregular as the perihelia descend. It is interesting to note that for later orbits, the *PSP* might spend the largest amount of time within any one of the three surfaces. Furthermore, for all orbits after 7, the *PSP* spends at least 20 hours within at least one of the critical surfaces. These 20 to 40 hour periods will represent opportunities for crucial

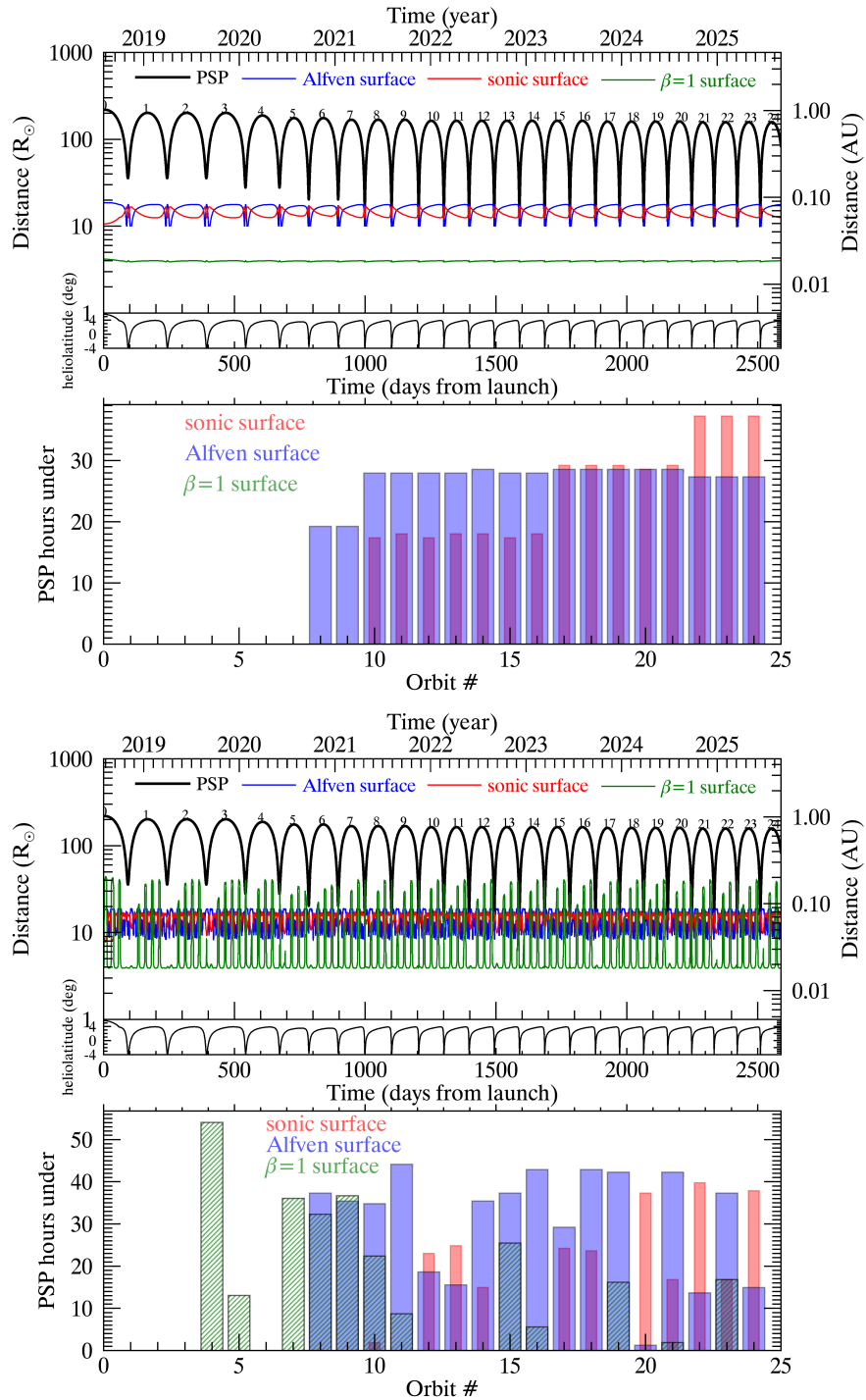


Figure 8.8: *PSP* surface crossings from simulations with 0° (top) and 5° (bottom) dipole tilt. In each plot, the top section shows the radial and latitudinal position of the *PSP* for each orbit, and the radial position of the critical surfaces, at the angular position of the *PSP*. The bottom section shows the time spent by the *PSP* under each surface, per orbit. The striped green, lavender, and narrow red bars represent the $\beta = 1$, Alfvén, and sonic surfaces, respectively.

observations. For instance, below the Alfvén surface the *PSP* might detect a large population of inward propagating Alfvén modes, and the enhanced turbulence seen in Figure 8.6 could be detected in the trans-Alfvénic region.

Two more cases with dipole boundary conditions are shown in Figure 8.9, with tilt angles of 10° and 30°. The results for a 60° dipole run (not shown) are very similar to the 30° case. It is apparent that the $\beta = 1$ surface is found at considerably larger radial distances as the tilt angle is increased. During solar maximum, the *PSP* is therefore likely to spend more than a hundred hours under the first beta unity surface per orbit. Furthermore, Figure 8.9 indicates that no time is spent within the sonic surface during any of the orbits in the 30° dipole case, except for a few hours during Orbit 21. The reason for this can be understood from the discussion of Figure 8.5 – Since the *PSP* trajectory stays within low heliolatitudes, it may be able to sample the extended portion of the sonic surface during solar minimum; However, during solar maximum, the height of this surface is generally too low to be crossed at the latitudes sampled by the spacecraft (see also Figure 8.2).

8.4.4 What *PSP* will see: Magnetogram-based simulations

Here we briefly show results for two cases in which the MHD simulation is driven by magnetogram: one from solar minimum conditions (July 1994; top panels) and another from solar maximum conditions (July 1989; bottom panels). Examining the solar minimum case, shown in the top panels of Figure 8.10, one sees immediately that the residence times below the $\beta = 1$ surface are much more irregularly distributed over the orbits compared to the dipole source cases. This reflects the relative complexity in space of the solar wind due to the complexity of the boundary data. Nevertheless it is a solar minimum condition, and the residence times under the Alfvén and sonic surfaces rarely, if ever, exceed twenty hours in a single orbit. The lower two panels of Figure 8.10 show a solar maximum case for a July 1989 magnetogram. The residence times under the beta=1 surface are again irregular, exceeding 100 hours during orbits 6 and 13. There are only a few orbits in which the Alfvén surface is encountered, and

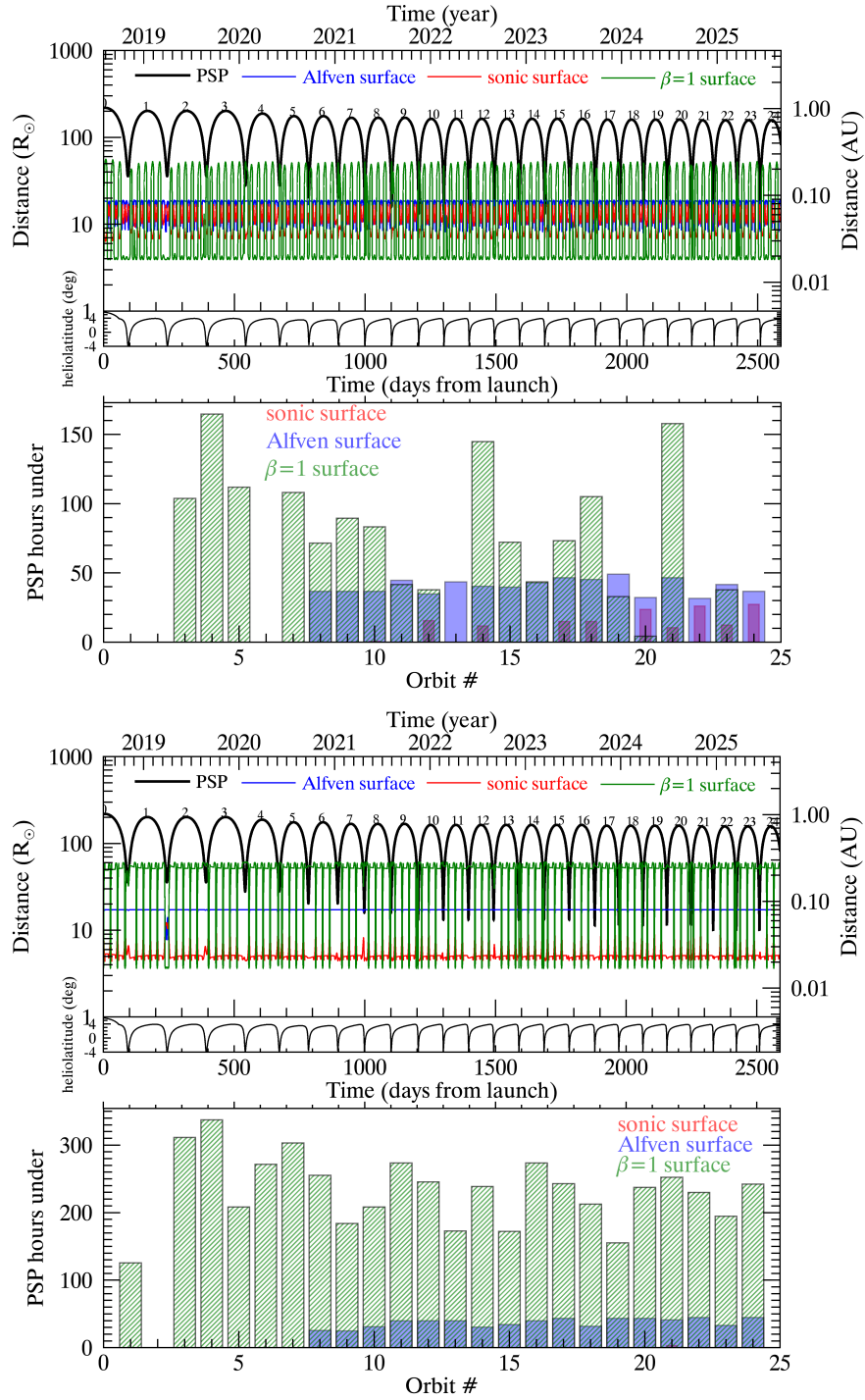


Figure 8.9: *PSP* surface crossings from simulations with a 10° (top) and a 30° (bottom) dipole tilt. The description of the elements of the figures follows Figure 8.8.

then for no more than about 20 hours in a single orbit (orbit 22 or 24). As indicated by the solar maximum case in Figure 8.10 and the 30° case in Figure 8.9, *PSP* crossings of the sonic surface are unlikely to occur during solar maximum.

The relative rarity of penetrating the Alfvén and sonic surfaces in these magnetogram cases appears to be due to the rapid radial decay of the higher multipole magnetic fields that are implied by a complex magnetogram boundary condition [Réville et al., 2015].

8.5 Conclusions and Discussion

We have shown here some detailed exercises in the use of a global heliospheric MHD code with turbulence modeling to simulate context that could be observed by the upcoming *Parker Solar Probe* mission. We emphasize that these results cannot be construed as predictions, since the boundary data employed is not only imprecise, but also is not appropriate to the conditions at the time when the *PSP* will fly, except perhaps in a qualitative sense. Nevertheless, it is interesting and even useful to explore the kind of conditions that *PSP* might experience, an approach that we call *context prediction*.

In this paper we have focused on ambient steady-state conditions in the solar wind, driven by boundary condition that are simple untilted or tilted dipoles, or otherwise magnetograms from previous solar minimum or solar maximum conditions. We note that a sensitive parameter is the total solar dipole strength, and we have used values that lead to agreement with near-Earth observations (Section 4.7).

To summarize, the present results are of two major types: First, we find broad agreement in our study with the interpretation of existing remote sensing results, both from heliospheric imaging and from radio scintillation studies. Our results confirm the likely association of the region near the first outgoing $\beta = 1$ surfaces with morphological changes in the solar wind as observed in *STEREO* imaging [DeForest et al., 2016]. Our global simulations also support the idea that a region near the critical Alfvén surfaces may be characterized by a local enhancement of turbulence levels, a feature that may

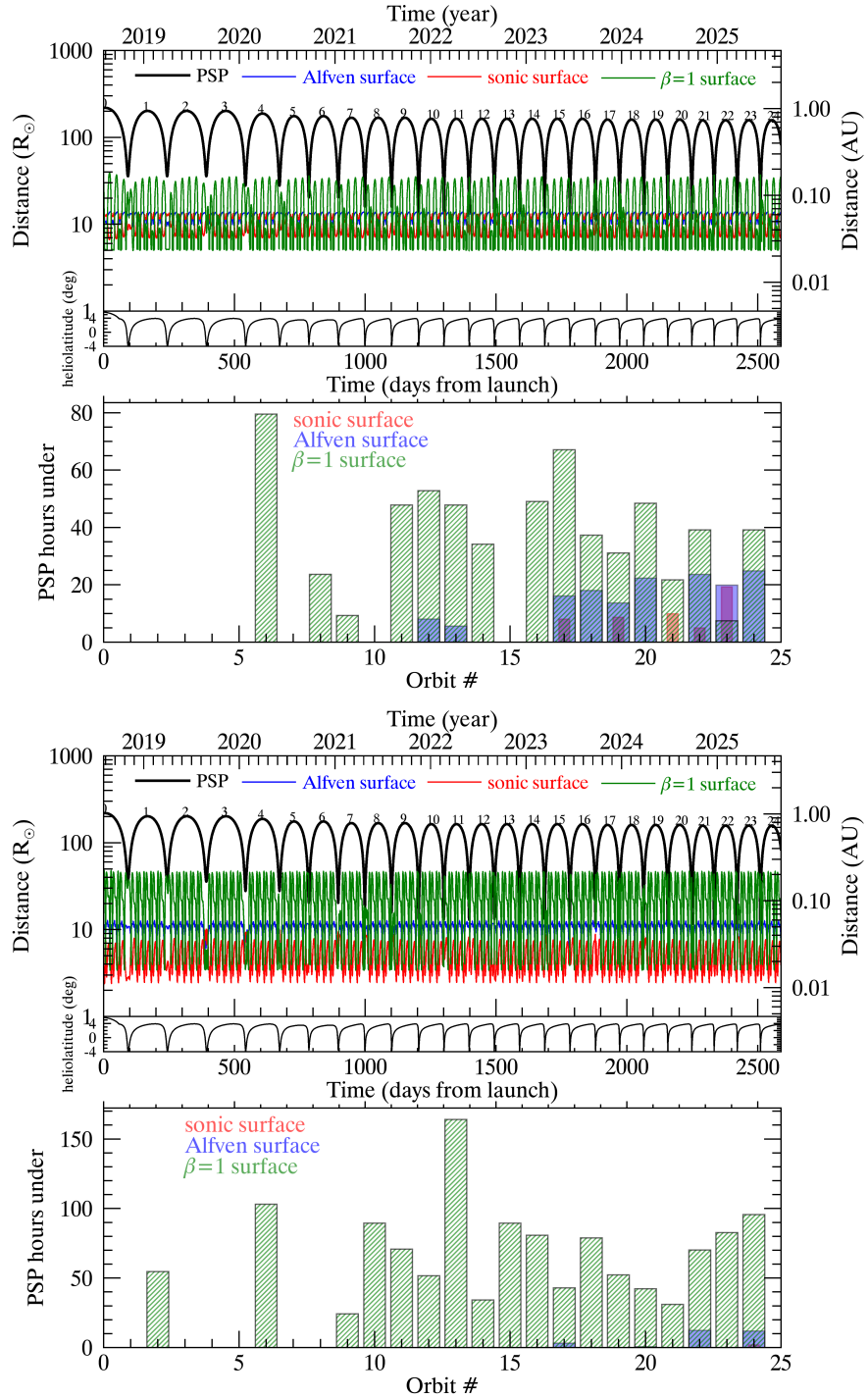


Figure 8.10: *PSP* surface crossings for a July 1994 solar minimum magnetogram run (top) and a July 1989 solar max magnetogram run (bottom). The description of the elements of the figures follows Figure 8.8.

have implications for additional heating and acceleration of the solar wind. Second, the trajectory analyses show that the period of time that *PSP* is likely to spend inside the $\beta = 1$, sonic and Alfvén surfaces depends sensitively on the degree of solar activity and the tilt of the solar dipole and the location of the heliospheric current sheet.

In this paper we have provided a first set of such context predictions, emphasizing the possible range of positions of the sonic and Alfvénic critical surfaces, and the first plasma beta unity surface. The importance of these surfaces [e.g., [DeForest et al., 2016](#); [Chhiber et al., 2018c](#)] lies in the fact that the physical character and conditions of the interplanetary medium are likely to be different on either side of these boundaries, which may in reality be very complex regions or at least corrugated surfaces. *Parker Solar Probe* seeks to address questions such as the physical mechanisms that heat the corona and accelerate the wind, and to reveal the structure of the electromagnetic fields, plasma and energetic particles in these very regions of the corona and wind. Therefore a baseline understanding of the ranges of distance at which these regions might be encountered and crossed becomes quite important for anticipating what the mission is likely to measure, for how long, and on which orbits. In an Appendix to this chapter, we will continue these investigations, and present preliminary results on the turbulence properties that are expected along the *PSP* orbits, along with an evaluation of the validity of Taylor hypothesis for *PSP* observations.

APPENDIX

8.A Contextual Predictions for Parker Solar Probe: Turbulence and Taylor Hypothesis

In this appendix we present preliminary results on contextual predictions for the *PSP* regarding the turbulence environment it will traverse, and also use our solar wind simulation to examine the validity of the Taylor hypothesis and its suggested modifications. Note that we use an untilted dipole simulation, which corresponds to solar minimum. These results are therefore relevant to the initial stages of the mission, when solar activity is expected to be at a minimum (Figure A.1). Extensions of this work to tilted-dipole and magnetogram-based simulations are underway [Chhiber et al., 2018e, in prep].

8.A.1 Turbulence Properties along *PSP* trajectory

Using data from an untilted dipole simulation (Run I-A), Figures 8.A.1 – 8.A.3 show the three turbulence descriptors – turbulence energy density Z^2 , correlation scale λ , and cross helicity σ_c – in a meridional plane and also along the *PSP* trajectory for selected orbits. The figures suggest that the *PSP* will encounter an increased Z^2 as it approaches the region where turbulent fluctuations are generated [e.g., Matthaeus et al., 1999b]. The turbulence is less “aged” in these regions, however, and therefore the correlation scale is expected to decrease as the spacecraft approaches its perihelia. Note that the trajectory plots have two “lobes”, since the inbound and outbound trajectories are not identical. The lobes intersect as the current sheet is crossed.

Figure 8.A.3 suggests that *PSP* aphelia will lie in regions of nonzero correlation between magnetic and velocity fluctuations; the orbit will spend some time in low- σ_c

regions as it crosses into the southern solar hemisphere, before spending its perihelia in a region with oppositely-signed σ_c (compared to aphelion).

We can also look at the relative strength of “inward” and “outward” modes (see Section 2.2.4) by using the identity $Z_{\pm}^2 = (1 \pm \sigma_c)Z^2$ (Equation 4.24), where $Z_{\pm}^2 = \langle |\mathbf{z}_{\pm}|^2 \rangle$. We plot the ratio Z_+/Z_- throughout the *PSP* trajectory in Figure 8.A.4. Once again, we see that the orbits will cross from regions of dominant \mathbf{z}_- to those where \mathbf{z}_+ is dominant. Note that in the simulation considered here, the “outward” propagating mode is \mathbf{z}_- in the Northern solar hemisphere (where the magnetic field points radially), while \mathbf{z}_+ propagates outward in the Southern hemisphere, as discussed in Section 2.2.4.

8.A.2 Validity of Taylor Hypothesis along *PSP* Trajectory

Spacecraft observations generally take the form of single-point (in space) time series of data. Such time-lagged correlation data can be interpreted as spatially-lagged correlation data if the turbulent structures being sampled are swept past the detector fast enough that they don’t distort during their transit. This requires the speed of convection past the spacecraft to be much larger than the characteristic speed of nonlinear interactions. The standard Taylor “frozen-in” approximation [Taylor, 1938] is useful [e.g., Matthaeus and Goldstein, 1982; Chhiber et al., 2018a]⁴ in the supersonic and super-Alfvénic solar wind that spacecraft encounter near Earth, *if* the dynamical process of interest can be described at the MHD level (kinetic-scale activity may have timescales shorter than the convection timescale; in that case the validity of the frozen-in approximation may be questioned even near Earth [e.g., Howes et al., 2014; Perri et al., 2017]).

At *PSP* perihelia, especially in later orbits, the speed of the wind is expected to be relatively low, and the standard Taylor hypothesis (TH) may not apply. To test its validity, we use an untilted dipole simulation (Run I-A) to plot the ratios $V_A/|\mathbf{U}_w - \mathbf{V}_{PSP}|$ and $\delta V/|\mathbf{U}_w - \mathbf{V}_{PSP}|$ along selected *PSP* orbits in Figure 8.A.5. The

⁴ See also Chapter 9.

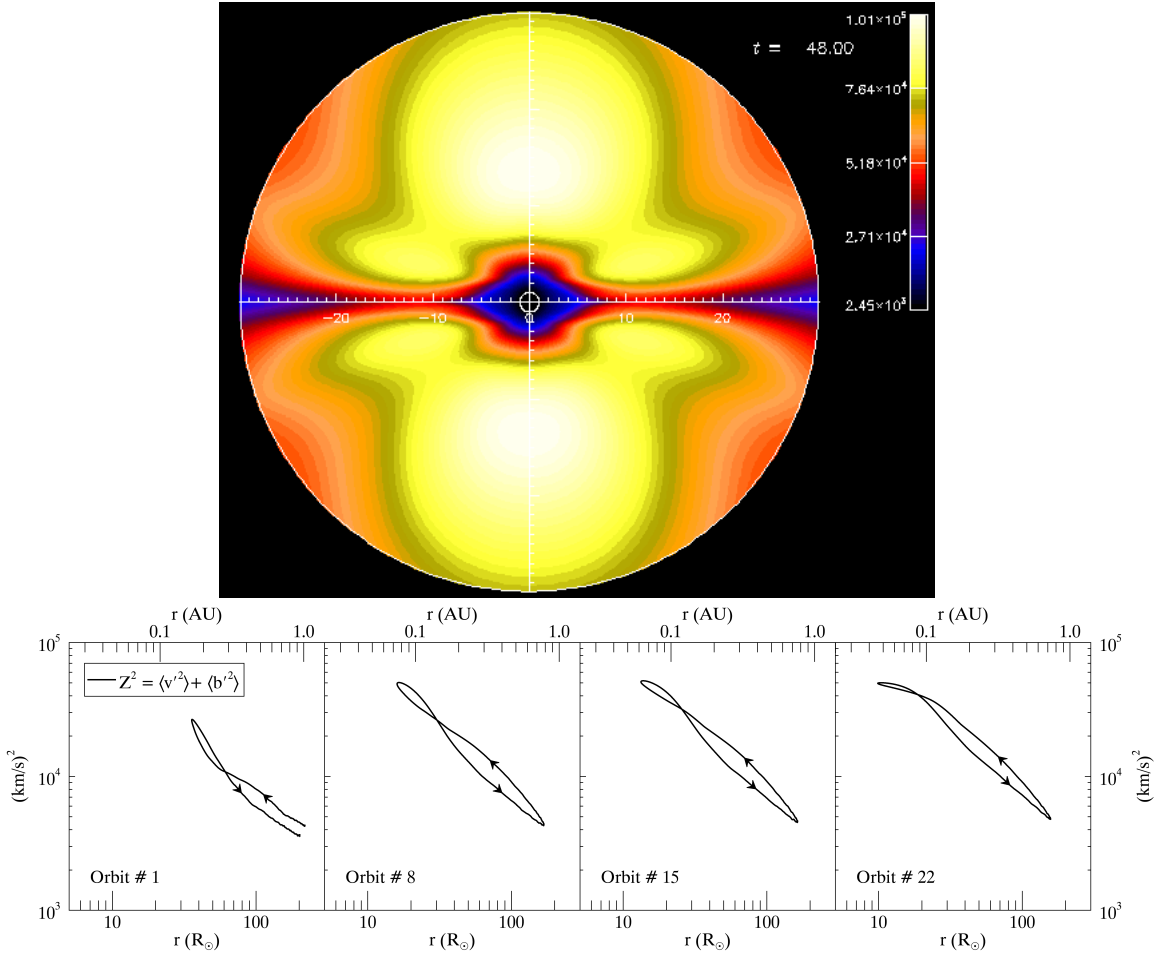


Figure 8.A.1: Top: Turbulence energy density Z^2 (units of $\text{km}^2 \text{s}^{-2}$) in a meridional plane in the region $1 - 30 R_\odot$, from an untilted dipole simulation. Bottom: Z^2 along PSP trajectory for selected orbits. Direction of arrows indicates inward/outward sections of orbits.

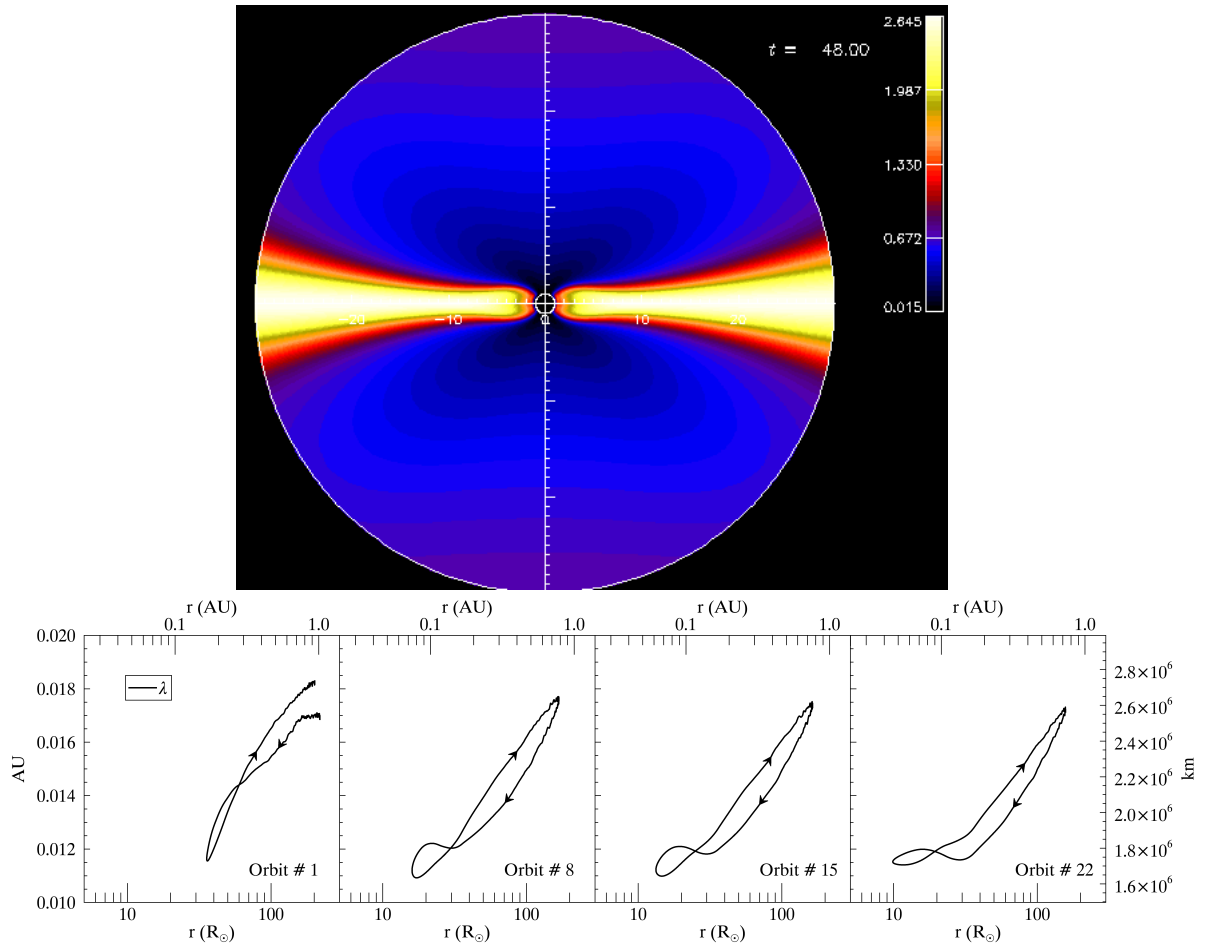


Figure 8.A.2: Top: Correlation scale of fluctuations (λ ; units of R_{\odot}) in a meridional plane in the region $1 - 30 R_{\odot}$, from an untilted dipole simulation. Bottom: λ along *PSP* trajectory for selected orbits. Direction of arrows indicates inward/outward sections of orbits.

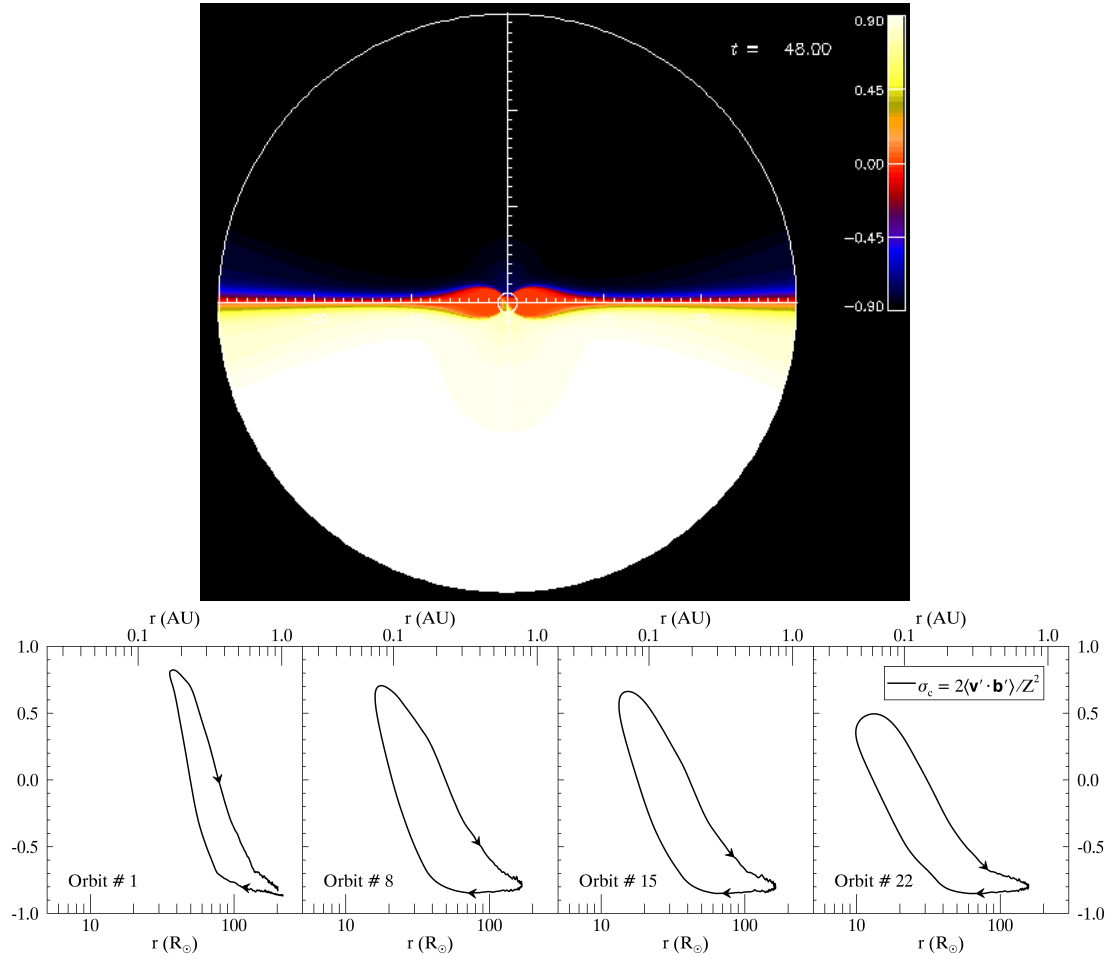


Figure 8.A.3: Top: Normalized cross helicity σ_c in a meridional plane in the region $1 - 30 R_\odot$, from an untilted dipole simulation. Bottom: σ_c along *PSP* trajectory for selected orbits. Direction of arrows indicates inward/outward sections of orbits.

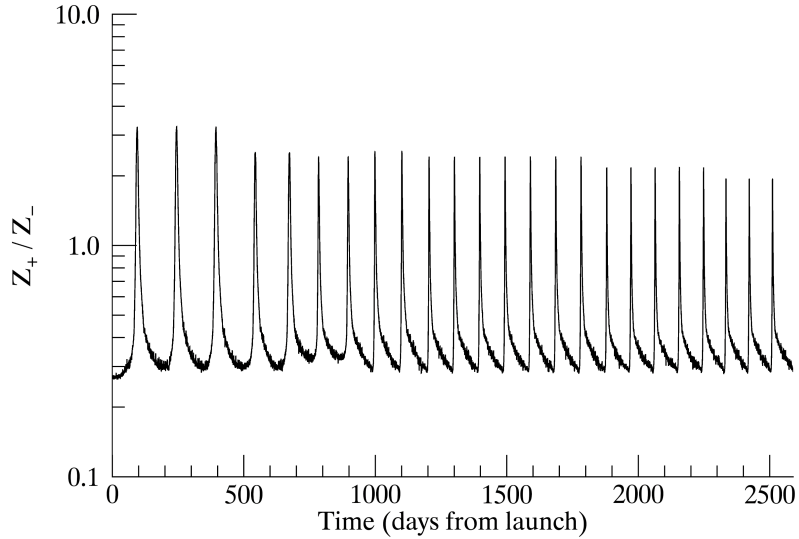


Figure 8.A.4: Relative strength of the two Elsässer modes along the *PSP* trajectory.

first of these ratios measures the speed of Alfvén waves (V_A) against the speed of convection of plasma past the spacecraft $|\mathbf{U}_w - \mathbf{V}_{PSP}|$, where \mathbf{U}_w is the velocity of the wind and \mathbf{V}_{PSP} is the *PSP* velocity (extracted from a [NASA SPICE kernel](#)). The second ratio measures a characteristic turbulent speed δV (taken to be the square root of the turbulent energy density Z^2 from the simulation) against the convection speed. We assume the TH to have high validity when these ratios are smaller than 0.1 (green-shaded region in Figure 8.A.5); when the ratios lie between 0.10 and 0.33 (orange-shaded region) we consider the TH to have intermediate-level validity; ratios greater than 0.33 imply poor validity (red-shaded region).

As seen in the top panel of Figure 8.A.5, the TH has good validity near Earth ($\sim 215 R_\odot$), and moderate validity into around $50 R_\odot$, but below this radial location the validity of the classical TH is questionable, with the perihelia of the later orbits laying deep within the poor-validity regime. The dips in the blue curve occur because of the *PSP* crossing the current sheet, where the vanishing magnetic field lowers the Alfvén speed. Note that the validity for the nonlinear speed δV is better during the

inbound part of the orbit, when the wind velocity and the *PSP* velocity are opposed.

Modified versions of the frozen-in hypothesis have been proposed [Matthaeus, 1997; Klein et al., 2015] for use with the *PSP* at its perihelia. We perform a preliminary evaluation of their validity here, but we also stress that the later *PSP* orbits will likely not experience an untilted-dipole type configuration, as solar activity is expected to be close to maximum at that time (see Figure A.1). Extension of these tests to tilted-dipole and magnetogram-based simulations is underway.

The magnetic field is radially directed close to the Sun, and it is possible that the *PSP* may sweep *across* the mean field with a speed $V_{\perp,PSP}$ that is fast enough to sample 2D fluctuations (see Section 3.3.1). Here $V_{\perp,PSP} = \sqrt{V_{\theta,PSP}^2 + V_{\phi,PSP}^2}$, where $V_{\theta,PSP}$ and $V_{\phi,PSP}$ are the polar and azimuthal speeds, respectively, of the PSP in a heliocentric inertial frame. This variation of the frozen-in approximation is tested in the bottom panel (blue curve) of Figure 8.A.5, indicating poor validity. Note that we have used an approximate speed $\delta V = Z$ to characterize 2D fluctuations; using a speed specific to 2D fluctuations (rather than the full turbulent speed) may improve the performance of this modified TH.

A second variation of the TH is motivated by the anticipation of high Alfvén speeds near the Sun. It is possible that slab fluctuations (Section 3.3.1) are convected past the spacecraft by Alfvénic propagation before nonlinear effects can distort them. The speed of convection in the *PSP* frame will be different for outgoing and ingoing modes: $V_A + U_{r,w} - V_{r,PSP}$ for the former and $V_A - U_{r,w} - V_{r,PSP}$ for the latter. Here $U_{r,w}$ and $V_{r,PSP}$ are the radial speeds of the solar wind and the PSP, respectively. Note that this variation of TH is not relevant for non-propagating 2D fluctuations. The black curves in the bottom panel of Figure 8.A.5 test this modification of TH, finding that it works somewhat reasonably for inward-propagating slab modes (dashed black curve), especially during the inbound part of the orbit.⁵

Finally, we remark on the modified TH of Klein et al. [2015]. Noting that the

⁵ It is interesting to note that these variations of TH would have been more successful in the original Solar Probe mission, which had a planned perihelion below $4 R_{\odot}$ [see Matthaeus, 1997].

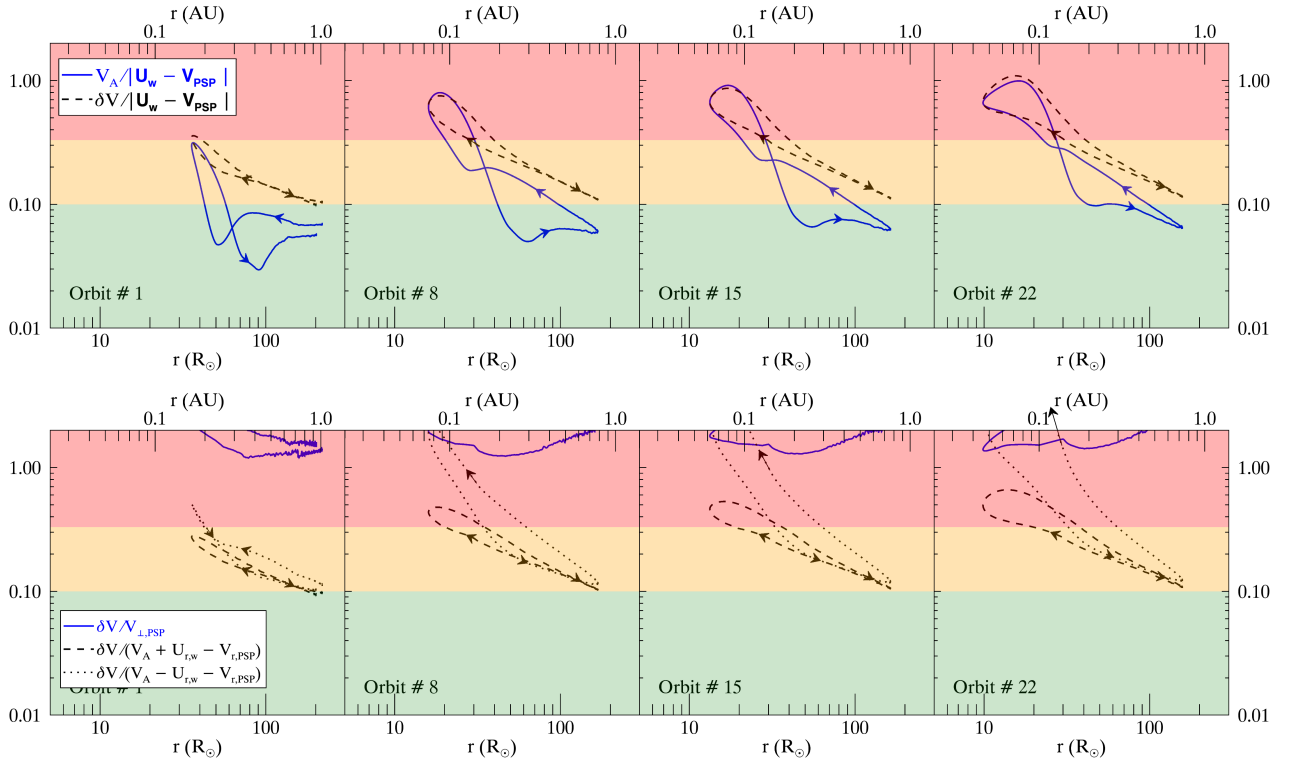


Figure 8.A.5: Top: The plotted ratios compare the transit speed of the solar wind plasma in the *PSP* frame $|\mathbf{U}_w - \mathbf{V}_{PSP}|$ to the Alfvén speed V_A (solid blue curve) and the characteristic speed of turbulent distortion $\delta V = Z$ (dashed black curve). Directions of arrows indicate ingoing and outgoing parts of the *PSP* trajectory. Regions shaded green, orange, and red represent, respectively, high (ratio < 0.1), moderate ($0.10 < \text{ratio} < 0.33$), and low (ratio > 0.33) degrees of validity of the Taylor hypothesis. Bottom: Tests of “modified” Taylor hypotheses along the *PSP* trajectory (see text).

Elsässer mode \mathbf{z}_{\pm} is convected by the oppositely signed mode \mathbf{z}_{\mp} (see Equations 2.28 and 3.32), Klein et al. argue that the frozen-in approximation may be valid near the Sun if outward propagating modes dominate ($Z_+ \gg Z_-$, assuming \mathbf{z}_+ is the outward mode) and if $V_{\perp, PSP}$ is much larger than the speed of convection Z_- . Considering Figure 8.A.4, we see that Z_+ is only a few times larger than Z_- in the simulation used here, so we do not consider this variation of TH further in the present discussion.

In ending, we note once again that these preliminary results are for an untilted dipole simulation, and that we plan to evaluate the performance of these modified frozen-in hypotheses in simulations that better represent solar maximum, by employing large dipole tilts as well as magnetograms from past solar-maximum epochs. This work is being prepared for publication in [Chhiber et al. \[2018e\]](#).

INTERLUDE II

In Chapters 5 – 8, we have studied a variety of problems using a global MHD model (Chapter 4), in which the large-scale solar wind is explicitly resolved while the smaller-scale turbulent fluctuations are treated statistically. The statistical turbulence transport model evolves dynamically and is coupled self-consistently to the bulk flow. This global perspective is valuable in understanding the relationships between different parts of the heliosphere and in tracking the evolving properties of the expanding solar wind.

In the final chapter of this thesis, we depart from this global view of the inner heliosphere, and dive into a more local analysis of turbulence properties of the solar wind and the Earth’s magnetosheath. We use new high-resolution measurements made by the Magnetospheric Multiscale Mission (MMS). The MMS mission’s primary objective is to study magnetic reconnection in the Earth’s magnetosheath, but it has recently made forays into the solar wind, and we use measurements made in both regions to perform a comparative study. This data also provides us with an opportunity to examine and compare turbulence properties from MHD scales down to scales where ion and electron (kinetic) effects come into play. The MMS is a multi-spacecraft mission constituting four spatially separated probes; we compare single-spacecraft data analysis using the Taylor hypothesis with a multi-spacecraft analysis, thus testing the validity of the frozen-in approximation at kinetic scales.

Chapter 9

MULTI-SPACECRAFT ANALYSES OF HIGHER-ORDER TURBULENCE STATISTICS IN THE EARTH'S MAGNETOSHEATH AND THE SOLAR WIND USING MAGNETOSPHERIC MULTISCALE OBSERVATIONS

9.1 Introduction

The Earth's magnetosphere is the region of space surrounding it where the behavior of charged particles is controlled by its magnetic field. The structure of the magnetosphere is influenced by the pressure exerted on it by the solar wind. As shown in Figure 9.1, the solar wind compresses the sunward side of the magnetosphere, whose outermost layer is the *bow shock* – the boundary between the interplanetary medium and the magnetosphere. The region where the pressure of Earth's magnetic field balances the pressure of the interplanetary magnetic field (IMF) is called the *magnetopause*; the magnetopause is separated from the bow shock by the *magnetosheath*. The night-side of the magnetosphere is dragged by the solar wind out to distances of perhaps 1000 Earth radii (R_E) – this extension of the magnetosphere is called the *magnetotail*.

As seen in Figure 9.1, magnetic field lines in the magnetosheath can be oppositely directed in adjacent regions. In this situation, the phenomenon of *magnetic reconnection* [e.g., Biskamp, 1996] can occur, in which individual field lines can “disconnect” and then “reconnect” with field lines in the adjacent region – this is shown in Figure 9.1, where red and white magnetic field lines in the dayside are reconnecting. In this process, the energy stored in the magnetic fields is released as kinetic energy and heat; reconnection is therefore an important mechanism of energy transfer throughout the universe, and it is believed to play a key role in the explosive release of solar plasma into space in the form of *coronal mass ejections*.

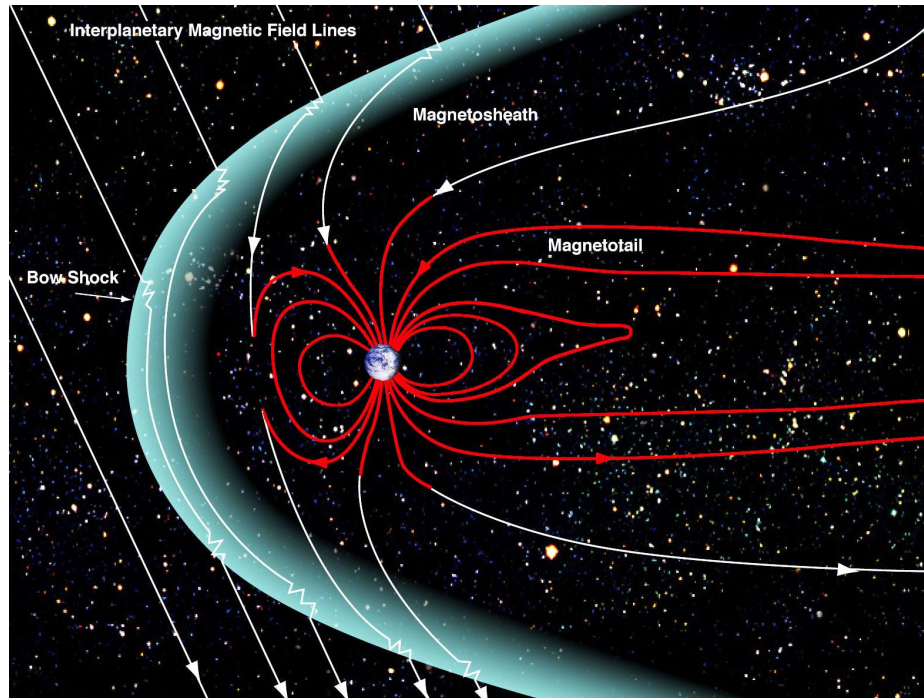


Figure 9.1: Artist's impression of the Earth's magnetosphere. *Image courtesy of NASA/Goddard/Aaron Kaase.*

The Magnetospheric Multiscale (MMS) mission was launched in 2012, with the study of reconnection in the magnetopause and the magnetotail as its primary mission goal [Burch et al., 2016]. The instrumental capabilities of the mission are also well suited to study questions relating to turbulent heating and dissipation in the interplanetary plasma at kinetic scales [e.g., Chasapis et al., 2017, 2018]. Such studies are enabled by the high time-resolution of the data and the small separation of the four spacecraft comprising the mission. In the current chapter we use recent MMS observations to perform a statistical analysis of intermittent turbulence in the magnetosheath and in the solar wind. We examine spectra, structure functions, probability density functions (PDFs), and scale-dependent kurtoses (SDK) of the magnetic field. We also perform tests of the Taylor frozen-in approximation by comparing single-spacecraft time-series analysis with direct multi-spacecraft measurements. Turbulence statistics are computed at scales spanning the inertial range down to proton and electron scales.

These results probe this set of turbulence properties more deeply into the kinetic range than what has been previously feasible using direct two spacecraft methods. As such, the present results confirm and extend several key results in space plasma turbulence observations [e.g., [Bruno and Carbone, 2013](#)], while reporting kinetic range statistics up to sixth order, which have previously been available [e.g., [Alexandrova et al., 2013](#)] only through use of the Taylor frozen-in flow hypothesis [[Taylor, 1938](#)].

The outline of this chapter is as follows: We describe the two data-intervals used in this study in [Section 9.2](#), and briefly review commonly used diagnostic tools for the study of intermittent turbulence in [Section 9.3](#); [Section 9.4](#) describes our single-spacecraft and two-spacecraft approaches for computing the primary variable used in this study – the increment of the magnetic field; In [Sections 9.5 – 9.7](#) we present results on structure functions, power-law energy spectra, PDFs, and scale-dependent kurtosis, while performing comparisons of solar wind and magnetosheath intervals, and of single and multi-spacecraft analyses; We conclude with discussion in [Section 9.8](#).¹

9.2 MMS Observations in the Solar Wind and the Magnetosheath

We use burst-mode (128 Hz) data provided by the MMS flux-gate magnetometer [[Russell et al., 2016](#)] during two intervals: (1) An ~ 11 minute interval on 2016 January 24, when MMS was taking measurements in the magnetosheath ([Figure 9.2](#)), and (2) a ~ 1 hour interval on 2017 November 24, when the MMS was sampling the ambient solar wind ([Figure 9.3](#)).² In these figures the *Geocentric Solar Ecliptic* (GSE) coordinate system is used, in which the XY -plane is defined by the Earth mean ecliptic of date and the $+X$ -axis is defined by the Earth–Sun vector of date [e.g., [Fränz and Harper, 2002](#)]. The tetrahedron formation of the four spacecraft during the magnetosheath interval is shown in [Figure 9.4](#); for our purposes, the configuration was similar during the solar wind interval. A description of the two intervals and the prevailing plasma

¹ The material presented in this Chapter is being prepared for publication in [Chhiber et al. \[2018a\]](#).

² The MMS data used in this study are available at the [MMS Science Data Center](#).

parameters is shown in Table 9.1. Note that a longer interval is selected for the solar wind, since correlation times are longer in it as well.

As can be seen from the parameters shown in Table 9.1, the magnetosheath interval is more turbulent, since it is essentially measuring shocked solar wind. The ratio of fluctuations to the mean is larger in the magnetosheath, as is the proton beta and the Alfvén speed.³ The average spacecraft separation for both intervals was about 15 km, which lies below the ion inertial scale. Multi-spacecraft analyses of these intervals can therefore directly probe kinetic-scale structures. Note that our analysis is based on increments of the magnetic field, which are relatively insensitive to large-scale fluctuations; we will also examine the kurtosis, which is a normalized quantity. Direct comparisons between the two intervals are therefore justified.

9.3 Diagnostics of Intermittent Turbulence

The notion of intermittency is associated with the “burstiness” observed in turbulent flows. Such intermittent events and structures are indicative of infrequently occurring, but strong and localized fluctuations, or sharp and strong gradients, with a distribution that is nonuniform and non-Gaussian. Intermittency has been established as a fundamental feature of turbulent flows, including the interplanetary plasma [e.g., Matthaeus et al., 2015]. Small-scale intermittent structures, such as the current sheets that form naturally in plasma turbulence [e.g., Dmitruk et al., 2004], are thought to play a role in the heating and dissipation of the solar wind plasma [Osman et al., 2012; Wu et al., 2013] and in the the acceleration of energetic particles in the heliosphere [Tessein et al., 2013].

The origin of intermittency lies in the tendency of nonlinear interactions to produce non-Gaussian features. This may be understood heuristically by considering the simple dynamical model, symbolically similar to the Navier–Stokes equation, described

³ The plasma density and velocity measurements were provided by the FPI instrument [Pollock et al., 2016].

MMS Location for 2016-01-24 23:00:00 UTC

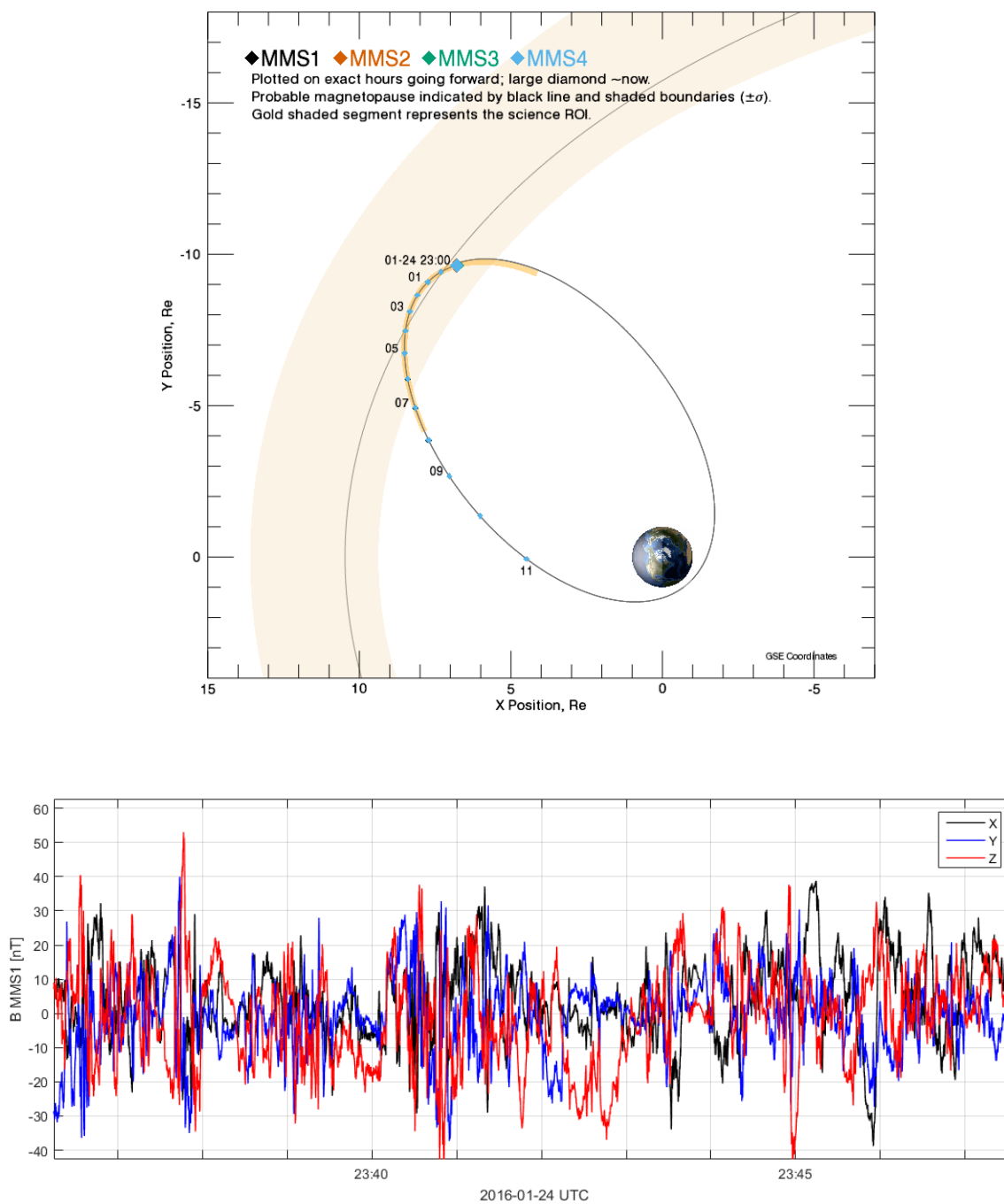


Figure 9.2: Top: MMS orbit on 2016 January 24, when the spacecraft was in the magnetosheath. Bottom: MMS1 observations of the components of magnetic field strength.

MMS Location for 2017-11-24 01:00:00 UTC

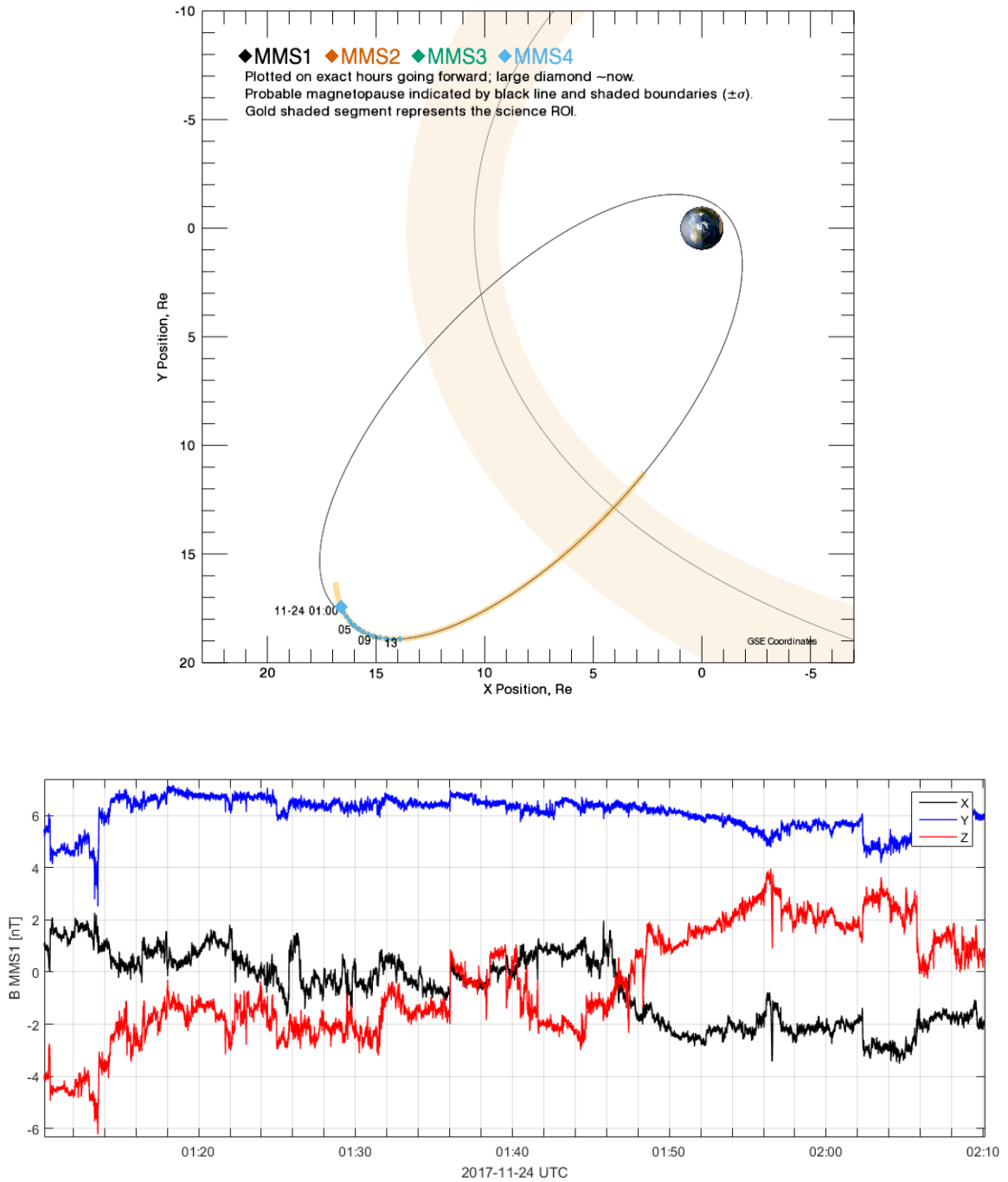


Figure 9.3: Top: MMS orbit on 2017 November 24, when the spacecraft was in the solar wind. Bottom: MMS1 observations of the components of magnetic field strength.

Table 9.1: Description of selected MMS data intervals and their average plasma properties. Here ‘MSH’ denotes magnetosheath and ‘SW’ denotes solar wind; The ‘Separation’ column indicates the mean separation between spacecraft; $|\langle \mathbf{B} \rangle|$ is the absolute value of the mean magnetic field; $\delta B \equiv \sqrt{|\langle \mathbf{B}(t) - \langle \mathbf{B} \rangle|^2}$ is the rms magnetic fluctuation; $\langle n \rangle$ is the mean plasma density; d_i and d_e are the ion and electron inertial scales, respectively; β_p is the proton beta; V_A and V are the mean Alfvén speed and mean flow speed, respectively.

Date	Time (UTC)	Separation (km)	$ \langle \mathbf{B} \rangle $ (nT)	$\delta B / \langle \mathbf{B} \rangle $	$\langle n \rangle$ (cm ⁻³)	d_i (km)	d_e (km)	β_p	V_A (km s ⁻¹)	V (km s ⁻¹)	
MSH	2016 Jan 24	23:36:14–23:47:33	14.10	19.42	4.74	34.75	38.54	0.90	12.03	71.86	245.68
SW	2017 Nov 24	01:10:03–02:10:02	15.60	6.62	0.41	8.61	75.98	1.81	1.34	49.21	377.00

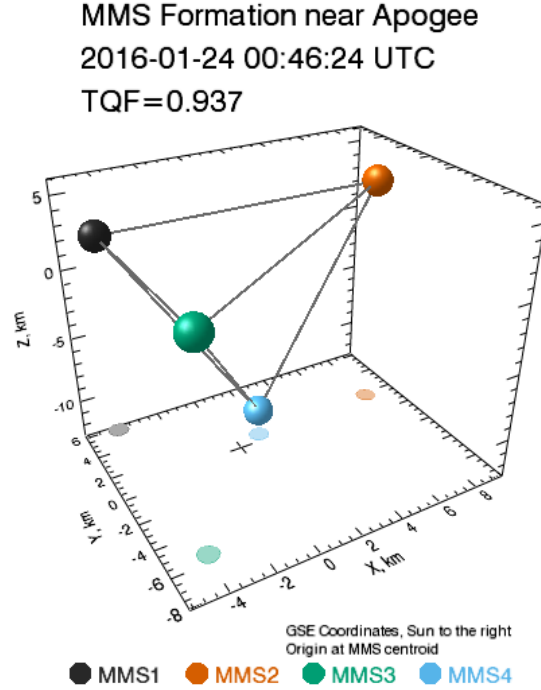


Figure 9.4: MMS formation on 2016 January 24, when the spacecraft was in the magnetosheath. For our purposes, the configuration on 2017 November 24 was similar to the one shown here.

by the equation $\dot{f} \sim fg$, where f and g are functions of space and time that are Gaussian random variables at the initial instant. Then the change in f over a short time Δt is $\Delta f \sim f(0)g(0)\Delta t$. Now, the product of two Gaussian functions is, in general, a non-Gaussian random function [e.g., Milano et al., 2002], and therefore the system under consideration will decrease in Gaussianity with time. This demonstrates how intermittent structure formation arises due to the nonlinear advective term in the momentum equation.⁴ These structures arise during the inertial range cascade (Section 3.1), and

⁴ The role of advection in producing non-Gaussianity has inspired methods that aim to *synthetically* generate intermittent fields, at a computational cost much lower than that of a full turbulence simulation. One such technique is the minimal multiscale Lagrangian mapping method developed for neutral fluids [Rosales and Meneveau, 2006]. Part of the research performed for the present thesis involved extending this technique to a magnetized fluid [Subedi et al., 2014]. This project has not been discussed in the current document in order to maintain a reasonable length.

become sites of enhanced dissipation at smaller scales [Matthaeus et al., 2015].⁵

Studies of intermittency commonly employ increments of the turbulent field $\mathbf{B}(\mathbf{x})$:

$$\delta B_r = \hat{\mathbf{r}} \cdot [\mathbf{B}(\mathbf{x} + \mathbf{r}) - \mathbf{B}(\mathbf{x})], \quad (9.1)$$

where the vector lag $\hat{\mathbf{r}}$ has magnitude r and direction $\hat{\mathbf{r}}$. We define the structure function (see also Section B.2.1.1) of order p :

$$D^{(p)}(r) \equiv \langle \delta B_r^p \rangle, \quad (9.2)$$

where the averaging $\langle \dots \rangle$ is performed over an ensemble [e.g., Panchev, 2016]. If B is intermittent, one expects the presence of structures at a wide range of scales, and the absence of scale-similarity implies that the slope of a $D^{(p)}(r)$ vs r plot would increase at smaller r , where the gradients are strongest.

We will also examine the probability density functions of the increments, which are defined for a random variable f as

$$\text{PDF}(f)df \equiv \text{probability that the random value lies between } f \text{ and } df, \quad (9.3)$$

for infinitesimal df . An intermittent field will manifest in the form of extended “tails” in the PDF, representing “extreme” events (or outliers). These PDFs are expected to be “fatter” for increments at small lag.

The final diagnostic of intermittency that we evaluate in this work is the scale-dependent kurtosis (SDK) of the increments:

$$\kappa(r) = \frac{\langle \delta B_r^4 \rangle}{\langle \delta B_r^2 \rangle^2}, \quad (9.4)$$

which can be considered to be the inverse of the filling fraction for structures at scale

⁵ Note that the dissipation term in the Navier–Stokes equation (1.1) contains the Laplacian operator ∇^2 , which serves to pick out regions with strong gradients.

r . That is, if $\kappa(r)$ increases with decreasing r , then the fraction of volume occupied by structures at scale r decreases with decreasing r . The Gaussian distribution has a kurtosis of 3, and a value larger than 3 is conventionally thought of as a manifestation of wider tails and peakedness in the distribution, relative to the Gaussian [e.g., DeCarlo, 1997]

Theoretical approaches to intermittency are often concerned with the *scaling exponents* $\zeta(p)$, which describe the scaling of increments with lag: $D^{(p)}(r) \sim r^{\zeta(p)}$. For Kolmogorov [1941a] turbulence we have $\zeta(p) = p/3$, while intermittency results in departures from this scaling: $\zeta(p) = p/3 - \xi(p)$, where $\xi(p)$ is the *intermittency correction* [e.g., Matthaeus et al., 2015, and references therein]. A study of the scaling exponents will be performed in future work.

9.4 Computation of Magnetic Field Increments

For the single-spacecraft time series, increments of components of the magnetic field are defined as

$$\delta B_i^r(t) = B_i(t + \tau) - B_i(t), \quad (9.5)$$

where i can be x, y , or z , referring to the GSE coordinate system, and τ is the time lag. The spacecraft speed is negligible compared to the flow speed, and we therefore assume that the spacecraft position is fixed in space during these measurements. To convert these time lags to spatial lags, we employ the Taylor frozen-in approximation [Taylor, 1938], according to which we have

$$\delta B_i^\ell(t) = B_i(t + \tau) - B_i(t). \quad (9.6)$$

Here $\ell = V\tau$, in which V is the mean speed of the flow (Table 9.1).⁶

⁶ The lag can be interpreted to be in the radial direction (x -direction in GSE coordinates), especially in the solar wind interval where the flow is essentially radial. We may therefore interpret δB_x^ℓ as the longitudinal increment and δB_y^ℓ and δB_z^ℓ as transverse increments (See Section B.2.1.1). However, such interpretations are not required for our analysis here.

For the two-spacecraft case, we define the increment of the i^{th} component as

$$\delta B_i^{ab}(t) = B_i^a(t + \tau) - B_i^b(t), \quad (9.7)$$

where t is the time of each measurement and the indices a, b each take the values $\{1, 2, 3, 4\}$, so that each of the (disregarding order) six possible pairings (a, b) corresponds to a pairing of two of the four MMS spacecraft. These six combinations are $\{(12), (13), (14), (23), (24), (34)\}$. The increment in this case corresponds to a spatial separation $\mathbf{r}_{ab} = \mathbf{x}_a - \mathbf{x}_b$, where \mathbf{x}_a and \mathbf{x}_b are the positions of spacecraft a and b , respectively. Note that the stability of intercalibration of the four MMS magnetometers was found to be satisfactory for this analysis.

9.5 Structure Functions and Spectra

If the medium is statistically homogeneous (Appendix B) and the turbulence is stationary in time and ergodic [e.g., [Panchev, 2016](#)], then the ensemble average in Equation (9.2) can be approximated by averaging over time at a fixed spatial lag. Accordingly, we compute the structure function of order p at lag $\ell (= V\tau)$ as

$$D_i^{(p)}(\ell) = \langle [\delta B_i^\ell(t)]^p \rangle_T, \quad (9.8)$$

where i is a component of the magnetic field, the increment $\delta B_i^\ell(t)$ is defined by Equation (9.6), and averaging is performed over the interval T that accommodates the time lag τ . The maximum time lag is taken to be one-tenth of the total length of the interval, as noted in Table 9.1.

The two-spacecraft structure function of order p at lag r_{ab} is computed as

$$D_i^{(p)}(r_{ab}) = \langle [\delta B_i^{ab}(t)]^p \rangle_T, \quad (9.9)$$

where i is again a component of the magnetic field, the increment $\delta B_i^{ab}(t)$ is defined by Equation (9.7), r_{ab} is the magnitude of the separation between the spacecraft pair

(*ab*), and averaging is performed over the full time interval.

In Figure 9.5 we plot the second, fourth, and sixth-order structure functions of the three components of the magnetic field. Structure functions of order p have been normalized by the p^{th} power of the root mean square (rms) magnetic fluctuation $\delta B \equiv \sqrt{\langle |\mathbf{B}(t) - \langle \mathbf{B} \rangle|^2 \rangle}$. Lines represent single-spacecraft calculations using MMS1 measurements with the Taylor approximation, and the filled symbols represent two-spacecraft values, computed with lag equal to spacecraft separation.

The results show that the slope of the structure functions steepens with decreasing lag, indicating the presence of structures with sharp gradients at smaller scales. The agreement between direct two-spacecraft measurements and the calculation based on the Taylor hypothesis (TH) is quite reasonable. This suggests that the TH is valid even at kinetic scales, in both the magnetosheath and the solar wind.

It is of interest to remark on the different behavior of the slopes below d_i in the two intervals – in the magnetosheath there is a continuous steepening of the slope with decreasing lag; in the solar wind the slopes appear to flatten at lags smaller than $\sim 0.5 d_i$. This suggests the absence of intermittent structure at sub- d_i scales in the solar wind, but we must keep in mind that the noise floor of the FGM instrument (~ 10 Hz) lies near $0.5 d_i$ in the solar wind interval considered here, so the observed flattening could be an artifact of noise-related Gaussianization. We expect that an examination of two-spacecraft PDFs and scale-dependent kurtoses (Sections 9.3 and 9.4) will clarify this issue.

Next, we move on to the computation of *equivalent spectra* of the magnetic field, using the structure function of order 2. We begin by recalling the definition of the two-point correlation function R of a statistically homogeneous random field f (Equation B.3): $R(\mathbf{r}) = \langle f(\mathbf{x} + \mathbf{r})f(\mathbf{x}) \rangle = \langle f'f \rangle$, which allows us to deduce the relationship between the 2nd-order structure function and the correlation function:

$$D^{(2)}(\mathbf{r}) = \langle f^2 \rangle + \langle f'^2 \rangle - 2R(\mathbf{r}) = 2\langle f^2 \rangle - 2R(\mathbf{r}) = 2R(0) - 2R(\mathbf{r}), \quad (9.10)$$

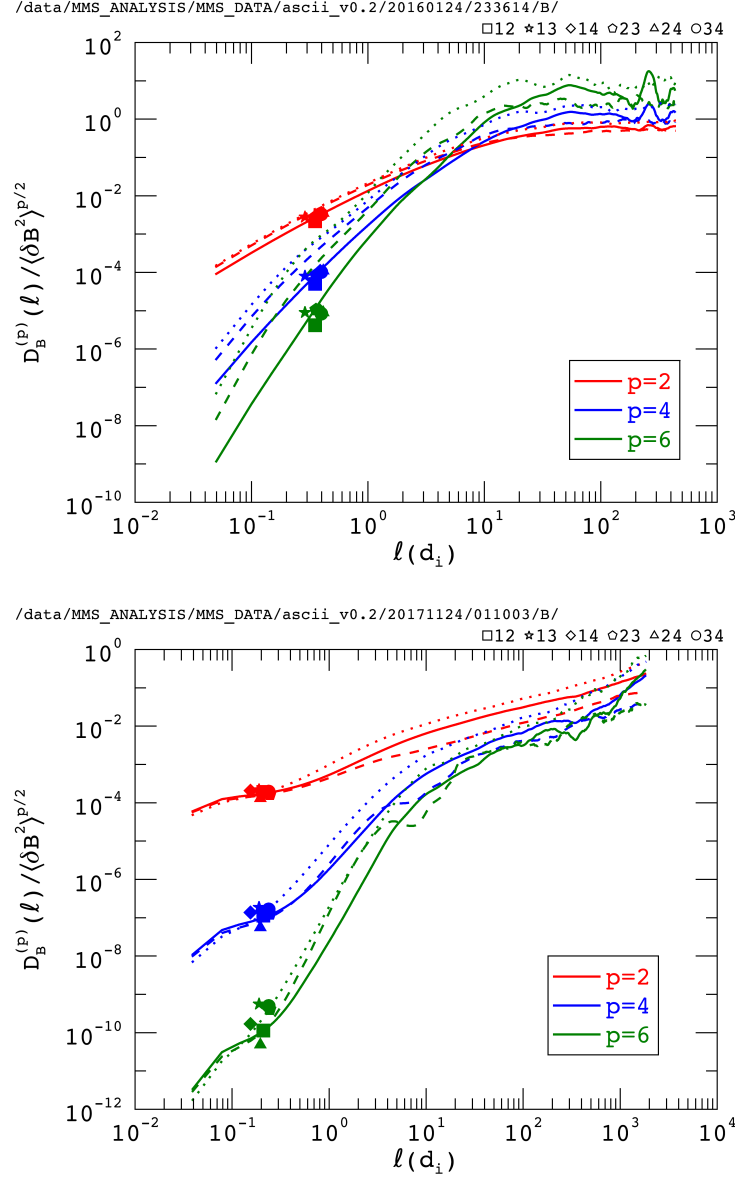


Figure 9.5: Second, fourth, and sixth-order structure functions of B_x (solid lines) in (top) magnetosheath and (bottom) solar wind. Structure functions of B_y and B_z are shown as dashed and dotted lines. Two-spacecraft structure functions of B_x are plotted using filled symbols that indicate different spacecraft pairings, labeled in the top right corner of each panel. Note that structure functions of order p have been normalized by the p^{th} power of the rms magnetic fluctuation, and the lag ℓ has been normalized to units of the ion inertial length d_i . The single-spacecraft structure functions have been computed using MMS1 measurements.

where the second equality follows from invariance of statistical quantities under translation. Now, the Fourier transform of the correlation function is the wavenumber spectrum, and integrating over all directions gives the omnidirectional energy spectrum $E(k)$ (see Section B.3.1). The quantity $S^{(2)}(\lambda) \equiv D^{(2)}(\lambda)\lambda$ then behaves as an “equivalent spectrum” in the inertial range, with an effective wavenumber defined by $k^* \equiv 1/\lambda$. If the omnidirectional spectrum exhibits power-law behavior $E(k) \sim k^{-\alpha}$ over a sufficient bandwidth, then we expect similar behaviour from the equivalent spectrum: $S^{(2)}(\lambda) \sim (1/\lambda)^{-\alpha}$. Note that this interpretation is consistent with the discussion following Equation (B.18) in Appendix B, where we interpret the second-order structure function as a filter that extracts information about structures of size $\leq \lambda$. We stress, however, that $S^{(2)}(\lambda)$ and the equivalent wavenumber k^* are *not identical* to the conventional spectrum and wavenumber (Section B.3.1).

We plot the equivalent spectra for the x -component of the magnetic field in Figure 9.6. The black line represents the single-spacecraft TH estimate, while the direct two-spacecraft measurements are plotted as filled symbols, with good agreement seen between the two calculations. For reference, the fast Fourier transform (FFT) spectrum is plotted in the background in a translucent purple shade.⁷ The results show a similar scaling with wavenumber for the equivalent and FFT spectra. A Kolmogorov $-5/3^{\text{rd}}$ slope spanning at least two decades in the inertial range of the solar wind is observed, suggesting a strong hydrodynamic-like incompressible turbulence regime. The inertial range gives way to a steeper slope in the kinetic/dissipation range, consistent with observational [Alexandrova et al., 2008; Sahraoui et al., 2009] and theoretical [Boldyrev

⁷ The FFT spectrum is simply given by the square of the Fourier amplitudes of the time series, with frequencies converted to wavenumbers using the TH. The resulting spectrum is divided by the bin-width (derived from the time interval between successive measurements) to obtain a spectral density. Note that at the low-wavenumber end, the FFT spectrum extends for a decade beyond the equivalent spectrum computed from the structure functions. This is because we take a maximum lag that is 1/10 of the total interval length while computing the structure functions. At the other end of the wavenumber axis, the highest wavenumber (frequency) in the FFT spectrum is half the maximum wavenumber (frequency) in the equivalent spectrum. This is due to the fact that the FFT discards negative wavenumbers, so that the highest wavenumber corresponds to half of the time-series’ resolution. For example, in a data series with 10 points, the maximum wavenumber is 5, and the negative wavenumbers $\{-1,-2,-3,-4\}$ carry no information.

et al., 2015] studies.

The magnetosheath (which is more compressible than the solar wind) kinetic range is well-described by a $-8/3^{\text{rd}}$ power-law, and here the first two decades above d_i show a scaling that is between $\sim -7/3$ and $-8/3$, again consistent with observations [Sahraoui et al., 2006]. It appears that the steeper $-8/3^{\text{rd}}$ spectrum transitions directly into the so-called “ $1/f$ ” regime [Matthaeus and Goldstein, 1986] without passing through an intermediate $-5/3^{\text{rd}}$ inertial range, in contrast to what is observed in the solar wind. This is consistent with the observations of [Czaykowska et al., 2001] [see also Alexandrova, 2008]. We note that the steepening in the magnetosheath occurs above the ion gyroradius (~ 133.7 km in our interval).

9.6 Probability Density Functions

Figure 9.7 shows PDFs (Equation 9.3) of the increment in the x -component of the magnetic field from MMS1, computed for different lags.⁸ In the magnetosheath (top panel), the maximum lag of $\sim 469 d_i$ is $1/10^{\text{th}}$ of the total interval, and here the PDF is close to a Gaussian (dashed green curve). As the lag is decreased, the PDF gets more peaked and the tails become wider, indicating the presence of intermittent structures down to scales just above the electron inertial length (see Table 9.1).

The PDF in the solar wind interval (bottom panel of Figure 9.7) indicates increased intermittency down to lags of $15 d_i$, below which the distribution begins to Gaussianize. As discussed in Section 9.5, the role of the noise floor ($\sim 0.5 d_i$) cannot be ruled out here, until we examine the two-spacecraft PDF, below.

In Figure 9.8 we compare PDFs of increments computed from a two-spacecraft analysis with the single-spacecraft computation (for a $0.35 d_i$ lag, equal to the separation between the two spacecraft considered). The agreement between the TH estimate and the direct two-spacecraft result is striking for the magnetosheath interval (top

⁸ We compute PDFs by first calculating the relative frequency of occurrence of increments within designated bins, and then divide these frequencies with the bin-width in order to obtain probability densities.

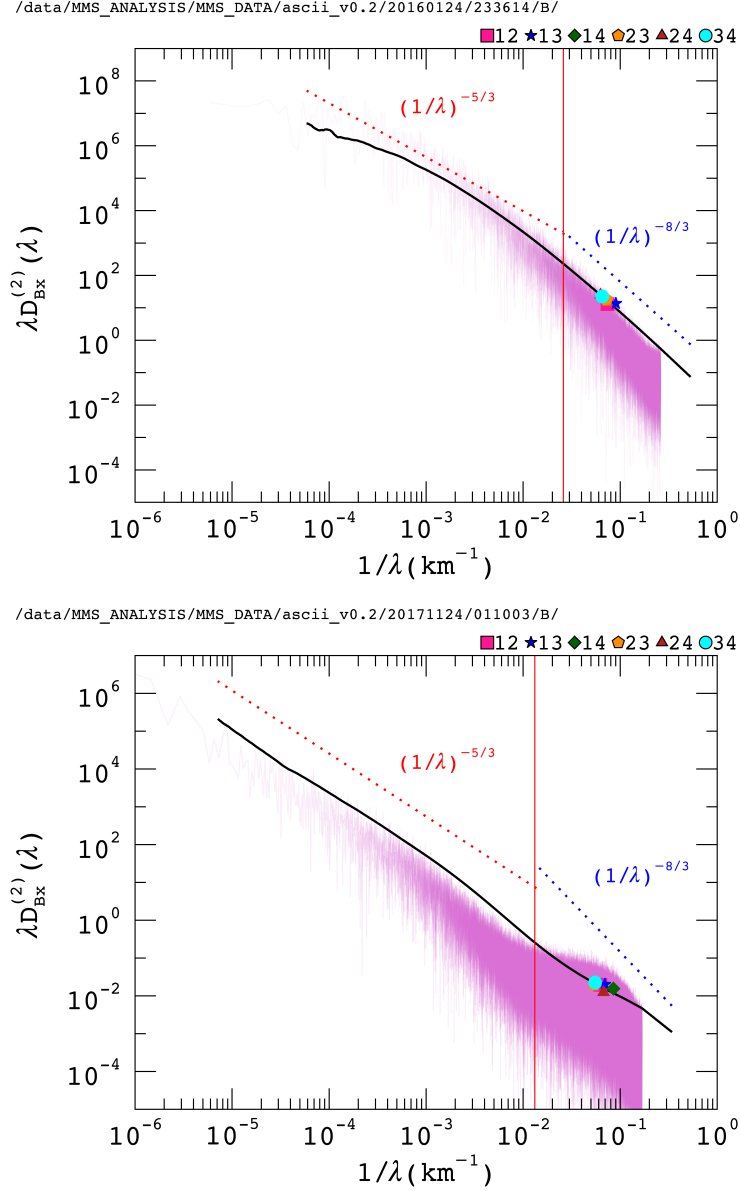


Figure 9.6: Equivalent spectra computed from the second-order structure function of the x -component of the magnetic field, in the magnetosheath (top) and the solar wind (bottom), shown as a function of equivalent wavenumber $k^* = 1/\lambda$, where λ is the lag. The single-spacecraft MMS1 result is shown as a solid black line, and multi-spacecraft values are plotted as filled symbols. The FFT spectrum of the x -component of \mathbf{B} is shown in a translucent purple shade. Dotted lines corresponding to spectral slopes of $-5/3$ and $-8/3$ are shown for reference, and the red vertical line marks the inertial length d_i .

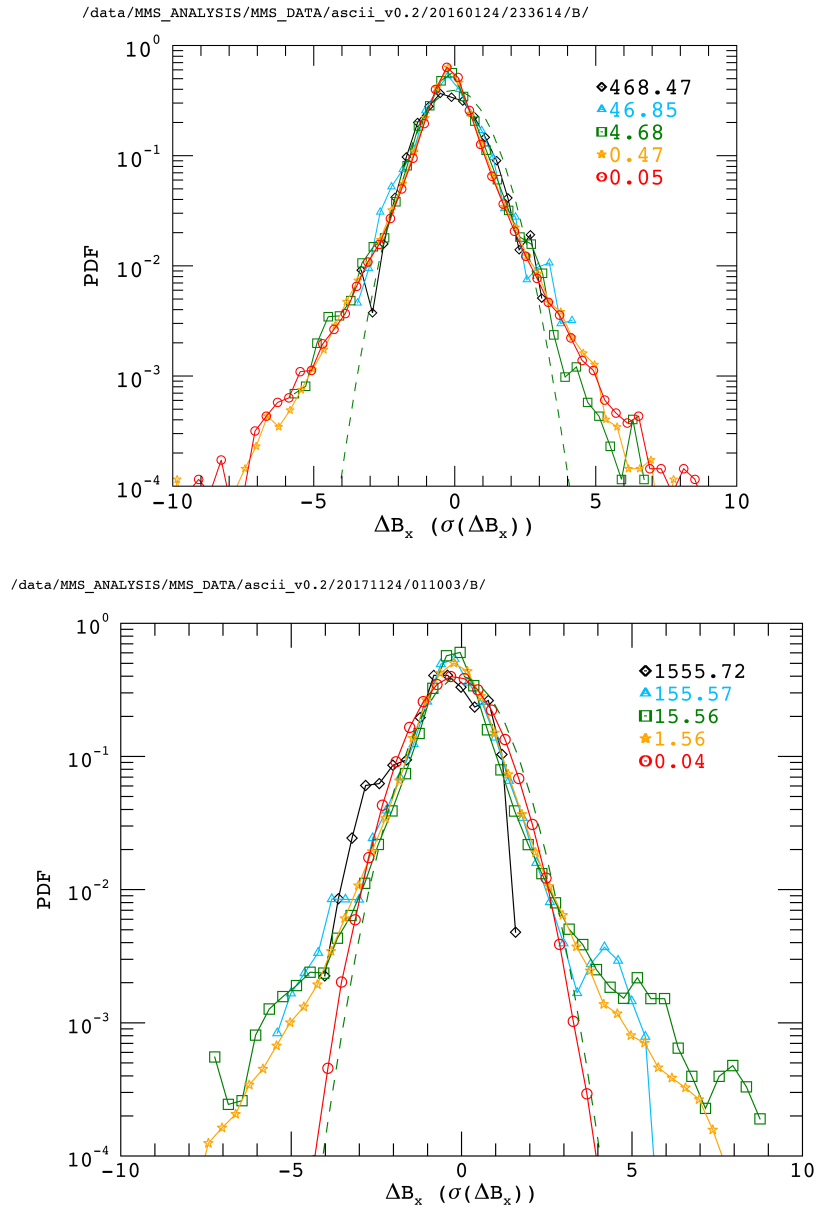


Figure 9.7: PDFs of the increment in the x -component of the magnetic field, in the magnetosheath (top) and the solar wind (bottom), using MMS1 measurements. The different lags used are listed in the top-right corner of the figures, in units of d_i ($= 38.54$ km in magnetosheath; 75.98 km in solar wind). The dashed green curve represents a Gaussian PDF, and the horizontal axes are normalized by the standard deviation of the increment $\sigma(\Delta B_x)$.

panel). In the solar wind interval, we see good agreement between the two approaches until about $3\text{-}\sigma$. Figure 9.8 also provides a direct confirmation of the presence of intermittent structure in the magnetosheath at sub- d_i scales, without the use of TH. In the solar wind interval, it appears that the two-spacecraft PDF is almost perfectly Gaussian, thus confirming the absence of intermittency at these scales, hinted at by Figure 9.5.

9.7 Scale-dependent Kurtosis

The kurtosis, or normalized fourth-order moment (introduced in Section 9.3), emphasizes the tails of the PDFs presented in the preceding section, and thus provides further insight into intermittency at different scales. We compute the single-spacecraft SDK (see Equation 9.4) using the structure functions defined by Equation (9.8):

$$\kappa_i(\ell) = \frac{D_i^{(4)}(\ell)}{[D_i^{(2)}(\ell)]^2}, \quad (9.11)$$

while the two-spacecraft version is computed using the structure functions defined by Equation (9.9):

$$\kappa_i(r_{ab}) = \frac{D_i^{(4)}(r_{ab})}{[D_i^{(2)}(r_{ab})]^2}. \quad (9.12)$$

We remind the reader that here i is the component of the magnetic field, $\ell(= V\tau)$ is the single-spacecraft lag estimated using the TH, and r_{ab} is the separation between spacecraft pair (a, b) .

The SDK computed using these formulae are plotted as functions of lag in Figure 9.9, for both magnetosheath (top panel) and solar wind intervals (bottom panel). There is a striking difference in the behavior of the SDK in the two cases. In both intervals, the kurtosis is close to the Gaussian value of 3 at the largest scales, and it increases as the lag decreases to $10 d_i$. However, in the magnetosheath interval the kurtosis continues to increase down to electron scales, while in the solar wind interval it drops to Gaussian values. These results (consistent across single and two-spacecraft analyses)

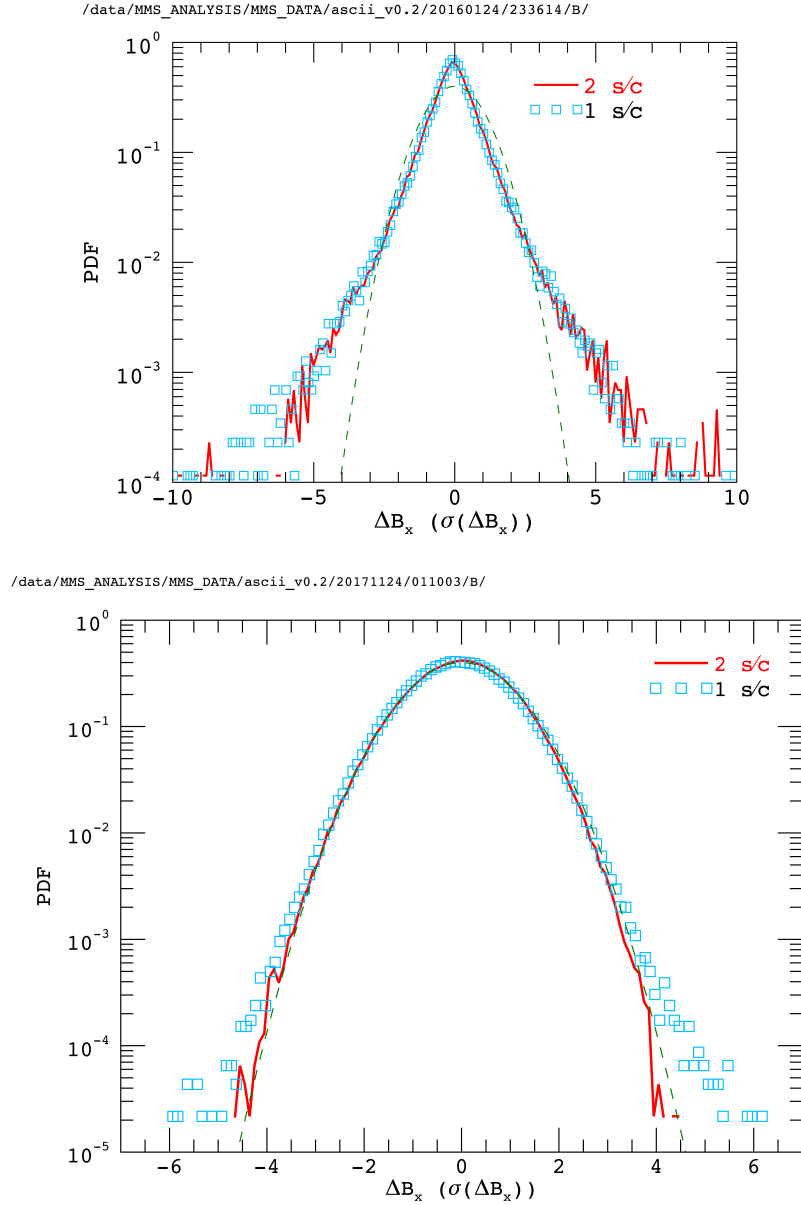


Figure 9.8: PDFs of the increment in the x -component of the magnetic field, in the magnetosheath (top) and the solar wind (bottom), using MMS1 measurements (blue squares) and the lag between MMS1 and MMS2 (red line). The lag in the top panel corresponds to 13 km (or $\sim 0.35 d_i$), and that in the bottom panel to 16 km (or $\sim 0.21 d_i$). These lags are the average separations for the two spacecraft considered. The dashed green curve represents a Gaussian PDF, and the horizontal axes are normalized by the standard deviation of the increment $\sigma(\Delta B_x)$.

are a clear signal of the existence of proton and electron scale intermittency in the magnetosheath, and the absence of intermittent structures at sub-proton scales in the solar wind. We also note that the different values of kurtosis for the increments of the three components of the magnetic field indicate the presence of anisotropic structures.

The kurtosis is more sensitive to impulsive signals than the other statistical measures analyzed here, and therefore one sees relatively larger discrepancies between the TH estimates and the two-spacecraft analyses. Nevertheless, we still find a reasonable agreement between the two approaches, although the degree of agreement varies for the x , y , and z components, once again pointing to the presence of anisotropic structures at kinetic scales. There are some cases where the frozen-in estimate is a few times larger than the two-spacecraft measurement. The reason for this may be that the frozen-in estimate realistically includes not just the variation due to advection of undistorted turbulent structures over a distance equal to the spatial lag, but also a contribution from the variation in time that accrues during the passage of structures past the spacecraft. In fact, such a systematic discrepancy between the two computations forms the basis for estimating the Eulerian decorrelation time from multiple-spacecraft measurements [Weygand et al., 2013].

9.8 Conclusions and Discussion

In this chapter, we have used MMS observations of the magnetic field in the Earth's magnetosheath and the solar wind, to perform a multi-spacecraft statistical study of intermittent plasma turbulence. The high time-resolution MMS data allows us to probe previously unattainable scales, and the small separation of the four MMS spacecraft permits the direct measurement of spatial structures at kinetic scales, without requiring use of the Taylor frozen-in approximation.

We find strong signatures of electron and ion scale intermittency in the magnetosheath, with the two-spacecraft measurements corroborating single-spacecraft analyses. These signatures appear to be absent at sub-ion scales in the solar wind interval considered here. Preliminary analyses (not shown here) of several other solar wind

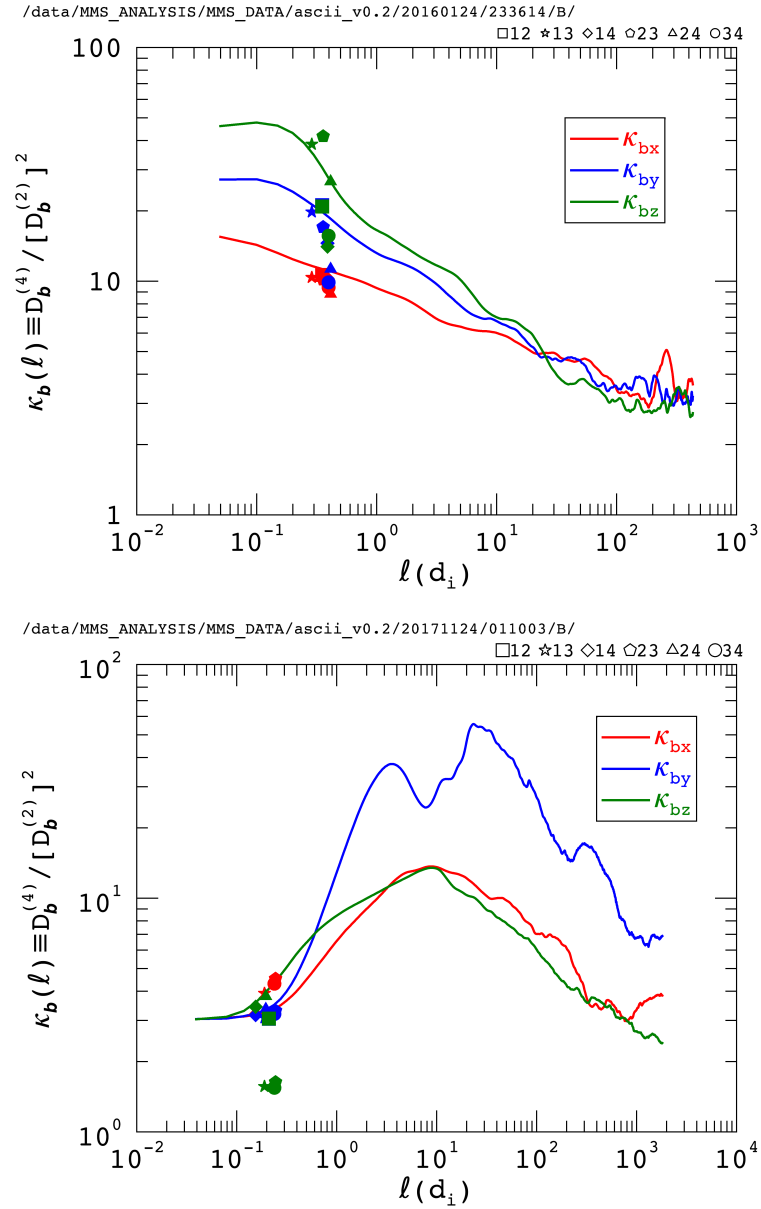


Figure 9.9: Scale-dependent kurtosis as a function of lag, for increments of the three components of the magnetic field, in the magnetosheath (top) and the solar wind (bottom). Single-spacecraft results using MMS1 are shown as lines, and direct two-spacecraft measurements are plotted using filled symbols.

intervals confirm this finding. Nevertheless, both magnetosheath and solar wind intervals show evidence for intermittent structures in the inertial range and at ion scales. By comparing single-spacecraft and two-spacecraft measurements, we verify that the Taylor hypothesis generally works quite well in both the solar wind and the magnetosheath. This finding complements the work of [Perri et al. \[2017\]](#), who perform Hall-magnetohydrodynamic turbulence simulations to affirm the robustness of the Taylor hypothesis to sub-proton scales, for the case of mean-flow speeds typical of fast solar wind.

We compute energy spectra using an FFT technique and a structure function-based calculation. A Kolmogorov power-law is observed in the inertial range of the solar wind, giving way to a steeper spectrum in the kinetic/dissipation range. In the magnetosheath we observe a direct transition from a shallow “ $1/f$ ”-type spectrum [[Matthaeus and Goldstein, 1986](#)] to a steep $\sim -8/3$ regime, without an intervening inertial range, confirming previous observations in the Earth’s [[Czaykowska et al., 2001](#); [Alexandrova, 2008](#)] as well as Saturn’s [[Hadid et al., 2015](#)] magnetosheath. The reason for the apparent absence of a Kolmogorov spectrum in the magnetosheath is not clear. One possibility could be that the transit time through the magnetosheath is too small for an inertial range to develop. However, rough estimates [[Alexandrova, 2008](#)] suggest that the shortest transit time (along the Sun-Earth direction) is several times longer than the characteristic nonlinear time. An inertial range spectrum should therefore be observed, particularly in the flanks of the magnetosheath, where the transit time is longer. In a recent statistical study of ~ 1600 data intervals from *Cluster* measurements in Earth’s magnetosheath, [Huang et al. \[2017\]](#) find a $-5/3^{\text{rd}}$ power-law in 17% of the cases, which lie in the flanks of the magnetosheath. Further studies are required to address this issue adequately.

Our observation of kinetic-scale intermittency is of relevance to broader heliophysics research, since structures at these scales terminate the turbulent cascade process that is believed to play a key role in heating and acceleration of the solar

corona (see Section 1.1.4). This work complements recent MMS observations of intermittent dissipation at kinetic scales in the magnetosheath [Chasapis et al., 2018]. Our finding of intermittent structure at electron scales is also consistent with the recent observation of electron-scale magnetic reconnection in the magnetosheath [Phan et al., 2018]. Such a reconnection process would generate localized current sheets that could manifest in signatures of electron-scale intermittency.

Electron scale current sheets have also been observed in the solar wind [Perri et al., 2012]. This view of strong subproton scale intermittency and coherent structures is supported by some kinetic simulations [Leonardis et al., 2013; Karimabadi et al., 2013], but there also have been solar wind observations that have noted a possible tendency for scale dependent kurtosis to decrease or saturate at scales below the proton inertial length [Wan et al., 2012a; Wu et al., 2013]. The latter view suggests a relative scarcity of electron scale current sheets in the solar wind, compared to the magnetosheath, consistent with the findings based on statistics in the present paper. A likely cause of this difference is the presence of incoherent plasma waves in the region upstream of the bow shock. It has been noted [Koga et al., 2007; Wan et al., 2012a] that such waves destroy coherence (and thus attenuate the kurtosis) even at small amplitudes.

In future work, we plan to extend these analyses to other MMS datasets in order to test the robustness of the present results. A more detailed study of the scaling behavior of higher-order structure functions is underway, in which we will examine intermittency corrections to the scaling exponents discussed in Section 9.3.

Chapter 10

CONCLUSIONS AND FUTURE WORK

This dissertation has primarily been concerned with the application of a well-tested 3D global two-fluid MHD code to study several problems related to multi-scale turbulent dynamics of the solar wind. The solar wind simulations used here are unique in that they self-consistently couple sophisticated models of both the large-scale flow and the smaller-scale turbulence. Most solar wind modeling approaches, in contrast, focus on either the bulk flow, with simple parametric or WKB-waves based turbulence models, or on the transport of turbulence, with simplified assumptions regarding the large-scale flow. In the present approach (detailed in Chapter 4), the dynamical evolution of the large scale fields drives the turbulence, and in turn, the transport of fluctuations leads to heating and acceleration of the solar wind.

The model has been developed over the past decade, and comparisons with observations have found reasonable agreement. We have incorporated several more recent improvements to the model [to be published in [Usmanov et al., 2018](#)], such as extension of the full turbulence transport model to sub-Alfvénic coronal regions, and a smooth transition from collisional to collisionless electron heat conduction close to the Sun. The numerical solution of the model provides us with a model heliosphere, which we have used in the studies summarized briefly below. Possible future extensions of these projects are also discussed.

Our study of the collisional age A_c of solar wind protons (Chapter 5) resulted in comparisons of three formulations of this measure of collisionality. It was found that the commonly used one-point measure of A_c does not provide a complete account of the collisional history of a plasma parcel, and may misleadingly lump collisionally young plasma with plasma that has “aged” through collisions early in its path. A simple

analytical model for A_c was developed and compared with the full integral formulation, yielding agreement when the initial point for integration is taken well above the coronal surface. The heliospheric current sheet (HCS) was found to be the primary collisional domain in the solar wind, in agreement with previous studies. The relationship of collisional age with the Knudsen number was also clarified, and future work could examine electron collisionality using the latter parameter. Another possible extension of this project would be a comparative study with the turbulence age of solar wind. Preliminary findings were reported in Appendix 5.B. Yet another interesting follow-up project would be to study electron-proton collisionality. Our two-fluid code tracks the evolution of electron and proton temperatures, and this would enable a study of the heliospheric evolution of the electron-proton temperature anisotropy. The effects of different collision models would also be interesting to compare.

In Chapter 6 we computed cosmic ray diffusion coefficients throughout the inner heliosphere, examining radial and latitudinal variation. A new explicit expression for the diffusion coefficient perpendicular to the mean magnetic field was derived, that is simpler to evaluate than the implicit equation used in some previous studies. We found the HCS to be a region of very strong perpendicular diffusion, and also that increased solar activity enhances perpendicular diffusion. This interpretation has been supported by the recent work of Zhao et al. [2018]. Another interesting finding is the radial evolution of the rigidity scaling of the parallel diffusion coefficient, which occurs due to resonant interactions of particles with energy-containing turbulent structures. An obvious future project could be the study of cosmic ray modulation in our model heliosphere, in which the computed diffusion tensor would be used in the cosmic ray transport equation. Similar studies have been performed in recent years using relatively simplified models [e.g., Guo and Florinski, 2016]. Another interesting follow up project, for which we have preliminary results, is an estimation of the random walk of magnetic field lines. Extension of the present results to the outer heliosphere would also be worthwhile, and of relevance to the modulation of galactic cosmic rays.

In Chapters 7 and 8, we examined critical surfaces and associated effects in

the solar wind. This work was partly motivated by recent *STEREO* observations that suggested a transition from a magnetically structured and radially aligned flow to more isotropic structures at radial distances of a few tens of solar radii. This interpretation was elaborated on in Chapter 7, and direct comparison of simulation results with the remote sensing images revealed that the observed transition occurred above the Alfvén surface, and near the first plasma-beta unity surface. Estimates of the “causality threshold” of solar wind fluctuations support the interpretation that the observed structures could be a manifestation of turbulence onset at the very largest scales allowed in the expanding solar wind. This “region of influence” of solar wind fluctuations was found to be roughly an order of magnitude larger than the correlation scale. The direct quantitative comparison of remote sensing images with global simulations that was demonstrated in this work could provide an effective means of mutual inter-calibration in future research. The implications of the causality threshold for spacecraft observations and numerical approaches such as the so-called “expanding box” simulations [Grappin et al., 1993] would also be worth investigating.

Further studies of critical surfaces and associated phenomena were carried out in Chapter 8. Comparisons of simulation results with remote sensing observations suggest that the transonic and trans-Alfvénic regions may be sites of enhanced turbulence. This chapter also presented contextual predictions for the soon-to-be-launched *Parker Solar Probe* (*PSP*) mission, which will likely spend a substantial amount of time below the first plasma-beta unity surface, and possibly the sonic and Alfvénic surfaces as well. The coarse resolution of our simulations implies an unrealistically wide HCS, presenting something of a confounding factor. Nevertheless, these studies provide valuable context for *PSP* observations. In the near future, we plan to perform simulations with boundary conditions tailored to specific *PSP* orbits, in order to provide more precise contextual predictions. Such simulations may be very valuable in planning for *PSP* observations, since we will be able to make contextual predictions regarding the turbulence environment sampled by the spacecraft, and examine issues pertaining to the applicability of Taylor’s hypothesis at *PSP* perihelia. A preliminary

study on turbulence context for *PSP* was presented in Section 8.A.

In the final chapter, we set aside the global perspective and carried out a more localized observational study of the statistics of intermittent turbulence in the Earth’s magnetosheath and the solar wind. We exploited the capabilities of the Magnetospheric Multiscale mission to probe structure at kinetic scales, and to validate single-spacecraft estimates using direct two-spacecraft analyses. This study revealed strong signatures of ion and electron scale intermittency in the magnetosheath, which was absent in the solar wind. This finding is consistent with recent observations of electron-scale reconnection in the magnetosheath. We also found different power-law spectral scalings in the solar wind and magnetosheath, which appear to be consistent with previous work. Future work will include an assessment of multiple data intervals to test the robustness of these results. More detailed studies of the nature of the observed intermittency are underway, in which we examine intermittency corrections to the scaling exponents of structure functions of different orders. The current study was restricted to observations of the magnetic field, and we have preliminary results on extending the present analysis to plasma velocities and densities.

There are certainly many improvements possible in the solar wind modeling approach used here as well. [Zank et al. \[2017\]](#) solve separate equations for the slab and 2D energies, with a simplified IMF and background solar wind flow. They find that the evolution of the two components is markedly different in the outer heliosphere (beyond ~ 3 AU), where driving by pickup ions leads to an increase in the slab component’s energy, while the energy of the 2D component continues to decrease with heliocentric distance. Their results show, however, that the radial evolution of slab and 2D energies is not too dissimilar below 3 AU. Similar results are presented by [Oughton et al. \[2011\]](#) using their two-component model. Extensions of the projects discussed in the present dissertation to the outer heliosphere would undoubtedly benefit from incorporating such refinements. Apart from our model’s assumption of single-component (predominantly 2D) turbulence, we also take the energy difference between kinetic and magnetic

fluctuations, or the “residual energy”, to be a constant (this is equivalent to the assumption of constant Alfvén ratio). A dynamically variable residual energy, and as many as three distinct dynamically evolving correlation lengths [Oughton et al., 2011; Zank et al., 2017] could be other possible improvements. These would also introduce more free parameters in the model, however.

As discussed in Chapter 4, our simulations do not explicitly resolve turbulent fluctuations, but instead follow the dynamical evolution of statistical descriptors of the turbulent field. A major future project could be the combination of our simulation datasets with *synthetic realizations* of turbulent fluctuations. These realizations would be constrained by the average values of the correlation scale, turbulence energy, and cross helicity taken from the simulation. A method to generate intermittent magnetized turbulence synthetically (that is, without the requirement of running a computationally expensive and time-consuming direct numerical simulation) was developed recently by [Subedi et al., 2014]¹, building on the minimal multiscale Lagrangian approach of [Rosales and Meneveau, 2006]. Combination of such synthetic fluctuations with the global large scale fields from our solar wind model could be used to study a number of interesting problems, such as the development of complexity in diffusing magnetic flux surfaces [Eyink et al., 2013; Servidio et al., 2014].

As computational power increases, the feasibility of large-eddy simulations (LES) for solar wind simulation may improve [Miesch et al., 2015], and we would eventually like to transition our Reynolds-averaged code into an LES paradigm, with dynamical optimization of simulation parameters [Germano et al., 1991]. Preliminary studies in this direction were presented in Appendix D. The causality lengthscale introduced in Chapter 7 provides a natural candidate for an LES filter scale.

¹ This project was part of the research conducted for the present thesis, but was not presented in this document in order to keep it at a reasonable length.

Bibliography

- L. Adhikari, G. P. Zank, R. Bruno, D. Telloni, P. Hunana, A. Dosch, R. Marino, and Q. Hu. The Transport of Low-frequency Turbulence in Astrophysical Flows. II. Solutions for the Super-Alfvénic Solar Wind. *ApJ*, 805:63, May 2015. doi: 10.1088/0004-637X/805/1/63.
- L. Adhikari, G. P. Zank, P. Hunana, D. Shiota, R. Bruno, Q. Hu, and D. Telloni. II. Transport of Nearly Incompressible Magnetohydrodynamic Turbulence from 1 to 75 au. *ApJ*, 841:85, June 2017. doi: 10.3847/1538-4357/aa6f5d.
- N. Agueda and D. Lario. Release History and Transport Parameters of Relativistic Solar Electrons Inferred From Near-the-Sun In Situ Observations. *ApJ*, 829:131, October 2016. doi: 10.3847/0004-637X/829/2/131.
- V. S. Airapetian and A. V. Usmanov. Reconstructing the Solar Wind from Its Early History to Current Epoch. *ApJL*, 817:L24, February 2016. doi: 10.3847/2041-8205/817/2/L24.
- O. Alexandrova. Solar wind vs magnetosheath turbulence and Alfvén vortices. *Non-linear Processes in Geophysics*, 15:95–108, February 2008.
- O. Alexandrova, V. Carbone, P. Veltri, and L. Sorriso-Valvo. Small-Scale Energy Cascade of the Solar Wind Turbulence. *ApJ*, 674:1153-1157, February 2008. doi: 10.1086/524056.
- O. Alexandrova, C. H. K. Chen, L. Sorriso-Valvo, T. S. Horbury, and S. D. Bale. Solar Wind Turbulence and the Role of Ion Instabilities. *Space Sci. Rev.*, 178:101–139, October 2013. doi: 10.1007/s11214-013-0004-8.
- J. D. Anderson, J. Degroote, G. Degrez, E. Dick, R. Grundmann, and J. Vierendeels. *Computational Fluid Dynamics: An Introduction*. Springer-Verlag Berlin Heidelberg, 2009. doi: 10.1007/978-3-540-85056-4.
- W. I. Axford. The modulation of galactic cosmic rays in the interplanetary medium. *Planet. Space Sci.*, 13:115–130, February 1965. doi: 10.1016/0032-0633(65)90181-9.
- H. W. Babcock. The Topology of the Sun’s Magnetic Field and the 22-YEAR Cycle. *ApJ*, 133:572, March 1961. doi: 10.1086/147060.

- A. Barnes. Collisionless Damping of Hydromagnetic Waves. *Physics of Fluids*, 9: 1483–1495, August 1966. doi: 10.1063/1.1761882.
- A. Barnes. *Hydromagnetic waves and turbulence in the solar wind*, pages 249–319. National Academies Press, 1979.
- A. Barnes and J. V. Hollweg. Large-amplitude hydromagnetic waves. *J. Geophys. Res.*, 79:2302, 1974. doi: 10.1029/JA079i016p02302.
- G. K. Batchelor. *The Theory of Homogeneous Turbulence*. Cambridge University Press, 1953.
- G. K. Batchelor. *An Introduction to Fluid Dynamics*. Cambridge University Press, February 2000.
- B. Bavassano, M. Dobrowolny, G. Fanfoni, F. Mariani, and N. F. Ness. Statistical properties of MHD fluctuations associated with high-speed streams from Helios-2 observations. *Sol. Phys.*, 78:373–384, June 1982a. doi: 10.1007/BF00151617.
- B. Bavassano, M. Dobrowolny, F. Mariani, and N. F. Ness. Radial evolution of power spectra of interplanetary Alfvénic turbulence. *J. Geophys. Res.*, 87:3617–3622, May 1982b. doi: 10.1029/JA087iA05p03617.
- B. Bavassano, R. Woo, and R. Bruno. Heliospheric plasma sheet and coronal streamers. *Geophys. Res. Lett.*, 24:1655–1658, 1997. doi: 10.1029/97GL01630.
- J. Beeck, G. M. Mason, D. C. Hamilton, G. Wibberenz, H. Kunow, D. Hovestadt, and B. Klecker. A multispacecraft study of the injection and transport of solar energetic particles. *ApJ*, 322:1052–1072, November 1987. doi: 10.1086/165800.
- J. W. Belcher and L. Davis, Jr. Large-amplitude Alfvén waves in the interplanetary medium, 2. *J. Geophys. Res.*, 76:3534, 1971. doi: 10.1029/JA076i016p03534.
- J. W. Belcher, L. Davis, Jr., and E. J. Smith. Large-amplitude Alfvén waves in the interplanetary medium: Mariner 5. *J. Geophys. Res.*, 74:2302, 1969. doi: 10.1029/JA074i009p02302.
- J. W. Bieber and W. H. Matthaeus. Perpendicular Diffusion and Drift at Intermediate Cosmic-Ray Energies. *ApJ*, 485:655–659, August 1997. doi: 10.1086/304464.
- J. W. Bieber, W. H. Matthaeus, C. W. Smith, W. Wanner, M.-B. Kallenrode, and G. Wibberenz. Proton and electron mean free paths: The Palmer consensus revisited. *ApJ*, 420:294–306, January 1994. doi: 10.1086/173559.
- J. W. Bieber, R. A. Burger, and W. H. Matthaeus. The Diffusion Tensor throughout the Heliosphere. *International Cosmic Ray Conference*, 4:694, 1995.

- J. W. Bieber, W. Wanner, and W. H. Matthaeus. Dominant two-dimensional solar wind turbulence with implications for cosmic ray transport. *J. Geophys. Res.*, 101: 2511–2522, February 1996. doi: 10.1029/95JA02588.
- J. W. Bieber, W. H. Matthaeus, A. Shalchi, and G. Qin. Nonlinear guiding center theory of perpendicular diffusion: General properties and comparison with observation. *Geophys. Res. Lett.*, 31:L10805, May 2004. doi: 10.1029/2004GL020007.
- L. Biermann. Solar corpuscular radiation and the interplanetary gas. *The Observatory*, 77:109–110, June 1957.
- M. K. Bird and P. Edenhofer. *Remote Sensing Observations of the Solar Corona*, page 13. Springer-Verlag Berlin Heidelberg, 1990.
- D. Biskamp. Magnetic Reconnection in Plasmas. *Ap&SS*, 242:165–207, March 1996. doi: 10.1007/BF00645113.
- D. Biskamp. *Magnetohydrodynamic Turbulence*. Cambridge University Press, July 2003.
- J. A. Bittencourt. *Fundamentals of Plasma Physics*. Springer-Verlag, 2004.
- S. Boldyrev, C. H. K. Chen, Q. Xia, and V. Zhdankin. Spectral Breaks of Alfvénic Turbulence in a Collisionless Plasma. *ApJ*, 806:238, June 2015. doi: 10.1088/0004-637X/806/2/238.
- A. Bonetti, H. S. Bridge, A. J. Lazarus, B. Rossi, and F. Scherb. Explorer 10 Plasma Measurements. *J. Geophys. Res.*, 68:4017, July 1963. doi: 10.1029/JZ068i013p04017.
- Jean Boussinesq. *Essai sur la théorie des eaux courantes*. Imprimerie nationale, 1877.
- William E Boyce, Richard C DiPrima, and Charles W Haines. *Elementary differential equations and boundary value problems*, volume 9. Wiley New York, 1969.
- A. Brandenburg and A. Lazarian. Astrophysical Hydromagnetic Turbulence. *Space Sci. Rev.*, 178:163–200, October 2013. doi: 10.1007/s11214-013-0009-3.
- A. Brandenburg and Å. Nordlund. Astrophysical turbulence modeling. *Reports on Progress in Physics*, 74(4):046901, April 2011. doi: 10.1088/0034-4885/74/4/046901.
- J. C. Brandt and J. P. Cassinelli. Interplanetary Gas. XI. An Exospheric Model of the Solar Wind. *Icarus*, 5:47–63, 1966. doi: 10.1016/0019-1035(66)90007-8.
- B. Breech, W. H. Matthaeus, J. Minnie, S. Oughton, S. Parhi, J. W. Bieber, and B. Bavassano. Radial evolution of cross helicity in high-latitude solar wind. *Geophys. Res. Lett.*, 32:L06103, March 2005. doi: 10.1029/2004GL022321.

- B. Breech, W. H. Matthaeus, J. Minnie, J. W. Bieber, S. Oughton, C. W. Smith, and P. A. Isenberg. Turbulence transport throughout the heliosphere. *Journal of Geophysical Research (Space Physics)*, 113:A08105, August 2008. doi: 10.1029/2007JA012711.
- B. Breech, W. H. Matthaeus, S. R. Cranmer, J. C. Kasper, and S. Oughton. Electron and proton heating by solar wind turbulence. *Journal of Geophysical Research (Space Physics)*, 114:A09103, September 2009. doi: 10.1029/2009JA014354.
- R. Bruno and V. Carbone. The Solar Wind as a Turbulence Laboratory. *Living Reviews in Solar Physics*, 10:2, December 2013. doi: 10.12942/lrsp-2013-2.
- J. L. Burch, T. E. Moore, R. B. Torbert, and B. L. Giles. Magnetospheric Multiscale Overview and Science Objectives. *Space Sci. Rev.*, 199:5–21, March 2016. doi: 10.1007/s11214-015-0164-9.
- J. Candia and E. Roulet. Diffusion and drift of cosmic rays in highly turbulent magnetic fields. *J. Cosmology Astropart. Phys.*, 10:007, October 2004. doi: 10.1088/1475-7516/2004/10/007.
- H. V. Cane, G. Wibberenz, I. G. Richardson, and T. T. von Rosenvinge. Cosmic ray modulation and the solar magnetic field. *Geophys. Res. Lett.*, 26:565–568, 1999. doi: 10.1029/1999GL900032.
- M. V. Canullo, A. Costa, and C. Ferro-Fontan. Nonlocal Heat Transport in the Solar Wind. *ApJ*, 462:1005, May 1996. doi: 10.1086/177214.
- V. M. Canuto. Large Eddy simulation of turbulence: A subgrid scale model including shear, vorticity, rotation, and buoyancy. *ApJ*, 428:729–752, June 1994. doi: 10.1086/174281.
- R. C. Carrington. Description of a Singular Appearance seen in the Sun on September 1, 1859. *MNRAS*, 20:13–15, November 1859. doi: 10.1093/mnras/20.1.13.
- B. D. G. Chandran, T. J. Dennis, E. Quataert, and S. D. Bale. Incorporating Kinetic Physics into a Two-fluid Solar-wind Model with Temperature Anisotropy and Low-frequency Alfvén-wave Turbulence. *ApJ*, 743:197, December 2011. doi: 10.1088/0004-637X/743/2/197.
- S. Chapman and T. G. Cowling. *The Mathematical Theory of Non-uniform Gases*. Cambridge University Press, January 1991.
- S. Chapman and H. Zirin. Notes on the Solar Corona and the Terrestrial Ionosphere. *Smithsonian Contributions to Astrophysics*, 2:1, 1957.

- A. Chasapis, W. H. Matthaeus, T. N. Parashar, S. A. Fuselier, B. A. Maruca, T. D. Phan, J. L. Burch, T. E. Moore, C. J. Pollock, D. J. Gershman, R. B. Torbert, C. T. Russell, and R. J. Strangeway. High-resolution Statistics of Solar Wind Turbulence at Kinetic Scales Using the Magnetospheric Multiscale Mission. *ApJL*, 844:L9, July 2017. doi: 10.3847/2041-8213/aa7ddd.
- A. Chasapis, W. H. Matthaeus, T. N. Parashar, M. Wan, C. C. Haggerty, C. J. Pollock, B. L. Giles, W. R. Paterson, J. Dorelli, D. J. Gershman, R. B. Torbert, C. T. Russell, P.-A. Lindqvist, Y. Khotyaintsev, T. E. Moore, R. E. Ergun, and J. L. Burch. In Situ Observation of Intermittent Dissipation at Kinetic Scales in the Earth’s Magnetosheath. *ApJL*, 856:L19, March 2018. doi: 10.3847/2041-8213/aaadf8.
- R. Chhiber, A. Usmanov, W. Matthaeus, and M. Goldstein. Solar Wind Collisional Age from a Global Magnetohydrodynamics Simulation. *ApJ*, 821:34, April 2016a. doi: 10.3847/0004-637X/821/1/34.
- R. Chhiber, A. V. Usmanov, W. H. Matthaeus, A. Petrosyan, T. Parashar, Y. Yang, and M. L. Goldstein. Turbulence Causality-Constrained PANS Model for MHD Simulation of the Solar Wind. *AGU Fall Meeting Abstracts*, December 2016b.
- R. Chhiber, P. Subedi, A. V. Usmanov, W. H. Matthaeus, D. Ruffolo, M. L. Goldstein, and T. N. Parashar. Cosmic-Ray Diffusion Coefficients throughout the Inner Heliosphere from a Global Solar Wind Simulation. *ApJS*, 230:21, June 2017a. doi: 10.3847/1538-4365/aa74d2.
- R. Chhiber, P. Subedi, A. V. Usmanov, W. H. Matthaeus, D. Ruffolo, M. L. Goldstein, and T. N. Parashar. VizieR Online Data Catalog: Solar wind 3D magnetohydrodynamic simulation (Chhiber+, 2017). *VizieR Online Data Catalog*, 223, August 2017b.
- R. Chhiber, A. G. Chasapis, R. Bandyopadhyay, T. N. Parashar, W. H. Matthaeus, B. A. Maruca, T. E. Moore, J. L. Burch, R. B. Torbert, C. T. Russell, R. J. Strangeway, C. J. Pollock, B. L. Giles, and D. J. Gershman. Higher-order Turbulence Statistics in the Earth’s Magnetosheath and the Solar Wind using Magnetospheric Multiscale Observations; In prep. 2018a.
- R. Chhiber, W. H. Matthaeus, A. V. Usmanov, T. N. Parashar, M. L. Goldstein, and S Oughton. Range of Influence of Turbulence in Solar Wind Fluctuations: Estimating a Causality Threshold; In prep. 2018b.
- R. Chhiber, A. V. Usmanov, C. E. DeForest, W. H. Matthaeus, T. N. Parashar, and M. L. Goldstein. Weakened Magnetization and Onset of Large-scale Turbulence in the Young Solar Wind—Comparisons of Remote Sensing Observations with Simulation. *ApJL*, 856:L39, April 2018c. doi: 10.3847/2041-8213/aab843.

- R. Chhiber, A. V. Usmanov, W. H. Matthaeus, and M. L. Goldstein. Contextual Predictions for Parker Solar Probe I: Critical Surfaces and Regions; Submitted. *ApJS*, 2018d.
- R. Chhiber, A. V. Usmanov, W. H. Matthaeus, T. N. Parashar, and M. L. Goldstein. Contextual Predictions for Parker Solar Probe II: Turbulence Properties, Taylor Hypothesis, and Causality; In prep. 2018e.
- A. R. Choudhuri. *The Physics of Fluids and Plasmas: An Introduction for Astrophysicists*. Cambridge University Press, November 1998.
- P. J. Coleman. Hydromagnetic Waves in the Interplanetary Plasma. *Physical Review Letters*, 17:207–211, July 1966. doi: 10.1103/PhysRevLett.17.207.
- P. J. Coleman, Jr. Wave-like phenomena in the interplanetary plasma: Mariner 2. *Planet. Space Sci.*, 15:953–973, June 1967. doi: 10.1016/0032-0633(67)90166-3.
- P. J. Coleman, Jr. Turbulence, Viscosity, and Dissipation in the Solar-Wind Plasma. *ApJ*, 153:371, August 1968. doi: 10.1086/149674.
- T. G. Cowling. *Magnetohydrodynamics*. Interscience, 1957.
- S. R. Cranmer and A. A. van Ballegooijen. On the Generation, Propagation, and Reflection of Alfvén Waves from the Solar Photosphere to the Distant Heliosphere. *ApJS*, 156:265–293, February 2005. doi: 10.1086/426507.
- S. R. Cranmer, A. A. van Ballegooijen, and R. J. Edgar. Self-consistent Coronal Heating and Solar Wind Acceleration from Anisotropic Magnetohydrodynamic Turbulence. *ApJS*, 171:520–551, August 2007. doi: 10.1086/518001.
- S. R. Cranmer, W. H. Matthaeus, B. A. Breech, and J. C. Kasper. Empirical Constraints on Proton and Electron Heating in the Fast Solar Wind. *ApJ*, 702:1604–1614, September 2009. doi: 10.1088/0004-637X/702/2/1604.
- A. Czaykowska, T. M. Bauer, R. A. Treumann, and W. Baumjohann. Magnetic field fluctuations across the Earth’s bow shock. *Annales Geophysicae*, 19:275–287, March 2001. doi: 10.5194/angeo-19-275-2001.
- Peter Davidson. *Turbulence: an introduction for scientists and engineers*. Oxford University Press, USA, 2015.
- T. de Kármán and L. Howarth. On the Statistical Theory of Isotropic Turbulence. *Proceedings of the Royal Society of London Series A*, 164:192–215, January 1938. doi: 10.1098/rspa.1938.0013.
- L. T. DeCarlo. On the Meaning and Use of Kurtosis. *Psychological Methods*, 2(3):292, 1997.

- C. E. DeForest, T. A. Howard, and D. J. McComas. Inbound Waves in the Solar Corona: A Direct Indicator of Alfvén Surface Location. *ApJ*, 787:124, June 2014. doi: 10.1088/0004-637X/787/2/124.
- C. E. DeForest, W. H. Matthaeus, N. M. Viall, and S. R. Cranmer. Fading Coronal Structure and the Onset of Turbulence in the Young Solar Wind. *ApJ*, 828:66, September 2016. doi: 10.3847/0004-637X/828/2/66.
- P. Dmitruk, W. H. Matthaeus, and N. Seenu. Test Particle Energization by Current Sheets and Nonuniform Fields in Magnetohydrodynamic Turbulence. *ApJ*, 617:667–679, December 2004. doi: 10.1086/425301.
- W. Dröge. Solar Particle Transport in a Dynamical Quasi-linear Theory. *ApJ*, 589:1027–1039, June 2003. doi: 10.1086/374812.
- W. Dröge, Y. Y. Kartavykh, N. Dresing, and A. Klassen. Multi-spacecraft Observations and Transport Modeling of Energetic Electrons for a Series of Solar Particle Events in August 2010. *ApJ*, 826:134, August 2016. doi: 10.3847/0004-637X/826/2/134.
- J. R. Dwyer, G. M. Mason, J. E. Mazur, J. R. Jokipii, T. T. von Rosenvinge, and R. P. Lepping. Perpendicular Transport of Low-Energy Corotating Interaction Region-associated Nuclei. *ApJL*, 490:L115–L118, November 1997. doi: 10.1086/311003.
- W. M. Elsasser. The Hydromagnetic Equations. *Physical Review*, 79:183–183, July 1950. doi: 10.1103/PhysRev.79.183.
- N. E. Engelbrecht and R. A. Burger. An Ab Initio Model for the Modulation of Galactic Cosmic-ray Electrons. *ApJ*, 779:158, December 2013. doi: 10.1088/0004-637X/779/2/158.
- G. Eyink, E. Vishniac, C. Lalescu, H. Aluie, K. Kanov, K. Bürger, R. Burns, C. Meneveau, and A. Szalay. Flux-freezing breakdown in high-conductivity magnetohydrodynamic turbulence. *Nature*, 497:466–469, May 2013. doi: 10.1038/nature12128.
- A Favre. Problems of hydrodynamics and continuum mechanics. *Society for Industrial and Applied Mathematics, Philadelphia*, 231:42, 1969.
- W. C. Feldman, J. R. Asbridge, and S. J. Bame. The solar wind He²⁺ to H⁺ temperature ratio. *J. Geophys. Res.*, 79:2319, 1974. doi: 10.1029/JA079i016p02319.
- W. C. Feldman, J. R. Asbridge, S. J. Bame, M. D. Montgomery, and S. P. Gary. Solar wind electrons. *J. Geophys. Res.*, 80:4181–4196, November 1975. doi: 10.1029/JA080i031p04181.
- L. A. Fisk. *The interactions of energetic particles with the solar wind*, pages 177–247. North-Holland Publishing Company, 1979.

- S. E. Forbush. World-Wide Cosmic-Ray Variations, 1937-1952. *J. Geophys. Res.*, 59: 525–542, December 1954. doi: 10.1029/JZ059i004p00525.
- N. J. Fox, M. C. Velli, S. D. Bale, R. Decker, A. Driesman, R. A. Howard, J. C. Kasper, J. Kinnison, M. Kusterer, D. Lario, M. K. Lockwood, D. J. McComas, N. E. Raouafi, and A. Szabo. The Solar Probe Plus Mission: Humanity’s First Visit to Our Star. *Space Sci. Rev.*, 204:7–48, December 2016. doi: 10.1007/s11214-015-0211-6.
- M. Fränz and D. Harper. Heliospheric coordinate systems. *Planet. Space Sci.*, 50: 217–233, February 2002. doi: 10.1016/S0032-0633(01)00119-2.
- M. Germano. Turbulence - The filtering approach. *Journal of Fluid Mechanics*, 238: 325–336, May 1992. doi: 10.1017/S0022112092001733.
- M. Germano, U. Piomelli, P. Moin, and W. H. Cabot. A dynamic subgrid-scale eddy viscosity model. *Physics of Fluids A*, 3:1760–1765, July 1991. doi: 10.1063/1.857955.
- S. Ghosh and M. L. Goldstein. Anisotropy in Hall MHD turbulence due to a mean magnetic field. *Journal of Plasma Physics*, 57:129–154, January 1997. doi: 10.1017/S0022377896005260.
- J. Giacalone and J. R. Jokipii. The Transport of Cosmic Rays across a Turbulent Magnetic Field. *ApJ*, 520:204–214, July 1999. doi: 10.1086/307452.
- S. Giordano, E. Antonucci, G. Noci, M. Romoli, and J. L. Kohl. Identification of the Coronal Sources of the Fast Solar Wind. *ApJL*, 531:L79–L82, March 2000. doi: 10.1086/312525.
- L. J. Gleeson. The equations describing the cosmic-ray gas in the interplanetary region. *Planet. Space Sci.*, 17:31–47, January 1969. doi: 10.1016/0032-0633(69)90121-4.
- P. Goldreich and S. Sridhar. Toward a theory of interstellar turbulence. 2: Strong alfvenic turbulence. *ApJ*, 438:763–775, January 1995. doi: 10.1086/175121.
- M. L. Goldstein. A nonlinear theory of cosmic-ray pitch-angle diffusion in homogeneous magnetostatic turbulence. *ApJ*, 204:900–919, March 1976. doi: 10.1086/154239.
- M. L. Goldstein, D. A. Roberts, and W. H. Matthaeus. Systematic errors in determining the propagation direction of interplanetary Alfvénic fluctuations. *J. Geophys. Res.*, 91:13357–13365, December 1986. doi: 10.1029/JA091iA12p13357.
- M. L. Goldstein, D. A. Roberts, and W. H. Matthaeus. Magnetohydrodynamic Turbulence In The Solar Wind. *ARA&A*, 33:283–326, 1995. doi: 10.1146/annurev.aa.33.090195.001435.
- J. T. Gosling and V. J. Pizzo. Formation and Evolution of Corotating Interaction Regions and their Three Dimensional Structure. *Space Sci. Rev.*, 89:21–52, July 1999. doi: 10.1023/A:1005291711900.

- S. Gottlieb, C.-W. Shu, and E. Tadmor. Strong Stability-Preserving High-Order Time Discretization Methods. *SIAM Review*, 43:89–112, January 2001. doi: 10.1137/S003614450036757X.
- R. R. Grail, W. A. Coles, M. T. KlingleSmith, A. R. Breen, P. J. S. Williams, J. Markkanen, and R. Esser. Rapid acceleration of the polar solar wind. *Nature*, 379:429–432, February 1996. doi: 10.1038/379429a0.
- R. Grappin, J. Leorat, and A. Pouquet. Dependence of MHD turbulence spectra on the velocity field-magnetic field correlation. *A&A*, 126:51–58, September 1983.
- R. Grappin, M. Velli, and A. Mangeney. Nonlinear wave evolution in the expanding solar wind. *Physical Review Letters*, 70:2190–2193, April 1993. doi: 10.1103/PhysRevLett.70.2190.
- D. H. Griffel and L. Davis. The anisotropy of the solar wind. *Planet. Space Sci.*, 17:1009–1020, May 1969. doi: 10.1016/0032-0633(69)90105-6.
- K. I. Gringauz, V. V. Bezrokh, V. D. Ozerov, and R. E. Rybchinskii. A Study of the Interplanetary Ionized Gas, High-Energy Electrons and Corpuscular Radiation from the Sun by Means of the Three-Electrode Trap for Charged Particles on the Second Soviet Cosmic Rocket. *Soviet Physics Doklady*, 5:361, September 1960.
- X. Guo and V. Florinski. Galactic Cosmic-Ray Intensity Modulation by Corotating Interaction Region Stream Interfaces at 1 au. *ApJ*, 826:65, July 2016. doi: 10.3847/0004-637X/826/1/65.
- S. R. Habbal, R. Esser, M. Guhathakurta, and R. R. Fisher. Flow properties of the solar wind derived from a two-fluid model with constraints from white light and in situ interplanetary observations. *Geophys. Res. Lett.*, 22:1465–1468, 1995. doi: 10.1029/95GL01064.
- L. Z. Hadid, F. Sahraoui, K. H. Kiyani, A. Retinò, R. Modolo, P. Canu, A. Masters, and M. K. Dougherty. Nature of the MHD and Kinetic Scale Turbulence in the Magnetosheath of Saturn: Cassini Observations. *ApJL*, 813:L29, November 2015. doi: 10.1088/2041-8205/813/2/L29.
- J. B. Hartle. *Gravity : an introduction to Einstein's general relativity*. Addison Wesley, 2003.
- R. E. Hartle and P. A. Sturrock. Two-Fluid Model of the Solar Wind. *ApJ*, 151:1155, March 1968. doi: 10.1086/149513.
- A. Hasegawa and T. Sato. *Space plasma physics: I - Stationary processes*. Springer-Verlag, 1989.

- B. Heber and M. S. Potgieter. Cosmic Rays at High Heliolatitudes. *Space Sci. Rev.*, 127:117–194, December 2006. doi: 10.1007/s11214-006-9085-y.
- M. Heinemann and S. Olbert. Non-WKB Alfvén waves in the solar wind. *J. Geophys. Res.*, 85:1311–1327, March 1980. doi: 10.1029/JA085iA03p01311.
- W. Heisenberg. On the Theory of Statistical and Isotropic Turbulence. *Proceedings of the Royal Society of London Series A*, 195:402–406, December 1948. doi: 10.1098/rspa.1948.0127.
- P. Hellinger, L. Matteini, Š. Štverák, P. M. Trávníček, and E. Marsch. Heating and cooling of protons in the fast solar wind between 0.3 and 1 AU: Helios revisited. *Journal of Geophysical Research (Space Physics)*, 116:A09105, September 2011. doi: 10.1029/2011JA016674.
- J. V. Hollweg. On electron heat conduction in the solar wind. *J. Geophys. Res.*, 79:3845, 1974. doi: 10.1029/JA079i025p03845.
- J. V. Hollweg. Collisionless electron heat conduction in the solar wind. *J. Geophys. Res.*, 81:1649–1658, April 1976. doi: 10.1029/JA081i010p01649.
- J. V. Hollweg. Transition region, corona, and solar wind in coronal holes. *J. Geophys. Res.*, 91:4111–4125, April 1986. doi: 10.1029/JA091iA04p04111.
- J. V. Hollweg. On WKB expansions for Alfvén waves in the solar wind. *J. Geophys. Res.*, 95:14873–14879, September 1990. doi: 10.1029/JA095iA09p14873.
- T. S. Horbury, M. A. Forman, and S. Oughton. Spacecraft observations of solar wind turbulence: an overview. *Plasma Physics and Controlled Fusion*, 47:B703–B717, December 2005. doi: 10.1088/0741-3335/47/12B/S52.
- M. Hossain, P. C. Gray, D. H. Pontius, Jr., W. H. Matthaeus, and S. Oughton. Phenomenology for the decay of energy-containing eddies in homogeneous MHD turbulence. *Physics of Fluids*, 7:2886–2904, November 1995. doi: 10.1063/1.868665.
- G. G. Howes. A prospectus on kinetic heliophysics. *Physics of Plasmas*, 24(5):055907, May 2017. doi: 10.1063/1.4983993.
- G. G. Howes, K. G. Klein, and J. M. TenBarge. Validity of the Taylor Hypothesis for Linear Kinetic Waves in the Weakly Collisional Solar Wind. *ApJ*, 789:106, July 2014. doi: 10.1088/0004-637X/789/2/106.
- S. Y. Huang, L. Z. Hadid, F. Sahraoui, Z. G. Yuan, and X. H. Deng. On the Existence of the Kolmogorov Inertial Range in the Terrestrial Magnetosheath Turbulence. *ApJL*, 836:L10, February 2017. doi: 10.3847/2041-8213/836/1/L10.

- P. Hunana and G. P. Zank. Inhomogeneous Nearly Incompressible Description of Magnetohydrodynamic Turbulence. *ApJ*, 718:148–167, July 2010. doi: 10.1088/0004-637X/718/1/148.
- A. J. Hundhausen. *Coronal Expansion and Solar Wind*. Springer-Verlag, 1972.
- P. S. Iroshnikov. Turbulence of a Conducting Fluid in a Strong Magnetic Field. *Soviet Ast.*, 7:566, February 1964.
- J. D. Jackson. *Electrodynamics*. Wiley, 1975.
- S. A. Jacques. Momentum and energy transport by waves in the solar atmosphere and solar wind. *ApJ*, 215:942–951, August 1977. doi: 10.1086/155430.
- S. A. Jacques. Solar wind models with Alfvén waves. *ApJ*, 226:632–649, December 1978. doi: 10.1086/156647.
- J. H. Jeans. *The Dynamical Theory of Gases*. Cambridge University Press, 1921.
- J. R. Jokipii. Cosmic-Ray Propagation. I. Charged Particles in a Random Magnetic Field. *ApJ*, 146:480, November 1966. doi: 10.1086/148912.
- J. R. Jokipii. Propagation of cosmic rays in the solar wind. *Reviews of Geophysics and Space Physics*, 9:27–87, 1971. doi: 10.1029/RG009i001p00027.
- J. R. Jokipii. Turbulence and Scintillations in the Interplanetary Plasma. *ARA&A*, 11:1, 1973. doi: 10.1146/annurev.aa.11.090173.000245.
- J. R. Jokipii and J. Kota. Three-Dimensional Cosmic-Ray Simulations: Heliographic Latitude and Current-Sheet Tilt. In R. G. Marsden, editor, *The High Latitude Heliosphere*, page 379, 1995.
- J. R. Jokipii and E. N. Parker. on the Convection, Diffusion, and Adiabatic Deceleration of Cosmic Rays in the Solar Wind. *ApJ*, 160:735, May 1970. doi: 10.1086/150465.
- J. R. Jokipii and B. Thomas. Effects of drift on the transport of cosmic rays. IV - Modulation by a wavy interplanetary current sheet. *ApJ*, 243:1115–1122, February 1981. doi: 10.1086/158675.
- H. Karimabadi, V. Roytershteyn, M. Wan, W. H. Matthaeus, W. Daughton, P. Wu, M. Shay, B. Loring, J. Borovsky, E. Leonardis, S. C. Chapman, and T. K. M. Nakamura. Coherent structures, intermittent turbulence, and dissipation in high-temperature plasmas. *Physics of Plasmas*, 20(1):012303, January 2013. doi: 10.1063/1.4773205.
- J. C. Kasper, A. J. Lazarus, and S. P. Gary. Hot Solar-Wind Helium: Direct Evidence for Local Heating by Alfvén-Cyclotron Dissipation. *Physical Review Letters*, 101(26):261103, December 2008. doi: 10.1103/PhysRevLett.101.261103.

- J. C. Kasper, K. G. Klein, T. Weber, M. Maksimovic, A. Zaslavsky, S. D. Bale, B. A. Maruca, M. L. Stevens, and A. W. Case. A Zone of Preferential Ion Heating Extends Tens of Solar Radii from the Sun. *ApJ*, 849:126, November 2017. doi: 10.3847/1538-4357/aa84b1.
- S. Klainerman and A. Majda. Singular limits of quasilinear hyperbolic systems with large parameters and the incompressible limit of compressible fluids. *Communications in Pure Applied Mathematics*, 34:481–524, July 1981.
- S. Klainerman and A. Majda. Compressible and incompressible fluids. *Communications in Pure Applied Mathematics*, 35:629–651, September 1982.
- K. G. Klein, J. C. Perez, D. Verscharen, A. Mallet, and B. D. G. Chandran. A Modified Version of Taylor’s Hypothesis for Solar Probe Plus Observations. *ApJL*, 801:L18, March 2015. doi: 10.1088/2041-8205/801/1/L18.
- L. W. Klein and L. F. Burlaga. Interplanetary magnetic clouds at 1 AU. *J. Geophys. Res.*, 87:613–624, February 1982. doi: 10.1029/JA087iA02p00613.
- L. W. Klein, K. W. Ogilvie, and L. F. Burlaga. Coulomb collisions in the solar wind. *J. Geophys. Res.*, 90:7389–7395, August 1985. doi: 10.1029/JA090iA08p07389.
- L. W. Klein, D. A. Roberts, and M. L. Goldstein. Anisotropy and minimum variance directions of solar wind fluctuations in the outer heliosphere. *J. Geophys. Res.*, 96:3779–3788, March 1991. doi: 10.1029/90JA02240.
- J. A. Klimchuk. On Solving the Coronal Heating Problem. *Sol. Phys.*, 234:41–77, March 2006. doi: 10.1007/s11207-006-0055-z.
- D. Koga, A. C.-L. Chian, R. A. Miranda, and E. L. Rempel. Intermittent nature of solar wind turbulence near the Earth’s bow shock: Phase coherence and non-Gaussianity. *Phys. Rev. E*, 75(4):046401, April 2007. doi: 10.1103/PhysRevE.75.046401.
- A. Kolmogorov. The Local Structure of Turbulence in Incompressible Viscous Fluid for Very Large Reynolds’ Numbers. *Akademiia Nauk SSSR Doklady*, 30:301–305, 1941a.
- A. N. Kolmogorov. Dissipation of Energy in Locally Isotropic Turbulence. *Akademiia Nauk SSSR Doklady*, 32:16, April 1941b.
- A. N. Kolmogorov. A refinement of previous hypotheses concerning the local structure of turbulence in a viscous incompressible fluid at high Reynolds number. *Journal of Fluid Mechanics*, 13:82–85, 1962. doi: 10.1017/S0022112062000518.
- R. A. Kopp and T. E. Holzer. Dynamics of coronal hole regions. I - Steady polytropic flows with multiple critical points. *Sol. Phys.*, 49:43–56, July 1976. doi: 10.1007/BF00221484.

- R. H. Kraichnan. The structure of isotropic turbulence at very high Reynolds numbers. *Journal of Fluid Mechanics*, 5:497–543, 1959. doi: 10.1017/S0022112059000362.
- R. H. Kraichnan. Inertial-Range Spectrum of Hydromagnetic Turbulence. *Physics of Fluids*, 8:1385–1387, July 1965a. doi: 10.1063/1.1761412.
- R. H. Kraichnan. Lagrangian-History Closure Approximation for Turbulence. *Physics of Fluids*, 8:575–598, April 1965b. doi: 10.1063/1.1761271.
- F. Krause and K.-H. Raedler. *Mean-field magnetohydrodynamics and dynamo theory*. Pergamon Press, 1980.
- R. Kulsrud and W. P. Pearce. The Effect of Wave-Particle Interactions on the Propagation of Cosmic Rays. *ApJ*, 156:445, May 1969. doi: 10.1086/149981.
- H. Kunow, G. Wibberenz, G. Green, R. Müller-Mellin, and M.-B. Kallenrode. *Energetic Particles in the Inner Solar System*, page 152. Springer-Verlag, 1991.
- A. Kurganov and D. Levy. A third-order semidiscrete central scheme for conservation laws and convection-diffusion equations. *SIAM Journal on Scientific Computing*, 22(4):1461–1488, 2000.
- R. J. Leamon, C. W. Smith, N. F. Ness, W. H. Matthaeus, and H. K. Wong. Observational constraints on the dynamics of the interplanetary magnetic field dissipation range. *J. Geophys. Res.*, 103:4775, March 1998. doi: 10.1029/97JA03394.
- E. Leer, T. E. Holzer, and T. Fla. Acceleration of the solar wind. *Space Sci. Rev.*, 33:161–200, March 1982. doi: 10.1007/BF00213253.
- E. Leonardis, S. C. Chapman, W. Daughton, V. Roytershteyn, and H. Karimabadi. Identification of Intermittent Multifractal Turbulence in Fully Kinetic Simulations of Magnetic Reconnection. *Physical Review Letters*, 110(20):205002, May 2013. doi: 10.1103/PhysRevLett.110.205002.
- M. Lesieur and O. Metais. New trends in large-eddy simulations of turbulence. *Annual Review of Fluid Mechanics*, 28:45–82, 1996. doi: 10.1146/annurev.fl.28.010196.000401.
- Marcel Lesieur. *Turbulence in fluids*, volume 40. Springer Science & Business Media, 2012.
- H. W. Liepmann. The rise and fall of ideas in turbulence. *American Scientist*, 67:221–228, April 1979.
- S. Livi, E. Marsch, and H. Rosenbauer. Coulomb collisional domains in the solar wind. *J. Geophys. Res.*, 91:8045–8050, July 1986. doi: 10.1029/JA091iA07p08045.

- N. A. Lotova, D. F. Blums, and K. V. Vladimirkii. Interplanetary scintillation and the structure of the solar wind transonic region. *A&A*, 150:266–272, September 1985.
- N. A. Lotova, K. V. Vladimirkii, and O. A. Korelov. Radio Maps of the Solar Wind Transition Region. *Sol. Phys.*, 172:225–231, May 1997. doi: 10.1023/A:1004910023642.
- B. T. MacBride, C. W. Smith, and M. A. Forman. The Turbulent Cascade at 1 AU: Energy Transfer and the Third-Order Scaling for MHD. *ApJ*, 679:1644–1660, June 2008. doi: 10.1086/529575.
- R. L. Mace, W. H. Matthaeus, and J. W. Bieber. Numerical Investigation of Perpendicular Diffusion of Charged Test Particles in Weak Magnetostatic Slab Turbulence. *ApJ*, 538:192–202, July 2000. doi: 10.1086/309093.
- K. D. Makwana, V. Zhdankin, H. Li, W. Daughton, and F. Cattaneo. Energy dynamics and current sheet structure in fluid and kinetic simulations of decaying magnetohydrodynamic turbulence. *Physics of Plasmas*, 22(4):042902, April 2015. doi: 10.1063/1.4916492.
- R. Marino, L. Sorriso-Valvo, R. D’Amicis, V. Carbone, R. Bruno, and P. Veltri. On the Occurrence of the Third-order Scaling in High Latitude Solar Wind. *ApJ*, 750:41, May 2012. doi: 10.1088/0004-637X/750/1/41.
- E. Marsch. *MHD Turbulence in the Solar Wind*, page 152. Springer-Verlag, 1991.
- E. Marsch. Kinetic Physics of the Solar Corona and Solar Wind. *Living Reviews in Solar Physics*, 3:1, July 2006. doi: 10.12942/lrsp-2006-1.
- E. Marsch and H. Goldstein. The effects of coulomb collisions on solar wind ion velocity distributions. *J. Geophys. Res.*, 88:9933–9940, December 1983. doi: 10.1029/JA088iA12p09933.
- E. Marsch and C.-Y. Tu. Dynamics of correlation functions with Elsasser variables for inhomogeneous MHD turbulence. *Journal of Plasma Physics*, 41:479–491, June 1989. doi: 10.1017/S0022377800014033.
- E. Marsch and C. Y. Tu. Electric field fluctuations and possible dynamo effects in the solar wind. In E. Marsch and R. Schwenn, editors, *Solar Wind Seven Colloquium*, pages 505–510, 1992.
- E. Marsch and C.-Y. Tu. Intermittency, non-Gaussian statistics and fractal scaling of MHD fluctuations in the solar wind. *Nonlinear Processes in Geophysics*, 4:101–124, 1997.
- M. S. Marsh, S. Dalla, J. Kelly, and T. Laitinen. Drift-induced Perpendicular Transport of Solar Energetic Particles. *ApJ*, 774:4, September 2013. doi: 10.1088/0004-637X/774/1/4.

- B. A. Maruca, S. D. Bale, L. Sorriso-Valvo, J. C. Kasper, and M. L. Stevens. Collisional Thermalization of Hydrogen and Helium in Solar-Wind Plasma. *Physical Review Letters*, 111(24):241101, December 2013. doi: 10.1103/PhysRevLett.111.241101.
- L. Matteini, P. Hellinger, S. Landi, P. M. Trávníček, and M. Velli. Ion Kinetics in the Solar Wind: Coupling Global Expansion to Local Microphysics. *Space Sci. Rev.*, 172:373–396, November 2012. doi: 10.1007/s11214-011-9774-z.
- W. H. Matthaeus. Turbulence properties along the Solar Probe trajectory. In S. R. Habbal, editor, *Robotic Exploration Close to the Sun: Scientific Basis*, volume 385 of *American Institute of Physics Conference Series*, pages 67–76, January 1997. doi: 10.1063/1.51768.
- W. H. Matthaeus and M. R. Brown. Nearly incompressible magnetohydrodynamics at low Mach number. *Physics of Fluids*, 31:3634–3644, December 1988. doi: 10.1063/1.866880.
- W. H. Matthaeus and M. L. Goldstein. Measurement of the rugged invariants of magnetohydrodynamic turbulence in the solar wind. *J. Geophys. Res.*, 87:6011–6028, August 1982. doi: 10.1029/JA087iA08p06011.
- W. H. Matthaeus and M. L. Goldstein. Low-frequency 1/f noise in the interplanetary magnetic field. *Physical Review Letters*, 57:495–498, July 1986. doi: 10.1103/PhysRevLett.57.495.
- W. H. Matthaeus and M. Velli. Who Needs Turbulence?. A Review of Turbulence Effects in the Heliosphere and on the Fundamental Process of Reconnection. *Space Sci. Rev.*, 160:145–168, October 2011. doi: 10.1007/s11214-011-9793-9.
- W. H. Matthaeus, M. L. Goldstein, and D. A. Roberts. Evidence for the presence of quasi-two-dimensional nearly incompressible fluctuations in the solar wind. *J. Geophys. Res.*, 95:20673–20683, December 1990. doi: 10.1029/JA095iA12p20673.
- W. H. Matthaeus, S. Oughton, D. H. Pontius, Jr., and Y. Zhou. Evolution of energy-containing turbulent eddies in the solar wind. *J. Geophys. Res.*, 99:19, October 1994a. doi: 10.1029/94JA01233.
- W. H. Matthaeus, Y. Zhou, G. P. Zank, and S. Oughton. Transport theory and the WKB approximation for interplanetary MHD fluctuations. *J. Geophys. Res.*, 99:23, December 1994b. doi: 10.1029/94JA02326.
- W. H. Matthaeus, P. C. Gray, D. H. Pontius, Jr., and J. W. Bieber. Spatial Structure and Field-Line Diffusion in Transverse Magnetic Turbulence. *Physical Review Letters*, 75:2136–2139, September 1995. doi: 10.1103/PhysRevLett.75.2136.

- W. H. Matthaeus, G. P. Zank, and S. Oughton. Phenomenology of hydromagnetic turbulence in a uniformly expanding medium. *Journal of Plasma Physics*, 56:659–675, December 1996. doi: 10.1017/S0022377800019516.
- W. H. Matthaeus, C. W. Smith, and S. Oughton. Dynamical age of solar wind turbulence in the outer heliosphere. *J. Geophys. Res.*, 103:6495, April 1998. doi: 10.1029/97JA03729.
- W. H. Matthaeus, C. W. Smith, and J. W. Bieber. Correlation lengths, the Ultrascale, and the spatial structure of interplanetary turbulence. In S. T. Suess, G. A. Gary, and S. F. Nerney, editors, *American Institute of Physics Conference Series*, volume 471 of *American Institute of Physics Conference Series*, pages 511–514, June 1999a. doi: 10.1063/1.58686.
- W. H. Matthaeus, G. P. Zank, S. Oughton, D. J. Mullan, and P. Dmitruk. Coronal Heating by Magnetohydrodynamic Turbulence Driven by Reflected Low-Frequency Waves. *ApJL*, 523:L93–L96, September 1999b. doi: 10.1086/312259.
- W. H. Matthaeus, G. P. Zank, C. W. Smith, and S. Oughton. Turbulence, Spatial Transport, and Heating of the Solar Wind. *Physical Review Letters*, 82:3444–3447, April 1999c. doi: 10.1103/PhysRevLett.82.3444.
- W. H. Matthaeus, G. Qin, J. W. Bieber, and G. P. Zank. Nonlinear Collisionless Perpendicular Diffusion of Charged Particles. *ApJL*, 590:L53–L56, June 2003. doi: 10.1086/376613.
- W. H. Matthaeus, J. Minnie, B. Breech, S. Parhi, J. W. Bieber, and S. Oughton. Transport of cross helicity and radial evolution of Alfvénicity in the solar wind. *Geophys. Res. Lett.*, 31:L12803, June 2004. doi: 10.1029/2004GL019645.
- W. H. Matthaeus, J. W. Bieber, D. Ruffolo, P. Chuychai, and J. Minnie. Spectral Properties and Length Scales of Two-dimensional Magnetic Field Models. *ApJ*, 667: 956–962, October 2007. doi: 10.1086/520924.
- W. H. Matthaeus, M. Wan, S. Servidio, A. Greco, K. T. Osman, S. Oughton, and P. Dmitruk. Intermittency, nonlinear dynamics and dissipation in the solar wind and astrophysical plasmas. *Philosophical Transactions of the Royal Society of London Series A*, 373:20140154–20140154, April 2015. doi: 10.1098/rsta.2014.0154.
- W. H. Matthaeus, T. N. Parashar, M. Wan, and P. Wu. Turbulence and Proton-Electron Heating in Kinetic Plasma. *ApJL*, 827:L7, August 2016a. doi: 10.3847/2041-8205/827/1/L7.
- W. H. Matthaeus, J. M. Weygand, and S. Dasso. Ensemble Space-Time Correlation of Plasma Turbulence in the Solar Wind. *Physical Review Letters*, 116(24):245101, June 2016b. doi: 10.1103/PhysRevLett.116.245101.

- D. J. McComas, B. L. Barraclough, H. O. Funsten, J. T. Gosling, E. Santiago-Muñoz, R. M. Skoug, B. E. Goldstein, M. Neugebauer, P. Riley, and A. Balogh. Solar wind observations over Ulysses' first full polar orbit. *J. Geophys. Res.*, 105:10419–10434, May 2000. doi: 10.1029/1999JA000383.
- D. J. McComas, H. A. Elliott, N. A. Schwadron, J. T. Gosling, R. M. Skoug, and B. E. Goldstein. The three-dimensional solar wind around solar maximum. *Geophys. Res. Lett.*, 30:1517, May 2003. doi: 10.1029/2003GL017136.
- W. D. McComb. *The Physics of Fluid Turbulence*. Clarendon Press Oxford, December 1990.
- J. F. McKenzie, M. Banaszekiewicz, and W. I. Axford. Acceleration of the high speed solar wind. *A&A*, 303:L45, November 1995.
- N. Meyer-Vernet. *Basics of the Solar Wind*. Cambridge University Press, January 2007.
- M. Miesch, W. Matthaeus, A. Brandenburg, A. Petrosyan, A. Pouquet, C. Cambon, F. Jenko, D. Uzdensky, J. Stone, S. Tobias, J. Toomre, and M. Velli. Large-Eddy Simulations of Magnetohydrodynamic Turbulence in Heliophysics and Astrophysics. *Space Sci. Rev.*, 194:97–137, November 2015. doi: 10.1007/s11214-015-0190-7.
- L. J. Milano, W. H. Matthaeus, B. Breech, and C. W. Smith. One-point statistics of the induced electric field in quasinormal magnetofluid turbulence. *Phys. Rev. E*, 65(2):026310, February 2002. doi: 10.1103/PhysRevE.65.026310.
- L. J. Milano, S. Dasso, W. H. Matthaeus, and C. W. Smith. Spectral Distribution of the Cross Helicity in the Solar Wind. *Physical Review Letters*, 93(15):155005, October 2004. doi: 10.1103/PhysRevLett.93.155005.
- J. Minnie, J. W. Bieber, W. H. Matthaeus, and R. A. Burger. Suppression of Particle Drifts by Turbulence. *ApJ*, 670:1149–1158, December 2007. doi: 10.1086/522026.
- A. S. Monin and A. M. Yaglom. *Statistical Fluid Mechanics: Mechanics Of Turbulence*. MIT Press, 1971.
- D Montgomery. Lecture notes on turbulence, 1989.
- D. C. Montgomery and D. A. Tidman. *Plasma kinetic theory*. McGraw-Hill Advanced Physics Monograph Series, 1964.
- H. Moraal. Observations of the eleven-year cosmic-ray modulation cycle. *Space Sci. Rev.*, 19:845–920, December 1976. doi: 10.1007/BF00173707.
- G. E. Morfill and H. J. Voelk. Latitude variation of interplanetary cosmic ray diffusion. *J. Geophys. Res.*, 84:4446–4450, August 1979. doi: 10.1029/JA084iA08p04446.

- R. Mueller-Mellin, K. Roehrs, and G. Wibberenz. Super-events in the inner solar system and their relation to the solar cycle. In R. G. Marsden, editor, *The Sun and the Heliosphere in Three Dimensions*, volume 123 of *Astrophysics and Space Science Library*, pages 349–354, 1986. doi: 10.1007/978-94-009-4612-5_38.
- D. J. Mullan. Sources of the solar wind - What are the smallest-scale structures? *A&A*, 232:520–535, June 1990.
- D. J. Mullan. Survival of discrete structures in the solar wind. *A&A*, 248:256–262, August 1991.
- Yasuhito Narita. Space–time structure and wavevector anisotropy in space plasma turbulence. *Living reviews in solar physics*, 15(1):2, 2018. doi: <https://doi.org/10.1007/s41116-017-0010-0>.
- M. Neugebauer. The role of Coulomb collisions in limiting differential flow and temperature differences in the solar wind. *J. Geophys. Res.*, 81:78–82, January 1976. doi: 10.1029/JA081i001p00078.
- M. Neugebauer and C. W. Snyder. Mariner 2 Observations of the Solar Wind, 1, Average Properties. *J. Geophys. Res.*, 71:4469, October 1966. doi: 10.1029/JZ071i019p04469.
- V. N. Obridko and O. L. Vaisberg. On the history of the solar wind discovery. *Solar System Research*, 51:165–169, March 2017. doi: 10.1134/S0038094617020058.
- S. A. Orszag. Analytical theories of turbulence. *Journal of Fluid Mechanics*, 41:363–386, 1970. doi: 10.1017/S0022112070000642.
- K. T. Osman and T. S. Horbury. Multispacecraft Measurement of Anisotropic Correlation Functions in Solar Wind Turbulence. *ApJL*, 654:L103–L106, January 2007. doi: 10.1086/510906.
- K. T. Osman, W. H. Matthaeus, M. Wan, and A. F. Rappazzo. Intermittency and Local Heating in the Solar Wind. *Physical Review Letters*, 108(26):261102, June 2012. doi: 10.1103/PhysRevLett.108.261102.
- S. Oughton and W. H. Matthaeus. Parallel and perpendicular cascades in solar wind turbulence. *Nonlinear Processes in Geophysics*, 12:299–310, February 2005.
- S. Oughton, E. R. Priest, and W. H. Matthaeus. The influence of a mean magnetic field on three-dimensional magnetohydrodynamic turbulence. *Journal of Fluid Mechanics*, 280:95–117, 1994. doi: 10.1017/S0022112094002867.
- S. Oughton, W. H. Matthaeus, C. W. Smith, B. Breech, and P. A. Isenberg. Transport of solar wind fluctuations: A two-component model. *Journal of Geophysical Research (Space Physics)*, 116:A08105, August 2011. doi: 10.1029/2010JA016365.

- S Oughton, WH Matthaeus, M Wan, and KT Osman. Anisotropy in solar wind plasma turbulence. *Phil. Trans. R. Soc. A*, 373(2041):20140152, 2015.
- M. J. Owens and R. J. Forsyth. The Heliospheric Magnetic Field. *Living Reviews in Solar Physics*, 10:5, November 2013. doi: 10.12942/lrsp-2013-5.
- I. D. Palmer. Transport coefficients of low-energy cosmic rays in interplanetary space. *Reviews of Geophysics and Space Physics*, 20:335–351, May 1982. doi: 10.1029/RG020i002p00335.
- S. Panchev. *Random Functions and Turbulence: International Series of Monographs in Natural Philosophy*, volume 32. Elsevier, 2016.
- T. N. Parashar. *On kinetic dissipation in collisionless turbulent plasmas*. PhD thesis, University of Delaware, 2011.
- T. N. Parashar, W. H. Matthaeus, M. A. Shay, and M. Wan. Transition from Kinetic to MHD Behavior in a Collisionless Plasma. *ApJ*, 811:112, October 2015. doi: 10.1088/0004-637X/811/2/112.
- E. N. Parker. Modulation of Primary Cosmic-Ray Intensity. *Physical Review*, 103:1518–1533, September 1956. doi: 10.1103/PhysRev.103.1518.
- E. N. Parker. Dynamics of the Interplanetary Gas and Magnetic Fields. *ApJ*, 128:664, November 1958. doi: 10.1086/146579.
- E. N. Parker. The Scattering of Charged Particles by Magnetic Irregularities. *J. Geophys. Res.*, 69:1755–1758, May 1964. doi: 10.1029/JZ069i009p01755.
- E. N. Parker. The passage of energetic charged particles through interplanetary space. *Planet. Space Sci.*, 13:9–49, January 1965a. doi: 10.1016/0032-0633(65)90131-5.
- E. N. Parker. Dynamical Theory of the Solar Wind. *Space Sci. Rev.*, 4:666–708, September 1965b. doi: 10.1007/BF00216273.
- Eugene N. Parker. Shielding space explorers from cosmic rays. *Space Weather*, 3(8), 2005. ISSN 1542-7390. doi: 10.1029/2005SW000176. S08004.
- C. Pei, J. W. Bieber, B. Breech, R. A. Burger, J. Clem, and W. H. Matthaeus. Cosmic ray diffusion tensor throughout the heliosphere. *Journal of Geophysical Research (Space Physics)*, 115:A03103, March 2010. doi: 10.1029/2009JA014705.
- S. Perri and A. Balogh. Differences in solar wind cross-helicity and residual energy during the last two solar minima. *Geophys. Res. Lett.*, 37:L17102, September 2010. doi: 10.1029/2010GL044570.

- S. Perri, M. L. Goldstein, J. C. Dorelli, and F. Sahraoui. Detection of Small-Scale Structures in the Dissipation Regime of Solar-Wind Turbulence. *Physical Review Letters*, 109(19):191101, November 2012. doi: 10.1103/PhysRevLett.109.191101.
- S. Perri, S. Servidio, A. Vaivads, and F. Valentini. Numerical Study on the Validity of the Taylor Hypothesis in Space Plasmas. *ApJS*, 231:4, July 2017. doi: 10.3847/1538-4365/aa755a.
- O. Pezzi. Solar wind collisional heating. *Journal of Plasma Physics*, 83(3):555830301, June 2017. doi: 10.1017/S0022377817000368.
- TD Phan, JP Eastwood, MA Shay, JF Drake, BU Ö Sonnerup, M Fujimoto, PA Cassak, M Øieroset, JL Burch, RB Torbert, et al. Electron magnetic reconnection without ion coupling in earths turbulent magnetosheath. *Nature*, 557(7704):202, 2018.
- V. Pierrard. The Kinetic Approach to Model Space Plasmas. In N. V. Pogorelov, E. Audit, and G. P. Zank, editors, *Numerical Modeling of Space Plasma Flows, Astronom-2009*, volume 429 of *Astronomical Society of the Pacific Conference Series*, page 233, September 2010.
- V. Pizzo. A three-dimensional model of corotating streams in the solar wind. I - Theoretical foundations. *J. Geophys. Res.*, 83:5563–5572, December 1978. doi: 10.1029/JA083iA12p05563.
- V. J. Pizzo. A three-dimensional model of corotating streams in the solar wind. III - Magnetohydrodynamic streams. *J. Geophys. Res.*, 87:4374–4394, June 1982. doi: 10.1029/JA087iA06p04374.
- G. W. Pneuman and R. A. Kopp. Gas-Magnetic Field Interactions in the Solar Corona. *Sol. Phys.*, 18:258–270, June 1971. doi: 10.1007/BF00145940.
- C. Pollock, T. Moore, A. Jacques, J. Burch, U. Gliese, Y. Saito, T. Omoto, L. Avanov, A. Barrie, V. Coffey, J. Dorelli, D. Gershman, B. Giles, T. Rosnack, C. Salo, S. Yokota, M. Adrian, C. Aoustin, C. Aulletti, S. Aung, V. Bigio, N. Cao, M. Chandler, D. Chornay, K. Christian, G. Clark, G. Collinson, T. Corris, A. De Los Santos, R. Devlin, T. Diaz, T. Dickerson, C. Dickson, A. Diekmann, F. Diggs, C. Duncan, A. Figueroa-Vinas, C. Firman, M. Freeman, N. Galassi, K. Garcia, G. Goodhart, D. Guerrerro, J. Hageman, J. Hanley, E. Hemminger, M. Holland, M. Hutchins, T. James, W. Jones, S. Kreisler, J. Kujawski, V. Lavu, J. Lobell, E. LeCompte, A. Lukemire, E. MacDonald, A. Mariano, T. Mukai, K. Narayanan, Q. Nguyen, M. Onizuka, W. Paterson, S. Persyn, B. Piepgrass, F. Cheney, A. Rager, T. Raghuram, A. Ramil, L. Reichenthal, H. Rodriguez, J. Rouzaud, A. Rucker, Y. Saito, M. Samara, J.-A. Sauvaud, D. Schuster, M. Shappirio, K. Shelton, D. Sher, D. Smith, K. Smith, S. Smith, D. Steinfeld, R. Szymkiewicz, K. Tanimoto, J. Taylor, C. Tucker,

- K. Tull, A. Uhl, J. Vloet, P. Walpole, S. Weidner, D. White, G. Winkert, P.-S. Yeh, and M. Zeuch. Fast Plasma Investigation for Magnetospheric Multiscale. *Space Sci. Rev.*, 199:331–406, March 2016. doi: 10.1007/s11214-016-0245-4.
- S. B. Pope. *Turbulent Flows*. Cambridge University Press, August 2000.
- S. B. Pope. Ten questions concerning the large-eddy simulation of turbulent flows. *New Journal of Physics*, 6:35, March 2004. doi: 10.1088/1367-2630/6/1/035.
- M. S. Potgieter. Solar Modulation of Cosmic Rays. *Living Reviews in Solar Physics*, 10:3, December 2013. doi: 10.12942/lrsp-2013-3.
- K. G. Powell. Approximate Riemann solver for magnetohydrodynamics (that works in more than one dimension). Technical report, NASA, March 1994.
- D. V. Reames. Particle acceleration at the Sun and in the heliosphere. *Space Sci. Rev.*, 90:413–491, October 1999. doi: 10.1023/A:1005105831781.
- F. Reif. *Fundamentals of Statistical and Thermal Physics*. Waveland Press, 1965.
- J. P. L. Reinecke, C. D. Steenberg, H. Moraal, and F. B. McDonald. An alternative approach to the modelling of galactic cosmic ray intensities in the heliosphere. *Advances in Space Research*, 19:901–904, May 1997. doi: 10.1016/S0273-1177(97)00300-1.
- V. Réville, A. S. Brun, S. P. Matt, A. Strugarek, and R. F. Pinto. The Effect of Magnetic Topology on Thermally Driven Wind: Toward a General Formulation of the Braking Law. *ApJ*, 798:116, January 2015. doi: 10.1088/0004-637X/798/2/116.
- O. Reynolds. An Experimental Investigation of the Circumstances Which Determine Whether the Motion of Water Shall Be Direct or Sinuous, and of the Law of Resistance in Parallel Channels. *Philosophical Transactions of the Royal Society of London Series I*, 174:935–982, 1883.
- O. Reynolds. On the Dynamical Theory of Incompressible Viscous Fluids and the Determination of the Criterion. *Philosophical Transactions of the Royal Society of London Series A*, 186:123–164, 1895. doi: 10.1098/rsta.1895.0004.
- J. D. Richardson, K. I. Paularena, A. J. Lazarus, and J. W. Belcher. Radial evolution of the solar wind from IMP 8 to Voyager 2. *Geophys. Res. Lett.*, 22:325–328, February 1995. doi: 10.1029/94GL03273.
- P. J. Roache. *Computational Fluid Dynamics*. Hermosa Publishers, 1976.
- D. A. Roberts, M. L. Goldstein, L. W. Klein, and W. H. Matthaeus. Origin and evolution of fluctuations in the solar wind - HELIOS observations and Helios-Voyager comparisons. *J. Geophys. Res.*, 92:12023–12035, November 1987a. doi: 10.1029/JA092iA11p12023.

- D. A. Roberts, L. W. Klein, M. L. Goldstein, and W. H. Matthaeus. The nature and evolution of magnetohydrodynamic fluctuations in the solar wind - Voyager observations. *J. Geophys. Res.*, 92:11021–11040, October 1987b. doi: 10.1029/JA092iA10p11021.
- D. A. Roberts, M. L. Goldstein, and L. W. Klein. The amplitudes of interplanetary fluctuations - Stream structure, heliocentric distance, and frequency dependence. *J. Geophys. Res.*, 95:4203–4216, April 1990. doi: 10.1029/JA095iA04p04203.
- D. A. Roberts, M. L. Goldstein, W. H. Matthaeus, and S. Ghosh. Velocity shear generation of solar wind turbulence. *J. Geophys. Res.*, 97:17, November 1992. doi: 10.1029/92JA01144.
- D. C. Robinson and M. G. Rusbridge. Structure of Turbulence in the Zeta Plasma. *Physics of Fluids*, 14:2499–2511, November 1971. doi: 10.1063/1.1693359.
- R. S. Rogallo and P. Moin. Numerical simulation of turbulent flows. *Annual Review of Fluid Mechanics*, 16:99–137, 1984. doi: 10.1146/annurev.fl.16.010184.000531.
- C. Rosales and C. Meneveau. A minimal multiscale Lagrangian map approach to synthesize non-Gaussian turbulent vector fields. *Physics of Fluids*, 18(7):075104-075104-14, July 2006. doi: 10.1063/1.2227003.
- D. Ruelle. The Claude Bernard Lecture, 1989 - Deterministic chaos: The science and the fiction. *Proceedings of the Royal Society of London Series A*, 427:241–248, February 1990. doi: 10.1098/rspa.1990.0010.
- D. Ruffolo, W. H. Matthaeus, and P. Chuychai. Separation of Magnetic Field Lines in Two-Component Turbulence. *ApJ*, 614:420–434, October 2004. doi: 10.1086/423412.
- D. Ruffolo, P. Tooprakai, M. Rujiwarodom, T. Khumlumlert, M. Wechakama, J. W. Bieber, P. Evenson, and R. Pyle. Relativistic Solar Protons on 1989 October 22: Injection and Transport along Both Legs of a Closed Interplanetary Magnetic Loop. *ApJ*, 639:1186–1205, March 2006. doi: 10.1086/499419.
- D. Ruffolo, T. Pianpanit, W. H. Matthaeus, and P. Chuychai. Random Ballistic Interpretation of Nonlinear Guiding Center Theory. *ApJL*, 747:L34, March 2012a. doi: 10.1088/2041-8205/747/2/L34.
- D. J. Ruffolo, T. Pianpanit, P. Chuychai, W. H. Matthaeus, and G. Qin. Directions of Improvement in the Theory of Perpendicular Diffusion of Energetic Charged Particles. *AGU Fall Meeting Abstract SH21A-2188*, December 2012b.
- M. E. Ruiz, S. Dasso, W. H. Matthaeus, and J. M. Weygand. Characterization of the Turbulent Magnetic Integral Length in the Solar Wind: From 0.3 to 5 Astronomical Units. *Solar Physics*, 289:3917–3933, October 2014. doi: 10.1007/s11207-014-0531-9.

- C. T. Russell, B. J. Anderson, W. Baumjohann, K. R. Bromund, D. Dearborn, D. Fischer, G. Le, H. K. Leinweber, D. Leneman, W. Magnes, J. D. Means, M. B. Moldwin, R. Nakamura, D. Pierce, F. Plaschke, K. M. Rowe, J. A. Slavin, R. J. Strangeway, R. Torbert, C. Hagen, I. Jernej, A. Valavanoglou, and I. Richter. The Magnetospheric Multiscale Magnetometers. *Space Sci. Rev.*, 199:189–256, March 2016. doi: 10.1007/s11214-014-0057-3.
- F. Sahraoui, G. Belmont, L. Rezeau, N. Cornilleau-Wehrin, J. L. Pinçon, and A. Balogh. Anisotropic Turbulent Spectra in the Terrestrial Magnetosheath as Seen by the Cluster Spacecraft. *Physical Review Letters*, 96(7):075002, February 2006. doi: 10.1103/PhysRevLett.96.075002.
- F. Sahraoui, M. L. Goldstein, P. Robert, and Y. V. Khotyaintsev. Evidence of a Cascade and Dissipation of Solar-Wind Turbulence at the Electron Gyroscale. *Physical Review Letters*, 102(23):231102, June 2009. doi: 10.1103/PhysRevLett.102.231102.
- C. Salem, D. Hubert, C. Lacombe, S. D. Bale, A. Mangeney, D. E. Larson, and R. P. Lin. Electron Properties and Coulomb Collisions in the Solar Wind at 1 AU: Wind Observations. *ApJ*, 585:1147–1157, March 2003. doi: 10.1086/346185.
- A. A. Schekochihin, S. C. Cowley, W. Dorland, G. W. Hammett, G. G. Howes, E. Quataert, and T. Tatsuno. Astrophysical Gyrokinetics: Kinetic and Fluid Turbulent Cascades in Magnetized Weakly Collisional Plasmas. *ApJS*, 182:310–377, May 2009. doi: 10.1088/0067-0049/182/1/310.
- W. Schmidt. Large Eddy Simulations in Astrophysics. *Living Reviews in Computational Astrophysics*, 1:2, October 2015. doi: 10.1007/lrca-2015-2.
- J. D. Scudder. Why all stars should possess circumstellar temperature inversions. *ApJ*, 398:319–349, October 1992. doi: 10.1086/171859.
- J. D. Scudder. Radial Variation of the Solar Wind Proton Temperature: Heat Flow or Addition? *ApJ*, 809:126, August 2015. doi: 10.1088/0004-637X/809/2/126.
- J. D. Scudder and H. Karimabadi. Ubiquitous Non-thermals in Astrophysical Plasmas: Restating the Difficulty of Maintaining Maxwellians. *ApJ*, 770:26, June 2013. doi: 10.1088/0004-637X/770/1/26.
- S. Servidio, W. H. Matthaeus, M. Wan, D. Ruffolo, A. F. Rappazzo, and S. Oughton. Complexity and Diffusion of Magnetic Flux Surfaces in Anisotropic Turbulence. *ApJ*, 785:56, April 2014. doi: 10.1088/0004-637X/785/1/56.
- S. Servidio, F. Valentini, D. Perrone, A. Greco, F. Califano, W. H. Matthaeus, and P. Veltri. A kinetic model of plasma turbulence. *Journal of Plasma Physics*, 81(1): 325810107, January 2015. doi: 10.1017/S0022377814000841.

- A. Shalchi. Extended nonlinear guiding center theory of perpendicular diffusion. *A&A*, 453:L43–L46, July 2006. doi: 10.1051/0004-6361:20065465.
- A. Shalchi, editor. *Nonlinear Cosmic Ray Diffusion Theories*, volume 362 of *Astrophysics and Space Science Library*, 2009. doi: 10.1007/978-3-642-00309-7.
- J. V. Shebalin, W. H. Matthaeus, and D. Montgomery. Anisotropy in MHD turbulence due to a mean magnetic field. *Journal of Plasma Physics*, 29:525–547, June 1983. doi: 10.1017/S0022377800000933.
- D. Shiota, G. P. Zank, L. Adhikari, P. Hunana, D. Telloni, and R. Bruno. Turbulent Transport in a Three-dimensional Solar Wind. *ApJ*, 837:75, March 2017. doi: 10.3847/1538-4357/aa60bc.
- J. Smagorinsky. General Circulation Experiments with the Primitive Equations. *Monthly Weather Review*, 91:99, 1963. doi: 10.1175/1520-0493(1963)091<0099:GCEWTP>2.3.CO;2.
- C. W. Smith, W. H. Matthaeus, G. P. Zank, N. F. Ness, S. Oughton, and J. D. Richardson. Heating of the low-latitude solar wind by dissipation of turbulent magnetic fluctuations. *J. Geophys. Res.*, 106:8253–8272, May 2001. doi: 10.1029/2000JA000366.
- E. J. Smith. The heliospheric current sheet. *J. Geophys. Res.*, 106:15819–15832, August 2001. doi: 10.1029/2000JA000120.
- C. W. Snyder, M. Neugebauer, and U. R. Rao. The Solar Wind Velocity and Its Correlation with Cosmic-Ray Variations and with Solar and Geomagnetic Activity. *J. Geophys. Res.*, 68:6361, December 1963.
- L. Sorriso-Valvo, V. Carbone, P. Veltri, G. Consolini, and R. Bruno. Intermittency in the solar wind turbulence through probability distribution functions of fluctuations. *Geophys. Res. Lett.*, 26:1801–1804, 1999. doi: 10.1029/1999GL900270.
- L. Spitzer. *Physics of fully ionized gases*. Interscience Publishers, 1965.
- L. Spitzer and R. Härm. Transport Phenomena in a Completely Ionized Gas. *Physical Review*, 89:977–981, March 1953. doi: 10.1103/PhysRev.89.977.
- H. C. Spruit. Magnetic flux tubes. *NASA Special Publication*, 450, July 1981.
- K. R. Sreenivasan. Fluid turbulence. *Reviews of Modern Physics Supplement*, 71: S383–S395, March 1999. doi: 10.1103/RevModPhys.71.S383.
- P. A. Sturrock and R. E. Hartle. Two-Fluid Model of the Solar Wind. *Physical Review Letters*, 16:628–631, April 1966. doi: 10.1103/PhysRevLett.16.628.

- P. Subedi, R. Chhiber, J. A. Tessein, M. Wan, and W. H. Matthaeus. Generating Synthetic Magnetic Field Intermittency Using a Minimal Multiscale Lagrangian Mapping Approach. *ApJ*, 796:97, December 2014. doi: 10.1088/0004-637X/796/2/97.
- P. Subedi, W. Sonsrtee, P. Blasi, D. Ruffolo, W. H. Matthaeus, D. Montgomery, P. Chuychai, P. Dmitruk, M. Wan, T. N. Parashar, and R. Chhiber. Charged Particle Diffusion in Isotropic Random Magnetic Fields. *ApJ*, 837:140, March 2017. doi: 10.3847/1538-4357/aa603a.
- Prachanda Subedi. *Transport of Charged Particles in Turbulent Magnetic Fields*. PhD thesis, University of Delaware, 2017.
- G. I. Taylor. Diffusion by continuous movements. *Proceedings of the London Mathematical Society*, s2-20(1):196–212, 1922. ISSN 1460-244X. doi: 10.1112/plms/s2-20.1.196.
- G. I. Taylor. The Spectrum of Turbulence. *Proceedings of the Royal Society of London Series A*, 164:476–490, February 1938. doi: 10.1098/rspa.1938.0032.
- H. Tennekes and J. L. Lumley. *First Course in Turbulence*. The MIT Press, 1972.
- J. A. Tessein, W. H. Matthaeus, M. Wan, K. T. Osman, D. Ruffolo, and J. Giacalone. Association of Suprathermal Particles with Coherent Structures and Shocks. *ApJL*, 776:L8, October 2013. doi: 10.1088/2041-8205/776/1/L8.
- C.-Y. Tu. The damping of interplanetary Alfvénic fluctuations and the heating of the solar wind. *J. Geophys. Res.*, 93:7–20, January 1988. doi: 10.1029/JA093iA01p00007.
- C.-Y. Tu and E. Marsch. Transfer equations for spectral densities of inhomogeneous MHD turbulence. *Journal of Plasma Physics*, 44:103–122, August 1990. doi: 10.1017/S002237780001504X.
- C.-Y. Tu and E. Marsch. MHD structures, waves and turbulence in the solar wind: Observations and theories. *Space Sci. Rev.*, 73:1–210, July 1995. doi: 10.1007/BF00748891.
- A. J. Tylka, J. H. Adams, P. R. Boberg, B. Brownstein, W. F. Dietrich, E. O. Flueckiger, E. L. Petersen, M. A. Shea, D. F. Smart, and E. C. Smith. CREME96: a revision of the Cosmic Ray Effects on Micro-Electronics code. *IEEE Transactions on Nuclear Science*, 44:2150–2160, December 1997. doi: 10.1109/23.659030.
- A. V. Usmanov. A global numerical 3-D MHD model of the solar wind. *Sol. Phys.*, 146:377–396, August 1993. doi: 10.1007/BF00662021.

- A. V. Usmanov. A global 3-D MHD solar wind model with Alfvén waves. In D. Winterhalter, J. T. Gosling, S. R. Habbal, W. S. Kurth, and M. Neugebauer, editors, *American Institute of Physics Conference Series*, volume 382 of *American Institute of Physics Conference Series*, pages 141–144, July 1996. doi: 10.1063/1.51468.
- A. V. Usmanov and M. L. Goldstein. A tilted-dipole MHD model of the solar corona and solar wind. *Journal of Geophysical Research (Space Physics)*, 108:1354, September 2003. doi: 10.1029/2002JA009777.
- A. V. Usmanov, M. L. Goldstein, B. P. Besser, and J. M. Fritzer. A global MHD solar wind model with WKB Alfvén waves: Comparison with Ulysses data. *J. Geophys. Res.*, 105:12675–12696, June 2000. doi: 10.1029/1999JA000233.
- A. V. Usmanov, W. H. Matthaeus, B. A. Breech, and M. L. Goldstein. Solar Wind Modeling with Turbulence Transport and Heating. *ApJ*, 727:84, February 2011. doi: 10.1088/0004-637X/727/2/84.
- A. V. Usmanov, M. L. Goldstein, and W. H. Matthaeus. Three-dimensional Magnetohydrodynamic Modeling of the Solar Wind Including Pickup Protons and Turbulence Transport. *ApJ*, 754:40, July 2012. doi: 10.1088/0004-637X/754/1/40.
- A. V. Usmanov, M. L. Goldstein, and W. H. Matthaeus. Three-fluid, Three-dimensional Magnetohydrodynamic Solar Wind Model with Eddy Viscosity and Turbulent Resistivity. *ApJ*, 788:43, June 2014. doi: 10.1088/0004-637X/788/1/43.
- A. V. Usmanov, M. L. Goldstein, and W. H. Matthaeus. A Four-fluid MHD Model of the Solar Wind/Interstellar Medium Interaction with Turbulence Transport and Pickup Protons as Separate Fluid. *ApJ*, 820:17, March 2016a. doi: 10.3847/0004-637X/820/1/17.
- A. V. Usmanov, W. H. Matthaeus, and M. L. Goldstein. Heating and Acceleration of the Solar Corona and Solar Wind: Effects of Turbulence Transport. *AGU Fall Meeting Abstracts*, December 2016b.
- A. V. Usmanov, W. H. Matthaeus, M. L. Goldstein, and R. Chhiber. The Steady Global Solar Corona and Solar Wind: A Three-dimensional Magnetohydrodynamic Simulation with Turbulent Transport and Heating; Submitted. 2018.
- M. Velli, R. Grappin, and A. Mangeney. Turbulent cascade of incompressible unidirectional Alfvén waves in the interplanetary medium. *Physical Review Letters*, 63:1807–1810, October 1989. doi: 10.1103/PhysRevLett.63.1807.
- A. Verdini and R. Grappin. Imprints of Expansion on the Local Anisotropy of Solar Wind Turbulence. *ApJL*, 808:L34, August 2015. doi: 10.1088/2041-8205/808/2/L34.
- A. Verdini and M. Velli. Alfvén Waves and Turbulence in the Solar Atmosphere and Solar Wind. *ApJ*, 662:669–676, June 2007. doi: 10.1086/510710.

- A. Verdini, M. Velli, W. H. Matthaeus, S. Oughton, and P. Dmitruk. A Turbulence-Driven Model for Heating and Acceleration of the Fast Wind in Coronal Holes. *ApJL*, 708:L116–L120, January 2010. doi: 10.1088/2041-8205/708/2/L116.
- M. K. Verma. Statistical theory of magnetohydrodynamic turbulence: recent results. *Phys. Rep.*, 401:229–380, November 2004. doi: 10.1016/j.physrep.2004.07.007.
- H. J. Völk, G. Morfill, W. Alpers, and M. A. Lee. Spatial Dependence of the Pitch-Angle and Associated Spatial Diffusion Coefficients for Cosmic Rays in Interplanetary Space. *Ap&SS*, 26:403–430, February 1974. doi: 10.1007/BF00645623.
- E. E. Vos and M. S. Potgieter. New Modeling of Galactic Proton Modulation during the Minimum of Solar Cycle 23/24. *ApJ*, 815:119, December 2015. doi: 10.1088/0004-637X/815/2/119.
- A. Vourlidas, R. A. Howard, S. P. Plunkett, C. M. Korendyke, A. F. R. Thernisien, D. Wang, N. Rich, M. T. Carter, D. H. Chua, D. G. Socker, M. G. Linton, J. S. Morrill, S. Lynch, A. Thurn, P. Van Duyne, R. Hagood, G. Clifford, P. J. Grey, M. Velli, P. C. Liewer, J. R. Hall, E. M. DeJong, Z. Mikic, P. Rochus, E. Mazy, V. Bothmer, and J. Rodmann. The Wide-Field Imager for Solar Probe Plus (WISPR). *Space Sci. Rev.*, 204:83–130, December 2016. doi: 10.1007/s11214-014-0114-y.
- M. Wan, S. Oughton, S. Servidio, and W. H. Matthaeus. Generation of non-Gaussian statistics and coherent structures in ideal magnetohydrodynamics. *Physics of Plasmas*, 16(8):080703, August 2009. doi: 10.1063/1.3206949.
- M. Wan, K. T. Osman, W. H. Matthaeus, and S. Oughton. Investigation of Intermittency in Magnetohydrodynamics and Solar Wind Turbulence: Scale-dependent Kurtosis. *ApJ*, 744:171, January 2012a. doi: 10.1088/0004-637X/744/2/171.
- M. Wan, S. Oughton, S. Servidio, and W. H. Matthaeus. von Kármán self-preservation hypothesis for magnetohydrodynamic turbulence and its consequences for universality. *Journal of Fluid Mechanics*, 697:296–315, April 2012b. doi: 10.1017/jfm.2012.61.
- E. J. Weber and L. Davis, Jr. The Angular Momentum of the Solar Wind. *ApJ*, 148: 217–227, April 1967. doi: 10.1086/149138.
- J. M. Weygand, W. H. Matthaeus, S. Dasso, M. G. Kivelson, L. M. Kistler, and C. Mouikis. Anisotropy of the Taylor scale and the correlation scale in plasma sheet and solar wind magnetic field fluctuations. *Journal of Geophysical Research (Space Physics)*, 114:A07213, July 2009. doi: 10.1029/2008JA013766.
- J. M. Weygand, W. H. Matthaeus, S. Dasso, and M. G. Kivelson. Correlation and Taylor scale variability in the interplanetary magnetic field fluctuations as a function of solar wind speed. *Journal of Geophysical Research (Space Physics)*, 116:A08102, August 2011. doi: 10.1029/2011JA016621.

- J. M. Weygand, W. H. Matthaeus, M. G. Kivelson, and S. Dasso. Magnetic correlation functions in the slow and fast solar wind in the Eulerian reference frame. *Journal of Geophysical Research (Space Physics)*, 118:3995–4004, July 2013. doi: 10.1002/jgra.50398.
- R. T. Wicks, D. A. Roberts, A. Mallet, A. A. Schekochihin, T. S. Horbury, and C. H. K. Chen. Correlations at Large Scales and the Onset of Turbulence in the Fast Solar Wind. *ApJ*, 778:177, December 2013. doi: 10.1088/0004-637X/778/2/177.
- T. Wiengarten, S. Oughton, N. E. Engelbrecht, H. Fichtner, J. Kleimann, and K. Scherer. A Generalized Two-component Model of Solar Wind Turbulence and ab initio Diffusion Mean-Free Paths and Drift Lengthscales of Cosmic Rays. *ApJ*, 833:17, December 2016. doi: 10.3847/0004-637X/833/1/17.
- D. Winterhalter, E. J. Smith, M. E. Burton, N. Murphy, and D. J. McComas. The heliospheric plasma sheet. *J. Geophys. Res.*, 99:6667–6680, April 1994. doi: 10.1029/93JA03481.
- P. Wu, S. Perri, K. Osman, M. Wan, W. H. Matthaeus, M. A. Shay, M. L. Goldstein, H. Karimabadi, and S. Chapman. Intermittent Heating in Solar Wind and Kinetic Simulations. *ApJL*, 763:L30, February 2013. doi: 10.1088/2041-8205/763/2/L30.
- V. Yakhot and S. A. Orszag. Renormalization group analysis of turbulence. I - Basic theory. *Journal of Scientific Computing*, 1:3–51, 1986.
- Y. Yang, W. H. Matthaeus, T. N. Parashar, C. C. Haggerty, V. Roytershteyn, W. Daughton, M. Wan, Y. Shi, and S. Chen. Energy transfer, pressure tensor, and heating of kinetic plasma. *Physics of Plasmas*, 24(7):072306, July 2017. doi: 10.1063/1.4990421.
- N. Yokoi. Cross helicity and related dynamo. *Geophysical and Astrophysical Fluid Dynamics*, 107:114–184, February 2013. doi: 10.1080/03091929.2012.754022.
- N. Yokoi and F. Hamba. An application of the turbulent magnetohydrodynamic residual-energy equation model to the solar wind. *Physics of Plasmas*, 14(11):112904–112904, November 2007. doi: 10.1063/1.2792337.
- N. Yokoi, R. Rubinstein, A. Yoshizawa, and F. Hamba. A turbulence model for magnetohydrodynamic plasmas. *Journal of Turbulence*, 9:N37, 2008. doi: 10.1080/14685240802433057.
- A. Yoshizawa, S.-I. Itoh, and K. Itoh. *Plasma and Fluid Turbulence: Theory and Modelling*. IOP Publishing, 2003.
- G. P. Zank. Interaction of the solar wind with the local interstellar medium: a theoretical perspective. *Space Sci. Rev.*, 89:413–688, July 1999. doi: 10.1023/A:1005155601277.

- G. P. Zank, editor. *Transport Processes in Space Physics and Astrophysics*, volume 877 of *Lecture Notes in Physics*, Berlin Springer Verlag. Springer, 2014. doi: 10.1007/978-1-4614-8480-6.
- G. P. Zank and W. H. Matthaeus. The equations of nearly incompressible fluids. I - Hydrodynamics, turbulence, and waves. *Physics of Fluids A*, 3:69–82, January 1991. doi: 10.1063/1.857865.
- G. P. Zank and W. H. Matthaeus. Waves and turbulence in the solar wind. *J. Geophys. Res.*, 97:17, November 1992. doi: 10.1029/92JA01734.
- G. P. Zank and W. H. Matthaeus. Nearly incompressible fluids. II - Magnetohydrodynamics, turbulence, and waves. *Physics of Fluids*, 5:257–273, January 1993. doi: 10.1063/1.858780.
- G. P. Zank, W. H. Matthaeus, and C. W. Smith. Evolution of turbulent magnetic fluctuation power with heliospheric distance. *J. Geophys. Res.*, 101:17093–17108, August 1996. doi: 10.1029/96JA01275.
- G. P. Zank, W. H. Matthaeus, J. W. Bieber, and H. Moraal. The radial and latitudinal dependence of the cosmic ray diffusion tensor in the heliosphere. *J. Geophys. Res.*, 103:2085, February 1998. doi: 10.1029/97JA03013.
- G. P. Zank, G. Li, V. Florinski, W. H. Matthaeus, G. M. Webb, and J. A. Le Roux. Perpendicular diffusion coefficient for charged particles of arbitrary energy. *Journal of Geophysical Research (Space Physics)*, 109:A04107, April 2004. doi: 10.1029/2003JA010301.
- G. P. Zank, A. Dosch, P. Hunana, V. Florinski, W. H. Matthaeus, and G. M. Webb. The Transport of Low-frequency Turbulence in Astrophysical Flows. I. Governing Equations. *ApJ*, 745:35, January 2012. doi: 10.1088/0004-637X/745/1/35.
- G. P. Zank, J. Heerikhuisen, B. E. Wood, N. V. Pogorelov, E. Zirnstein, and D. J. McComas. Heliospheric Structure: The Bow Wave and the Hydrogen Wall. *ApJ*, 763:20, January 2013. doi: 10.1088/0004-637X/763/1/20.
- G. P. Zank, L. Adhikari, P. Hunana, D. Shiota, R. Bruno, and D. Telloni. Theory and Transport of Nearly Incompressible Magnetohydrodynamic Turbulence. *ApJ*, 835:147, February 2017. doi: 10.3847/1538-4357/835/2/147.
- M. Zhang, J. R. Jokipii, and R. B. McKibben. Perpendicular Transport of Solar Energetic Particles in Heliospheric Magnetic Fields. *ApJ*, 595:493–499, September 2003. doi: 10.1086/377301.
- M. Zhang, G. Qin, and H. Rassoul. Propagation of Solar Energetic Particles in Three-Dimensional Interplanetary Magnetic Fields. *ApJ*, 692:109–132, February 2009. doi: 10.1088/0004-637X/692/1/109.

- L.-L. Zhao, L. Adhikari, G. P. Zank, Q. Hu, and X. S. Feng. Cosmic Ray Diffusion Tensor throughout the Heliosphere Derived from a Nearly Incompressible Magnetohydrodynamic Turbulence Model. *ApJ*, 849:88, November 2017. doi: 10.3847/1538-4357/aa932a.
- L.-L. Zhao, L. Adhikari, G. P. Zank, Q. Hu, and X. S. Feng. Influence of the Solar Cycle on Turbulence Properties and Cosmic-Ray Diffusion. *ApJ*, 856:94, April 2018. doi: 10.3847/1538-4357/aab362.
- V. Zhdankin, S. Boldyrev, and J. Mason. Distribution of Magnetic Discontinuities in the Solar Wind and in Magnetohydrodynamic Turbulence. *ApJL*, 760:L22, December 2012. doi: 10.1088/2041-8205/760/2/L22.
- Y. Zhou and W. H. Matthaeus. Models of inertial range spectra of interplanetary magnetohydrodynamic turbulence. *J. Geophys. Res.*, 95:14881–14892, September 1990a. doi: 10.1029/JA095iA09p14881.
- Y. Zhou and W. H. Matthaeus. Transport and turbulence modeling of solar wind fluctuations. *J. Geophys. Res.*, 95:10291–10311, July 1990b. doi: 10.1029/JA095iA07p10291.
- Y. Zhou, W. H. Matthaeus, D. A. Roberts, and M. L. Goldstein. Physical consistency in modeling interplanetary magnetohydrodynamic fluctuations. *Physical Review Letters*, 64:2591, May 1990. doi: 10.1103/PhysRevLett.64.2591.
- Y. Zhou, W. H. Matthaeus, and P. Dmitruk. Colloquium: Magnetohydrodynamic turbulence and time scales in astrophysical and space plasmas. *Reviews of Modern Physics*, 76:1015–1035, December 2004. doi: 10.1103/RevModPhys.76.1015.
- J. B. Zirker and O. Engvold. Why is the Sun’s corona so hot? Why are prominences so cool? *Physics Today*, 70(8):36–43, August 2017. doi: 10.1063/PT.3.3659.

Appendix A
PROPERTIES OF THE SOLAR WIND

Table A.1: Properties of the interplanetary medium at 1 au in the ecliptic.

Composition of ions	$\sim 96\% \text{ H}^+, 4\% \text{ He}^{++}$
Flow velocity	Slow wind: $\sim 350 \text{ km s}^{-1}$; Fast wind: $\sim 750 \text{ km s}^{-1}$
Density	$\sim 6 \text{ protons cm}^{-3}$
Magnetic field	$\sim 5 \text{ nT}$; 45° to radial
Proton temperature	$\sim (.4 - 1) \times 10^5 \text{ K}$
Electron temperature	$\sim (1 - 2) \times 10^5 \text{ K}$

Table A.2: Characteristic lengths in the solar wind.

Astronomical Unit (au)	$1.5 \times 10^{11} \text{ m}$
Radius of Sun (R_\odot)	$7 \times 10^8 \text{ m}$ ($\frac{1}{205} \text{ au}$)
Proton gyroradius at 1 au	$\sim 100 \text{ km}$
Electron gyroradius at 1 au	$\sim 1 \text{ km}$
Debye length at 1 au	$\sim 6 \text{ m}$
Correlation scale of fluctuations at 1 au	$\sim 10^9 \text{ m}$
Mean free path for proton-proton Coulomb collisions	$\sim 3 \text{ au}$

Table A.3: Characteristic times in the solar wind.

Solar magnetic cycle period	$\simeq 22$ years
Solar rotation period	$\simeq 27$ days
Typical transit time from sun to earth for a solar wind parcel	≈ 4 days
Proton gyroperiod (gyrofrequency) at 1 au	~ 10 s (~ 0.08 Hz)
Electron gyroperiod (gyrofrequency) at 1 au	$\sim 10^{-2}$ s (~ 150 Hz)
Proton-proton Coulomb collision time (frequency)	$\sim 10^6$ s ($\sim 10^{-6}$ Hz)

Table A.4: Characteristic speeds in the solar wind at 1 au.

Alfvén speed	~ 35 km s $^{-1}$
Ion sound speed	~ 50 km s $^{-1}$
Proton thermal speed	~ 50 km s $^{-1}$
Electron thermal speed	~ 2000 km s $^{-1}$

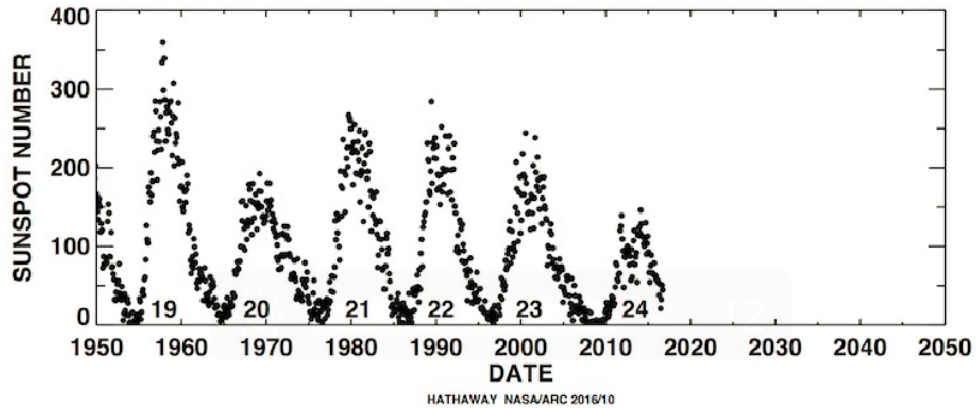


Figure A.1: The solar sunspot cycle. More sunspots indicate higher solar activity.
Image courtesy of NASA Marshall Space Flight Center.

Appendix B

ISOTROPIC TURBULENCE

B.1 Introduction

Our purpose here is to present some fundamental ideas of the formal theory of homogeneous and isotropic fluid turbulence. We will introduce the theory in real and spectral space. We largely follow the treatment of the subject given by [Batchelor \[1953\]](#) and [Davidson \[2015\]](#). Different sections of this appendix are referred to at various points in the main body of the thesis.

B.1.1 The Study of Homogeneous and Isotropic Turbulence

We imagine an infinite uniform body of fluid which can be characterized by a density ρ and molecular transport coefficients such as the viscosity ν . If the motion is turbulent, the velocity at any given time and position in the fluid is not found to be the same when it is measured several times under seemingly identical conditions. The velocity takes random values, which are not determined by the “controllable”, or “macroscopic”, data of the flow. We aim to study the *average* properties of the motion.

The assumption of homogeneity implies that the average properties of the motion are independent of position in the fluid. This is an idealized conception, but in the departure from homogeneity can be made very small in certain circumstances, such as the in the motion resulting from the passage of a uniform stream of fluid through a regular grid. The study of homogeneous turbulence also has practical utility, in that it can help us in understanding at least some aspects of the non-homogeneous turbulence that we see in nature.

For tractability, we can make further assumptions about the directional symmetry of the average properties of the turbulent motion. In the simplest case we have

statistical isotropy, and so the turbulence depends on neither the position nor the direction of the axes of reference. Of course, certain directions would be preferred by lack of homogeneity, and so isotropy can exist only in homogeneous turbulence. We note that even the simplest case of homogeneous and isotropic turbulence has defied satisfactory mathematical analysis.

B.1.2 Mathematical Formulation of the Problem

The equations determining the variation of the turbulent velocity \mathbf{u} in position and time are the continuity equation expressing the conservation of mass of the fluid, which in the case of incompressible flow takes the form $\nabla \cdot \mathbf{u} = 0$, and the Navier–Stokes equation expressing momentum conservation:

$$\frac{\partial \mathbf{u}}{\partial t} + \mathbf{u} \cdot \nabla \mathbf{u} = -\frac{1}{\rho} \nabla p + \nu \nabla^2 \mathbf{u}, \quad (\text{B.1})$$

where ρ is the mass density, ν is the kinematic viscosity, and p represents pressure. Both \mathbf{u} and the position \mathbf{x} are referred to axes such that the fluid has no average motion.

In homogeneous turbulence, the boundary conditions with respect to position are specified effectively by the statistical uniformity, with the fluid extending to infinity in all directions. The boundary conditions with respect to time are that at some initial instant the velocity is a random function of position. We rely on the tendency of dynamical systems with a large number of coupled degrees of freedom to approach a statistical state that is *independent* of the initial conditions.

B.2 Isotropic Turbulence in Real Space

B.2.1 Kinematics

Here we introduce the various statistical quantities used to characterize turbulence, and examine the restrictions imposed on them by isotropy and continuity. The most fundamental of these quantities is perhaps the velocity correlation function. Two other important quantities are the energy spectrum and the structure function.

B.2.1.1 Velocity Correlation Functions and Structure Functions

With $\langle \dots \rangle$ denoting ensemble-averages, the *second-order velocity correlation tensor* is defined as

$$Q_{ij}(\mathbf{r}, \mathbf{x}, t) = \langle u_i(\mathbf{x})u_j(\mathbf{x} + \mathbf{r}) \rangle. \quad (\text{B.2})$$

This represents the correlation of the velocity at a point in space with the velocity at another point, separated from the first by the vector \mathbf{r} , often called the *lag*. If the velocity fluctuations at the two points are statistically independent, $Q_{ij} = 0$. This might be if $r = |\mathbf{r}|$ is much greater than the typical eddy size. On the other hand, as $r \rightarrow 0$, $Q_{xx} \rightarrow \langle u_x^2 \rangle$.

In homogeneous turbulence, all statistical quantities are independent of \mathbf{x} , and so

$$Q_{ij}(\mathbf{r}) = \langle u_i(\mathbf{x})u_j(\mathbf{x} + \mathbf{r}) \rangle, \quad (\text{B.3})$$

where the time dependence of Q_{ij} is understood. In a concise notation,

$$Q_{ij}(\mathbf{r}) = \langle u_i u'_j \rangle, \quad (\text{B.4})$$

where the primed quantity is evaluated at the point $\mathbf{x}' = \mathbf{x} + \mathbf{r}$. This correlation tensor has the geometrical property

$$Q_{ij}(\mathbf{r}) = Q_{ji}(-\mathbf{r}) \quad (\text{B.5})$$

in homogeneous turbulence.

Some other properties of Q_{ij} are:

$$\frac{1}{2}Q_{ii}(0) = \frac{1}{2}\langle \mathbf{u}^2 \rangle = \text{kinetic energy density}; \quad (\text{B.6})$$

$$Q_{ij}(0) = -\tau_{ij}/\rho = (\text{Reynolds stress})/\rho; \quad (\text{B.7})$$

$$\frac{\partial Q_{ij}}{\partial r_i} = \frac{\partial Q_{ij}}{\partial r_j} = 0, \quad (\text{B.8})$$

where repeated indices imply summation. Equation (B.7) gives us another interpretation of Q_{ij} ; for the special case of $r = 0$, it is proportional to the Reynolds stress, $\tau_{ij} = \langle u_i u_j \rangle$. To derive Equation (B.8), we note that in homogeneous turbulence,

$$\frac{\partial}{\partial x_i} = -\frac{\partial}{\partial r_i}, \quad \frac{\partial}{\partial x'_i} = \frac{\partial}{\partial r_i}, \quad (\text{B.9})$$

since the statistical quantities being differentiated are functions only of $r_i = x'_i - x_i$. This, combined with the continuity equation and the fact the operations $\langle \dots \rangle$ and spatial differentiation commute, yields (B.8).

Three important forms of Q_{ij} are:

$$R(r) = \frac{1}{2} Q_{ii} = \frac{1}{2} \langle \mathbf{u} \cdot \mathbf{u}' \rangle, \quad (\text{B.10})$$

$$u^2 f(r) = Q_{xx}(r \hat{\mathbf{e}}_x), \quad (\text{B.11})$$

$$u^2 g(r) = Q_{yy}(r \hat{\mathbf{e}}_x). \quad (\text{B.12})$$

Here

$$u = \langle u_x^2 \rangle^{1/2} = \langle u_y^2 \rangle^{1/2} = \langle u_z^2 \rangle^{1/2} = \left(\frac{1}{3} \langle \mathbf{u}^2 \rangle \right)^{1/2}, \quad (\text{B.13})$$

where $\hat{\mathbf{e}}_x$ is a unit vector in the x -direction. Note that R is a function solely of $r = |\mathbf{r}|$ by virtue of the spherical symmetry of statistical quantities. The functions f and g are called the *longitudinal* and *lateral velocity correlation functions*. These quantities can be measured easily in an experimental setup. Note that here \mathbf{r} lies solely along the x direction, and the y direction is normal to \mathbf{r} . f and g are dimensionless and satisfy $f(0) = g(0) = 1$ and $f, g \leq 1$. Their behavior with varying r is shown in Figure B.1.

The integral scale, l , which represents the size of the large, energy-containing eddies is conventionally defined as

$$l = \int_0^\infty f(r) dr. \quad (\text{B.14})$$

This quantity provides a measure of the extent of the region in which velocities are

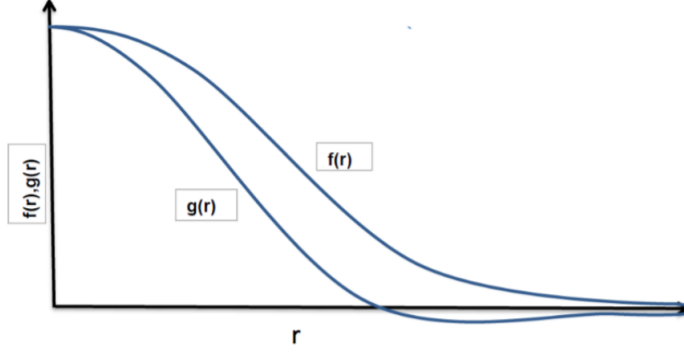


Figure B.1: Longitudinal (f) and transverse (g) correlation functions, shown as functions of varying lag r . $f(r)$ is believed to always be positive for incompressible flow ($\nabla \cdot \mathbf{u} = 0$), while $g(r)$ can be negative if $\nabla \times \mathbf{u} \neq 0$ and eddies span the lag r . Figure reproduced from [Subedi \[2017\]](#) with permission (see [Appendix E](#))

correlated appreciably. The *third-order velocity correlation function* is defined as

$$S(\mathbf{r})_{ijk} = \langle u_i(\mathbf{x})u_j(\mathbf{x})u_k(\mathbf{x} + \mathbf{r}) \rangle. \quad (\text{B.15})$$

A special case of this is

$$u^3 K(r) = \langle u_x^2(\mathbf{x})u_x(\mathbf{x} + r\hat{\mathbf{e}}_x) \rangle, \quad (\text{B.16})$$

where $K(r)$ is the *longitudinal triple correlation function*.

An alternative measure of the state of a field of turbulence is provided by the so-called *structure functions*. These are defined in terms of the longitudinal velocity increment $\Delta v = u_x(\mathbf{x} + r\hat{\mathbf{e}}_x) - u_x(\mathbf{x})$. For example, the *second-order longitudinal structure function* is defined as

$$\langle [\Delta v]^2 \rangle = \langle [u_x(\mathbf{x} + r\hat{\mathbf{e}}_x) - u_x(\mathbf{x})]^2 \rangle. \quad (\text{B.17})$$

It is easily seen that this is related to f by

$$\langle [\Delta v]^2 \rangle = 2u^2(1 - f), \quad (\text{B.18})$$

where we have used the fact that $\langle u_x(\mathbf{x} + r\hat{\mathbf{e}}_x) \rangle = \langle u_x(\mathbf{x}) \rangle$ for homogeneous turbulence.

The physical significance of $\langle [\Delta v]^2 \rangle$ is that it acts as a kind of filter, extracting information about eddies of size r or less. All eddies of size less than or equal to r contribute to $\langle [\Delta v]^2 \rangle$, as they tend to generate different velocities at \mathbf{x} and \mathbf{x}' , while eddies much larger than r tend to have similar velocities at \mathbf{x} and \mathbf{x}' [see Figure 6.14 of [Davidson, 2015](#)].

B.2.1.2 The Simplifications of Isotropy

The continuity equation and the symmetries associated with isotropy impose severe constraints on the general form of our tensors. Homogeneity implies the invariance of statistical quantities with respect to arbitrary translations. With isotropy, we also have invariance with respect to reflection and arbitrary rigid rotations of the configuration formed by the two (or more) points and the various directional velocity vectors. Group-theoretic methods lead to the following general form of isotropic tensors that are functions of \mathbf{r} alone [see [Batchelor, 1953](#)]:

$$Q_i(\mathbf{r}) = Ar_i, \quad (\text{B.19})$$

$$Q_{ij}(\mathbf{r}) = Ar_i r_j + B\delta_{ij}, \quad (\text{B.20})$$

$$Q_{ijk}(\mathbf{r}) = Ar_i r_j r_k + Br_i \delta_{jk} + Cr_j \delta_{ki} + Dr_k \delta_{ij}, \quad (\text{B.21})$$

where A, B, \dots are symmetric functions of r . Using (B.11) and (B.12), we can see that

$$B = u^2 g, \quad (\text{B.22})$$

since $r_y = 0$ in this case, and

$$A = u^2(f - g)/r^2. \quad (\text{B.23})$$

The general form of Q_{ij} becomes

$$Q_{ij}(\mathbf{r}) = u^2 \left[\frac{f - g}{r^2} r_i r_j + g \delta_{ij} \right]. \quad (\text{B.24})$$

Using the continuity equation in the form of (B.8), we get

$$\frac{\partial Q_{ij}}{\partial r_i} = [rA_r + 4A + r^{-1}B_r]r_j = 0, \quad (\text{B.25})$$

where the r subscript indicates differentiation with respect to r . Using (B.22) and (B.23) in the equation above gives

$$g = f + \frac{1}{2}r f_r. \quad (\text{B.26})$$

This allows us to eliminate g from (B.24) and write Q_{ij} as a function of f alone:

$$Q_{ij}(\mathbf{r}) = \frac{u^2}{2r} [(r^2 f)_r \delta_{ij} - f_r r_i r_j]. \quad (\text{B.27})$$

Note that the Reynolds stresses $\langle u_x u_y \rangle$, $\langle u_y u_z \rangle$, $\langle u_z u_x \rangle$ are all zero in isotropic turbulence, since $Q_{ij}(0) = 0$.

From (B.27) we have

$$R(r) = \frac{1}{2}Q_{ii} = \frac{u^2}{2r^2}(r^3 f)_r. \quad (\text{B.28})$$

A similar analysis lets us rewrite the third-order velocity correlation function S_{ijk} as a function of the longitudinal triple correlation function $K(r)$:

$$S(\mathbf{r})_{ijk} = u^3 \left[\frac{K - rK_r}{2r^3} r_i r_j r_k + \frac{2K + rK_r}{4r} (r_i \delta_{jk} + r_j \delta_{ik}) - \frac{K}{2r} r_k \delta_{ij} \right]. \quad (\text{B.29})$$

The above expressions are extremely useful, as they tell us that the seemingly complicated tensors Q_{ij} and S_{ijk} are simply determined by the scalar functions $f(r)$. This drastic simplification is what makes isotropic turbulence relatively easy to analyze.

B.2.2 Dynamics

To obtain an evolution equation for the velocity correlation $\langle u_i u'_j \rangle$, we write the Navier–Stokes equation for u_i :

$$\frac{\partial u_i}{\partial t} = -\frac{\partial(u_i u_k)}{\partial x_k} - \frac{\partial(p/\rho)}{\partial x_i} + \nu \nabla_x^2 u_i. \quad (\text{B.30})$$

where we have used the continuity equation $\partial u_k / \partial x_k = 0$. Similarly, for u'_j we have

$$\frac{\partial u'_j}{\partial t} = -\frac{\partial(u'_j u'_k)}{\partial x'_k} - \frac{\partial(p'/\rho)}{\partial x'_i} + \nu \nabla_{x'}^2 u'_j. \quad (\text{B.31})$$

We multiply (B.30) and (B.31) by u'_j and u_i , respectively, add the two before averaging to get

$$\begin{aligned} \frac{\partial}{\partial t} \langle u_i u'_j \rangle &= - \left\langle u_i \frac{\partial u'_j u'_k}{\partial x'_k} + u'_j \frac{\partial u_i u_k}{\partial x_k} \right\rangle - \frac{1}{\rho} \left\langle u_i \frac{\partial p'}{\partial x'_j} + u'_j \frac{\partial p}{\partial x_i} \right\rangle \\ &\quad + \nu \langle u_i \nabla_{x'}^2 u'_j + u'_j \nabla_x^2 u_i \rangle. \end{aligned} \quad (\text{B.32})$$

To simplify this complicated equation, we first note that: (1) the operations of averaging and differentiation commute; (2) as noted before, $\frac{\partial}{\partial x_i} = -\frac{\partial}{\partial r_i}$ and $\frac{\partial}{\partial x'_i} = \frac{\partial}{\partial r_i}$; and (3) u_i is independent of \mathbf{x}' and u'_j is independent of \mathbf{x} .

Next we show that the pressure terms vanish. Consider $\langle u_i p' \rangle$. This is an isotropic first-order tensor which has, from (B.19), the general form

$$\langle u_i p' \rangle = A(r) r_i. \quad (\text{B.33})$$

The equation of continuity demands that

$$\frac{\partial \langle u_i p' \rangle}{\partial r_i} = \frac{\partial (A r_i)}{\partial r_i} = 0, \quad (\text{B.34})$$

which yields

$$A' r + 3A = 0. \quad (\text{B.35})$$

This has the general solution $A \sim r^{-3}$, which blows up at $r = 0$. Thus, the only acceptable solution is $A(r) = 0$, and so $\langle u_i p' \rangle = 0$, and the pressure terms vanish.

Now consider $\langle u_i u'_j u'_k \rangle$. We have

$$\begin{aligned} \langle u_i(\mathbf{x}) u_j(\mathbf{x} + \mathbf{r}) u_k(\mathbf{x} + \mathbf{r}) \rangle &= \langle u_i(\mathbf{x} - \mathbf{r}) u_j(\mathbf{x}) u_k(\mathbf{x}) \rangle \\ &\quad (\text{because of homogeneity}) \\ &= \langle u_j(\mathbf{x}) u_k(\mathbf{x}) u_i(\mathbf{x} - \mathbf{r}) \rangle \\ &= S_{jki}(-\mathbf{r}) \\ &= -S_{jki}(\mathbf{r}), \end{aligned} \quad (\text{B.36})$$

where the last line follows from the anti-symmetry of S_{jki} , as defined by (B.21).

Putting it all together, we find

$$\frac{\partial Q_{ij}}{\partial t} = \frac{\partial}{\partial r_k} [S_{ikj} + S_{jki}] + 2\nu \nabla^2 Q_{ij}, \quad (\text{B.37})$$

where ∇ is with respect to \mathbf{r} . Substituting for Q_{ij} and S_{ijk} from (B.27) and (B.29) yields

$$\frac{\partial}{\partial t} [u^2 r^4 f(r)] = u^3 \frac{\partial}{\partial r} [r^4 K(r)] + 2\nu u^2 \frac{\partial}{\partial r} [r^4 f_r(r)]. \quad (\text{B.38})$$

This equation is known as the *Kármán–Howarth equation* [de Kármán and Howarth, 1938]. We can rewrite it in terms of R :

$$\frac{\partial R}{\partial t} = \Gamma(r) + 2\nu \nabla^2 R, \quad \Gamma = \frac{1}{2r^2} \frac{\partial}{\partial r} \left[\frac{1}{r} \frac{\partial}{\partial r} (r^4 u^3 K) \right]. \quad (\text{B.39})$$

The problem with the two dynamical equations above is that the evolution of f and R cannot be predicted without knowledge of the form of $K(r)$. The evolution of $K(r)$ will in turn depend on the fourth-order correlation. This is the infamous *closure problem* of turbulence (see Section 3.2). Nevertheless, the equations can still be used to extract useful information, such as *Kolmogorov's four-fifths law*, which is one of the few exact results in turbulence theory [e.g., Section 6.2.2.2 of Davidson, 2015]:

$$\langle [\Delta v]^3 \rangle = -\frac{4}{5}\varepsilon r \quad (\eta \ll r \ll l), \quad (\text{B.40})$$

where ε is the energy dissipation rate and η is the *Kolmogorov microscale* (Section 3.1).

B.3 Isotropic Turbulence in Spectral Space

B.3.1 The Transform of the Correlation Tensor and the Energy Spectrum

We introduce the *spectrum tensor*, $\Phi_{ij}(\mathbf{k})$, which is defined as the Fourier transform of Q_{ij} .¹

$$\Phi_{ij}(\mathbf{k}) = \frac{1}{(2\pi)^3} \int Q_{ij}(\mathbf{r}) e^{-i\mathbf{k}\cdot\mathbf{r}} d\mathbf{r} \quad (\text{B.41a})$$

$$Q_{ij}(\mathbf{r}) = \int \Phi_{ij}(\mathbf{k}) e^{i\mathbf{k}\cdot\mathbf{r}} d\mathbf{k}. \quad (\text{B.41b})$$

Incompressibility (Equation B.8) requires

$$k_j \Phi_{ij} = k_i \Phi_{ij} = 0. \quad (\text{B.42})$$

For isotropic turbulence Φ_{ij} is an isotropic tensor with the general form (Equation B.20) $\Phi_{ij} = A(k)k_i k_j + B(k)\delta_{ij}$, where A and B are even functions of k . From (B.42), we have $(Ak^2 + B)k_j = 0$, and we can eliminate A to write

$$\Phi_{ij} = B(k) \left[\delta_{ij} - \frac{k_i k_j}{k^2} \right]. \quad (\text{B.43})$$

¹ Recall that the Fourier transform (Section 3.1.1) may be thought of as a *filter* that separates the different scales present in the turbulent signal [see Section 8.1.2 of Davidson, 2015].

From (B.43) and (B.28), we see that Φ_{ii} and Q_{ii} are spherically symmetric functions given by

$$\frac{1}{2}\Phi_{ii} = B(k), \quad (\text{B.44})$$

and

$$\frac{1}{2}Q_{ii} = \frac{1}{2}\langle \mathbf{u} \cdot \mathbf{u}' \rangle = R(r). \quad (\text{B.45})$$

With $r = 0$, (B.41b) gives

$$\frac{1}{2}\langle \mathbf{u}^2 \rangle = \frac{1}{2} \int \Phi_{ii} d\mathbf{k} = \int_0^\infty 2\pi k^2 \Phi_{ii} dk, \quad (\text{B.46})$$

that is, integrating $\frac{1}{2}\Phi_{ii}$ over all \mathbf{k} -space gives the kinetic energy density of the turbulence. Φ_{ii} can be thought to represent the ‘distribution’ of kinetic energy in spectral space.

We now introduce the *three-dimensional energy spectrum* of the velocity field:

$$E(k) = 2\pi k^2 \Phi_{ii}, \quad E(k) \geq 0 \quad (\text{B.47})$$

from which we have

$$\frac{1}{2}\langle \mathbf{u}^2 \rangle = \int_0^\infty E dk. \quad (\text{B.48})$$

$E(k)$ represents the contribution of Φ_{ii} to $\frac{1}{2}\langle \mathbf{u}^2 \rangle$ which is contained in a spherical annulus in \mathbf{k} -space of thickness dk .

B.3.2 An Evolution Equation for $E(k)$

Starting from Equation (B.41a), it is easy to show that

$$E(k) = \frac{2}{\pi} \int_0^\infty R(r) k r \sin(kr) dr, \quad (\text{B.49})$$

which can be combined with the Kármán–Howarth Equation (B.39) to get an evolution equation for the energy spectrum:

$$\frac{\partial E}{\partial t} = T(k, t) - 2\nu k^2 E, \quad (\text{B.50})$$

where

$$T(k, t) = \frac{k}{\pi} \int_0^\infty \frac{1}{r} \frac{\partial}{\partial r} \frac{1}{r} \frac{\partial}{\partial r} [r^4 u^3 K] \sin(kr) dr. \quad (\text{B.51})$$

This is the spectral equivalent of the Kármán–Howarth equation. $T(k)$ is known as the *spectral kinetic energy transfer function*. In the framework of the energy cascade (Section 3.1), we take $T(k)$ to represent the removal of energy from the large scales and its deposition in the small scales. We therefore expect $T(k)$ to be negative for small k and positive for large k . We also have

$$\int_0^\infty T(k) dk = 0, \quad (\text{B.52})$$

which we would expect to follow from conservation of *total* energy.

The energy equation (B.50) is sometimes written in the alternative form

$$\frac{\partial E}{\partial t} = -\frac{\partial \Pi_E}{\partial k} - 2\nu k^2 E, \quad (\text{B.53})$$

where

$$\Pi_E = -\int_0^k T(k) dk = \int_0^\infty T(k) dk \quad (\text{B.54})$$

is called the *spectral kinetic energy flux* and represents the net transfer of energy from eddies of wave number less than k to those of wave number greater than k .

Appendix C

WKB ALFVÉN WAVE MODEL FOR THE SOLAR WIND

The governing MHD equations for single-fluid polytropic inviscid flow driven by gradients of thermal and Alfvén wave (WKB) pressure, in the frame rotating with the Sun, are [Usmanov and Goldstein, 2003]¹

$$\frac{\partial \rho}{\partial t} + \nabla \cdot \rho \mathbf{v} = 0, \quad (\text{C.1})$$

$$\begin{aligned} \frac{\partial \rho \mathbf{v}}{\partial t} + \nabla \cdot \left[\rho \mathbf{v} \mathbf{v} + \left(P + \frac{\mathcal{E}}{2} + \frac{B^2}{8\pi} \right) \mathbf{I} - \frac{\mathbf{B} \mathbf{B}}{4\pi} \right] \\ + \rho \left[\frac{GM_\odot}{r^2} \hat{\mathbf{r}} + 2\boldsymbol{\Omega} \times \mathbf{v} + \boldsymbol{\Omega} \times (\boldsymbol{\Omega} \times \mathbf{r}) \right] = 0, \end{aligned} \quad (\text{C.2})$$

$$\frac{\partial \mathbf{B}}{\partial t} = \nabla \times (\mathbf{v} \times \mathbf{B}), \quad (\text{C.3})$$

$$\begin{aligned} \frac{\partial}{\partial t} \left[\frac{\rho}{2} (v^2 - |\boldsymbol{\Omega} \times \mathbf{r}|^2) + \frac{P}{\gamma - 1} + \frac{B^2}{8\pi} - \frac{\rho GM_\odot}{r} + \mathcal{E} \right] \\ + \nabla \cdot \left\{ \left[\frac{\rho}{2} (v^2 - |\boldsymbol{\Omega} \times \mathbf{r}|^2) + \frac{\gamma P}{\gamma - 1} - \frac{\rho GM_\odot}{r} \right] \mathbf{v} \right. \\ \left. + \frac{\mathbf{B}}{4\pi} \times (\mathbf{v} \times \mathbf{B}) + \left(\frac{3}{2} \mathbf{v} + \mathbf{V}_A \right) \mathcal{E} \right\} = 0, \end{aligned} \quad (\text{C.4})$$

$$\frac{\partial \mathcal{E}}{\partial t} + \nabla \cdot [(\mathbf{v} + \mathbf{V}_A) \mathcal{E}] = -\frac{\mathcal{E}}{2} \nabla \cdot \mathbf{v} - |\mathbf{v} + \mathbf{V}_A| \frac{\mathcal{E}}{L}, \quad (\text{C.5})$$

¹ See also Jacques [1977, 1978].

where the dependent variables are the plasma density ρ , the flow velocity in the frame rotating with the Sun \mathbf{v} , the magnetic field \mathbf{B} , the thermal pressure P , and the Alfvén wave energy density \mathcal{E} . The parameters appearing in the equations are the sidereal solar rotation rate $\mathbf{\Omega}$, the gravitational constant G , the adiabatic index γ , and the solar mass M_\odot . The independent variables are the heliocentric position vector \mathbf{r} and the time t , and \mathbf{I} is the unit matrix. \mathbf{V}_A is the velocity of outward propagating Alfvén waves $\mathbf{V}_A = \pm \mathbf{B}/(4\pi\rho)^{-1/2}$, where the positive sign holds if the magnetic field is radially outward ($B_r \geq 0$), and the negative sign holds otherwise. The waves are assumed to be damped by an unspecified mechanism that is characterized by a dissipation length L .

The driven Alfvén wave velocity amplitude ($\sqrt{\mathcal{E}/\rho}$) is assumed to be 35 km s^{-1} on the coronal base. The polytropic index is assumed to depart from the adiabatic value to implicitly account for thermal conduction in the region $1 - 20 R_\odot$: $\gamma = 1.08$, that is, close to the isothermal value. Above $20 R_\odot$, we take $\gamma = 5/3$. The waves are assumed to be undamped below $20 R_\odot$, while above this height the dissipation length L is set to $20 R_\odot$ [Usmanov and Goldstein, 2003; Usmanov et al., 2014]. Note that the solar wind model described in Chapter 4 assumes an adiabatic polytropic index throughout the simulation domain, so that the heating and acceleration of the wind proceeds self-consistently through turbulence transport and electron heat conduction, without requiring any unspecified sources, in contrast to the WKB model.

Appendix D

INVARIANCE OF AVERAGING METHODS FOR TURBULENCE SIMULATION

The solar wind simulations employed in this thesis are based on a Reynolds-averaging (RANS) approach (Section 1.1.5), in which all fluctuations are “averaged-over”, and only the mean part of the flow is explicitly resolved. In this Appendix we briefly consider another major approach that is widely used to reduce the number of degrees of freedom in turbulence simulation – the *large eddy simulation* (LES) approach, based on a *filtering* operation. LES is computationally more expensive than RANS, but resolves the large-scale fluctuations, and therefore provides a more complete description of the turbulence. In future work, our aim is to transition our global simulation from RANS toward LES, and here we briefly discuss some preliminary efforts to that end.

D.1 Implicit Averaging – Discretizing on a Numerical Grid

The act of representing flow variables on the discrete mesh of a simulation corresponds to an implicit averaging process. The second-order central difference formula for the derivative of a continuous variable $u(x)$ represents *exactly* the derivative of a *second* continuous variable that is an *average* of the first one [Rogallo and Moin, 1984]:

$$\frac{u(x+h) - u(x-h)}{2h} = \frac{d}{dx} \left\{ \frac{1}{2h} \int_{x-h}^{x+h} u(\xi) d\xi \right\}. \quad (\text{D.1})$$

Thus, a discrete operator filters out scales smaller than the mesh size h . This approach is acceptable when the simulation mesh completely resolves the flow (direct numerical simulation or DNS), and the average does not cause any loss of information. At high Reynolds numbers, a reduction of the degrees of freedom to a resolvable size is needed,

and an averaging/filtering process that formally separates the resolved and subgrid scales is defined. The interaction of the resolved and subgrid scales must then be modeled.

D.2 Reynolds Averaging (RA)

This approach involves a statistical description of the flow. The flow equations are subject to an averaging operator, and the simulation then solves the Reynolds-averaged equations for the mean flow, with all of the turbulent motions being unresolved and requiring the use of a mathematical model. This greatly reduces computational cost, and the RA approach is still the more commonly used one in applications.

RA involves a separation into a mean and a fluctuation:

$$\tilde{u}_i = u_i + u'_i, \quad (\text{D.2})$$

where $u_i = \langle \tilde{u}_i \rangle$; $\langle u'_i \rangle = 0$ and $\langle u_i u'_j \rangle = 0$. The central moments for the Reynolds operator are:

$$\langle u'_i u'_j \rangle = \langle u_i u_j \rangle - \langle u_i \rangle \langle u_j \rangle. \quad (\text{D.3})$$

Examples of Reynolds-averaged equations can be found in Chapter 4.

D.3 Filtering and LES

This approach lies between the direct and the statistical approach. A scale separation is effected through a filtering operation applied to the flow equations, so that the simulation resolves the large turbulent eddies. Modeling assumptions typically made in LES require that the cut off be placed in the inertial range of the energy spectrum, and this requirement causes the computational cost to rapidly increase in situations where complex flows and high Reynolds numbers are involved [e.g., [Lesieur and Metais, 1996](#)].

The filtered field can be formally represented by a convolution integral given by

$$u_i(\mathbf{x}, t)_{l,\theta} = \int \tilde{u}_i(\mathbf{x}', t') \mathcal{G}(\mathbf{x} - \mathbf{x}', t - t'; l, \theta) d\mathbf{x}' dt', \quad (\text{D.4})$$

with

$$\int \mathcal{G}(\mathbf{x} - \mathbf{x}', t - t'; l, \theta) d\mathbf{x}' dt' = 1, \quad (\text{D.5})$$

where l and θ are a characteristic filter length and time, respectively, and various choices are possible for the kernel \mathcal{G} , such as a sharp cutoff or a Gaussian filter.

We decompose the velocity and magnetic fields into a large and a small-scale component: $\tilde{u}_i = u_i + u'_i$, where the assumption that the mean and fluctuation are uncorrelated is no longer valid:

$$\langle u'_i \rangle \neq 0, \langle u_i u'_j \rangle \neq 0. \quad (\text{D.6})$$

We now have (in contrast to Equation D.3):

$$\langle u_i u_j \rangle - \langle u_i \rangle \langle u_j \rangle = \langle u'_i u'_j \rangle + \langle u'_i u_j \rangle + \langle u_i u'_j \rangle. \quad (\text{D.7})$$

Clearly, this approach will yield a set of filtered large-scale equations that are different from the RA equations. However, in the next section we demonstrate the *averaging invariance* of the system, when appropriately-defined generalized central moments are introduced [Germano, 1992].

D.4 Generalized Central Moments and Averaging Invariance of the MHD Equations

To simplify filtering the equations of compressible MHD, we will employ Favre (mass-weighted) filtering [Favre, 1969] to avoid extra terms associated with variable density. A Favre-filtered field is defined as

$$\tilde{f} = \frac{\overline{\rho f}}{\bar{\rho}}, \quad (\text{D.8})$$

where ρ is the mass density and the overline ‘ \bar{f} ’ denotes filtering via Equation (D.4). We define the *generalized central moment* [Germano, 1992]:

$$\tau(f, g) = \overline{fg} - \bar{f}\bar{g}. \quad (\text{D.9})$$

With the added complication of Favre filtering, we need the following additional specifications when any of the arguments of τ is a component of the velocity field \mathbf{u} :

$$\tau(u_i, g) = \tau(g, u_i) = \overline{u_i g} - \tilde{u}_i \bar{g}, \quad (\text{D.10})$$

and

$$\tau(u_i, u_j) = \widetilde{u_i u_j} - \tilde{u}_i \tilde{u}_j. \quad (\text{D.11})$$

We now filter the continuity, momentum, and energy equations for ideal compressible MHD (Section 2.2.1).

The continuity equation:

$$\frac{\partial \rho}{\partial t} + \frac{\partial \rho u_j}{\partial x_j} = 0 \quad (\text{D.12})$$

The filtered equation is

$$\frac{\partial \bar{\rho}}{\partial t} + \frac{\partial \overline{\rho u_j}}{\partial x_j} = 0, \quad (\text{D.13})$$

which may be written as

$$\frac{\partial \bar{\rho}}{\partial t} + \frac{\partial \bar{\rho} \tilde{u}_j}{\partial x_j} = 0. \quad (\text{D.14})$$

The momentum equation:

$$\frac{\partial \rho u_i}{\partial t} + \frac{\partial}{\partial x_j} (\rho u_i u_j) + \frac{\partial P}{\partial x_i} + \frac{\partial}{\partial x_i} \frac{B^2}{2M_a^2} - \frac{\partial}{\partial x_j} \frac{B_i B_j}{M_a^2} = 0, \quad (\text{D.15})$$

where P is the fluid pressure, \mathbf{B} is the magnetic field, and $M_a = u_0/u_A$ is the magnetic Mach number, defined in terms of a constant system speed u_0 and a constant Alfvén

speed u_A . Filtering the equation yields, after some algebra:

$$\frac{\partial \bar{\rho} \tilde{u}_i}{\partial t} + \frac{\partial}{\partial x_j} (\bar{\rho} \tilde{u}_i \tilde{u}_j) + \frac{\partial \bar{P}}{\partial x_i} + \frac{\partial}{\partial x_i} \frac{\bar{B}^2}{2M_a^2} - \frac{\partial}{\partial x_j} \frac{\bar{B}_i \bar{B}_j}{M_a^2} = -\frac{\partial \tau_{ij}^u}{\partial x_j}, \quad (\text{D.16})$$

where

$$\tau_{ij}^u = \bar{\rho} \tau(u_i, u_j) + \frac{1}{2M_a^2} \tau(B_k, B_k) \delta_{ij} - \frac{1}{M_a^2} \tau(B_i, B_j). \quad (\text{D.17})$$

Note that in $\tau(B_k, B_k)$, repeated indices are summed over.

Equation (D.16) has the same form as the Reynolds-averaged ($f = \langle f \rangle + f'$) momentum equation, which has, instead of the generalized moments $\tau(f, g)$, the well-known Reynolds stresses $\langle f' g' \rangle$.

The induction equation:

$$\frac{\partial B_i}{\partial t} + \frac{\partial}{\partial x_j} (u_j B_i - u_i B_j) = 0 \quad (\text{D.18})$$

Filtering this yields, after some algebra

$$\frac{\partial \bar{B}_i}{\partial t} + \frac{\partial}{\partial x_j} (\tilde{u}_j \bar{B}_i - \tilde{u}_i \bar{B}_j) = -\frac{\partial \tau_{ji}^b}{\partial x_j}, \quad (\text{D.19})$$

where

$$\tau_{ij}^b = \tau(u_i, B_j) - \tau(u_j, B_i). \quad (\text{D.20})$$

As with the momentum equation, Equation (D.19) has the same form as the Reynolds-averaged induction equation, with the Reynolds stresses replaced by the generalized moments.

Next, we compare the Reynolds-averaged energy equation with the filtered energy equation. The energy equation is (see Equation 4.4)

$$\frac{\partial P}{\partial t} + u_j \frac{\partial P}{\partial x_j} + \gamma P \frac{\partial u_j}{\partial x_j} = Q, \quad (\text{D.21})$$

where γ is the polytropic index and Q includes heating effects. Filtering yields the

following equation:

$$\frac{\partial \bar{P}}{\partial t} + \tilde{u}_j \frac{\partial \bar{P}}{\partial x_j} + \gamma \bar{P} \frac{\partial \tilde{u}_j}{\partial x_j} = -\frac{\partial}{\partial x_j} \tau(u_j, P) - (\gamma - 1) \tau(P, \partial_j u_j) + \bar{Q}, \quad (\text{D.22})$$

while the Reynolds-averaged equation (assuming $\rho' = 0$) is

$$\frac{\partial \bar{P}}{\partial t} + \bar{u}_j \frac{\partial \bar{P}}{\partial x_j} + \gamma \bar{P} \frac{\partial \bar{u}_j}{\partial x_j} = -\frac{\partial}{\partial x_j} \langle u'_j P' \rangle - (\gamma - 1) \langle P' (\partial_j u'_j) \rangle + \bar{Q}. \quad (\text{D.23})$$

It is clear that the averaging-invariance of the filtered equations holds for compressible MHD. Models used for closing the RANS-MHD equations may therefore be applied within an LES paradigm. Care must be taken regarding the filter width, which is conventionally taken to lie in the inertial range for LES. Resolving the inertial range in a solar wind simulation is computationally prohibitive, but there may be justification for filtering at the energy-containing scales [Pope, 2004]. We also remark that the causality threshold discussed in Section 7.A offers a possible filter scale for LES of the solar wind; since fluctuations cannot have a causal influence at distances larger than this threshold, any averaging procedure should be restricted to scales contained within it. We defer further consideration of these issues to future work.

Appendix E

PERMISSION LETTERS

E.1 Permission from Annual Reviews for Figure 1.6

Copyright Clearance Center

<https://www.copyright.com/printOrder.do?id=11...>



Confirmation Number: 11703929
Order Date: 03/10/2018

Customer Information

Customer: Rohit Chhiber
Account Number: 3001258377
Organization: Rohit Chhiber
Email: rohitcchhiber@gmail.com
Phone: +1 (302) 229-4641
Payment Method: Invoice

This is not an invoice

Order Details

Annual review of astronomy and astrophysics Billing Status:
N/A

<p>Order detail ID: 71059925 ISSN: 1545-4282 Publication Type: e-Journal Volume: Issue: Start page: Publisher: ANNUAL REVIEWS</p>	<p>Permission Status: ✔ Granted Permission type: Republish or display content Type of use: Thesis/Dissertation Order License Id: 4305661368213</p> <p>Requestor type: Publisher, for-profit Format: Electronic Portion: chart/graph/table/figure Number of charts/graphs/tables /figures: 1 The requesting person/organization: Rohit Chhiber Title or numeric reference of the portion(s): Figure 1 Title of the article or chapter the portion is from: Magnetohydrodynamic turbulence in the solar wind Editor of portion(s): N/A Author of portion(s): Melvyn Goldstein Volume of serial or monograph: 33 Page range of portion: 285 Publication date of portion: 1995 Rights for: Main product Duration of use: Life of current edition Creation of copies for the disabled: no With minor editing privileges: no For distribution to: Worldwide</p>
--	--

Note: This item was invoiced separately through our [RightsLink service](#). [More info](#) **\$ 0.00**

E.2 Permission from Dr. Tulasi Parashar for Figure 2.2



Rohit Chhiber <rohitc@udel.edu>

Permission letter for reproducing figure from your thesis

Tulasi Parashar <tulasinandan@gmail.com>
To: Rohit Chhiber <rohitc@udel.edu>

Tue, Jul 3, 2018 at 2:11 PM

Rohit,

Yes, you have my permission to use the figure.

Best,
Tulasi

On Tue, Jul 3, 2018, 11:41 AM Rohit Chhiber <rohitc@udel.edu> wrote:

Dear Tulasi,

I am writing to request your permission to reproduce Figure 2.2 from your thesis [Parashar 2011] in Chapter 2 of my dissertation (attached below; see Figure 2.2).

Best regards,
Rohit

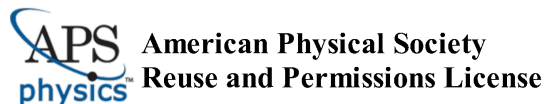
https://drive.google.com/open?id=1sdKT0URYt_byn8nO0kHkYgn4mXKueJfY

--

Rohit Chhiber
Dept. of Physics and Astronomy
University of Delaware
Newark, DE

Phone: 302-831-4355

E.3 Permission from the American Physical Society and Dr. William Matthaheus for Figure 3.1



05-Apr-2018

This license agreement between the American Physical Society ("APS") and Rohit Chhiber ("You") consists of your license details and the terms and conditions provided by the American Physical Society and SciPris.

Licensed Content Information

License Number: RNP/18/APR/003033
License date: 05-Apr-2018
DOI: 10.1103/RevModPhys.76.1015
Title: Colloquium
Author: Ye Zhou, W. H. Matthaheus, and P. Dmitruk
Publication: Reviews of Modern Physics
Publisher: American Physical Society
Cost: USD \$ 0.00

Request Details

Does your reuse require significant modifications: No
Specify intended distribution locations: Worldwide
Reuse Category: Reuse in a thesis/dissertation
Requestor Type: Publisher, for profit
Items for Reuse: Figures/Tables
Number of Figure/Tables: 1
Figure/Tables Details: Figure 1
Format for Reuse: Electronic

Information about New Publication:

University/Publisher: UNIVERSITY MICROFILMS INC.
Title of dissertation/thesis: STUDIES IN MULTI-SCALE TURBULENT DYNAMICS OF THE SOLAR WIND
Author(s): Rohit Chhiber
Expected completion date: May, 2018

License Requestor Information

Name: Rohit Chhiber
Affiliation: Individual
Email Id: rohitc@udel.edu
Country: United States

Permission letter for reproducing figure from Zhou et al., RMP [2004]

William Matthaues <whm@udel.edu>
To: Rohit Chhiber <rohitc@udel.edu>

Tue, Jul 3, 2018 at 2:09 PM

Dear Rohit,

Yes, you have my permission.

Best Regards

bill

On 7/3/2018 12:27 PM, Rohit Chhiber wrote:

Dear Bill,

I am writing to request your permission to reproduce Figure 1 from Zhou et al., RMP [2004] in my dissertation (attached below; see Figure 3.1).

Best regards,
Rohit

https://drive.google.com/open?id=1sdKT0URYt_byn8nO0kHkYgn4mXKueJfY

--

Rohit Chhiber
Dept. of Physics and Astronomy
University of Delaware
Newark, DE

Phone: 302-831-4355

E.4 Permission from Springer Nature for Figure 8.4

RightsLink Printable License

<https://s100.copyright.com/CustomerAdmin/PLFj...>

SPRINGER NATURE LICENSE TERMS AND CONDITIONS

Jul 03, 2018

This Agreement between Mr. Rohit Chhiber ("You") and Springer Nature ("Springer Nature") consists of your license details and the terms and conditions provided by Springer Nature and Copyright Clearance Center.

License Number	4330580858871
License date	Apr 16, 2018
Licensed Content Publisher	Springer Nature
Licensed Content Publication	Solar Physics
Licensed Content Title	RADIO MAPS OF THE SOLAR WIND TRANSITION REGION
Licensed Content Author	N. A. LOTOVA, K. V. VLADIMIRSKII, O. A. KORELOV
Licensed Content Date	Jan 1, 1997
Licensed Content Volume	172
Licensed Content Issue	1
Type of Use	Thesis/Dissertation
Requestor type	academic/university or research institute
Format	electronic
Portion	figures/tables/illustrations
Number of figures/tables /illustrations	1
Will you be translating?	no
Circulation/distribution	<501
Author of this Springer Nature content	no
Title	Studies in Solar Wind Dynamics
Instructor name	n/a
Institution name	n/a
Expected presentation date	May 2018
Portions	Figure 2
Requestor Location	Mr. Rohit Chhiber 260 S Main St E3 NEWARK, DE 19711 United States Attn: Mr. Rohit Chhiber
Billing Type	Invoice

E.5 Permission from Dr. Prachanda Subedi for Figure B.1



Rohit Chhiber <rohitc@udel.edu>

Permission letter for reproducing figure from your thesis

Prachanda Subedi <prasub@udel.edu>
To: Rohit Chhiber <rohitc@udel.edu>

Tue, Jul 3, 2018 at 12:44 PM

Granted

Sent from my iPhone

On Jul 3, 2018, at 11:46 AM, Rohit Chhiber <rohitc@udel.edu> wrote:

Dear Prachanda,

I am writing to request your permission to reproduce Figure 3.2 from your thesis [Subedi 2017] in Appendix B of my dissertation (attached below; see Figure B.1).

Best regards,
Rohit

https://drive.google.com/open?id=1sdKT0URYt_byn8nO0kHkYgn4mXKueJfY

--

Rohit Chhiber
Dept. of Physics and Astronomy
University of Delaware
Newark, DE

Phone: 302-831-4355